Search for Scalar Bottom and Top Quarks with the ATLAS Detector at the LHC

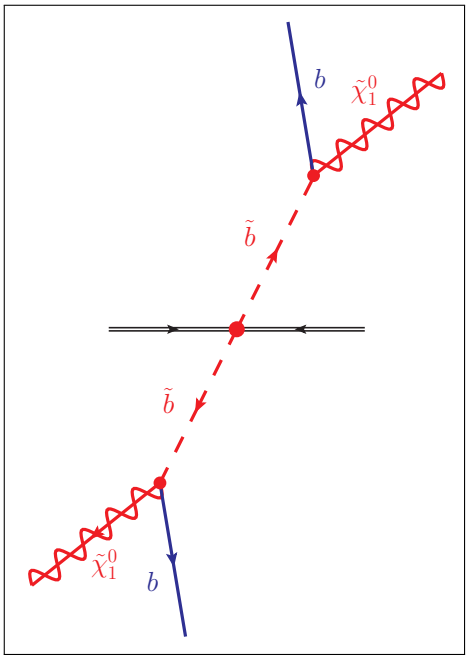

Dissertation zur Erlangung des Doktorgrades der Fakultät für Mathematik und Physik der Albert-Ludwigs-Universität Freiburg im Breisgau

vorgelegt von

Mirjam Fehling-Kaschek

Juni 2013

Dekan:	Prof. Dr. Michael Růžička
Betreuer der Arbeit:	Prof. Dr. Karl Jakobs
Referent:	Prof. Dr. Karl Jakobs
Koreferent:	Prof. Dr. Jochum Johan van der Bij
Prüfer (Theoretische Physik):	JProf. Dr. Harald Ita
Prüfer (Experimentalphysik):	Prof. Dr. Gregor Herten
Datum der mündlichen Prüfung:	17.07.2013

Contents

CHAPTER 1

Introduction

In November 2009, a new era of high-energy physics started. The first proton-proton collisions were observed at the world's most powerful particle accelerator, the Large Hadron Collider (LHC). Since then, a great number of measurements have been accomplished. For the first time, it was possible to test the Standard Model of particle physics in proton-proton collisions for centre-of-mass energies up to 8 TeV. The biggest success so far was the discovery of a particle which appears to be the last missing item of the Standard Model, the Higgs boson. Another major area of interest at the LHC is the search for physics beyond the Standard Model. This includes the search for supersymmetric partners of the third generation quarks, which is the main topic of this thesis.

The Standard Model of particle physics (SM) describes the elementary structure of matter and the fundamental interactions of the elementary particles. In the past decades, it has successfully described the observations made in particle physics. A good confirmation of the SM was obtained by the discovery of the W and Z bosons in 1983 at CERN [1–4] and the discovery of the top quark in 1995 at Fermilab [5, 6]. In 2012, a particle consistent with the Higgs boson predicted by the SM was discovered by the ATLAS and CMS experiments [7, 8]. So far, no significant deviation from the prediction of the SM is observed. It should be stressed, however, that the SM contains about 20 free parameters that need to be determined experimentally. This raises the question if the SM can be embedded in a superior theory that explains these parameters. Furthermore, the SM only considers the weak, the electromagnetic and the strong interactions, while it is not possible to describe gravity, and there is no explanation for the hierarchy between the Planck scale and the electroweak scale which plays an important role for the stability of the mass of the Higgs boson. In addition, the SM does not provide an explanation for the large amount of dark matter in the universe that can be inferred from cosmological measurements. These open questions suggest that the SM is not the ultimate answer to the fundamental questions of particle physics.
A possible extension of the SM arises from the postulation of a new symmetry between the fermionic and bosonic states, called Supersymmetry. The supersymmetric extension of the SM predicts a supersymmetric partner particle for each SM particle. Several of the open questions of the SM can be resolved by Supersymmetry. However, in order to provide a solution for the hierarchy problem, the masses of the supersymmetric particles should not exceed the TeV scale.[1]
A large class of supersymmetric models predicts that the lightest supersymmetric particle

1 Natural units are assumed within this thesis: $c = 1$, $\hbar = 1$.

(LSP) is stable and only weakly interacting. The stable LSP can provide a candidate for dark matter. Its experimental signature is missing transverse momentum as it leaves the detector undetected.
This thesis focuses on the search for supersymmetric partners of third generation quarks, the sbottom and the stop, with the ATLAS detector. This is motivated by the fact, that these particles are predicted to be lighter than other supersymmetric particles to provide a natural solution of the hierarchy problem. Two scenarios for the production of sbottom and stop particles are considered depending on the mass hierarchy, the direct pair production and the gluino-mediated production (in cases where the gluino is light). The signatures exploited in this thesis are based on missing transverse momentum (due to the LSP), b-jets (from the decays of the sbottoms and stops), and no leptons (a focus is set on the sbottom production, where no leptons occur in the decay chains).

The thesis is structured as follows:
In Chapter 2, the theoretical foundation for the relevant aspects of particle physics is presented. This includes a brief description of the Standard Model of particle physics, an introduction to Supersymmetry and a discussion of the phenomenology of proton-proton collisions. Special emphasis is given on the motivation to search for third generation squarks.
In Chapter 3, an overview of the LHC and the ATLAS detector is given, including a brief description of the individual subdetectors and the detector simulation.
In Chapter 4, the performance of the ATLAS experiment is described. Within this chapter, the data taking periods are briefly summarised and methods to reconstruct physical objects are explained.
In Chapter 5, a general overview of searches for Supersymmetry with the ATLAS detector is given. It includes a brief introduction to the phenomenology of supersymmetric processes at the LHC, the various searches performed by the ATLAS collaboration and the common analysis techniques that are also applied for the analyses presented in the following chapters.
In Chapter 6, an analysis investigating the direct production of sbottom and stop particles is presented. The main focus is set on the search for pair-produced sbottoms that decay to a neutralino and a b-quark, including a detailed discussion of the event selection and background estimation. The results of this search are used to make interpretations for scenarios with direct stop production, where the stop decays via a chargino to the neutralino for a small mass splitting between the chargino and neutralino. During the course of this thesis, major contributions were made to all parts of this analysis, including optimisation studies, background estimation, estimation of systematic uncertainties and the statistical interpretation of the results.
In Chapter 7, the gluino-mediated production of sbottom and stop particles is investigated. Two analyses are presented, that were performed at different stages of the data taking. The main contributions to these analyses made within this thesis are an alternative method to validate the background estimation and the estimation of various sources of systematic uncertainties.
In Chapter 8, the major results of this thesis are summarised.
Two topics that were investigated in addition within this thesis are discussed in the appendix: a search strategy for $h \to b\bar{b}$ resonances is presented in Appendix A, and a user interface for the offline data monitoring is presented in Appendix B.

CHAPTER 2

Theoretical Overview

In this chapter, the fundamental theoretical aspects of the presented work are introduced. The Standard Model (SM) of particle physics is briefly summarised in Section 2.1. It is the basis of modern particle physics. An extension of the SM is provided by Supersymmetry (SUSY). Since the search for SUSY is the main topic of this thesis, the general concepts and relevant details are presented in Section 2.2. A special focus is set in Section 2.3 on the physics in pp collisions.

2.1 The Standard Model of Particle Physics

The elementary structure and interaction of matter is formulated within the Standard Model of particle physics, based on the theoretical framework of quantum field theory.
The SM was developed in the 1960-1970s and is able, after fixing the free parameters, to describe the current experimental data with great success. To begin with, a short overview of the particle content of the SM is given, followed by an introduction to the particle interactions. A more comprehensive description of the SM can be found in various textbooks, for example in Refs. [9, 10].

2.1.1 Particle Content

The particles are described by quantum mechanics and characterised by their quantum numbers, as for example the electric charge, colour charge, spin or weak isospin. They are grouped into two categories: fermions (half-integer spin) as matter constituents and bosons (integer spin) as force carriers.

Matter Particles
The known fermions are the leptons and quarks, both with spin $\frac{1}{2}$. They are grouped into three generations. In Table 2.1, the particles are listed together with their electric charge. For each of the listed particles, also an anti-particle with opposite charge and parity but the same mass and spin exists. The first generation consists of the electron and the electron-neutrino (lepton sector) and the up- and down-quarks (quark sector). The visible matter is built from these particles. The particles of the second and third generation are heavy copies of the first generation, having the same quantum numbers but a different mass. In principle, the existence of further generations is possible and direct searches for it are performed by the

LHC experiments [11, 12].[1]
A general difference of leptons and quarks is that quarks are colour charged and therefore cannot be observed as free particles. They are confined to bound states, called hadrons. Two types of hadrons are known: the mesons formed by a $q\bar{q}$ pair with integer spin and the baryons formed by quark triples (qqq or $\bar{q}\bar{q}\bar{q}$) with half-integer spin.
The lepton masses range from 0.511 MeV for the electron to 1776 MeV for the tau lepton [14]. Neutrinos are implemented in the SM as massless particles even though evidence for massive neutrinos is given by numerous experiments measuring neutrino oscillations [15].[2] Masses for the quarks, except the top quark, need to be extrapolated with the help of theoretical models as the hadrons contain a large portion of potential binding energy. They are of the order of a few MeV for the first generation quarks and increase to about 4.2 GeV for the bottom quark [14]. The mass of the top quark can be measured directly as the top quark decays after approximately $4 \cdot 10^{-25}$ s, before it can be bound into a hadron. With a mass of 173 ± 0.6 (stat) ± 0.8 (syst) GeV [14] it is the most massive particle within the SM.

	1st Generation	2nd Generation	3rd Generation	Charge [e]
Leptons	ν_e (electron neutrino)	ν_μ (muon neutrino)	ν_τ (tau neutrino)	0
	e (electron)	μ (muon)	τ (tau)	-1
Quarks	u (up)	c (charm)	t (top)	$+\frac{2}{3}$
	d (down)	s (strange)	b (bottom)	$-\frac{1}{3}$

Table 2.1: Leptons and quarks with their electric charge.

Force Carriers

The gauge bosons are regarded as transmitters of the particle interactions and carry spin 1. The photon (γ) is the carrier of the electromagnetic force, the $W^\pm$ and Z bosons mediate the weak interaction and the gluon (g) is associated with the strong interaction. In Table 2.2 the particles are listed together with their electric charge and mass. More information on the interactions and the meaning of the gauge bosons is given in the next section.

Gauge Boson	Charge [e]	Mass [GeV]
γ	0	$< 10^{-27}$
$W^\pm$	± 1	80.385 ± 0.015
Z	0	91.1876 ± 0.0021
g	0	0

Table 2.2: The gauge bosons with their electric charge and mass [14].[3]

1 The existence of further light neutrinos is ruled out by the decay width of the Z boson [13].
2 The SM Lagrangian density can be extended with a right handed neutrino term to include the neutrino masses.
3 The photon and gluons are assumed massless and do not carry electric charge. Experimentally only upper limits can be obtained that are summarised in Ref. [14].

Higgs Boson

The incorporation of masses for the massive vector bosons into the SM can be achieved via the Higgs mechanism, described in the next section. An additional field with spin 0, the Higgs field, is thereby introduced. Up to the start of the LHC, the Higgs boson was the only undetected particle of the SM. Its discovery therefore was (and still is) one of the main interests of the LHC. The discovery of a particle consistent with the Higgs boson was published in 2012 by the ATLAS [7] and CMS [8] collaborations. The mass of the new boson is measured to be 125.5 ± 0.2 (stat) $^{+0.5}_{-0.6}$ (syst) GeV by the ATLAS experiment [16] and 125.8 ± 0.4 (stat) $\pm$ 0.4 (syst) GeV by the CMS experiment [17].

2.1.2 Particle Interactions

The SM describes the electromagnetic, the weak and the strong interactions of particles. Gravitation is the only known force that could not be included so far, but its effect is negligible compared to the other interactions at the energy ranges of the current particle colliders. All three interactions are described by quantum field theories. The Quantum Electrodynamics (QED) is the oldest and simplest formulation of such a theory and describes the electromagnetic interaction of charged particles. A closed formulation of the weak interaction is only possible in the electroweak unification which was developed by Glashow, Salam and Weinberg (GSW) [18–20]. Also the Higgs mechanism is implemented within this context. The strong interaction is described by Quantum Chromodynamics (QCD). In the following, the theories will be briefly introduced.

Quantum Electrodynamics

The Lagrangian density of a free particle with mass m and spin $\frac{1}{2}$, described by the Dirac spinor ψ, is given by

$$\mathcal{L} = i\overline{\psi}\gamma_\mu\partial_\mu\psi - m\overline{\psi}\psi, \tag{2.1}$$

where ∂_μ ($\mu = 0,\ldots,3$) are the partial space-time derivatives, γ^μ ($\mu = 0,\ldots,3$) are the 4×4 Dirac matrices and $\overline{\psi} = \psi^\dagger\gamma^0$ is the adjoint of ψ. It is invariant under global gauge transformations of the form $\psi \to e^{i\theta}\psi$ for any real parameter θ. The postulation of local gauge invariance $\theta \to \theta(x)$ is the main principle to establish QED. The Lagrangian density given in Eq. (2.1) is not invariant under $\psi \to e^{i\theta(x)}\psi$ transformations, but invariance is achieved by replacing the partial derivatives with gauge covariant derivatives: $\partial_\mu \to D_\mu \equiv \partial_\mu - iqA_\mu$. Thereby, a gauge field A_μ is introduced that couples to the Dirac particle of charge q. The new field can be interpreted as photon field if a free field term of the form $F_{\mu\nu}F^{\mu\nu}$ with $F_{\mu\nu} = \partial_\mu A_\nu - \partial_\nu A_\mu$ is added to the Lagrangian density. A mass term is not allowed as it would destroy the invariance again. A new, local gauge invariant Lagrangian density is built:

$$\mathcal{L} = i\overline{\psi}\gamma_\mu\partial_\mu\psi - m\overline{\psi}\psi + q\overline{\psi}\gamma^\mu A_\mu\psi - \frac{1}{4}F_{\mu\nu}F^{\mu\nu}. \tag{2.2}$$

It comprises the free Lagrangian density of a Dirac field, the free Lagrangian density of the massless photon field and the coupling of the photon to the Dirac field.
The phase transitions $e^{i\theta}$ belong to the group of unitary 1×1 matrices $U(1)$. Hence, the underlying symmetry is denoted as $U(1)$ gauge invariance. According to the theorem of Noether [21], a law of conservation is associated with the symmetry. In QED the conservation of the electric charge q follows.

Perturbative Cross-Section Calculation

One of the main theoretical aspects in particle physics is the calculation of probabilities for scattering processes. In general, the probability for a transition from an initial to a final state is given by the integration over the Hamiltonian density of the system. As usually no exact solution for the integral can be found, perturbation theory is applied. Each term of the perturbation series can be graphically displayed by a so-called Feynman diagram. The diagrams are built from three ingredients: external lines show the incoming and outgoing particles, internal lines describe virtual particles that do not obey the energy momentum relation ($E^2 = m^2 + p^2$) and vertices are the points of interaction where the external and internal lines are connected.[4] The QED vertex is shown in Fig. 2.1a.

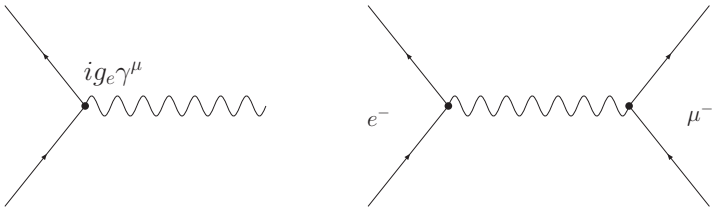

(a) QED vertex **(b)** e-μ scattering

Figure 2.1: QED interaction vertex (a) and leading order Feynman diagram for electron-muon scattering (b).

The Feynman diagrams are translated back to mathematical expressions by the Feynman rules, which are derived from the Lagrangian density. A mathematical term is associated with each element of the diagram and the expression for the whole diagram corresponds to one term of the sum of the perturbation series for the transition probability. Each vertex contributes with a term proportional to the expansion parameter of the series, the coupling constant[5]. The order of a diagram is determined by the number of vertices. The contributions of higher orders can often be neglected, assuming the coupling constant is small. Cross-sections are usually calculated in leading order (LO), next-to-leading order (NLO) or next-to-next-to-leading order (NNLO).[6] In Figure 2.1b, the leading order contribution for electron-muon scattering is shown.
Corrections to higher-order calculations can contain virtual loops. The loops lead to divergences, because the virtual particles in the loops do not obey the energy momentum relation and all possible energy-momentum combinations inside the loop need to be integrated over. The divergences are absorbed by a redefinition of the measurable quantities such as the coupling constants and masses. This process, referred to as renormalisation, leads to an energy dependence of the observables and the introduction of a reference energy scale, the renormalization scale μ_R.

Quantum Chromodynamics

The strong interaction is binding the quarks to hadrons and is also known for binding the nucleons in the nucleus. The coupling is connected to the colour charge of the interacting

4 The time axis is chosen vertical within this thesis: the incoming particles are shown at the bottom and the final state particles at the top of the diagrams.
5 In QED, the coupling constant g_e is proportional to the electric charge q of the interacting fermion.
6 In some cases, the expansion is rearranged to include the leading-logarithmic terms, referred to as resummation. The next-to-leading-logarithmic order is denoted as NLL.

particles, analogous to the electric charge in QED. In contrast to the electric charge, three colour states exist. Thus, the gauge symmetry is described by the $SU(3)$ group (unitary 3×3 matrices with unity determinant). Each (anti-)quark carries an (anti-)colour, but only colourless particles are observed in nature. As a consequence, the confinement of quarks into hadrons is attained: colourlessness is achieved by adding a colour-anticolour pair (meson) or all colours with equal amounts (baryon). Leptons do not participate in the strong interaction as they do not carry colour.
The strong interaction is mediated via gluons which carry a colour and anticolour in contrast to the electrically neutral photons. Nine possible combinations can be built from the colour and anticolour charges. Under $SU(3)_c$ they form a singlet and an octet. Only the colour singlet could propagate as free particle, but would introduce a long distance interaction with a strong coupling which is not observed in nature. The eight gluons of the colour-octet are the known mediators of the strong interaction and change the quark colours when coupling to them. In Figure 2.2a, the QCD vertex for quark-gluon coupling is shown. The coupling constant g_s is accompanied by a Gell-Mann matrix λ^α, $\alpha = 1, \ldots, 8$ which form a fundamental representation of $SU(3)_c$. A further difference to QED is given by the fact that $SU(3)_c$ is a non-Abelian group and therefore self couplings of the gluons are introduced as shown in Fig. 2.2b.

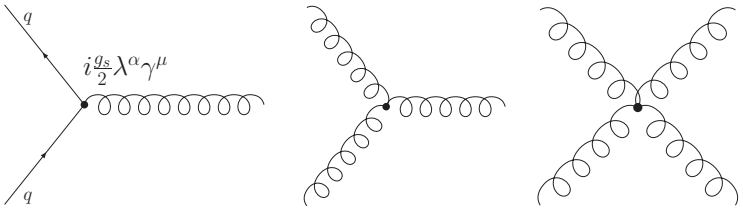

(a) g-q coupling **(b)** self couplings of the gluons

Figure 2.2: QCD vertices for the quark-gluon (a) and the gluon self couplings (b).

At the LHC, QCD processes play a fundamental role. A more detailed description of the hadron-hadron interaction is given in Section 2.3.

Weak Interaction

The weak interaction is mediated via the three vector bosons ($W^\pm, Z$). In Figure 2.3, the vertices for the couplings to the matter particles are shown. In addition, there are self couplings of the vector bosons and couplings to the photon. The couplings to the $W^\pm$ bosons change the flavour of the interacting fermions. In the lepton sector, a lepton ℓ is converted to the associated neutrino ν_ℓ or vice versa, as shown in Fig. 2.3a. In the quark sector, any "up-type" quark (u, c, t) is converted to any "down-type" quark (d, s, b), as shown in Fig. 2.3b. A mixing of the interacting quarks is thereby introduced, meaning that the mass eigenstates do not correspond to the eigenstates of the weak interaction. The mixing is described by the Cabibbo-Kobayashi-Maskawa matrix [22].[7] The neutral boson Z couples to any quark or lepton as shown in Fig. 2.3c. At leading order, the incoming and outgoing fermion is identical. The existence of flavour changing couplings to the Z boson is strongly restrained by theory and experimental observations but could occur in higher orders or processes beyond the SM.

7 In the SM, no mixing is allowed for the lepton sector due to the massless neutrinos. However, a mixing of the weak and mass eigenstates is observed by the neutrino experiments, as reported in Ref. [15].

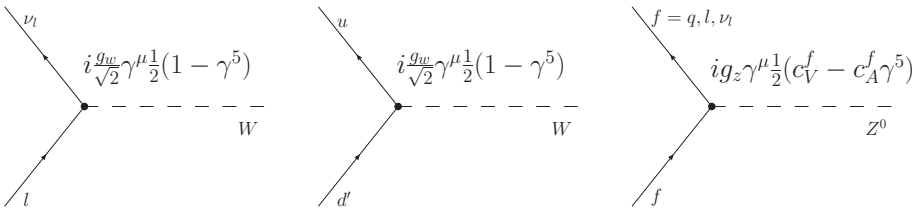

(a) $W^\pm$ coupling in the lepton sector

(b) $W^\pm$ coupling in the quark sector

(c) Z coupling to fermions

Figure 2.3: Vertices for the weak interaction.

A general difference is observed between the weak interaction vertices and the electromagnetic or strong interaction vertices: the factor $(1-\gamma^5)$, where $\gamma^5 = i\gamma^0\gamma^1\gamma^2\gamma^3$. The term $\overline{\psi}\gamma^\mu\psi$ corresponds to a vector, while $\overline{\psi}\gamma^\mu\gamma^5\psi$ is an axial vector that transforms differently under parity transformations. For the $W^\pm$ interaction vertex, a pure vector-axial vector (V-A) structure with equal strength is obtained. In case of the Z vertex, the vector and axial-vector couplings can be different, parametrised by the axial-coupling constant c_A and the vector-coupling constant c_V which depend on the fermion type.

Electroweak Unification

Glashow, Salam and Weinberg were able to unify the weak interaction with the electromagnetic interaction to the electroweak theory [18–20].
Charged currents are obtained by multiplying the $W^\pm$ vertices with the incoming and outgoing spinors. The charge raising current for an incoming lepton and outgoing neutrino is given by $J_\mu^+ = \overline{v}\gamma_\mu\frac{1}{2}(1-\gamma^5)u$, where $\overline{v}$ and u are the spinors for the neutrino and the lepton. By splitting the spinors into a right handed and left handed part

$$u = \frac{1}{2}(1-\gamma^5)u + \frac{1}{2}(1+\gamma^5)u \equiv u_L + u_R, \tag{2.3}$$

the current becomes $J_\mu^+ = \overline{v}_L\gamma_\mu u_L$, only involving the left handed components. In general, it can be shown that only the left handed particles and the right handed anti-particles participate in the charged weak interaction. The neutral current is given by $J_\mu^{NC} = \overline{u}\gamma_\mu\frac{1}{2}(c_V - c_A\gamma^5)u$. It includes both, a right handed and a left handed component, unless $c_V = c_A$.
The charged currents can be written in a two-component form of $J_\mu^\pm = \overline{\chi}_L\gamma_\mu\tau_\pm\chi_L$, where χ_L denotes the isospin doublet for leptons or quarks[8] and $\tau_\pm$ correspond to the creation and annihilation operators built from the Pauli matrices $\tau_{1/2}$ ($\tau_\pm = \frac{1}{2}(\tau_1 \pm i\tau_2)$). This suggests that the underlying symmetry of the weak interaction is described by the $SU(2)$ group. For an isospin triplet of weak currents, a third neutral current would follow as $J_\mu^3 = \overline{\chi}_L\gamma_\mu\tau_3\chi_L$ that would only couple to left handed particles. It can be split into two components via the Gell-Mann-Nishijima relation $Q = T^3 + \frac{1}{2}Y$: an electromagnetic current for the electric charge Q ($j_\mu^{em} = -\overline{u}_L\gamma_\mu u_L - \overline{u}_R\gamma_\mu u_R$) and a current for the hypercharge Y ($j_\mu^Y = 2j_\mu^{em} - 2J_\mu^3$). An additional $U(1)$ symmetry is imposed by the hypercharge, denoted as $U(1)_Y$. In total, the

8 The isospin doublets are given by $\chi_L = \begin{pmatrix} \nu_l \\ l \end{pmatrix}_L$ and $\chi_L = \begin{pmatrix} u \\ d' \end{pmatrix}_L$, where d' denotes the down-type quarks mixed by the CKM matrix.

symmetry of the electroweak theory is given by:

$$SU(2)_L \times U(1)_Y. \tag{2.4}$$

The generators of both groups commute and therefore all particles of an isospin multiplet carry the same hypercharge. An isospin triplet of fields W_μ^i is introduced that couples to the isospin currents with strength g and a singlet field B_μ is introduced that couples to j_μ^Y with strength $g'/2$. The $W^\pm$ bosons are built from the charged fields: $W_\mu^\pm = \frac{1}{2}(W_\mu^1 \mp iW_\mu^2)$. The photon and the Z boson result from a mixture of the neutral fields:

$$A_\mu = B_\mu \cos\theta_w + W_\mu^3 \sin\theta_w, \tag{2.5}$$
$$Z_\mu = -B_\mu \sin\theta_w + W_\mu^3 \cos\theta_w. \tag{2.6}$$

The mixing angle θ_w is called weak mixing angle and connects the coupling constants g and g' via $g \sin\theta_w = g' \cos\theta_w$.

Higgs Mechanism

It is not possible to include mass terms for the massive gauge bosons of the form $M^2 W_\mu W^\mu$ in the SM Lagrangian density without destroying local gauge invariance. The SM would loose its predictive power as non renormalisable divergences would be induced.
A way of generating the masses while conserving the gauge invariance is provided by the Higgs mechanism [23–25]. Scalar fields ϕ_i with a potential $V = \frac{1}{2}\mu^2\phi_i^2 + \frac{1}{4}\lambda(\phi_i^2)^2$, where $\lambda > 0$ and $\mu^2 < 0$, are introduced. The one-dimensional projection of the potential is shown in Fig. 2.4. The ground state of the field ϕ_i is given by the potential minima which are observed at $\phi_i = \pm v = \pm\sqrt{\frac{-\mu^2}{\lambda}}$ and not at the origin $\phi_i = 0$. By choosing any of the ground states, the explicit symmetry of the Lagrangian density is broken. This is also denoted as spontaneous symmetry breaking. The theorem of Goldstone shows that massless scalar particles, the Goldstone bosons, are generated by the symmetry breaking. These bosons are no real particles and only show up in the Lagrangian density for certain parametrizations of the fields. Nevertheless, their degrees of freedom can be absorbed into longitudinal polarisations of the boson fields to make them massive.

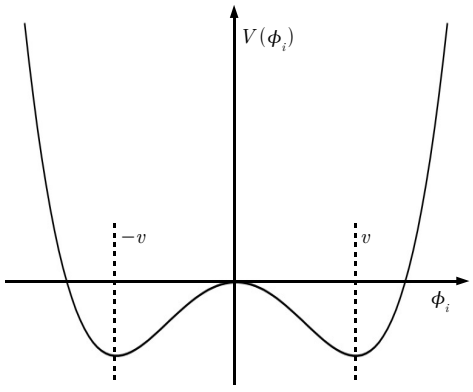

Figure 2.4: One-dimensional projection of the Higgs potential $V(\phi_i)$ with minima at $\phi_i = \pm v$.

To give mass to the three gauge bosons, $W^\pm$ and Z, the Lagrangian density of the Higgs field must obey the $SU(2)_L \times U(1)_Y$ symmetry:

$$\mathcal{L}_{\text{Higgs}} = |(i\partial_\mu - g\vec{\tau}\cdot\vec{W}_\mu - g'\frac{Y}{2}B_\mu)\phi|^2 - V(\phi), \tag{2.7}$$

where $V(\phi)$ is of the structure shown above. Four real scalar fields ϕ_i are introduced and usually arranged to an isospin doublet with $Y = 1$:

$$\phi = \frac{1}{\sqrt{2}} \begin{pmatrix} \phi_1 + i\phi_2 \\ \phi_3 + i\phi_4 \end{pmatrix}. \tag{2.8}$$

A common choice of the ground state is given by $\phi_0 = \sqrt{\frac{1}{2}} \begin{pmatrix} 0 \\ v \end{pmatrix}$, which breaks the local symmetries of $SU(2)_L$ and $U(1)_Y$. When inserting ϕ_0 in the Lagrangian density the following terms are obtained:

$$\left(\frac{1}{2}vg\right)^2 W_\mu^+ W^{-\mu} + \frac{1}{8}v^2 (W_\mu^3, B_\mu) \begin{pmatrix} g^2 & -gg' \\ -gg' & g'^2 \end{pmatrix} \begin{pmatrix} W^{3\mu} \\ B^\mu \end{pmatrix}. \tag{2.9}$$

They can be interpreted as mass terms and the matrix of the second term is diagonalised through a basis transformation from (W_μ^3, B_μ) to (Z_μ, A_μ). A massless photon and massive W and Z bosons follow:

$$M_W = \frac{1}{2}vg, \qquad M_Z = \frac{1}{2}v\sqrt{g^2 + g'^2} = \frac{M_W}{\cos\theta_w}, \qquad M_\gamma = 0. \tag{2.10}$$

Also the lepton and quark masses can be generated with the Higgs doublet of Eq. (2.8). Another term respecting the $SU(2)_L \times U(1)_Y$ symmetry, denoted as $\mathcal{L}_{\text{Yukawa}}$, is added to the Lagrangian density:

$$\mathcal{L}_{\text{Yukawa}} = -G_l^{ij} \bar{L}_L^i \phi l_R^j - G_d^{ij} \bar{Q}_L^i \phi d_R^j - G_u^{ij} \bar{Q}_L^i \phi_C u_R^j + \text{hermitian conjugate}, \tag{2.11}$$

where $\bar{L}_L^i$ ($\bar{Q}_L^i$) are the lepton (quark) isospin doublets and l_R^j (d_R^j, u_R^j) are the corresponding isospin singlets. The coupling constants are denoted by G_l^{ij}, G_d^{ij} and G_u^{ij} and also account for the mixing of the weak eigenstates in the quark sector. The field $\phi_C \equiv -i\tau_2\phi^*$ is needed in order to generate masses for the up-type quarks. There is no prediction for the size of the masses since they appear in the form of free coupling parameters (e.g. $m_e = \frac{G_e v}{\sqrt{2}}$).
The Higgs field arises as fluctuation around the ground state: $v \to v + h(x)$. It is the only field left of the four initial fields, as the other three fields are absorbed to give masses to the vector bosons. The mass of the Higgs boson follows as $m_h = v\sqrt{2\lambda}$.
In addition to the mass terms, various couplings of the Higgs boson to the vector bosons, the photon and the fermions are obtained from $\mathcal{L}_{\text{Higgs}}$ and $\mathcal{L}_{\text{Yukawa}}$. Two examples are shown in Fig. 2.5: the trilinear vertices for the h-W coupling and the h-e coupling. In general, the coupling strength is proportional to the mass of the interacting particle. The chirality of a fermion is changed by the Higgs coupling, as shown for the electron in Fig. 2.5b.

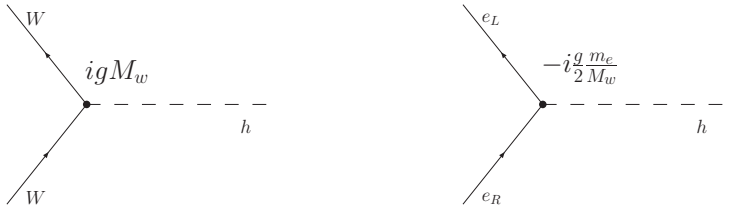

(a) h-W coupling **(b)** h-e coupling

Figure 2.5: Trilinear coupling of the Higgs boson to the W boson (a) and the electron (b).

Summary of the Standard Model
In summary, the gauge symmetry of the SM is described by

$$SU(3)_c \times SU(2)_L \times U(1)_Y. \tag{2.12}$$

The total Lagrangian density of the SM is obtained by adding the different terms for the previously introduced processes ($\mathcal{L}_{\mathrm{SM}} = \mathcal{L}_{\mathrm{EW}} + \mathcal{L}_{\mathrm{QCD}} + \mathcal{L}_{\mathrm{Higgs}} + \mathcal{L}_{\mathrm{Yukawa}}$) and consists of:

- Kinetic terms for the gauge bosons and fermions.
- Couplings of the fermions to the gauge bosons.
- Couplings of the fermions and gauge bosons to the Higgs boson.
- Self interactions of the gauge bosons and the Higgs boson.
- Mass terms for the fermions, gauge bosons and the Higgs boson.

It contains 19 free parameters, like the particle masses, coupling constants and mixing parameters. They need to be estimated experimentally which is unsatisfactory from a theoretical point of view. Attempts are made to unify the interactions at high energies to a grand unified theory (GUT) that would be described by only one unified coupling parameter.
There are a few problems, or better open questions, within the current version of the SM. They will be introduced in Section 2.2.1 in order to motivate a supersymmetric extension of the SM.

2.2 Supersymmetry

Supersymmetry (SUSY) provides a possible extension of the SM by introducing a new symmetry between bosonic and fermionic states. In Section 2.2.1, arguments to motivate this extension of the SM are given. An introduction to the fundamental concepts of the new symmetry follow in Section 2.2.2. The minimal supersymmetric extension of the SM (MSSM) is discussed in Section 2.2.3. An overview of various SUSY models is given in Section 2.2.4. In this thesis, the focus is set on the search for light third generation SUSY particles. A discussion on the aspects related to this is given in Section 2.2.5. For a more detailed introduction to SUSY, see for example Refs. [26, 27].

2.2.1 Motivation for an Extension of the SM

By construction, a supersymmetric extension of the SM contains the SM completely and can also describe the experimental observations made in accordance with the SM. The main motivation for the supersymmetric extension at the electroweak scale is given by the natural solution of the hierarchy problem. The hierarchy problem and a number of additional aspects in favour of a supersymmetric extension are briefly described in the following.

Hierarchy Problem
The hierarchy problem is related to the renormalisation of the mass of the Higgs boson. There is no symmetry in the SM that would prevent the Higgs boson suffering from radiative corrections in form of loop diagrams with the matter particles, the electroweak gauge bosons

and the Higgs boson itself.[9] The Higgs boson mass is therefore given as the sum of the "naked" mass $m_{h,N}$ and the contribution arising from the corrections Δm_h:

$$m_h^2 = m_{h,N}^2 + \Delta m_h^2. \tag{2.13}$$

The one-loop correction given by a fermion is shown in Fig. 2.6a and gives a contribution proportional to the coupling λ_F:

$$\Delta m_{h,\text{fermion}}^2 = \frac{\lambda_F^2}{8\pi^2}\left[-\Lambda^2 + 3m_f^2 \ln(\Lambda/m_f) + \ldots\right], \tag{2.14}$$

where m_f is the fermion mass and Λ denotes a cut-off scale that is introduced to handle the divergence of the loop integration.[10] The coupling λ_F is proportional to the fermion mass. Therefore the dominant contribution is given by the top quark. Bosonic loop corrections give contributions with the opposite sign compared to the fermionic loop corrections. After the top contribution, the next largest contributions come from the gauge bosons, followed by the Higgs boson. However, the gauge and Higgs boson contributions cannot cancel out the top contribution as they are much smaller in size.

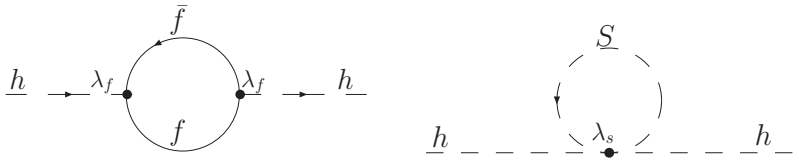

(a) Fermion loop **(b)** Boson loop

Figure 2.6: Loop corrections for the Higgs boson propagator.

The large radiation contribution has to be balanced by the naked Higgs boson mass ($m_{h,N}^2 \simeq -\Delta m_h^2$ for $m_h \sim \mathcal{O}(100\text{ GeV})$). For the cut-off at the Planck scale, this has to happen with a precision of 34 orders of magnitude, referred to as fine-tuning problem. Theoretically, the fine-tuning of the Higgs boson mass is possible. However, it appears unnatural from a physical point of view.

A natural solution of the fine-tuning problem is provided by SUSY: the divergent terms are cancelled out by additional terms from supersymmetric particles. The contribution of a scalar loop (Fig. 2.6b) is given by:

$$\Delta m_{h,\text{scalar}}^2 = \frac{\lambda_S}{16\pi^2}\left[\Lambda^2 - 2m_S^2 \ln(\Lambda/m_S) + \ldots\right], \tag{2.15}$$

where λ_S is the coupling of the scalar to the Higgs boson and m_S the mass of the scalar particle. An exact cancellation of the quadratic divergences can be achieved by adding a boson of the same mass for each fermion. There is no exact SUSY (see below), but the cancellation is still possible, provided that the masses of the SUSY particles are not too large ($m_S \sim \mathcal{O}(100\text{ GeV} - 1\text{ TeV})$).

9 For fermions, equivalent corrections are forbidden by chiral symmetry.

10 The cut-off represents the energy scale at which the theory breaks down (no longer describes the reality). It is typically placed at the Planck energy scale, at which gravity begins to play an important role. The Planck scale is about 17 orders of magnitude above the electroweak scale ($M_P \sim 10^{19}$).

Dark Matter

The visible matter, described by the SM, only contributes a small portion to the total energy density of the universe. Only about 4.9% consist of baryonic matter, while the rest is made of so-called dark energy (68.3%) and dark matter (26.8%) [28]. Dark energy is postulated to describe cosmological phenomena like the time dependence of the expansion of the universe. The existence of dark matter is anticipated because of gravitational effects: the rotational velocity of galaxies and gravitational lensing of background galaxies by foreground galaxies yield higher mass accumulations than the observed visible matter. Different sources to explain the missing matter were considered, like for example brown dwarfs or neutrinos, but the contributions from these known objects were found to be too small. One possible explanation for the dark matter contribution is the existence of a weakly interacting massive particle (WIMP). A number of experiments target the direct detection of those particles [29].
A good WIMP candidate is provided by the lightest supersymmetric particle, under the assumption of R-parity conservation (see below).

Unification

It may be possible to unify the SM interactions at high energies to a GUT. A GUT is usually described by a larger symmetry group, as for example SO(10), which breaks down to the SM symmetry groups at lower energies. As a result the three SM couplings would be unified to only one coupling constant. However, the evolution of the SM coupling constants shows that they do not meet at a common energy scale. The energy evolution of the inverse coupling constants is shown in Fig. 2.7. In case of a supersymmetric extension, it is possible to unify the three couplings at one energy scale: the unification for a MSSM scenario (see Section 2.2.3) at $\sim 10^{16}$ GeV is also shown in Fig. 2.7.

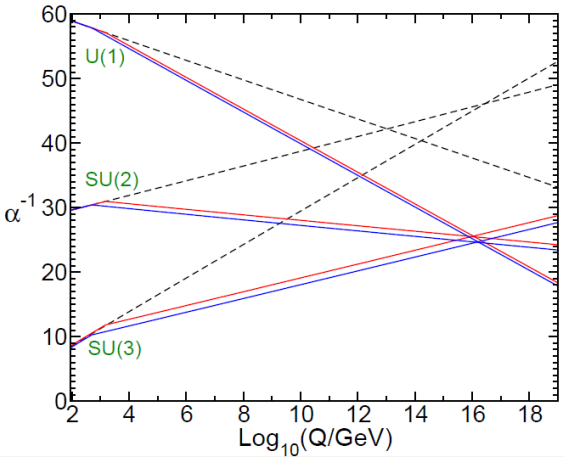

Figure 2.7: The evolution of the inverse coupling constants of the interactions with energy for the SM (dashed lines) and SUSY (solid lines) [26]. The SUSY model is based on a MSSM scenario, varying the masses of the supersymmetric particles between 500 GeV and 1.5 TeV and assuming $\alpha_3(Z)$ to lie between 0.117 and 0.121.

Gravity

On cosmological scales, gravity is well described by Einstein's general theory of relativity [30]. However, it is the only known force not contained in the SM. A consistent formulation as a quantum field theory is not feasible, since it would introduce non-renormalisable terms. Also, gravity does not follow from the postulation of local gauge invariance within the SM.

The effect of gravity is negligible at the energy scales of current accelerator experiments, but needs to be taken into account at the latest at the Planck-scale ($M_P \sim 10^{19}$ GeV).
The postulation of local gauge invariance under SUSY transformations leads to the introduction of a graviton-gravitino pair. Though, to make the theory renormalisable, it has to be embedded in a greater theory, as for example string theory.

2.2.2 Introduction to Supersymmetric Extensions of the SM

In SUSY, a transition from fermionic states to bosonic states and vice versa is introduced:

$$Q|\text{Boson}\rangle \propto |\text{Fermion}\rangle \tag{2.16}$$
$$Q|\text{Fermion}\rangle \propto |\text{Boson}\rangle, \tag{2.17}$$

where Q is the generator of the SUSY transformations.[11] A generalisation of the Coleman-Mandula theorem, the Haag-Lopuszanski-Sohnius theorem [32], shows that SUSY can be embedded in a consistent quantum field theory, implying that the SUSY generator is fermionic. In the SM, the symmetry generators of the $SU(3)_c \times SU(2)_L \times U(1)_Y$ gauge group are scalars and only particles of the same spin belong to the multiplets formed by the symmetry groups. The generator Q and its conjugate $Q^\dagger$ have spin $\frac{1}{2}$ and are described by Weyl spinors[12]. They satisfy the following algebra of commutator and anti-commutator rules:

$$\{Q, Q^\dagger\} = P^\mu, \quad \{Q, Q\} = \{Q^\dagger, Q^\dagger\} = 0, \quad [P^\mu, Q] = \left[P^\mu, Q^\dagger\right] = 0, \tag{2.18}$$

where P^μ is the momentum operator.
The invariant subspaces of the irreducible SUSY representation are called supermultiplets. Each supermultiplet contains a bosonic and a fermionic state, which are referred to as each others superpartners. The same number of degrees of freedom must be included for the fermionic and the bosonic state: $n_F = n_B$.

Chiral Supermultiplet:

- Spin $\frac{1}{2}$: Weyl fermion
- Spin 0: complex scalar field

The two chirality states of the fermion give $n_F = 2$ and therefore the bosonic state is expressed as complex scalar field.

Vector Supermultiplet:

- Spin 1: vector field
- Spin $\frac{1}{2}$: Weyl fermion

Two degrees of freedom are assigned to the vector field, which is assumed to be massless.[13]

11 In general, more than one SUSY generators can be introduced. The minimalistic option of one SUSY generator (plus its conjugate $Q^\dagger$), referred to as the Wess-Zumino model [31], is sufficient to describe the most interesting phenomenology and is considered here.

12 A Dirac spinor can be decomposed into two Weyl spinors (a left and a right handed). The Weyl spinor indices are omitted here.

13 As in the SM, no direct mass terms can be introduced and masses are obtained via symmetry breaking.

All particles of the SM can be included in these multiplets: the quarks, leptons and Higgs bosons[14] belong to chiral supermultiplets, while the gauge bosons belong to vector multiplets. The supersymmetric partner particles are distinguished from the SM particles by a tilde and denoted with a prefixed "s" in case of scalars (sfermion, squark, slepton, stop, sbottom, ...) and an appended "ino" in case of fermions (gaugino, higgsino, wino, ...).
The SUSY generators commute with the generators of the gauge group, which is chosen to be the SM gauge group. Therefore, the superpartners possess the same quantum numbers (electric charge, isospin, colour charge) and only differ in their spin. In addition, it follows from Eq. (2.18) that Q and $P^2 = P_\mu P^\mu$ commute, meaning that the superpartners have the same mass. However, no supersymmetric particles with masses equal to the SM masses are observed. Therefore, SUSY must be a broken symmetry if realised in nature (see below).
The Lagrangian density of the SM is extended to include additional terms for the supersymmetric partner particles. In general, terms for the following contributions are added:

- Couplings among the SUSY particles.
- Couplings of the SUSY particles to the SM particles.
- Kinetic terms for the SUSY particles.
- Mass terms for the SUSY particles.[15]

In Figure 2.8, a selection of possible vertices for the new interaction terms is shown.[16] On the one hand, gauge interactions, as shown in Fig. 2.8a, are added: they show the couplings of the scalar particles to the gauge bosons and additional couplings for the gauginos. On the other hand, couplings among the particles of the chiral multiplets, as shown in Fig. 2.8b, are in principle possible. They comprise Yukawa couplings between the fermions and scalars and couplings among the scalar particles. The triple scalar coupling has the dimension of a mass, while the quartic scalar coupling and the Yukawa coupling are dimensionless.

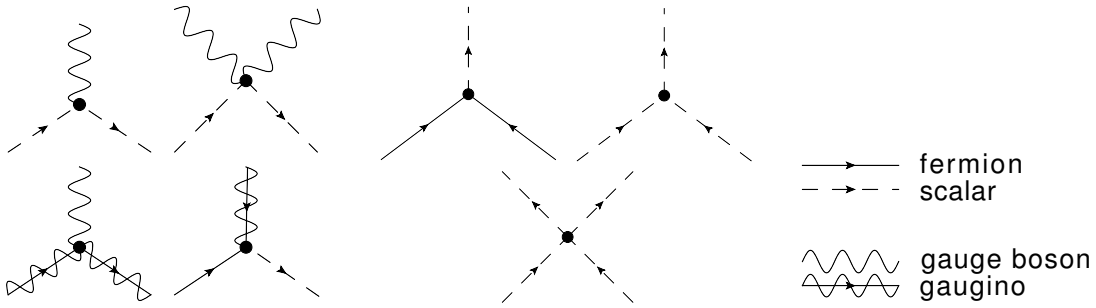

(a) gauge interactions **(b)** chiral vertices

Figure 2.8: Additional interaction vertices involving the supersymmetric partner particles.

14 In SUSY at least two Higgs doublets need to be included, which leads to more than one Higgs boson (see Section 2.2.3).
15 Most of the mass terms are included only by SUSY breaking, as these terms are highly restricted by the unbroken (SUSY invariant) part of the Lagrangian density.
16 It should be noted that the list of diagrams is not complete. A more detailed discussion can be found for example in Ref. [26].

R-parity

The general supersymmetric Lagrangian density contains terms that violate the conservation of the lepton and baryon number. This violation is constrained by a number of experimental observations from direct searches, searches for neutral flavour changing currents, measurements of the proton lifetime and cosmological measurements. The mentioned terms can be suppressed by constraining the models on the basis of the experimental boundaries. Another approach is the introduction of a new preservative quantum number, R-parity, which explicitly forbids the terms. It is a multiplicative quantum number, defined by the baryon number B, the lepton number L and the spin S of the particle:

$$R = (-1)^{3(B-L)+2S} = \begin{cases} +1 & \text{SM particle} \\ -1 & \text{SUSY particle} \end{cases} \tag{2.19}$$

All SM particles have $R = 1$ and all SUSY particles have $R = -1$. If R-parity is conserved, the following restrictions on the SUSY models result:

- SUSY particles are produced in pairs.
- A SUSY particle decays into an odd number of SUSY particles.
- The lightest SUSY particle (LSP) is stable.

One of the main motivations for SUSY is hereby fulfilled: a candidate for dark matter is provided in form of the stable LSP. In this context, the LSP must be electrically neutral and cannot participate in the strong interaction, because otherwise it would have accumulated in the galaxies like normal matter and formed heavy isotopes that are not observed. The LSP also accounts for one of the most crucial SUSY signatures in R-parity conserving models, missing transverse momentum, since it leaves the detector undetected.
In the following, the conservation of R-parity is assumed. An exception is made in Section 5.9, where a short introduction on R-parity violating SUSY searches is given.

Supersymmetry Breaking

The masses of the SM particles cannot have arbitrary high values, as they arise from the electroweak symmetry breaking [33, 34]. In contrast, the SUSY particles are not bound by this condition and can have high masses in general. However, they should be at the order of a TeV to provide a natural solution of the hierarchy problem.
The breaking mechanism for SUSY is unknown. Most models consider a spontaneous symmetry breaking, which is theoretically favoured.[17] General constraints follow by retaining the natural solution of the hierarchy problem: the breaking must not induce terms in the Lagrangian density that destroy the cancellation of quadratic divergences for the Higgs boson mass or that result in new divergences. A common approach is to add all possibilities of the so-called soft SUSY breaking terms to the Lagrangian density:

$$\mathcal{L} = \mathcal{L}_{\text{SUSY}} + \mathcal{L}_{\text{SOFT}}, \tag{2.20}$$

where $\mathcal{L}_{\text{SUSY}}$ is SUSY invariant while $\mathcal{L}_{\text{SOFT}}$ breaks SUSY but still allows for a natural solution of the hierarchy problem and keeps the theory renormalisable. Terms included in

17 The explicit breaking of the symmetry is in principle possible, but would for example lead to inconsistencies in models including supergravity.

$\mathcal{L}_{\mathrm{SOFT}}$ are mass terms and coupling terms with the dimension of a mass (or higher powers thereof), as for example trilinear scalar couplings.[18]
Often, it is assumed that SUSY breaking occurs in a hidden sector, whose constituents hardly interact with the particles of the visible sector. The soft SUSY breaking terms occur when the breaking is transferred from the hidden to the visible sector, which is accomplished by a renormalisable interaction.

2.2.3 The Minimal Supersymmetric Standard Model

The MSSM contains the minimal particle content needed to make a supersymmetric extension of the SM and is based on the SM gauge group. A supersymmetric partner is assigned for each SM particle. The only possibility to identify the known bosons and fermions contained in the SM as each others partners is a supermultiplet built of the Higgs boson and the neutrino (the gauge bosons differ by their quantum numbers from the fermions). However, within the MSSM this multiplet is ruled out for different reasons, as for example a lepton number violation and a too massive neutrino would result.[19]
The chirality of the SM fermions is transferred to the sfermions. As for the SM, these states correspond to the interaction eigenstates and hence the W boson only couples e.g. to the $\tilde{u}_L$ and $\tilde{d}_L$, but not the $\tilde{u}_R$ and $\tilde{d}_R$. In general, the mass eigenstates are a mixture of the left and right states (see below). The Zino and the Photino are built from the Wino and Bino following the SM prescription:

$$\tilde{Z} = -\sin\theta_w \tilde{B} + \cos\theta_w \tilde{W}^3 \tag{2.21}$$

$$\tilde{\gamma} = \cos\theta_w \tilde{B} + \sin\theta_w \tilde{W}^3. \tag{2.22}$$

However, these states are not necessarily the mass eigenstates. Since SUSY is broken, the gauginos and higgsinos with different $SU(2)_L \times U(1)_Y$ numbers can mix to the following mass eigenstates:

Charginos $\tilde{\chi}^{\pm}_{1,2}$: mixture of the electrically charged fields ($\tilde{W}^{\pm}$,$\tilde{H}^{+}_{2}$,$\tilde{H}^{-}_{1}$).

Neutralinos $\tilde{\chi}^{0}_{1,2,3,4}$: mixture of the neutral fields ($\tilde{B}, \tilde{W}^3, \tilde{H}^{0}_{1,2}$).

The lightest neutralino $\tilde{\chi}^0_1$ is the LSP for the models studied in this thesis.[20]
There are two reasons, that two Higgs doublets are needed in the MSSM:

- In the SM, the masses of up-type quarks are obtained via the conjugated Higgs field H^* (see Section 2.1.2), but the Lagrangian density $\mathcal{L}(H,H^*)$ is not SUSY invariant. A second Higgs doublet allows to generate all the masses while keeping the Lagrangian density SUSY invariant.

- The supersymmetric partner of the Higgs boson contributes to gauge anomalies which destroy the renormalisability of the theory. The contributions can be cancelled by introducing a second Higgs doublet with inverted hypercharge.

18 In exact SUSY, the dimensionless couplings for the fermionic and scalar loops are related such that the quadratic loop divergences cancel. Therefore, no additional dimensionless couplings are allowed in $\mathcal{L}_{\mathrm{SOFT}}$, as they would destroy the cancellation.

19 The discussion of a model containing the Higgs-neutrino multiplet is given for example in Ref. [35].

20 Other candidates for the LSP are the sneutrino or gravitino (in models including gravity). The sneutrino being the LSP is, however, excluded by LEP data [36].

Chiral Supermultiplets		Spin 1/2	Spin 0
Lepton	L	$(\nu_e,\, e_L)$	$(\tilde{\nu}_e,\, \tilde{e}_L)$
	$\bar{e}$	$e_R^\dagger$	$\tilde{e}_R^*$
Quark	Q	$(u_L,\, d_L)$	$(\tilde{u}_L,\, \tilde{d}_L)$
	$\bar{u}$	$u_R^\dagger$	$\tilde{u}_R^*$
	$\bar{d}$	$d_R^\dagger$	$\tilde{d}_R^*$
Higgs	H_1	$(\tilde{H}_1^0, \tilde{H}_1^-)$	$(H_1^0,\, H_1^-)$
	H_2	$(\tilde{H}_2^+, \tilde{H}_2^0)$	$(H_2^+,\, H_2^0)$
Vector Supermultiplets		Spin 1	Spin 1/2
$U(1)$	$\hat{B}$	B	$\tilde{B}$
$SU(2)$	$\hat{W}$	$W^3 \quad W^\pm$	$\tilde{W}^3 \quad \tilde{W}^\pm$
$SU(3)$	$\hat{G}$	g	$\tilde{g}$

Table 2.3: Particle content of the MSSM. Only the first generation of the chiral lepton and quark fields are shown, the second and third generation follow analogously.

The doublets are denoted by

$$H_1 = \begin{pmatrix} H_1^0 \\ H_1^- \end{pmatrix}, \quad H_2 = \begin{pmatrix} H_2^+ \\ H_2^0 \end{pmatrix}, \tag{2.23}$$

where the leptons and down-type quarks couple to H_2 (also referred to as H_d) and the up-type quarks couple to H_1 (also denoted as H_u). Eight degrees of freedom are provided by the two doublets. Three are needed to give mass to the gauge bosons and the rest is left to built a set of five Higgs bosons:

- h, H^0: two CP even and neutral scalars.
- A: one CP odd and neutral scalar.
- $H^\pm$: two charged scalars.

The lightest one is the h boson, which can have similar properties as the SM Higgs boson. A MC study on the feasibility to find the h boson for different SUSY scenarios is given in Appendix A. At tree-level, the Higgs sector is described by only two free parameters. Typically, the mass of the pseudoscalar boson (M_A) and the ratio of the vacuum expectation values of the two Higgs doublets ($\tan\beta = \frac{v_2}{v_1}$) are chosen. A summary of the MSSM particle content is given in Table 2.3.
The MSSM is a R-parity conserving model. The SUSY invariant Lagrangian density contains a generalisation of the SM gauge couplings (e.g. $\tilde{g} \to q\tilde{q}$, $\tilde{W}^3 \to l\tilde{l}$), a generalisation of the SM Yukawa interactions (e.g. $\tilde{t}_L \to \tilde{H}_1^0 t_R$) and a supersymmetric version of the Higgs potential.[21] In addition, a minimal set of soft SUSY breaking terms is included. They

21 The couplings have the same strength as the ones given by the SM model gauge and Yukawa couplings. This follows by the construction of the SUSY invariant Lagrangian density and provides the natural solution of the hierarchy problem.

contain mass terms for the gauginos, sfermions and Higgs bosons, bilinear Higgs couplings and trilinear scalar couplings of the sfermions to the Higgs fields. It should be noted that SUSY breaking introduces a large number of additional parameters to the model. A total of 105 free parameters is added in form of masses, mixing angles and phases.

2.2.4 Model Building

The use of generic MSSM models for a physics analysis is impractical due to the large number of free parameters. In general, two classes of models with a reduced number of free parameters are distinguished:

Bottom-up models: phenomenological models (pMSSM) [37] or simplified models [38] are used to target specific scenarios by fixing the mass hierarchy of the SUSY particles and considering only a few dominant decay chains of the SUSY particles.

Top-down models: a high reduction of the parameters is obtained by assuming the unification at a GUT scale. The number of free parameters in the MSSM can be reduced down to five in the so-called constrained MSSM (cMSSM). In addition, specific assumptions on the SUSY breaking mechanism are made by the minimal supergravity model (mSUGRA) [39–43] and the gauge-mediated SUSY breaking model (GMSB) [44–49]. Another type of scenarios is obtained by supersymmetric versions of the SO(10) GUT [50].

Phenomenological MSSM

A significant reduction of the MSSM parameters can be obtained by considering general phenomenological observations. The number of free parameters is reduced to 22 by the following assumptions [37]:

- All SUSY breaking parameters are real, to prevent the theory from additional CP violating processes.
- The scalar mass matrices are diagonal and the trilinear coupling matrices are proportional to the corresponding Yukawa couplings[22], to prevent the theory from flavour changing neutral currents.
- Universality for the first and second sfermion generation is demanded (corresponding to equal mass parameters and equal trilinear couplings) to take into account several constraints as for example from kaon mixing.

The remaining parameters consist of the gaugino and sfermion masses, the proportionality factors A_f of the trilinear couplings, the squared Higgs boson masses and $\tan\beta$.

Constrained MSSM

The cMSSM is obtained by considering the MSSM as the solution of a GUT at low energies: the unification of the coupling constants at the GUT scale is assumed. A further reduction of the parameter space is achieved by adding the following GUT relations:

- unification of the trilinear couplings to A_0.

22 This means $\mathbf{a}_f = A_f \cdot \mathbf{y}_f$, e.g. for $\tilde{\bar{u}}\mathbf{a}_u\tilde{Q}H_1$ and $\bar{u}\mathbf{y}_u Q H_1$.

- unification of the gaugino masses to $m_{1/2}$.
- unification of the scalar masses to m_0.

The values for the masses and couplings at lower energy scales, like for example the electroweak scale, are obtained by applying the renormalization group equations. The evolution of the mass parameters is sketched in Fig. 2.9.

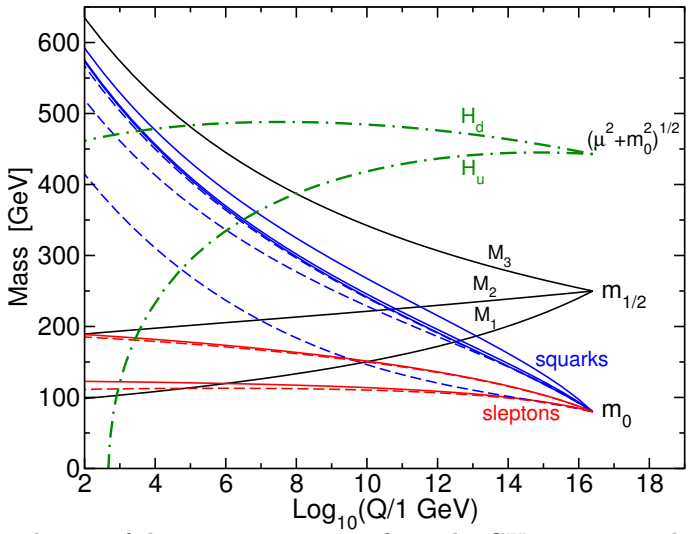

Figure 2.9: The evolution of the mass parameters from the GUT energy scale to the electroweak energy scale [26]. For the Higgs boson masses, the $(\mu^2 + m^2_{H_u,H_d})^{1/2}$ values are shown ($H_u \equiv H_1, H_d \equiv H_2$).

When all GUT relations are taken into account, the model is described by only four parameters and a sign:

$$m_0, \quad m_{1/2}, \quad A_0, \quad \tan\beta, \quad \text{sign}(\mu). \tag{2.24}$$

The absolute size of the Higgs boson mass parameter μ is determined from the values of m_0 and $\tan\beta$.

mSUGRA

So far, SUSY was considered as a global symmetry. Scenarios that are based on a local SUSY are referred to as supergravity (SUGRA) models. A new gauge field with spin $\frac{3}{2}$ is introduced under the postulation of local SUSY invariance. This field can be interpreted as gravitino. Together with its superpartner, the massless graviton with spin 2, it forms the gravitational supermultiplet. Therefore, the fourth interaction, gravity, is included in SUGRA models as a consequence of local SUSY invariance.
In the mSUGRA model, the SUSY breaking is mediated via gravity from a hidden sector to the visible sector, which consists of the MSSM particle spectrum. The same GUT relations as for the cMSSM are assumed, leading to the same set of free parameters. The LSP is the neutralino.

GMSB

In the GMSB model, SUSY breaking is induced by the electroweak and strong interactions. In contrast to the mSUGRA scenario, a light gravitino is predicted, which usually is the LSP.

SO(10) GUT

The grand unified theory SO(10) [51] can be considered in supersymmetric scenarios. The unification of the gauge couplings as well as the unification of the matter superfields are allowed by the SO(10) group. A general feature, arising from the matter unification, is that right-handed neutrinos need to be added. In addition, the unification of the third generation Yukawa couplings is assumed for the SUSY SO(10) models considered within this thesis. These models are briefly summarised in the following, details are given in Ref. [50].
The SO(10) SUSY is described by the following free parameters:

$$m_{1/2}, \quad m_{16}(1,2,3), \quad m_{10}, \quad M_D^2, \quad A_0, \quad \tan\beta, \quad \text{sign}(\mu), \tag{2.25}$$

where $m_{1/2}$, $m_{16}(1,2,3)$ and m_{10} are the unified masses of the gauginos, the scalar matter particles (per generation) and the soft Higgs terms (m_{H_1},m_{H_2}), respectively. The parameter M_D^2 describes a potential splitting of the soft Higgs terms, which arises when breaking the SO(10) symmetry. The other parameters are the trilinear coupling constants A_0, the ratio of the Higgs vacuum expectation values and the sign of the Higgs boson mass parameter μ.
The SO(10) splitting can affect all scalar masses via so-called D-term contributions, referred to as DT splitting. Another possibility is that the splitting only affects the Higgs sector ($m_{H_{1,2}}^2 = m_{10}^2 \pm M_D^2$), referred to as Higgs splitting (HS splitting). The unification of the Yukawa couplings is better described by the HS model. In case of the DT splitting model, specific assumptions on the neutrino Yukawa coupling and the mass splitting between the first+second and the third generation need to be added to allow for an approximate Yukawa coupling unification. Models obtained under this assumption are referred to as DR3 models.
A common feature of the HS and DR3 models is that large masses are predicted for the first and second generation sfermions (~ 10 TeV), while the third generation sfermion masses are lower ($\sim 1-3$ TeV). Light masses are obtained for the gluinos ($\sim 300-500$ GeV) and the lightest charginos and neutralinos ($m_{\tilde{\chi}_1^\pm}$,$m_{\tilde{\chi}_2^0} \sim 100-180$ GeV, $m_{\tilde{\chi}_1^0} \sim 50-90$ GeV).

Simplified Models

For the simplified models, each model is constructed by considering a general phenomenology of interest. The dominant production channels (e.g. $\tilde{g}\tilde{g}$ production) and decay modes (e.g. $\tilde{g} \to b\tilde{b}$ and $\tilde{b} \to b\tilde{\chi}_1^0$) are identified and implemented. Other processes are suppressed by setting the masses of non-contributing particles to large values (~ 5 TeV). The scenarios are therefore characterised by a small number of additional particles and branching ratios. Often, the model is described by only two free mass parameters, for example $m_{\tilde{b}}$ and $m_{\tilde{\chi}_1^0}$ for a model considering $\tilde{b}\tilde{b}$ production and $\tilde{b} \to b\tilde{\chi}_1^0$ with a 100% branching ratio.

2.2.5 Third Generation SUSY

This thesis focuses on the search for third generation squarks. This is motivated by the fact that the top squark (stop) and the bottom squark (sbottom) are predicted to be the lightest squarks for a large class of SUSY models.
One argument for the existence of light stop and sbottom mass eigenstates is given by the mixing of the weak eigenstates. In general, all sfermions with the same electric and colour charge can mix to new mass eigenstates. However, only the flavour conserving mixing of the

third generation sfermions can play an important role and is discussed here.[23] There are various terms in the SUSY-invariant and broken Lagrangian density that contribute to the squark masses. In case of the pMSSM, the following mass matrices result in the basis of the chiral eigenstates $\{\tilde{t}_L, \tilde{t}_R\}$ and $\{\tilde{b}_L, \tilde{b}_R\}$:

$$\mathcal{M}^2_{\tilde{t}} = \begin{pmatrix} m_t^2 + m^2_{\tilde{t}_L,\tilde{b}_L} + (\frac{1}{2} - \frac{2}{3}s^2_W)M_Z^2 c_{2\beta} & m_t(A_t - \mu\cot\beta) \\ m_t(A_t - \mu\cot\beta) & m_t^2 + m^2_{\tilde{t}_R} - \frac{2}{3}s^2_W c_{2\beta} M_Z^2 \end{pmatrix}, \tag{2.26}$$

$$\mathcal{M}^2_{\tilde{b}} = \begin{pmatrix} m_b^2 + m^2_{\tilde{t}_L,\tilde{b}_L} - (\frac{1}{2} - \frac{1}{3}s^2_W)M_Z^2 c_{2\beta} & m_b(A_b - \mu\tan\beta) \\ m_b(A_b - \mu\tan\beta) & m_b^2 + m^2_{\tilde{b}_R} + \frac{1}{3}s^2_W c_{2\beta} M_Z^2 \end{pmatrix}, \tag{2.27}$$

with $s_W = \sin\theta_w$ and $c_{2\beta} = \cos 2\beta$.[24] The transformation to the mass eigenstates gives a lighter mass eigenstate, denoted by $\tilde{t}_1$ and $\tilde{b}_1$, respectively, and a heavier mass eigenstate, denoted by $\tilde{t}_2$ and $\tilde{b}_2$. In case of the stop, a significant mixing is induced by the off-diagonal terms due to the large top mass. For the sbottom, the off-diagonal terms only account for a significant mixing if e.g. $\tan\beta$ reaches a large value. However, even if the off-diagonal terms vanish, the evolution of the common mass parameter $m_{\tilde{t}_L,\tilde{b}_L}$ down to the electroweak scale leads to a light $\tilde{b}_L$, because of a dependence on the top-Yukawa coupling.
Another argument in favour of light third generation squarks comes by demanding a natural solution of the hierarchy problem. Light stops are required, since the dominant contribution to the Higgs boson mass correction comes from the top quark. A light $\tilde{b}_L$ follows due to the joint mass evolution mentioned above. Also the gluino mass is constrained by naturalness arguments, because it adds large corrections to the stop masses via loop diagrams. In addition, there must be light higgsinos that lead to light neutralinos and/or charginos. For the other sparticles there are usually no strong constraints on the masses, which can reach values above the TeV scale without a significant effect on the Higgs boson mass. For more information, see for example Ref. [52]. The models providing a natural solution of the hierarchy problem are referred to as natural SUSY models. In Figure 2.10, a schematic view of a typical mass spectrum for natural SUSY models is shown.
According to the natural SUSY mass spectra, scenarios of interest include gluino production, where the gluino decays via a stop or sbottom to the LSP, and the direct stop or sbottom production. Within this thesis, both the direct production as well as the gluino-mediated production are investigated.
A general feature of searches for third generation squarks is the production of bottom quarks. The sbottom dominantly decays to a bottom quark and a neutralino. The stop can either decay to a bottom quark and a chargino or a top quark and a neutralino, where the top decay involves a bottom quark. The final state topology is therefore based on b-jets (see Section 4.2.3 for the definition of b-jets). The first searches for third generation squarks were performed in mSUGRA scenarios with large $\tan\beta$ values ($\tan\beta \sim 50$). In the recent analyses, simplified models with dedicated production channels for third generation squarks are studied.

23 The mixing of particles of different generations is neglected as it would induce flavour changing neutral currents. The mixing for the first and second generation is expected to be small compared to the third generation mixing, because of the small fermion masses.

24 The mixing matrix for the tau slepton has the same structure as the one for the sbottom.

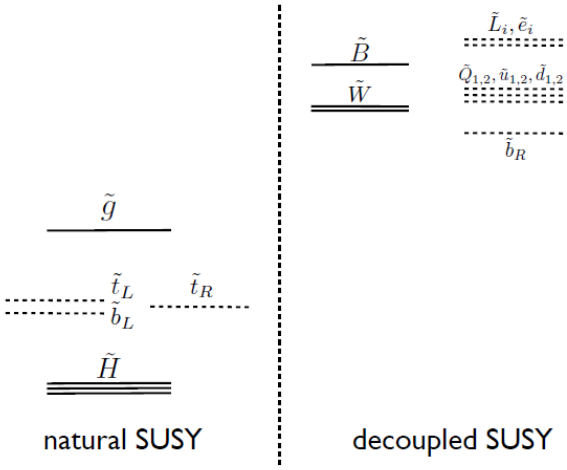

Figure 2.10: Natural SUSY mass spectrum: the particles on the left need to be light to provide a natural solution of the hierarchy problem, while the particles on the right may be heavy ($m \gg$ 1 TeV) [52].

2.3 Physics in pp Collisions

The interaction of high-energetic protons is explored at the LHC. In Figure 2.11, the cross-sections for relevant SM processes are shown. A large part of the collisions contributing to the total cross-section σ_{tot} are elastic or soft inelastic scattering processes with a small momentum transfer, which are not the main interest at the LHC. Hard scattering processes with high momentum transfers provide the interesting events. For example, the cross-section for W production lies more than 5 orders of magnitude below σ_{tot} for the design centre-of-mass energy of 14 TeV.
The ability to simulate a complete scattering process is of paramount relevance to compare theoretical predictions with the data and to design and optimise the analysis strategy. The following steps are considered for the description of the inelastic pp scattering. The fundamental interactions, introduced in the previous sections, need to be transferred to particles with a substructure. The essential feature for this transition, the factorization theorem, and the main ingredient, the parton distribution functions (PDFs), are described in Section 2.3.1. The particles produced in this step are usually not yet the final state particles, but undergo further radiation or fragmentation until hadrons are formed. The hadrons, or their decay products if they are unstable, are the particles that are measured in the detector. Further activity comes from initial state radiation and interactions between the proton remnants. The different aspects of the processes involved when building a final state are described in Section 2.3.2. A schematic view of an exemplary hard pp scattering process is shown in Fig. 2.12.
In Section 2.3.3, an overview of the MC generators used in this thesis is given. General quantities and expressions related to the experimental setup, like the luminosity and pile-up, are introduced in Section 2.3.4.

2.3.1 The Hadron-Hadron Interaction

The proton is built of three valence quarks (uud) that permanently interact with each other by the exchange of gluons. Virtual $q\bar{q}$ pairs, called sea quarks, are constantly formed by gluon

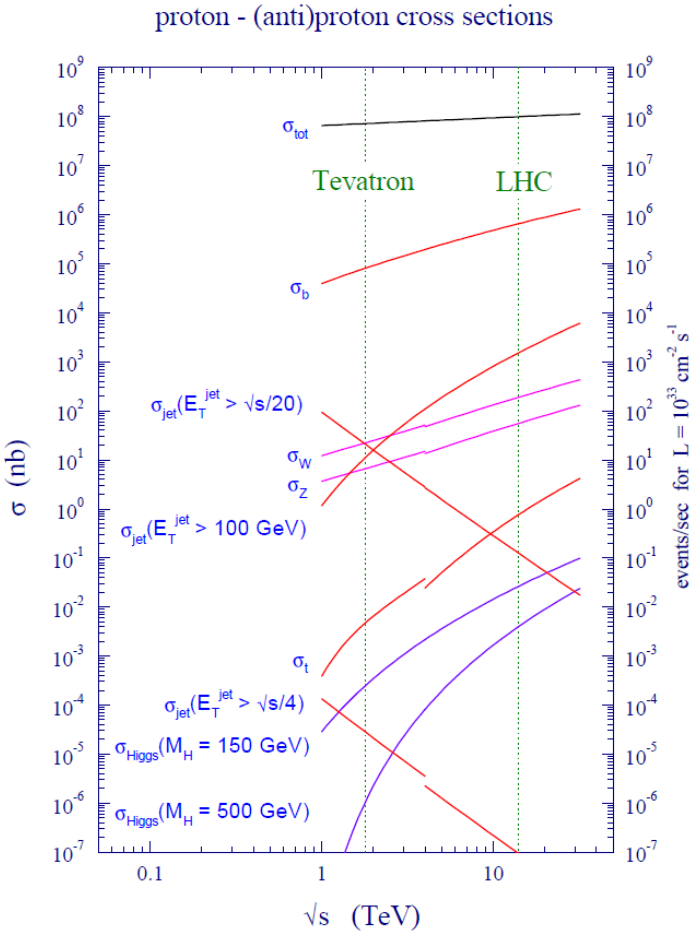

Figure 2.11: Cross-sections for the SM processes as a function of the centre-of-mass energy [53]. The vertical lines represent the Tevatron energy ($\sqrt{s} = 1.96$ TeV) and LHC design energy ($\sqrt{s} = 14$ TeV). On the right axis the expected event rate is given for a luminosity of 10^{33} cm^{-2}s^{-1}. The discontinuities for some of the cross-sections are due to the transition of $p\bar{p}$ to pp collisions.

splitting. The constituents of the proton, or any other hadron, are called partons and consist of the valence quarks, gluons and sea quarks.
In an inelastic pp scattering, a hard interaction of two partons, q_i and q_j, occurs. Assuming a final state A is produced by the parton interaction, the cross-section $\sigma(q_i q_j \to A)$ can be calculated based on perturbation theory. The factorisation theorem [55] allows to calculate the cross-section for the hadronic process, $pp \to A + X$, where X denotes the hadronic debris of the protons. It is based on the factorisation of the cross-section into soft (long-distance) and the hard (short-distance) interactions.
The soft interactions define the parton behaviour inside the proton. Each parton q_i carries a fraction of the total proton momentum, denoted by x_i. The probability of finding a parton q_i with a momentum fraction x_i is given by the PDF $f_{q_i}(x_i, Q^2)$. The dependence on the momentum transfer Q^2 is induced by higher-order corrections that take into account radiation processes for the probed parton. The cross-section for the hadronic process is then given by:

$$\sigma(pp \to A + X) = \sum_{i,j} \int f_{q_i}(x_i, Q^2) f_{q_j}(x_j, Q^2) \sigma(q_i q_j \to A) dx_i dx_j, \tag{2.28}$$

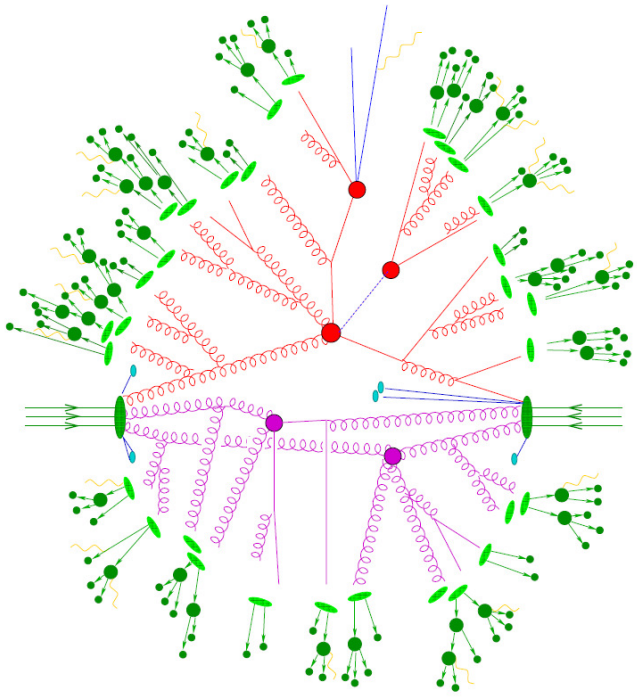

Figure 2.12: Schematic view of a hadron-hadron collision, taken from Ref. [54]. The hard parton interaction is followed by two decays, each indicated by a red blob. Secondary radiation is added for the partons in form of gluon emission and quark-pair production. The hadronisation is indicated by the green ellipses and further decays of the hadrons are pictured. The purple part represents the underlying event, including two hard parton interactions.

where the sum runs over all possible parton pairs that can produce the final state A. The integrals over the probability densities account for the unknown parton momenta. The value of the scale Q^2 which is assumed to separate the hard process from the soft parts is called the factorisation scale μ_F.
The calculation of the PDFs would require the ability to perform QCD calculations for a kinematic region where the momentum transfer between the partons is small. In this regime, however, the strong coupling constant is large and no perturbative calculation is possible. Therefore, the PDFs are determined experimentally. However, once measured at a given energy Q^2, they can be extrapolated to other energies using the DGLAP (Dokshitzer-Gribov-Lipatov-Altarelli-Parisi) evolution equations [56–58].[25]
Different experiments allow to probe the proton PDFs at different points in the $x - Q^2$ phase space. Important contributions are provided by deep inelastic ep scattering, measured by the HERA experiments [59]. Also collider experiments, like Tevatron and LHC, provide input for the PDF determination. Usually, a parametrization of the PDFs with about 20 parameters is fitted to the experimental data. In Figure 2.13, the PDF sets determined by the MSTW group [60] are shown for two values of Q^2. The parametrizations produced by the CTEQ group [61–63] are used by the MC generators for most of the samples within this thesis.

25 The equations are based on the so-called splitting functions, which give the probability that a parton originates from another parton with higher momentum fraction, e.g. a quark that originates from another quark after gluon radiation.

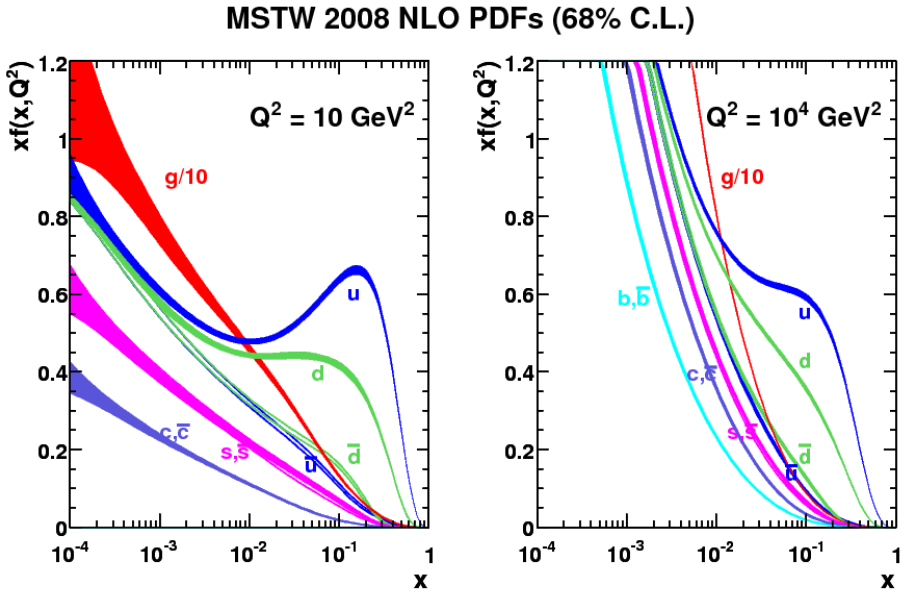

Figure 2.13: Parton distribution functions for the proton determined by the MSTW group at $Q^2 = 10$ GeV^2 (left) and $Q^2 = 10^4$ GeV^2 (right) [60]. They are calculated at NLO and the bands represent the uncertainties at 68% CL.

2.3.2 From Partons to Final State Particles

Further aspects need to be considered in order to simulate events that sufficiently describe the final states for any considered SM or SUSY process. In the following, the transition of the partons produced by the hard scattering process to the hadrons observed by the experiment are described.

Parton Showers

The partons produced by the hard scattering process usually carry high momenta and will subsequently split into partons with lower momenta (e.g. via $q \to gq$ or $g \to q\bar{q}$). In principle, these processes can be included by considering higher-order Feynman diagrams, but the full calculation of detailed parton showers is not feasible. In addition, divergences can occur in case of the collinear emission of partons. Therefore, iterative algorithms based on phenomenological models are implemented in the MC generators to describe the showering. The iterative procedure uses the Sudakov form factors, $\Delta_{p_i}(q_1^2, q_2^2)$, that are based on the splitting functions (see above) and give the probability that no splitting occurs for parton p_i when evolving from the energy scale q_1^2 to the lower energy scale q_2^2.[26] A random number R is used by the algorithm to decide at each step if a splitting is included by setting $\Delta_{p_i}(q_1^2, q_2^2) = R$. The procedure is carried on for all resulting partons until they reach the energy scale where hadronisation takes place.

When combining a calculation at fixed order for the hard scattering process (where radiation to a certain extent is already included) with the parton showering, special care needs to be taken to avoid double-counting. Commonly used tools are the CKKW [64] and MLM [65] algorithms.

26 Virtual effects as loop corrections are included in the probability of no splitting.

Initial and Final State Radiation

In general, the final state radiation (FSR) refers to any radiation that is emitted by outgoing particles of the hard scattering process. For outgoing partons, it corresponds to the parton showers, as described above. The FSR can also consist of QED radiation, for example the radiation of a photon in case a lepton pair is produced by the hard scattering process.
Analogously, the initial state radiation (ISR) refers to the parton showers developed from radiation of the incoming partons.

Hadronisation

The final step after the showering process is the formation of hadrons, referred to as hadronisation. This process has to be described with non-perturbative methods and different approaches are implemented in the MC generators. The most important methods are the Lund string model [66] and the cluster model [67]. The Lund model is based on connecting the initial partons via strings that break up to produce new $q\bar{q}$ pairs. For the cluster model, colourless parton clusters are formed during the hadronisation process which decay into the final state hadrons. Experimental observations are used to constrain the parameters for both models.
The hadrons formed by the showering and hadronisation of one initial parton are sprayed into a cone along the direction of the initial parton. This motivates the definition of particle jets.

Underlying Event

Additional activity is caused by the interaction and hadronisation of the proton remnants, summarised in the so-called underlying event. The interactions are usually soft scattering processes and are included in the event simulation by phenomenological models. Experimental data are used to constrain the parameters of the models [68, 69].

2.3.3 Monte Carlo Generators

Theoretical predictions for the SM and SUSY processes are explored with Monte Carlo generators. All steps described previously need to be taken into account to simulate physical events: the structure of the protons (PDF set), the hard scattering process, the parton showering, the hadronisation, the decay of unstable hadrons and the underlying event.
Some generators have a satisfactory implementation of all these features and can be used standalone:

PYTHIA: an all purpose generator, where the hard scattering process is calculated as a $2 \to 2$ process in leading order [70]. The leading order calculation makes it easy to add the parton showers on top, but results in a limited accuracy for events with large jet multiplicities.

HERWIG: an all purpose generator, where the hard scattering process is calculated as a $2 \to 2$ process in leading order [71]. The main differences to PYTHIA come from a different implementation for the parton shower and hadronisation model.
Even though a simulation of the underlying event is implemented in HERWIG, usually JIMMY [72] is used for this purpose. The JIMMY generator is particularly designed to model the multiparton interactions for HERWIG.

HERWIG++: an all purpose generator relying on the on the experience gained with the HERWIG generator [73]. It is implemented independently of HERWIG (switching from

Fortran to C++) and includes improvements for the parton shower and hadronisation models.

SHERPA: an all purpose generator, where additional partons are included in the calculation of the hard scattering process by considering the leading order contributions for the $2 \to n$ processes [54]. It is useful for processes with high jet multiplicities and the overlap obtained when adding the parton shower is taken care of with the CKKW algorithm.

There are also generators that are interfaced to other generators for specific steps, as for example the parton showering and the underlying event. The following generators are used to calculate the hard scattering process only and rely on HERWIG or PYTHIA for the parton shower implementation:

ALPGEN: a generator used to calculate processes with n additional partons by considering the leading order contribution for each process [74]. In ATLAS, it is interfaced mainly to HERWIG for the parton shower, using the MLM procedure to remove the overlap.

MADGRAPH: a similar generator as ALPGEN, but with a different technical implementation [75].

ACERMC: a generator designed to calculate dedicated SM processes for the LHC, using an internal library for the specific hard scattering processes [76]. It can be interfaced to PYTHIA or HERWIG for the showering.

There are also generators that calculate higher-order diagrams for the hard scattering process:

MC@NLO: a generator including NLO calculations for the hard scattering process [77]. The higher-order calculations provide a more precise cross-section prediction and also the description of kinematic distributions is improved. The HERWIG generator is used to add further showering and events are subtracted via negative weights to remove the resulting overlap.

POWHEG: a method to interface the NLO calculations for the hard scattering process with any parton shower generator [78]. In contrast to MC@NLO, positive event weights are assigned independently from the subsequent showering.

For the SUSY processes, specific programs such as SUSYHIT [79] or ISASUSY [80] are used to calculate the mass spectra and branching ratios that are passed as input to the event generators. In many cases, predictions of the SUSY cross-sections are calculated at NLO with PROSPINO [81].

2.3.4 Kinematics, Luminosity and Pile-up

In the previous sections, the theoretical description of the pp scattering process was covered. Additional aspects related to the experimental setup are discussed in the following.

The protons collide at a given centre-of-mass energy ($\sqrt{s}$) that is defined by the LHC operation. However, the longitudinal momentum fraction of the colliding partons is not known and the centre-of-mass system for the hard scattering process of the partons can be boosted with respect to the laboratory system in longitudinal direction.
Two important quantities are therefore used to describe the processes: the transverse momentum (p_{T}) and the pseudorapidity η. The rapidity of an object with energy E is defined as

$y = \ln[(E - p_z)/(E + p_z)]$ where p_z is the momentum in direction of the proton momentum. The pseudorapidity is obtained from the rapidity in the massless limit and only depends on the scattering angle θ of the scattered particle:

$$\eta = -\ln(\tan\theta/2). \tag{2.29}$$

The pseudorapidity behaves approximately additively under longitudinal Lorentz boosts and therefore the difference in rapidity between two particles is Lorentz-invariant.

The luminosity $\mathcal{L}$ relates the cross-section of a physics process σ to the measurable interaction rate for the process:

$$\dot{N} = \mathcal{L}\sigma. \tag{2.30}$$

It may vary with time and is therefore usually called instantaneous luminosity. The integrated luminosity $L = \int \mathcal{L}dt$ characterises the amount of data taken within the considered time interval, as it is proportional to the total number of events ($N = L\sigma$).
The instantaneous luminosity is determined by the beam parameters of the accelerator. For proton bunches that collide with the frequency f, the luminosity is given by

$$\mathcal{L} = f N_b \frac{N_p^2}{4\pi\sigma_x\sigma_y}, \tag{2.31}$$

where N_b is the number of bunches, N_p is the number of protons per bunch and $\sigma_{x,y}$ is the width of Gaussian shaped beam profiles.[27]
Another variable related to the LHC operation is the expected number of interactions per bunch crossing, denoted by μ. It is related to the cross-section and luminosity via:

$$\mu = \frac{\sigma \cdot \mathcal{L}}{f_{\mathrm{BC}}}, \tag{2.32}$$

where f_{BC} is the bunch crossing rate.[28]
The fact that more than one pp interaction occurs at the same time is generally denoted as pile-up. This is either caused by multiple pp interactions within one bunch crossing ('in-time" pile-up) or by signal overlapping of two subsequent bunch crossings within the detector ("out-of-time" pile-up). The latter occurs when the detector response takes longer than the given bunch spacing.

27 More information for the setup of the LHC experiment are given in Section 3.1.

28 The bunch crossing rate may vary over time and μ usually refers to the mean value obtained for a small amount of data (luminosity block).

CHAPTER 3

The ATLAS Experiment

In this chapter the experimental setup of the ATLAS detector (**A** **T**oroidal **L**HC **A**ppara**tuS**) is described. It is located at the worlds largest particle accelerator, the Large Hadron Collider (LHC), at CERN (french: **C**onseil **E**uropéen pour la **R**echerche **N**ucléaire) near Geneva, Switzerland. A short introduction to the LHC is given in Section 3.1 followed by a description of the ATLAS detector in Section 3.2.
An important tool for many analyses is a reliable simulation of the detector response, which is briefly described in Section 3.3.

3.1 The Large Hadron Collider

Located in the 27 km long underground tunnel that was used previously for the e^+e^- collider LEP (**L**arge **E**lectron-**P**ositron Collider), the LHC is the most powerful particle accelerator in the world. It is designed to reach centre-of-mass energies of 14 TeV in proton-proton collisions at an instantaneous luminosity of $L = 10^{34}$ cm^{-2}s^{-1}. In the past years, the LHC was running with a lower instantaneous luminosity and a reduced energy of $\sqrt{s} = 7$ TeV (2010-2011) and $\sqrt{s} = 8$ TeV (2012).[1] The data taking phases are described in more detail in Section 4.1. Besides protons, the LHC can also be operated with heavy-ion beams[2].
Two evacuated beam pipes, embedded in superconducting magnets, carry the proton beams in opposite directions. The protons are packed into bunches of about 10^{11} particles running at a nominal bunch spacing of 25 or 50 ns[3]. When LHC runs at 25 ns bunch spacing, each pipe holds about 2800 proton bunches.
The protons are obtained by ionising hydrogen gas in a duoplasmatron. They are passed through several acceleration steps before they are injected with an energy of 450 GeV in the LHC. A layout of the injector chain, also including the ion pre-accelerators, is shown in Fig. 3.1. A linear accelerator (LINAC 2) accelerates the protons to 50 MeV and brings them into the Proton Synchrotron Booster (PSB) from where they are passed with 1.4 GeV to the Proton Synchrotron (PS) which accelerates them to 25 GeV. As last step the protons enter

1 In September 2008, the first protons successfully circulated in the LHC. A few days later, before any collisions took place, a technical defect forced a one year shutdown to repair parts of the magnets. To avoid further accidents the collision energy was lowered and will only reach 14 TeV after another shutdown needed to upgrade the connections between the dipole magnets of the accelerator.

2 In the following only the proton operation mode is discussed as heavy-ion collisions are not covered in this thesis.

3 The design bunch spacing is 25 ns, but the LHC started running with larger bunch spacings. Both $\sqrt{s} = 7$ TeV and $\sqrt{s} = 8$ TeV runs had 50 ns bunch spacing.

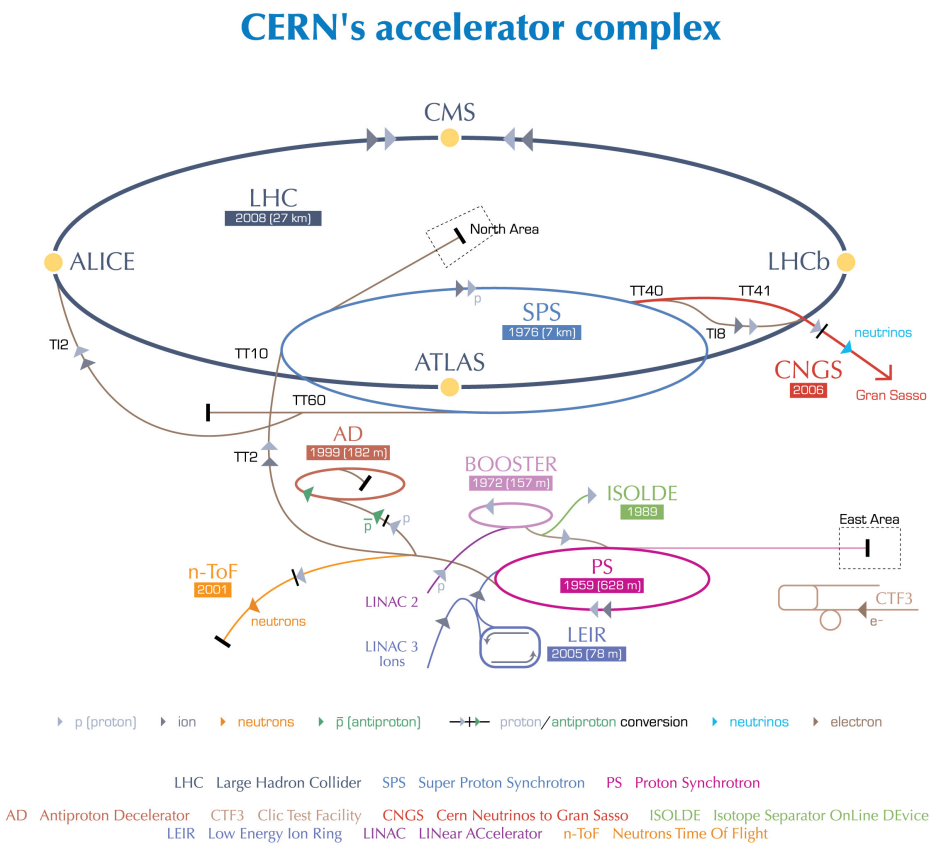

Figure 3.1: Schematic view of the LHC and its pre-accelerators with the four experiments ALICE, ATLAS, CMS and LHCb [82]. Also other experiments attached to the CERN accelerators, like for example the CERN Neutrinos to Gran Sasso (CNGS), are included in the picture.

the Super Proton Synchrotron (SPS) that can inject proton bunches with 450 GeV in both directions in the LHC ring.
In about 20 min the LHC brings the protons to their final collision energy. Eight superconducting cavities produce a high-frequency alternating electrical field of 5 MV/m strength to achieve the final acceleration. They also compensate the energy loss due to synchrotron radiation while the protons are in the ring[4]. The proton bunches can last in the LHC during the collision phase for several hours. They have a length of several cm, but a very narrow diameter of about 30 μm in the interaction regions.
To keep the protons on a circular path, 1232 superconducting dipole magnets are used. Each of them can generate a field up to 8.33 Tesla at a temperature of 1.9 K that is reached thanks to a cooling system using superfluid helium. Superconducting quadrupole magnets are used to focus the beams. More detailed information about the LHC and its magnets can be found in Ref. [83].
The beams are crossing at four collision points where the detectors are situated[5]. ATLAS and CMS (**C**ompact **M**uon **S**olenoid) are general purpose detectors and have as main interest the searches of the Higgs boson and new physics beyond the SM. LHCb is dedicated to study

4 The energy loss is about 10 keV per proton and turn in the LHC at a proton energy of 7 TeV. This can be converted to a total energy loss of approximately 0.5 W/m for two beams under nominal running conditions.
5 The crossing angle is 300 μrad for ATLAS and CMS.

heavy-flavour physics. The fourth detector, ALICE (**A** **L**arge **I**on **C**ollider **E**xperiment), was built to investigate heavy-ion collisions.

3.2 The ATLAS Detector

In this section an overview of the ATLAS detector is given. A detailed description can be found in Ref. [84], from where all numbers and figures in this section were extracted, unless stated otherwise.
A good reconstruction of the final state objects is essential for high quality physics results and in particular for the search of physics beyond the Standard Model. Hence the main design criteria were:

- Fast and efficient triggering of interesting events from a high event rate.
- A fine segmentation of the individual components for a high resolution of all measured quantities.
- Efficient vertex reconstruction for a good identification of tau leptons and b-jets.
- Good identification and momentum resolution for jets, electrons, photons and muons.
- High hermeticity to achieve a good reconstruction of missing transverse energy.

The detector is located almost 100 m underground. Its mass is about 7000 tons and it has a length of 44 m and a diameter of 25 m. A schematic view is shown in Fig. 3.2. The coordinates are chosen such that the z-axis points along the beam axis, the x-axis towards the centre of the LHC ring and the y-axis upwards. Directional information is usually expressed in spherical coordinates. The pseudorapidity $\eta = -\ln(\tan\theta/2)$ is used instead of the polar angle θ and the azimuthal coordinate is denoted as ϕ. The distance of two points at different (η, ϕ) values is given by $\Delta R = \sqrt{\Delta\eta^2 + \Delta\phi^2}$.
The pp collisions take place at the centre of the detector and coordinate system. The detector is built in cylindrical layers around the beam axis. The central region, also called the barrel region, is closed by end-caps at both sides.

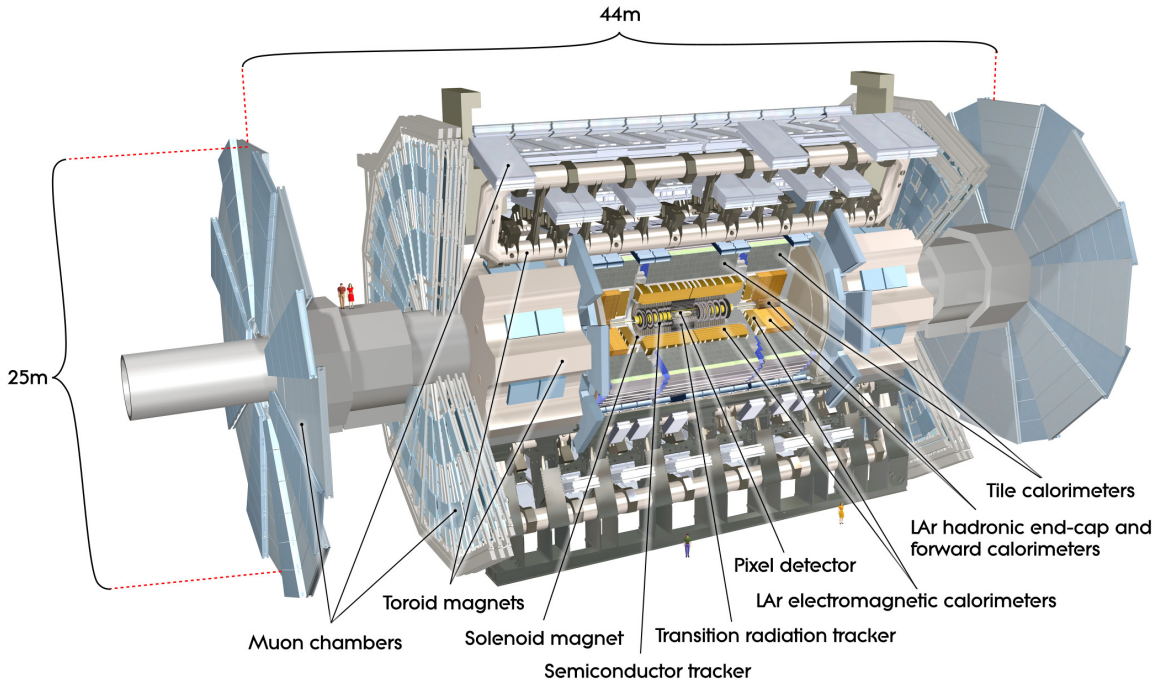

Figure 3.2: Schematic view of the ATLAS detector [84].

The ATLAS detector is built by three main parts: the inner detector (Section 3.2.1), the calorimeter (Section 3.2.2) and the muon system (Section 3.2.3). In addition the ATLAS trigger system and detector control system (DCS) are discussed in Section 3.2.4 and 3.2.5, respectively. Not included here are the forward detectors (LUCID, ZDC and ALFA) that are built close to the beam pipe at distances of 17 m to 240 m from the primary interaction point with the purpose of measuring the luminosity.

3.2.1 The Inner Detector

The purpose of the inner detector is the measurement of tracks of ionising particles. A schematic overview is shown in Fig. 3.3. It is made of three subdetectors: the pixel detector, the semiconductor tracker (SCT) and the transition radiation tracker (TRT). Each subdetector is covering the central region by cylindrical layers and has end-caps in form of discs perpendicular to the beam axis. This provides an overall coverage up to $|\eta| < 2.5$.
The inner detector is surrounded by a solenoid magnet providing a magnetic field of 2 T parallel to the beam axis. The bending of charged particles allows to measure their transverse momentum and charge.
Other important variables obtained from the track measurements are the positions of the primary and secondary vertices (see Section 4.2.1).

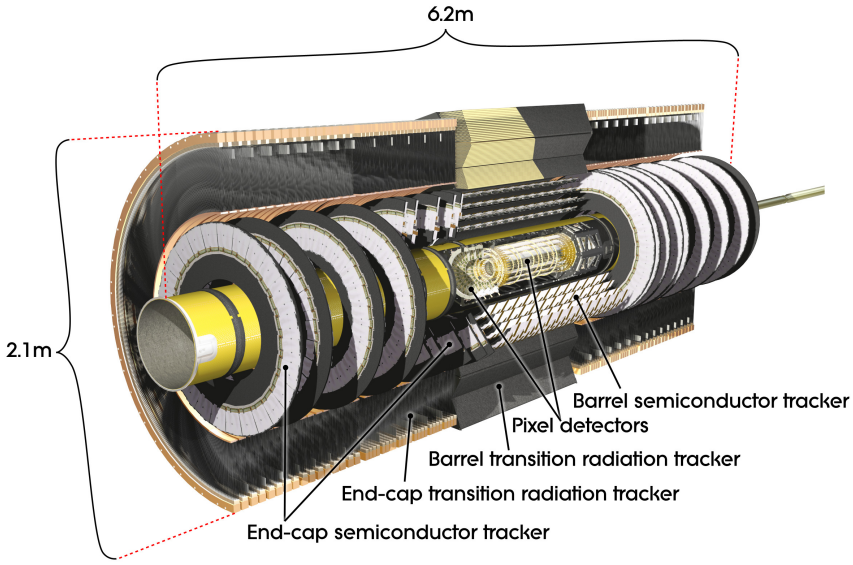

Figure 3.3: Schematic view of the ATLAS inner detector consisting of the pixel detector in the centre, followed by the TRT and SCT [84].

Pixel Detector

The silicon pixel detector is located directly around the beam axis. It consists of three pixel layers for the barrel and end-cap regions such that three space points can be reconstructed per track. The size of the majority of the pixels is 50 μm $\times$ 400 μm and about 10% have a larger size of 50 μm $\times$ 600 μm. This yields an intrinsic resolution of 10 μm in transverse and 115 μm in longitudinal direction. In total there are approximately 80 million pixels that are clustered into 1744 modules.
The innermost layer is exposed to a very high radiation dose being close to the beam line. During the 2013-2014 shutdown it is foreseen to add a new layer of pixel modules [85]. This

fourth layer will be inserted upstream the current inner detector at a radius of 33 mm[6].

Semiconductor Tracker

The pixel detector is surrounded by silicon strip detectors forming the SCT. Four layers in the barrel and nine discs in each end-cap allow to measure at least four space points per track.
In the barrel the sensors are 6.4 cm long and daisy chained in pairs of two. The strips have a pitch of 80 μm and are running parallel to the beam axis. To allow measuring the z position a second layer of strips is added under an angle of 40 mrad in each detector layer. In the end-caps three different types of wedge shaped sensors are used with different sensor length (5.4-6.6 cm) and pitch sizes (57-83 μm at the innermost point). The strips are running radially and again a second layer is added under 40 mrad to measure the radial component. The resolution of the SCT strip detectors is 17 μm in transverse and 580 μm in longitudinal direction.
About 4088 modules of strip detectors add up to a total of 6.3 million readout channels. The SCT and pixel detectors allow for a precise track measurement for the central region ($|\eta| < 2.5$) permitting to identify long-living particles via their secondary vertices.

Transition Radiation Tracker

The outermost component of the inner detector is the TRT. About 36 points in r-ϕ space are measured per track up to $|\eta| = 2.0$. It consists of straw tubes filled with a Xenon based gas mixture. A gold-plated tungsten wire is running in the middle of each tube and is read out at both ends[7]. High-energy particles produce transition radiation when passing from one medium to another with different refraction indices. This effect is exploited by adding radiating material between the straws. The Xenon gas is then used to make those photons detectable. The transition radiation can be discriminated from the tracking hits using the signal height. It plays an important role in the electron identification.
The tubes are running parallel to the beam axis in the barrel region and radial in the end-caps. They have a diameter of 4 mm and a length of 144 cm in the barrel and 39 cm in the end-caps. The intrinsic resolution of a tube is 130 μm. In total there are approximately 351000 readout channels.
Compared to the silicon detectors the TRT has a worse r-ϕ resolution but measures more points per track in the bending plane of the charged particles over a larger distance. This allows for a precise momentum measurement.

3.2.2 The Calorimeter System

After leaving the inner detector volume, the particles enter the calorimeter. The calorimeter absorbs most of the particles and measures their energy and position. In contrast to the inner detector, the calorimeter is also sensitive to neutral particles. A schematic view is presented in Fig. 3.4. The inner sections around the beam pipe, including the electromagnetic calorimeter, the hadronic end-cap calorimeters and the forward calorimeter, are covered by calorimeters using liquid argon as active material, referred to as LAr calorimeters. The barrel region of the hadronic calorimeter is covered by a tile calorimeter. The different constituents cover a region up to $|\eta| < 4.9$ and are described in the following.

6 The current innermost layer is at $r = 50.5$ mm.
7 This applies only for the barrel region where the straws are divided in two to reduce the detector occupancy. The straws in the end-caps are read out only at the outer radius.

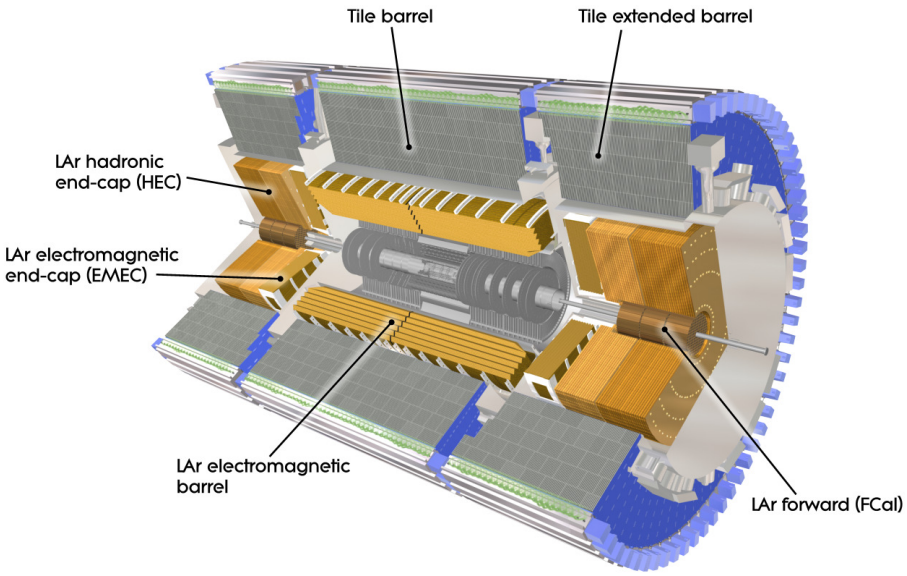

Figure 3.4: Schematic view of the ATLAS calorimeter consisting of an electromagnetic and a hadronic calorimeter [84].

Electromagnetic Calorimeter

Mainly electrons and photons are stopped in the LAr electromagnetic calorimeter using liquid argon as active detector material. Accordion shaped copper plates are used as electrodes and alternated with lead absorber plates as passive material. The argon is filled in between the copper and lead plates. The accordion geometry guarantees a complete azimuthal coverage. The calorimeter is segmented into a barrel region ($|\eta| < 1.475$) and end-caps ($1.375 < |\eta| < 3.2$). The central region ($|\eta| < 2.5$) is divided into three layers with different granularities. The innermost layer has a fine η granularity ($\Delta\eta \times \Delta\phi = 0.0032 \times 0.098$) followed by a layer of ($\Delta\eta \times \Delta\phi = 0.025 \times 0.0245$) and ($\Delta\eta \times \Delta\phi = 0.05 \times 0.0245$). Beyond the central region only two layers with a coarse granularity compared to the strip layers are used. The total thickness adds up to about 22-24 radiation lengths providing a good shower containment within the electromagnetic calorimeter.
Service lines, like electric cables or cooling devices, are passed through a gap between the barrel and end-caps causing a worse resolution in this so-called crack region. An additional calorimeter, the pre-sampler, is placed in front of the first layer. Based on the deposited energy in this layer, it provides an estimate of the energy loss of particles from passive detector material in front of the calorimeter up to $|\eta| = 1.8$.

Hadronic Calorimeter

The hadronic calorimeter completes the measurement of the charged and neutral hadron energies. The barrel region ($|\eta| < 1.7$) is covered by a tile calorimeter and the end-caps ($1.5 < |\eta| < 3.2$) with LAr calorimeters.
The tile calorimeter is a sampling calorimeter using scintillating tiles as active and iron as passive material. Each tile is read out at two sides by wave length shifting fibres which bring the scintillator light to two separate photomultipliers.
Three layers with coarser granularity compared to the electromagnetic calorimeter are used: $\Delta\eta \times \Delta\phi = 0.1 \times 0.1$ for the first two layers and $\Delta\eta \times \Delta\phi = 0.2 \times 0.1$ for the third layer.
The hadronic end-caps are built in a similar way as the electromagnetic calorimeter. The

main difference is that copper is used as absorber material. The granularity ranges from $\Delta\eta \times \Delta\phi = 0.1 \times 0.1$ for $1.5 < |\eta| < 2.5$ to $\Delta\eta \times \Delta\phi = 0.2 \times 0.2$.

Forward Calorimeter

The forward calorimeter measures particles close to the beam pipe ($3.1 < |\eta| < 4.9$) and is important for the reconstruction of missing transverse momentum.
It is a LAr calorimeter segmented in three layers. The first layer is optimized to measure electromagnetic interactions and uses copper as absorber material. The other two layers are optimized for the measurement of hadronic particles and use tungsten as absorber material. The granularity is about $\Delta\eta \times \Delta\phi = 0.2 \times 0.2$.

3.2.3 The Muon System

An efficient muon reconstruction is vital for many new physics processes. Muons are not absorbed by the calorimeter and a specific detector system, the muon spectrometer, is used to measure them precisely. The muon system is the outermost detector layer and drives the total size of the ATLAS detector. A schematic view is shown in Fig. 3.5.

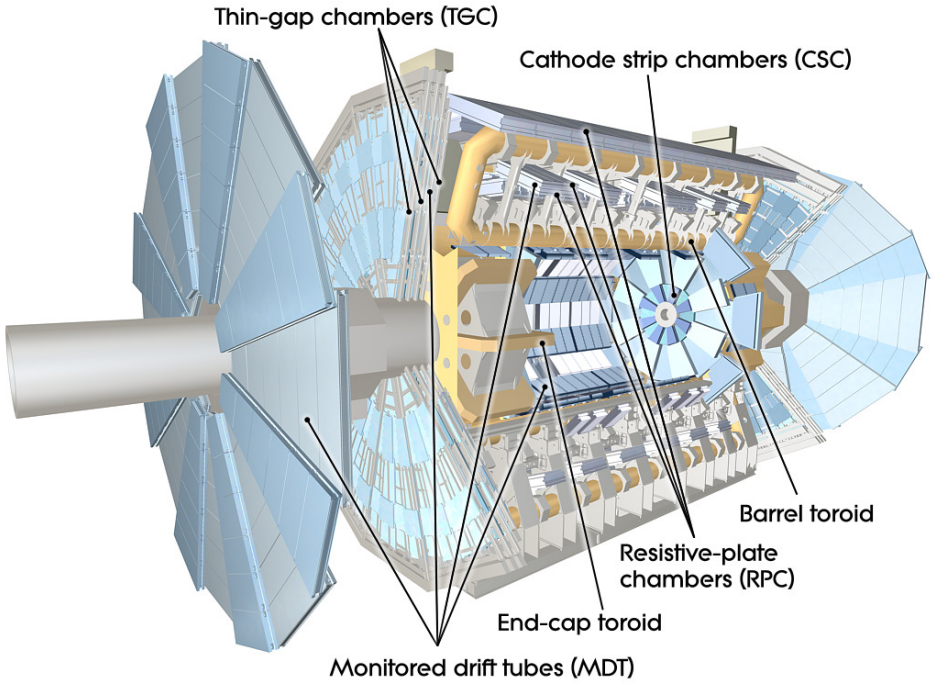

Figure 3.5: Schematic view of the ALTAS muon system [84].

Muons reaching the muon spectrometer are bent in the magnetic field of three air-core toroid magnets. This allows for a second, independent measurement of their momentum and charge. One large toroid in the central region and two smaller ones in the end-caps produce a field mostly perpendicular to the muon flight direction. Each toroid has eight coils and is installed symmetrically around the beam axis. The field strength is about 0.5 T in the central and 1 T in the end-cap region.
Two types of muon chambers are used to detect and reconstruct muon tracks: trigger chambers and precision chambers. The trigger chambers have a fast response but a rather low accuracy (few mm). Resistive-plate chambers cover the very central region ($|\eta| < 1.05$) and thin gap chambers the end-caps ($1.05 < |\eta| < 2.7$). A high spacial accuracy is obtained from

the precision chambers. A mixture of 1150 monitored drift tubes ($|\eta| < 2.7$) and 32 cathode strip chambers ($2.0 < |\eta| < 2.7$) is used. The average resolution is 80 μm for the drift tubes and 60 μm for the cathode strip chambers. Therefore a good momentum resolution can be achieved using the muon system standalone, but it can be further improved by combining the information of the inner detector.

3.2.4 The Trigger System

The LHC is designed to provide a pp collision rate of 40 MHz. Technical constraints and limited resources lead to a maximal rate of 200 Hz that can be processed and recorded.[8] A dedicated trigger system is used to select the physically interesting events and to provide the needed event rate reduction. It is split in three levels, the Level-1 trigger (L1) followed by the Level-2 trigger (L2) and finally an event filter (EF). The Level-2 trigger and event filter are referred to as the high level trigger (HLT).

Level-1

Within approximately 2 μs the L1 trigger decides if an event is interesting and passed to the next trigger level[9]. It is looking for events with particles or jets with high momentum and/or high missing or total transverse momentum. Only the information from the muon trigger chambers and calorimeters with reduced resolution ($\Delta\eta \times \Delta\phi = 0.1 \times 0.1$) is considered. The inner detector does not play any role. Regions of Interest (RoI) are marked and passed to the L2 trigger by their η and ϕ coordinates. A reduction of the event rate to 75 kHz is achieved.

Level-2

For the next decision of the L2 trigger all detector information with full granularity is available for the RoIs passed by the L1 trigger. The decision takes about 40 ms and the event rate is reduced to approximately 3.5 kHz.

Event Filter

For the last trigger level, software algorithms as in the offline data analysis are applied on the full detector information. The processing time is about 4 s per event and the total rate is reduced to the available 200 Hz. The selected events are transmitted to the CERN computing centre where they are stored, further processed, and distributed worldwide for physics analyses. One event has a size of about 1.3 MB.

3.2.5 The Detector Control System

The whole ATLAS detector with all its subdetectors and infrastructure is constantly monitored by the DCS described in detail in Ref. [86]. It is used for the operation of any detector equipment and ensures safe operation. Different types of sensors (e.g. to measure the temperature or pressure) are placed throughout the detector. Their output is controlled during operation to detect any abnormal behavior.
Besides the physics data also this meta data is stored. It is archived in a database and can be accessed at any point in the offline monitoring. A user interface was developed within this thesis to facilitate the access and provide common tools to display the data. It is described in Appendix B.

8 The plan is to increase the rate to 1 kHz after the 2013-2014 shutdown.
9 The data is stored in detector-specific digital buffers to accommodate the trigger latency.

3.3 Detector Simulation

A precise prediction of SM and beyond SM processes is often needed for the interpretation of the results of a physics analysis. Also the predictions are needed to develop and optimise the analysis prior to its interpretation. The processes are generated using Monte Carlo generators (see Section 2.3.3). Afterwards the response pattern of the detector is simulated to obtain events that can be compared with the real data. Two different tools for the detector simulation are used in this thesis: the full simulation and a fast simulation, called ATLFAST-II.

Full Simulation

The full simulation uses a precise description of the geometry of the detector and the interactions between the particles and the detector material, employed in the Geant4 [87, 88] package. The showers initialized by the particles in the calorimeters are simulated in detail for each particle, making this step the most time consuming part. In total, the full simulation takes of the order of one minute per event but the time can also go up to 20 - 30 minutes for more complex events.
The full simulation provides a realistic detector description under the assumption that the detector geometry and material properties are correctly described. The main disadvantage is the long simulation time, especially for processes where a large number of events needs to be simulated.

ATLFAST-II

The fast simulation ATLFAST-II is based on a fast simulation of the calorimeter, FastCaloSim [89]. The absolute shower energy and its distribution in the different calorimeter layers are parametrized. In addition, a simplified geometry of the calorimeter is used. For the inner detector and the muon system the full simulation is used[10].
The simulation is about 10 times faster using ATLFAST-II compared to the full simulation and compatible results are obtained.

All computing tools needed for the simulation and reconstruction of events are provided by the ATLAS framework Athena [90].

10 Also for the inner detector a fast simulation exists (FATRAS: **Fa**st **Tra**ck **S**imulation) and can be used in combination with FastCaloSim.

CHAPTER 4

Performance of the ATLAS Experiment

The ATLAS experiment has shown an outstanding performance in the first years of data taking. The conditions of the different data taking periods are specified in Section 4.1. In Section 4.2, the reconstruction methods for physical objects and their performance on real data compared to MC estimates are described.

4.1 Data Taking

After the incident in autumn 2008 the LHC restarted operations in November 2009. The first pp collisions were achieved at the end of 2009 at a centre-of-mass energy of $\sqrt{s} = 900$ GeV and $\sqrt{s} = 2.36$ TeV. In March 2010, data taking at $\sqrt{s} = 7$ TeV started. An integrated luminosity of 49 pb^{-1} was delivered by the LHC of which 45 pb^{-1} were recorded by the ATLAS experiment until the end of 2010. The instantaneous luminosity was increased up to a peak value of $2.1 \cdot 10^{32}$ cm^{-2}s^{-1}. The mean number of interactions per bunch crossing μ was measured for small blocks of luminosity and an average value of $\langle\mu\rangle \sim 3$ was obtained. The first physics results, including those on SUSY searches, were published with the 2010 dataset. Some results from the ATLAS performance groups shown in the following section are still based on this rather small dataset due to the low level of pile-up.
In 2011 the instantaneous luminosity was raised further, reaching a peak value of $3.65 \cdot 10^{33}$ cm^{-2}s^{-1} and increasing the average number of interactions per bunch crossing to $\langle\mu\rangle \sim 9$. In total 5.3 fb^{-1} of proton-proton collisions were recorded by the ATLAS experiment (out of 5.6 fb^{-1} delivered by the LHC).
The centre-of-mass energy was raised to 8 TeV in 2012. In total 23 fb^{-1} were delivered by the LHC and 22 fb^{-1} recorded by the ATLAS experiment. The peak instantaneous luminosity reached $7.73 \cdot 10^{33}$ cm^{-2}s^{-1} and the average number of interactions per bunch crossing went up to $\langle\mu\rangle \sim 20$ in the 2012 dataset. The distribution of the mean number of interactions per bunch crossings μ is shown in Fig. 4.1a for the 2011 and 2012 data. The latest results in this thesis only include the fraction of data that was recorded until September 2012. This dataset corresponds to 14 fb^{-1} of integrated luminosity.
For all three datasets, the bunch spacing was kept at 50 ns and the data taking efficiency was about 94%. The small inefficiency causing the difference between delivered and recorded luminosity is mainly due to the so-called warm-start[1], or the malfunctioning of any part of the detector. In Figure 4.1b the integrated luminosities for the 2010, 2011 and 2012 datasets

1 The warm-start applies to the tracking detectors. The voltages are ramped up and the preamplifiers turned on after the beams are declared to be stable.

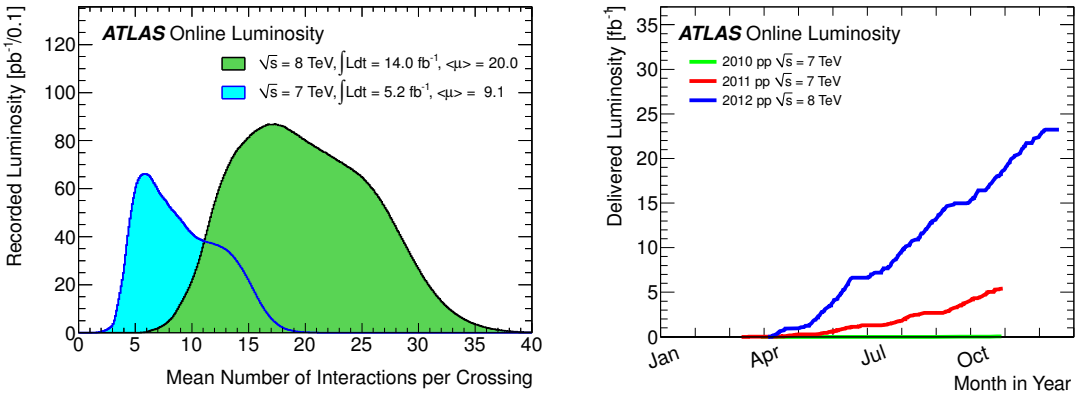

(a) Interactions per Crossing (μ) **(b)** Integrated Luminosity

Figure 4.1: (a): Luminosity weighted mean number of interactions per bunch crossing [91]. In blue the numbers for pp collisions at $\sqrt{s} = 7$ TeV in 2011 are shown and in green the numbers for 14 fb^{-1} of $\sqrt{s} = 8$ TeV data recorded from 04.04.2012 - 17.09.2012. (b): Integrated luminosity delivered by the LHC to ATLAS for pp collisions at $\sqrt{s} = 7$ TeV in 2010 (green) and 2011 (red) and at $\sqrt{s} = 8$ TeV in 2012 (blue) [91]. The luminosities were measured by the forward detectors, as mentioned in Section 3.2.

are shown as a function of time. The numbers for the data taking periods used in this thesis are summarized in Table 4.1.

Quantity	2010	2011	2012 until September
Centre-of-mass energy $\sqrt{s}$	7 TeV	7 TeV	8 TeV
Peak instantaneous luminosity [cm^{-2}s^{-1}]	$2.1 \cdot 10^{32}$	$3.65 \cdot 10^{33}$	$7.73 \cdot 10^{33}$
Total integrated luminosity (recorded)	45 pb^{-1}	5.25 fb^{-1}	14.0 fb^{-1}
Data taking efficiency	93.6%	93.5%	93.7%
Average number of interactions per bunch crossing	3	9	20

Table 4.1: Parameters for the pp data taking periods in 2010, 2011 and 2012. For the 2012 dataset, the values are shown for data recorded up to September 2012. The values are extracted from Refs. [91, 92].

4.2 Object Reconstruction

For any physics analysis it is important to identify the final state objects in a given event. The methods for identifying objects needed in this thesis are described in the following sections: track and vertex reconstruction (4.2.1), jet reconstruction (4.2.2), b-jets reconstruction (4.2.3), lepton identification (4.2.4) and $E_{\mathrm{T}}^{\mathrm{miss}}$ reconstruction (4.2.5).

4.2.1 Track and Vertex Reconstruction

The reconstruction of tracks of charged particles in the inner detector is essential for the subsequent vertex reconstruction and the identification of charged particles.
The track reconstruction for the inner detector is started by a preprocessing step, converting the information from the pixel and SCT detector into three-dimensional space points and the TRT information into calibrated drift circles. The default track-reconstruction algorithm is seeded by at least three space-points from the pixel layers and the first SCT layer. The track seeds are extended to the remaining SCT layers and a fit is performed to remove outlying space-points. The tracks are completed by associating them to the drift circles of the TRT. The final step is to refit the track using the information of the whole inner detector. More information on the track finding algorithms and their performance are given in Ref. [93].

The position where the pp interaction takes place is referred to as the primary vertex. It is characterised by a high number of particles originating from it.
The vertex reconstruction uses the reconstructed tracks as input and is started by a vertex finding procedure. A vertex candidate is seeded by the local maximum in the distribution of z coordinates at the beamline of the tracks. An iterative method is exploited to associate the tracks to the vertex candidate, by using the result of a χ^2 fit to decide whether the track is compatible with the vertex. The remaining tracks are then used to restart the procedure by finding a new vertex candidate. More information on the vertex reconstruction and its performance are given in Ref. [93]. Due to pile-up, more than one primary vertex can be observed in a single event. In this case, the primary vertex of interest is chosen to be the one that has the largest sum of squared transverse track momenta of the tracks associated to the vertex ($\sum p_{\mathrm{T}}^2$).

4.2.2 Jet Reconstruction

Jets of particles are mainly reconstructed from the energy deposits in the calorimeters. Several algorithms were proposed to define a jet, either based on maximising the energy in a geometric cone or a pair-wise clustering of different objects. The default algorithm chosen is the anti-k_t [94] algorithm and it uses topological clusters as input. Topological clusters are reconstructed by an iterative noise-suppressing process from the calorimeter cells: cells with an energy deposit significantly larger than their noise width ($E_{\mathrm{cell}} > 4 \cdot \sigma_{\mathrm{noise}}$) are selected as seeds and neighboring cells are added if their energy is above a threshold depending on the expected noise [95].
The anti-k_t algorithm belongs to a larger class of jet reconstruction algorithms, that iteratively merges clusters together, until a boundary condition is reached based on two distance measures d_{ij} and d_{iB}:

$$d_{ij} = min\left(p_{Ti}^{2p}, p_{Tj}^{2p}\right) \frac{(y_i - y_j)^2 + (\phi_i - \phi_j)^2}{R^2}, \tag{4.1}$$

$$d_{iB} = p_{Ti}^{2p}, \tag{4.2}$$

where p_{Ti}, y_i and ϕ_i are the transverse momentum, rapidity and azimuthal angle for object i. The parameter R is related to the resolution of separating different jets. It is set to 0.4 for jets used in this thesis. Each algorithm uses a different value for p defining in which way the objects are clustered. The smallest value of all combinations of d_{ij} and d_{iB} is iteratively calculated. If a d_{ij} is found as smallest value the objects i and j are merged to a new object, while a minimal d_{iB} results in removing the final jet i from the list of objects.

The parameter p is set to -1 for the anti-k_t algorithm. This implies that first softer objects are merged to a close-by hard object, making the jets stable with respect to soft radiation. The energy of two close hard objects is distributed among them according to the relative transverse momentum and distance, making the algorithm collinear safe [96].

Several detector effects have an impact on the measured jet energy. The main effects are that only part of the hadronic energy is measured (calorimeter non-compensation [97]) and that dead detector material causes inefficiencies. Other sources for mis-measurements are energy leakage outside of the calorimeter, energy contributions that are not included in the reconstructed jet (out-of-cone energy) and losses in the clustering and reconstruction due to noise thresholds and particle reconstruction efficiencies. These effects are corrected for by calibrating the measured jet energy. Different methods and their performance are reported in Ref. [98] and are briefly summarized here.
One of the main calibration schemes starts with jets reconstructed from clusters calibrated at the electromagnetic (EM) scale[2]. The hadronic energy scale is obtained by applying a multiplicative factor (JES) computed from MC simulation. The full calibration is referred to as EM+JES calibration. It was used for the SUSY analyses until summer 2012. After that, it was replaced by a local calibration weighting procedure (LCW). Here, clusters are calibrated to the hadronic scale before executing the jet reconstruction algorithm. The calibration is obtained from simulated pion events and corrected for by dedicated measurements. Also for this calibration scheme, jet energy scale corrections are applied on the reconstructed jets. The full scheme is therefore called LCW+JES. The JES corrections are larger for EM calibrated jets than for LCW calibrated jets, as shown in Fig. 4.2.
For both calibrations the uncertainties on the final jet energy scale and resolution were measured and corresponding values are provided to estimate the resulting systematic uncertainties in any analysis using reconstructed jets. Additional pile-up corrections are applied on top of the calibration depending on the data-taking period and the number of primary vertices [99].

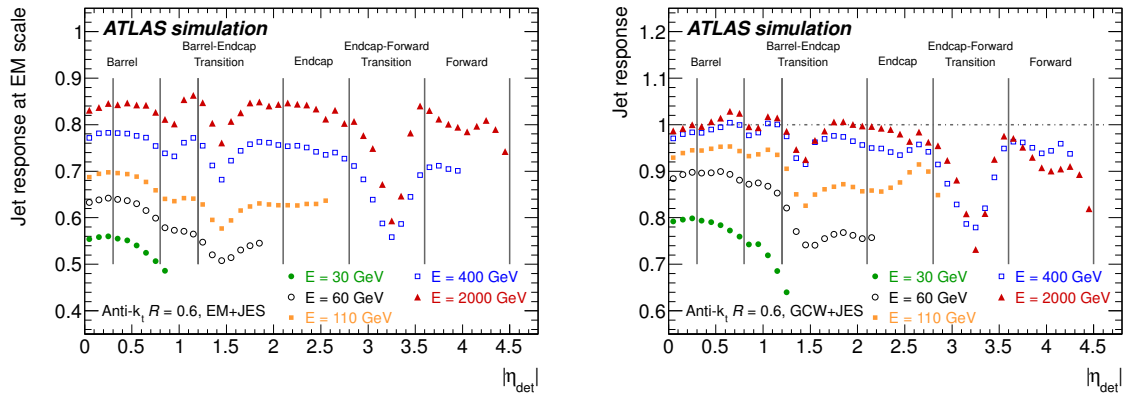

Figure 4.2: Reconstructed jet energy divided by the truth energy (jet response) as a function of $|\eta|$ for jets at the EM (left) and LCW scale (right) obtained from MC simulation [98]. The distributions are shown for jets of different energies.

2 A calorimeter is calibrated at the electromagnetic scale if the ratio of the measured energy divided by the energy of the incoming particle fulfills $E_{\text{meas}}/E_{\text{input}} = 1$ for electrons. If the calorimeter is non-compensating, this implies that $E_{\text{meas}}/E_{\text{input}} < 1$ for hadrons. The EM calibration is derived from test-beam measurements and tested and corrected using $Z \to ee$ events.

4.2.3 Reconstruction of *b*-jets

The long lifetime of b-hadrons can be used to identify jets originating from them (b-jets). They typically decay at a distance of a few millimeters[3] to the primary interaction vertex generating a secondary vertex. Two other classes of jet flavours are used to examine the performance of the b-tagging algorithms: c-jets refer to jets originating from a c-quark and other quark flavours plus gluon initiated jets are collectively referred to as light jets[4].
There are two main classes of b-tagging algorithms based either on the measurement of the impact parameters of tracks or the explicit reconstruction of a secondary vertex. The impact parameter is calculated for tracks in the inner detector and is defined as the minimal distance to the primary vertex at the point of closest approach. It is positive for a decay in the jet direction and negative for a decay in opposite direction. The secondary vertex can be reconstructed if at least two tracks have a significant impact parameter. A schematic view of the decay of a b-hadron with its primary and secondary vertex is shown in Fig. 4.3.

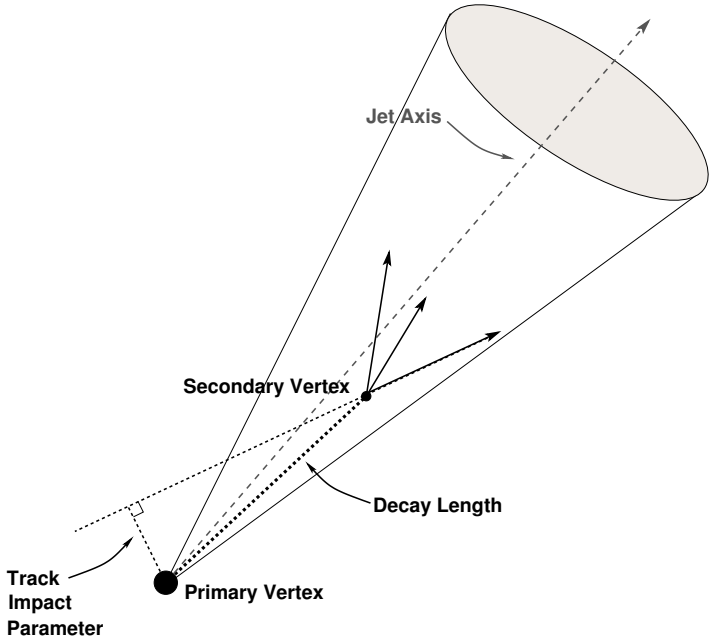

Figure 4.3: Schematic view of a b-hadron decay [100]. Primary and secondary vertex are indicated and one track is extended to visualise the impact parameter.

The following list contains a short description of the most basic high-performance b-tagging algorithms. More details can be found in Refs. [100–102].

- *IP3D:* impact parameter tagger based on a likelihood ratio built from the signed transverse and longitudinal impact parameter significance[5].
- *SV0:* secondary vertex tagger based on the decay length L (see Fig. 4.3) and its significance L/σ_L, where σ_L is the decay length resolution.

3 A 50 GeV b-hadron will travel an average distance $\langle L \rangle$ of 5 mm before it decays. The average distance is related to the lifetime τ by $\langle L \rangle = \beta\gamma c\tau$. For a $B^{\pm}$ meson, the lifetime is about 1.6 ps ($c\tau \sim 0.5$ mm) [14].

4 For the SUSY analyses all jets that are neither a b- or c-jet are classified as light jets, which implies that hadronically decaying tau leptons are also included.

5 The significance of the transverse (longitudinal) impact parameter d_0 (z_0) is given by d_0/σ_{d_0} (z_0/σ_{z_0}), where $\sigma_{d_0(z_0)}$ is the impact parameter resolution.

- *SV1:* secondary vertex tagger based on a likelihood ratio built from the invariant mass of the tracks associated to the secondary vertex, the ratio of the sum of the energies of the tracks from the secondary vertex compared to all tracks in the jet, and the number of two-track vertices.
- *JetFitter:* secondary vertex tagger, taking into account possible tertiary vertices from c-hadrons inside the b-hadron decay. It builds a likelihood from similar variables as SV1 and SV0.

Each algorithm assigns a weight value to every jet in an event indicating how likely it is that the jet is a b-jet. In the analysis, b-jets can be selected at different efficiencies depending on the weight threshold used to tag a jet as b-jet. Working with a higher efficiency implies to have a worse rejection against light and c-jets. To further improve the rejection power at a given tagging efficiency the output of different b-tagging algorithms can be combined. The most common combinations used in ATLAS are:

- *IP3D+SV1*: combined by adding the weight outputs of IP3D and SV1.
- *JetFitterCombNN*: combining JetFitter with IP3D via a neural network which is trained on MC samples.
- *MV1*: using the outputs from IP3D, SV1 and JetFitterCombNN as input to a neural network.

The JetFitterCombNN algorithm was used for the sbottom search analyses performed in 2011. In 2012, the MV1 tagger became the default algorithm as it provides the best performance. In Figure 4.4 the rejection against light jets and c-jets can be seen as a function of the b-tagging efficiency for the combined tagging algorithms and SV0. It was obtained from a simulated sample of $t\bar{t}$ events at $\sqrt{s} = 7$ TeV.

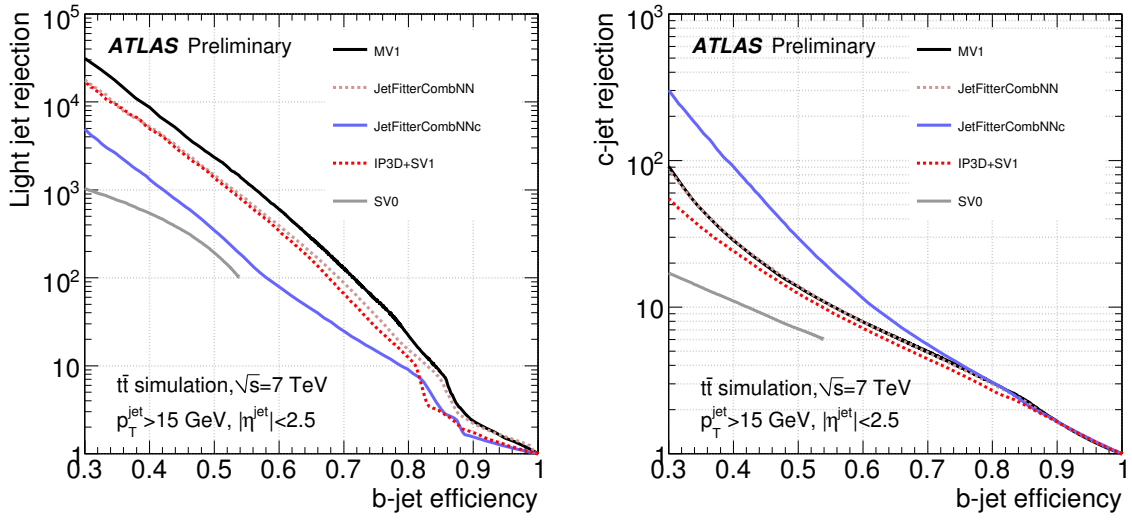

Figure 4.4: Rejection against light jets (left) and c-jets (right) as a function of the b-tagging efficiency for a sample of simulated $t\bar{t}$ events at $\sqrt{s} = 7$ TeV [103]. It is shown for the combined tagging algorithms and SV0. The JetFitterCombNNc algorithm is similar to JetFitterCombNN, but trained to reject c-jets rather than light jets.

The performance of the b-taggers is constantly evaluated and scale factors are derived to correct the b-tagging efficiency and rejection power observed in MC to those measured in data. Momentum dependent scale factors (SF) are provided separately for b-, c- and light jets:

$$SF_{\mathrm{X}}\left(p_{\mathrm{T}}\right) = \frac{\varepsilon_{\mathrm{X}}^{\mathrm{data}}\left(p_{\mathrm{T}}\right)}{\varepsilon_{\mathrm{X}}^{\mathrm{MC}}\left(p_{\mathrm{T}}\right)}, \quad \mathrm{X} = b,\, c,\, \mathrm{light}, \tag{4.3}$$

where $\varepsilon_{\mathrm{X}}^{\mathrm{data}}$ is the efficiency measured in data and $\varepsilon_{\mathrm{X}}^{\mathrm{MC}}$ is the MC estimated efficiency. If a jet is tagged as b-jet the scale factor is directly used as weight value while the weight for a non-tagged b-jet[6] is given by $\frac{1-\varepsilon_b^{\mathrm{data}}}{1-\varepsilon_b^{\mathrm{MC}}}$. An event weight is assigned by multiplying the individual weights of the jets.
The methods to measure the efficiencies and hence the scale factors are described in Refs. [103, 104]. The main technique applied to obtain the b-tagging efficiency in data is based on using a subset of events with muons inside the b-jets. It exploits the fact that the distribution of the relative muon momentum transverse to the jet momentum has a different shape for b-jets and c- and light jets. An example of b-tagging efficiencies obtained with this method is shown in Fig. 4.5 for b-jets selected with a 60% efficiency operating point using the JetFitterCombNN and MV1 algorithms.

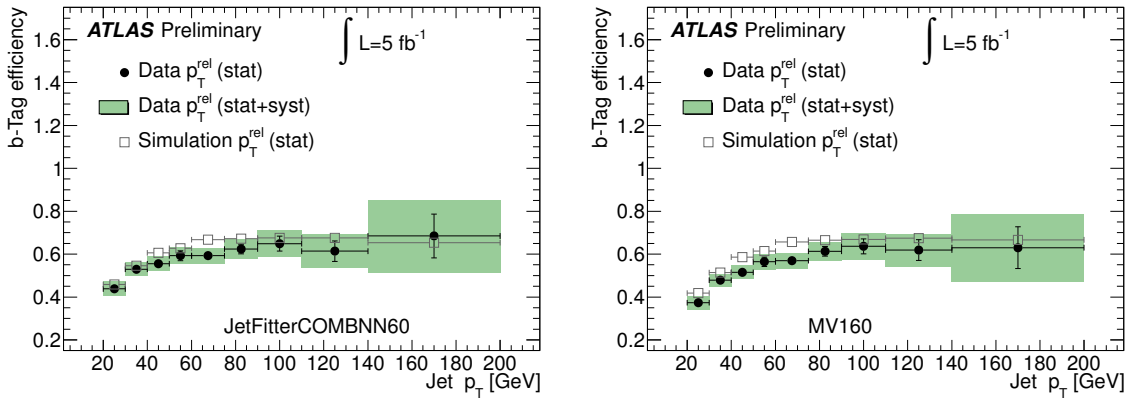

Figure 4.5: The b-tagging efficiency in data and MC simulation as a function of the jet momentum obtained from a subsample of 2012 data with muons inside of b-jets at a 60% efficiency operating point for JetFitterCombNN (left) and MV1 (right) [103]. The ratios of the data and MC values correspond to the scale factors described in the text.

4.2.4 Lepton Identification

For the studies shown in this thesis, events with electrons or muons are rejected. Nevertheless, the leptons need to be identified to do so. In addition control regions with light leptons are used for the background estimation. No attempt is made to identify τ leptons as it is not relevant for the SUSY processes studied.

6 The truth flavour of a jet is stored as a variable in the MC samples and analogous formulas apply for light and c-jets.

Electron Identification

Electrons are reconstructed using information from the inner detector and the calorimeter. Selection criteria defined in Ref. [105] provide a good separation from the main background coming from jets that fake an electron signal. In the central region ($|\eta| < 2.47$) the criteria are split into three quality classes: *loose*, *medium* and *tight*. The jet rejection power estimated from MC samples increases from approximately 500 (loose) over 5000 (medium) to 50000 (tight) [106].

For the loose selection, shower shape variables from the middle layer of the electromagnetic calorimeter and the leakage into the first layer of the hadronic calorimeter are used for the identification. For the medium selection, information from the first electromagnetic calorimeter layer and requirements on the track quality are added on top of the loose selection. The track quality criteria include a minimum number of hits in the pixel detector and SCT and a small transverse impact parameter[7]. In addition, the track direction needs to match the position of the calorimeter cluster. The tight selection improves the track-cluster matching by including the ratio of cluster energy and track momentum, the track quality, and the suppression of hadrons by adding information from the TRT. Electrons from photon conversions are reduced by specific requirements added to the tight selection. The full details on all selection criteria can be found in Refs. [105, 106].

The electron identification performance was studied in $W \to e\nu$, $Z \to ee$ and $J/\Psi \to ee$ events for the 2010 dataset [106]. Efficiencies obtained for 2011 and 2012 data are shown in Fig. 4.6 as a function of the number of reconstructed vertices. To adapt to the 2012 data taking conditions, the electron identification was re-optimised to be more pile-up robust, resulting in flatter efficiency distributions. Discrepancies between data and MC simulation are used to derive correction factors that can be applied by analyses using electrons.

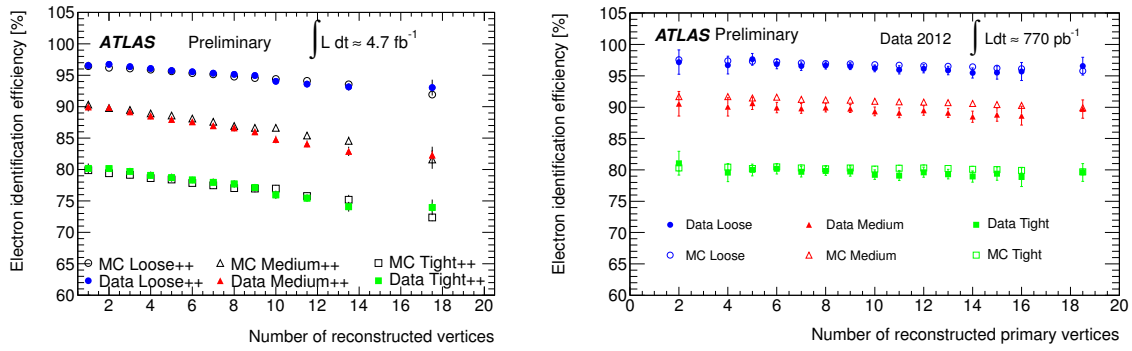

Figure 4.6: Electron identification efficiencies as a function of the number of reconstructed vertices for the 2011 data (left) and 0.77 fb^{-1} of the 2012 dataset (right) for the loose, medium and tight selection [107, 108]. The efficiency is measured in $Z \to ee$ events for both datasets and $J/\Psi \to ee$ events are additionally used for the 2012 results.

Muon Identification

Muons can be reconstructed either standalone by the muon spectrometer or in combination with the tracks from the inner detector. The STACO algorithm [109] used in this thesis applies a statistical method to combine the tracks of the two subdetectors. Muons for which

7 The transverse impact parameter is defined in the b-tagging section and is required to be smaller than 5 mm for the medium and 1 mm for the tight selection.

only segments of the tracks are reconstructed in the muon spectrometer can also be accepted to enhance the efficiency for low momentum muons. The muon momentum is calculated as the weighted average of the momenta measured in both subsystems. For low momenta the inner detector dominates ($p_{\mathrm{T}} < 80$ GeV in the barrel and $p_{\mathrm{T}} < 20$ GeV in the end-caps) while the muon spectrometer is more precise for high momenta ($p_{\mathrm{T}} > 100$ GeV) [110].
Selection criteria for the muon reconstruction are defined in Ref. [110]. They are based on variables as the number of hits in the different inner detector parts. The reconstruction efficiency was studied for $Z \to \mu\mu$ events using 2010 data [110]. In Figure 4.7 the efficiency and the resulting scale factors are shown as a function of the muon momentum and pseudorapidity.

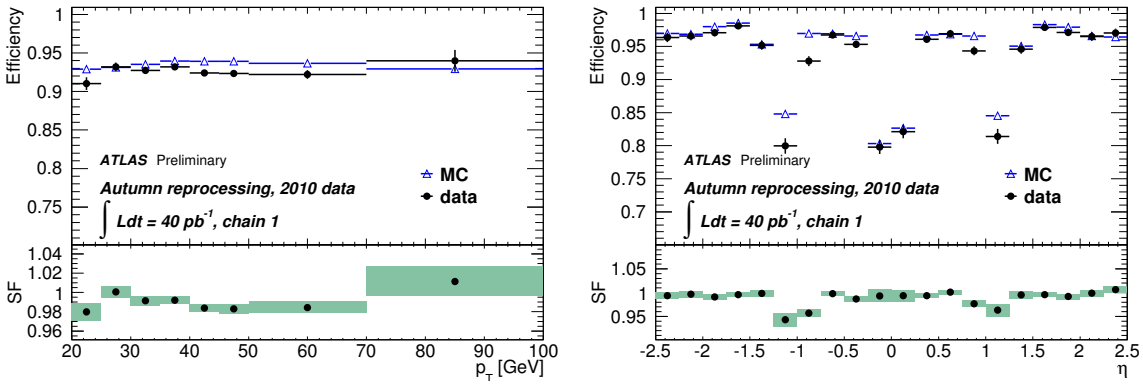

Figure 4.7: Combined muon identification efficiencies as a function of p_{T} (left) and η (right) for $\sqrt{s} = 7$ TeV data recorded in 2010 [110]. The scale factors are given by the data/MC ratio and are shown in the lower parts of the figures. They were measured for $Z \to \mu\mu$ events and the *chain1* label refers to the fact that the STACO algorithm is applied.

In addition the momentum scale and resolution were measured in $Z \to \mu\mu$ and $W \to \mu\nu$ events [111]. Looking at the di-mass distribution for $Z \to \mu\mu$ events a worse resolution was found in data compared to the MC prediction. To correct for this a p_{T} and η dependent function is provided that smears the muon momentum in MC events.

Isolated Leptons

Isolation criteria are defined to select those leptons, that are promptly produced in the primary interaction (e.g. by a W or Z decay). Non-prompt leptons are normally produced in heavy-flavour quark decays and are not isolated from the other decay products.
A good separation from other objects is achieved by adding the following isolation requirement to the lepton selection definitions: the track momenta in a $\Delta R = 0.2$ cone around the lepton are summed and may not exceed 10% of the electron momentum or 1.8 GeV in the case of muons.

4.2.5 Missing Transverse Momentum Reconstruction

Any particle leaving the detector undetected leads to missing transverse momentum. In the SM, neutrinos are the only such particles. A large missing transverse momentum is expected for any R-parity conserving SUSY model, because of the production of the dark matter candidate. The missing transverse momentum is obtained by adding the transverse momenta of all particles in the event vectorially.
The energy deposits in the calorimeter and the information from the muon spectrometer

enter the computation. Topological calorimeter clusters are associated with reconstructed physics objects and calibrated according to the type of the object. For muons, the transverse momentum measurement is taken from the muon spectrometer and the corresponding calorimeter clusters are not added. In addition, the inner detector information is used to recover contributions from low momentum particles that do not reach the calorimeter and muons not entering the muon spectrometer.
All contributions are projected on the x and y directions and are decomposed in the following terms:

$$\begin{aligned} E_{\mathrm{x(y)}}^{\mathrm{miss}} =& E_{\mathrm{x(y)}}^{\mathrm{miss},e} + E_{\mathrm{x(y)}}^{\mathrm{miss},\gamma} + E_{\mathrm{x(y)}}^{\mathrm{miss},\tau} + E_{\mathrm{x(y)}}^{\mathrm{miss,jets}} + \\ &+ E_{\mathrm{x(y)}}^{\mathrm{miss,softjets}} + E_{\mathrm{x(y)}}^{\mathrm{miss,CellOut}} + E_{\mathrm{x(y)}}^{\mathrm{miss},\mu}. \end{aligned} \tag{4.4}$$

A separate calibration is used for electrons ($E_{\mathrm{x(y)}}^{\mathrm{miss},e}$), photons ($E_{\mathrm{x(y)}}^{\mathrm{miss},\gamma}$) and tau leptons ($E_{\mathrm{x(y)}}^{\mathrm{miss},\tau}$). For jets two different calibrations are used depending on their momentum: jets with $p_{\mathrm{T}} > 20$ GeV ($E_{\mathrm{x(y)}}^{\mathrm{miss,jets}}$) and "soft" jets with $7 < p_{\mathrm{T}} < 20$ GeV ($E_{\mathrm{x(y)}}^{\mathrm{miss,softjets}}$). The muon term $E_{\mathrm{x(y)}}^{\mathrm{miss},\mu}$ takes muons into account. Other clusters not associated with any physics object are summed in the $E_{\mathrm{x(y)}}^{\mathrm{miss,CellOut}}$ term.
The absolute $E_{\mathrm{T}}^{\mathrm{miss}}$ value[8] and its direction ϕ^{miss} are computed from the projections:

$$E_{\mathrm{T}}^{\mathrm{miss}} = \sqrt{(E_{\mathrm{x}}^{\mathrm{miss}})^2 + \left(E_{\mathrm{y}}^{\mathrm{miss}}\right)^2}, \tag{4.5}$$

$$\phi^{\mathrm{miss}} = \arctan\left(E_{\mathrm{y}}^{\mathrm{miss}} / E_{\mathrm{x}}^{\mathrm{miss}}\right). \tag{4.6}$$

Any detector inefficiency due to a limited coverage or dead material or other sources as noise or cosmic muons can generate a fake $E_{\mathrm{T}}^{\mathrm{miss}}$ signal. Their impact is suppressed by placing specific selection criteria that remove affected events. A more detailed discussion on precautions applied to the sbottom searches can be found in the respective event selection sections.

The performance of the $E_{\mathrm{T}}^{\mathrm{miss}}$ reconstruction has been studied under different pile-up conditions for $\sqrt{s} = 7$ TeV data taken in 2010 [112] and 2011 [113] and for $\sqrt{s} = 8$ TeV data in 2012 [114]. Pile-up from additional pp interactions has a large impact on the reconstruction performance. Different methods were developed to suppress the pile-up effects based on a combination of the tracking and calorimeter information.[9]
To assess the performance of the $E_{\mathrm{T}}^{\mathrm{miss}}$ reconstruction, two different samples were analysed: one without an intrinsic $E_{\mathrm{T}}^{\mathrm{miss}}$ source ($Z \to \ell\ell$), and the other with a $E_{\mathrm{T}}^{\mathrm{miss}}$ source ($W \to \ell\nu$). The $E_{\mathrm{T}}^{\mathrm{miss}}$ resolution $\sigma\left(E_{\mathrm{x(y)}}^{\mathrm{miss}}\right)$ is, to a good approximation, proportional to $\sqrt{\sum E_{\mathrm{T}}}$, i.e. $\sigma\left(E_{\mathrm{x(y)}}^{\mathrm{miss}}\right) = k \cdot \sqrt{\sum E_{\mathrm{T}}}$, where $\sum E_{\mathrm{T}}$ is the scalar sum of the transverse energies of the objects used for the $E_{\mathrm{T}}^{\mathrm{miss}}$ calculation. The factor k is of the order of 0.8 $\mathrm{GeV}^{1/2}$ (0.5 $\mathrm{GeV}^{1/2}$) for 2011 data before (after) pile-up corrections. The distributions of the resolution versus $\sqrt{\sum E_{\mathrm{T}}}$ and the number of primary vertices are shown in Fig. 4.8. Similar results are presented in Fig. 4.9 for 2012 data. A good agreement between MC prediction and data is seen and the pile-up suppression significantly improves the resolution.

8 Note, that $E_{\mathrm{T}}^{\mathrm{miss}}$ always refers to the missing transverse momentum, even though it is computed from energy contributions.
9 The pile-up suppression is not applied for the analyses presented within this thesis.

Systematic uncertainties affect all terms of Eq. (4.4). The reconstruction uncertainties for all objects propagate to the total $E_{\mathrm{T}}^{\mathrm{miss}}$ uncertainty. For the softjets and CellOut terms specific uncertainties were estimated covering the MC modelling and pile-up effects.

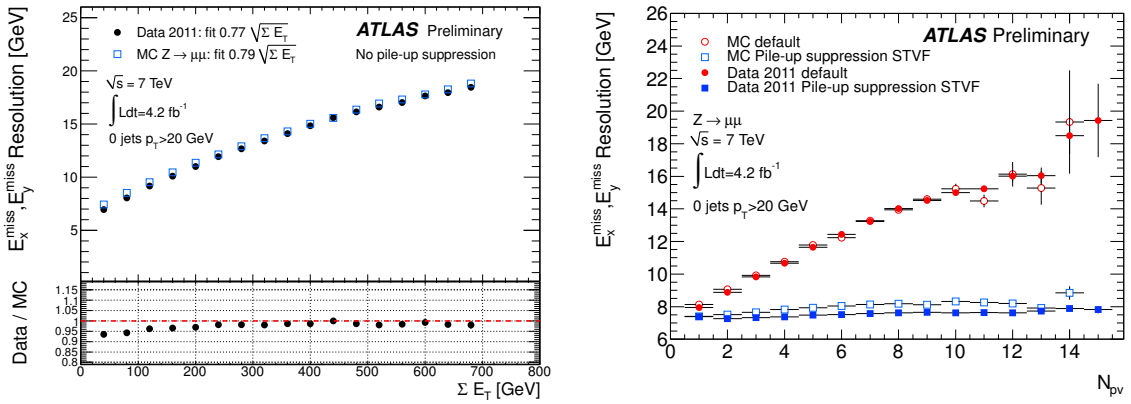

Figure 4.8: Resolution of $E_{\mathrm{x(y)}}^{\mathrm{miss}}$ for $Z \to \mu\mu$ events for $\sqrt{s} = 7$ TeV data recorded in 2011 [113]. Left: resolution as a function of $\sum E_{\mathrm{T}}$ before pile-up suppression methods are applied. Right: resolution as a function of the number of primary vertices for events with no jet with $p_{\mathrm{T}} > 20$ GeV, before (red) and after (blue) pile-up suppression.

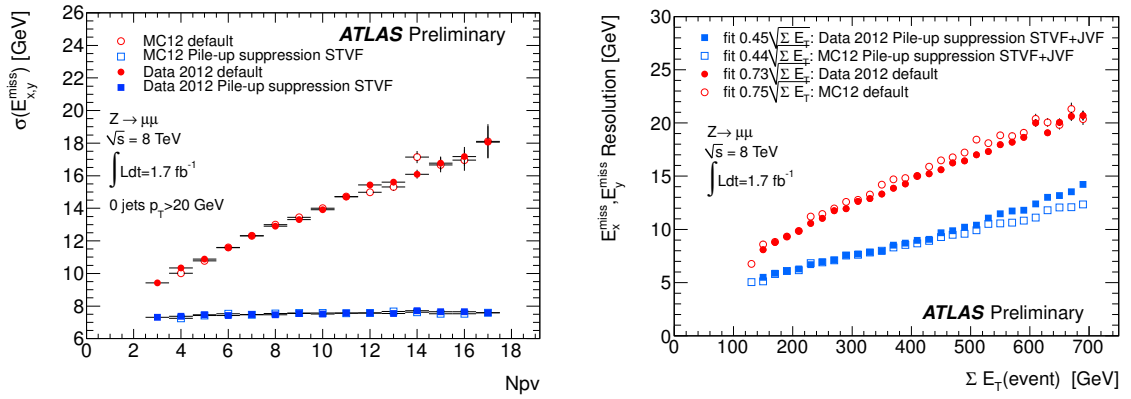

Figure 4.9: Resolution of $E_{\mathrm{x(y)}}^{\mathrm{miss}}$ for $Z \to \mu\mu$ events for $\sqrt{s} = 8$ TeV data recorded in 2012 [114]. Left: resolution as a function of the number of primary vertices for events with no jet with $p_{\mathrm{T}} > 20$ GeV. Right: resolution as a function of the scalar sum of transverse momentum. Both MC and data distributions are shown before (red) and after (blue) pile-up corrections. Pile-up corrections are not applied to the $\sum E_{\mathrm{T}}$ on the x-axis of the right figure.

CHAPTER 5

SUSY Searches at ATLAS

In this chapter, a general overview of R-parity conserving SUSY searches with the ATLAS experiment is given. Common approaches on selection criteria and background estimation are described, while the detailed information for the specific methods used in the sbottom analyses can be found in Chapters 6 and 7, respectively.
The production processes of supersymmetric particles at the LHC are summarised in Section 5.1. An overview of the SUSY analyses performed by the ATLAS collaboration is given in Section 5.2. It is followed by more technical aspects as the trigger selection and general issues on the data preselection in Section 5.3, and the resolving of overlapping final state objects and corrections for the Monte Carlo simulation in Section 5.4. Definitions of relevant variables used in SUSY searches are given in Section 5.5. Different methods for the background estimation are discussed in Section 5.6, and an overview of relevant systematic uncertainties is given in Section 5.7. The statistical framework for interpreting the results obtained by the analyses is summarised in Section 5.8. Finally, current results from SUSY searches with the ATLAS detector are presented in Section 5.9.

5.1 SUSY Production at the LHC

The production cross-sections for various SUSY processes at the LHC are shown in Fig. 5.1 as a function of the mass for the produced particles for a centre-of-mass energy of 7 TeV.
The production of SUSY particles at the LHC is dominated by strong interaction processes. Gluino pairs, squark pairs and squark-gluino pairs are produced by gluon-gluon, quark-gluon or quark-quark interactions:

$$gg \to \tilde{g}\tilde{g}, \tilde{q}\tilde{q}^* \quad gq \to \tilde{g}\tilde{q} \quad qq \to \tilde{q}\tilde{q} \quad q\bar{q} \to \tilde{g}\tilde{g}, \tilde{q}\tilde{q}^*. \tag{5.1}$$

Feynman diagrams for these processes are shown in Fig. 5.2. A lower cross-section is obtained for the third generation squarks compared to the first and second generation squarks, at a given mass value.[1] This is due to the substructure of the proton that is taken into account via the PDF sets. However, as motivated in Section 2.2.5, the masses of the third generation squarks can be well below the masses of the first and second generation squarks, which in contrast enhances the production cross-sections.
The direct production of charginos, neutralinos and sleptons via the electroweak interaction is not considered within this thesis. In comparison to the strong interaction processes, the

1 The production cross-section for the sbottom coincides with the stop cross-section within few percent.

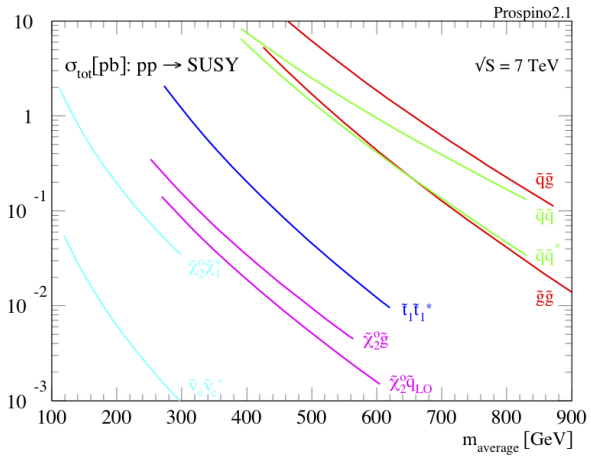

Figure 5.1: Production cross-sections for a selection of SUSY processes as a function of the average mass of the produced particles, calculated for $\sqrt{s} = 7$ TeV at next-to-leading order with PROSPINO [81].

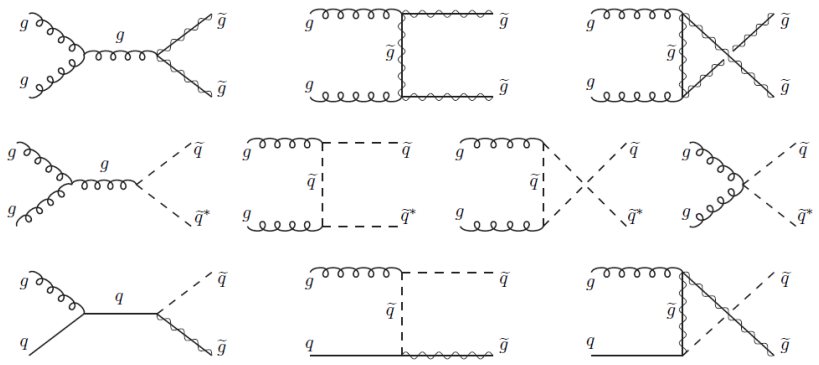

(a) gluon-gluon and gluon-quark processes

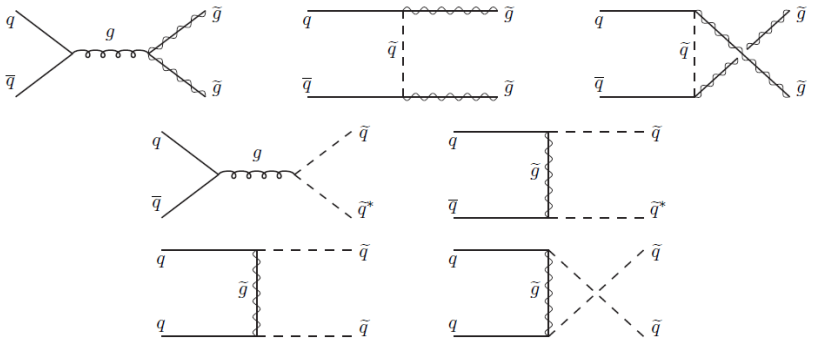

(b) quark-quark processes

Figure 5.2: Feynman diagrams for the production of SUSY particles via the strong interaction [26].

electroweak processes are expected to be sub-dominant at the LHC.
For a centre-of-mass energy of 8 TeV, the general structure stays the same but the cross-sections increase compared to the values at 7 TeV: ∼75% (140%) for gluino-pair production at $m_{\tilde{g}} = 500$ GeV(1 TeV) and ∼76% (150%) for stop/sbottom-pair production at $m_{\tilde{b}_1/\tilde{t}_1} = 500$ GeV(1 TeV).

5.2 Overview of the SUSY Search Channels

A large number of different analyses searching for SUSY are performed by the ATLAS collaboration. In the following, a short overview of the various R-parity conserving search channels is given.[2]
The common signature to R-parity conserving (RPC) SUSY channels is the presence of $E_{\mathrm{T}}^{\mathrm{miss}}$. Besides that, the individual channels are characterised by the number of required jets, b-jets, leptons and photons, depending on the studied signature. The RPC searches can be grouped into three main categories:

Inclusive Searches: The inclusive searches are usually performed on constrained SUSY models, like GMSB or mSUGRA, or phenomenological models. Strong limits on the first and second generation squark and gluino masses are obtained from these analyses. Especially the search channels with no or one lepton and multiple jets were powerful SUSY discriminators even for the early data analyses.

3rd generation searches: The search for third generation squarks became more and more popular as the inclusive searches pushed up the limits on the 1^{st} and 2^{nd} generation squark and gluino masses, and the increasing amount of data opened up new search possibilities.[3] The searches are typically performed on simplified models targeting a specific production and decay mode. The production can be a direct production of sbottom or stop pairs or a gluino-mediated production where the gluino decays via a sbottom or stop. Most channels include b-jets that come from the stop or sbottom decays, but there are also searches based on multiple leptons.

Electroweak Production: Searches for SUSY particles produced via the electroweak interaction cover the direct production of gauginos or sleptons. These might be the dominant processes to produce SUSY particles if the squarks and gluinos are heavy. Simplified models are used for the interpretation of results and the decay chains usually involve sleptons and sneutrinos leading to multiple leptons in the final state.

5.3 Preselection: Trigger and Data Quality

Each analysis needs to define which trigger is the most efficient to record the collision events of interest. In addition, preselection criteria are defined to ensure a good quality of the events and to avoid non-collision background events and noisy events to pass the analysis selection.

5.3.1 Trigger

Depending on the explored signature, events are selected that were flagged by a trigger on one or more of the final state objects. Whenever the final event selection requires at least one electron or muon, a lepton trigger can be used. Final states with no leptons can be triggered based on the amount of missing transverse momentum or the presence of high transverse momentum jets.
The trigger efficiency reaches a stable value (the trigger plateau) above the actual trigger threshold. As this turn-on characteristics is not necessarily well described in Monte Carlo simulation, the analysis selection thresholds are normally adapted and chosen such that full

2 A brief introduction to the R-parity violating searches is given in Section 5.9.
3 For a motivation of models with light third generation particles see Section 2.2.5.

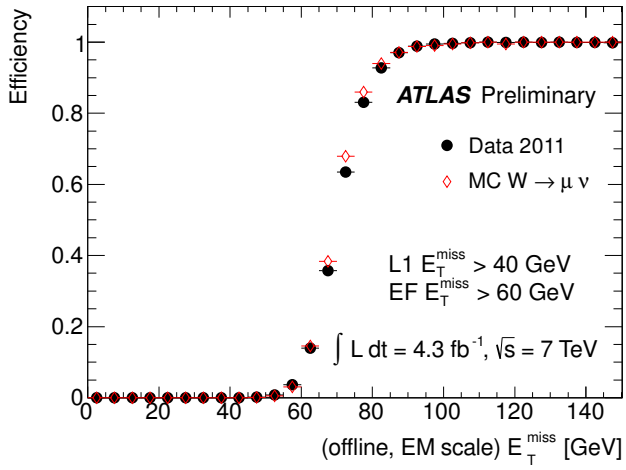

Figure 5.3: Trigger efficiency for an $E_{\mathrm{T}}^{\mathrm{miss}}$ trigger as a function of the offline $E_{\mathrm{T}}^{\mathrm{miss}}$ threshold obtained for the 2011 dataset [115]. The Level-1 trigger threshold is set to 40 GeV and the event filter threshold to 60 GeV. The efficiency is evaluated with respect to events selected by a muon trigger for $W \to \mu\nu$ events.

efficiency (in the region of the plateau) is reached. In Figure 5.3, the turn-on behaviour as measured for an $E_{\mathrm{T}}^{\mathrm{miss}}$ trigger with the 2011 dataset is shown.
For the lepton triggers, scale factors to adapt the trigger efficiencies in MC events to those measured in data are available. They are applied depending of the energy and pseudorapidity of the lepton firing the trigger.[4]

5.3.2 Data Quality

The quality of the data to be analysed can be compromised because of detector malfunctioning or the presence of particles not originating from a proton-proton collision (cosmic rays, beam background). In the following, an overview of quality-derogating sources and specific requirements to improve the quality are described. Events that fail one of the criteria are removed.

General Event Cleaning Requirements

A few general selection criteria are applied prior to specific requirements for the reconstructed objects or temporary detector defects.

Data Quality: Events are flagged to be of bad quality via an external list when relevant detector devices were found to be malfunctioning after reprocessing. The total integrated luminosity is scaled down accordingly to allow for a correct normalization of the MC samples.

Vertex Selection: Non collision background events are rejected by requiring the presence of an interaction vertex with at least four associated tracks.

Corrupted Events: Events, where part of the information was not written to buffer and is lost, are rejected. In addition, events are rejected if either a noise burst in the LAr

4 Matching procedures allow to detect if a reconstructed lepton can be associated with the triggering object.

calorimeter or a data corruption in the tile calorimeter was observed. Only a very small fraction of events is affected by this.

Object Cleaning

The analyses presented in this thesis are particularly sensitive to fake $E_{\mathrm{T}}^{\mathrm{miss}}$ contributions, which can be caused by mis-measurements of any of the objects passed to the $E_{\mathrm{T}}^{\mathrm{miss}}$ calculation.

Bad Jets: Different sources can produce a signal in the calorimeter that is mis-interpreted as a jet. For example, real particles from cosmic events or non-collision background can create spurious jet signatures. Coherent calorimeter noise can also lead to the reconstruction of a fake jet.
A set of criteria have been defined to detect these *bad jets*. They are based on the energy fractions deposited in different regions or layers of the calorimeter, the quality of the fit of the calorimeter pulse shapes, the negative energy contribution to the jet, the jet charged fraction (see next item) and the timing of the calorimeter signal compared to that of the bunch crossing. Events are removed if any of the reconstructed jets with $p_{\mathrm{T}} > 20$ GeV fulfills the bad jet criteria.

Jet Charged Fraction: The charged fraction of a jet, chf, is obtained by dividing the momenta of the tracks associated with the jet by the reconstructed jet momentum. It is used already for the bad jet definition but a stricter selection on the highest momentum jets was found helpful to further reject events with jets produced by cosmic rays or beam backgrounds, for which no associated tracks are expected.

Timing: The timing of the jets with respect to that of the triggered bunch crossing is used to further reduce the contribution from cosmic or beam backgrounds. The energy weighted mean time for the selected jets is calculated and needs to be smaller than 5 ns.

Fake $E_{\mathrm{T}}^{\mathrm{miss}}$: A few cells of the tile calorimeter are not functioning[5] and lead to a wrong energy response and resolution of reconstructed jets and fake $E_{\mathrm{T}}^{\mathrm{miss}}$ contributions. The B_{jet}^{corr} variable provides an extrapolation of the fractional jet energy correction for bad cells that is derived from comparing jet energy profiles. Events are removed if they contain a jet with $p_{\mathrm{T}} > 40$ GeV, $B_{\mathrm{jet}}^{corr} > 0.05$ and $\Delta\phi(\mathrm{jet},\mathrm{E}_{\mathrm{T}}^{\mathrm{miss}}) < 0.2$.

Negative Energy: Data corruption in the tile calorimeter can lead to cells or reconstructed topological clusters with a large negative energy contribution. These cells and clusters are not associated to any reconstructed jet but contribute to the $E_{\mathrm{x(y)}}^{\mathrm{miss,CellOut}}$ term in the $E_{\mathrm{T}}^{\mathrm{miss}}$ calculation. The significance of the contribution is estimated by the following variable: $f_{\mathrm{CellOut}} = \frac{E_{\mathrm{T}}^{\mathrm{miss,CellOut}}}{E_{\mathrm{T}}^{\mathrm{miss}}} \cdot \cos(\Delta\phi(E_{\mathrm{T}}^{\mathrm{miss,CellOut}},E_{\mathrm{T}}^{\mathrm{miss}}))$. Events with a large value are rejected.

Bad Muons: The punch through of very energetic jets into the muon spectrometer or a wrong matching of badly measured jet tracks in the inner detector to track segments in the muon spectrometer can produce fake muons. Such events need to be rejected as the fake muons can lead to a wrong $E_{\mathrm{T}}^{\mathrm{miss}}$ reconstruction. It is done by requesting a small significance of the charge-momentum ratio $\left(\frac{\sigma(\frac{q}{p})}{|\frac{q}{p}|} < 0.2\right)$ in both data and MC events.

5 This is mainly due to a non-functional low voltage power supply.

Cosmic Muons: The transverse impact parameter d_0 and axial impact parameter z_0 are used to distinguish cosmic muons from muons originating from the primary vertex. A veto on events with $|d_0| > 0.2$ mm or $|z_0| > 1$ mm is applied.

Temporary Detector Effects

There were periods when a small region of one of the detectors was not working properly. Only parts of the datasets are affected by these features and need to be treated.

LAr Hole: In the 2011 data taking period a loss of several front end boards in the barrel region of the electromagnetic calorimeter occurred. They were recovered about a month later and in total 0.86 fb^{-1} of the total integrated luminosity has been collected with this problem. Multiple calorimeter layers in the $0.0 < \eta < 1.4$ and $-0.74 < \phi < 0.64$ region were failing, leading to a decrease of reconstructed object energy in this region. The energy loss is in particular important for the $E_{\mathrm{T}}^{\mathrm{miss}}$ reconstruction in the SUSY analyses. In a first attempt all events with a jet pointing in the affected region were rejected but this procedure has a negative effect on the signal selection efficiency. A more advanced method is used that does hardly decrease the efficiency but still removes the affected events. It is based on estimating the energy contribution of the dead cells from the surrounding cells and comparing it to the size and direction of the reconstructed $E_{\mathrm{T}}^{\mathrm{miss}}$. Data events are removed if a significant $E_{\mathrm{T}}^{\mathrm{miss}}$ fraction comes from a mis-measured jet of the affected region.

Noisy Tile Cell: In the beginning of the 2012 data taking period a cell in the tile calorimeter became noisy but was not masked in the data reconstruction. Data events are rejected if a jet points in direction of the cell ($-0.2 < \eta < -0.1$, $2.65 < \phi < 2.75$), the largest energy fraction of the jet is deposited in the second calorimeter layer and this fraction is large ($E_{\mathrm{layer}}/E_{\mathrm{jet}} > 0.6$).

Forward Calorimeter: A problem in the power setting occurred in two quadrants of the forward calorimeter during the 2012 data taking period corresponding to a total integrated luminosity of 1.2 fb^{-1}. It affects the jet energy scale of jets reconstructed in this region ($|\eta|$ >3.2 and 1.6< ϕ <3.1) by 10-20%. In this thesis no jets with $|\eta|$ >2.8 are used, but the effect is transmitted to the $E_{\mathrm{T}}^{\mathrm{miss}}$ reconstruction. Therefore, data events from the affected data taking period are discarded if a jet with $p_{\mathrm{T}} > 20$ GeV points to the region. A corresponding fraction of MC simulated events is treated by the same procedure.

5.4 Overlap Removal and Monte Carlo Reweighting

In this section two further aspects that are considered by the analyses are discussed. They include the removal of overlapping reconstructed objects, referred to as overlap removal, and the reweighting of MC events to better describe data.

Overlap Removal

The object reconstruction methods are described in detail in Section 4.2. For each analysis, it needs to be decided which procedure is applied when multiple choices are available and where to set the momentum and η thresholds for the selected objects.

It can happen that the same measured object is reconstructed as two (or more[6]) different physical objects and thus counted twice. This problem is solved by the so-called overlap removal procedure. It is applied in two consecutive steps:

1. Remove a jet from the list of jets if it is found within $\Delta R = 0.2$ of an identified electron.
2. Remove an electron or muon from the list of leptons if it is found within $\Delta R = 0.4$ of a jet.

The first step accounts for the fact that every sufficiently energetic electron produces a calorimeter shower and is thus also reconstructed as a jet. For larger electron-jet distances it is more likely that the electron is a decay product of a hadron inside the jet. This is accounted for by the second step. Muons hardly leave any significant signature in the calorimeter and are only considered as decay products in the second step.

Monte Carlo Reweighting

As mentioned when describing the object reconstruction performance, the reconstruction efficiencies in MC samples need to be adapted to the ones measured in data. In particular this affects the lepton reconstruction and b-tagging efficiency.
In addition, a weighting of MC events is applied to better match the pile-up conditions present in data. When MC events are generated, specific values are assumed for the mean number of interactions per bunch crossing μ. The pile-up reweighting procedure assigns events weights in such a way that the μ distribution matches the one observed in the analysed dataset.

5.5 Relevant Variables

To enhance the separation power for SUSY and SM events a number of variables calculated from the kinematic quantities of the physical objects are considered. The ones relevant to the studies presented in this thesis are defined and explained in the following.

Effective Mass

The effective mass M_{eff} is generally defined as the scalar sum of the missing transverse momentum $E_{\text{T}}^{\text{miss}}$ and the transverse momenta of the reconstructed jets and isolated leptons that play a role in the event selection. In an analysis selecting n jets and m leptons it is calculated as:

$$M_{\text{eff}} = E_{\text{T}}^{\text{miss}} + \sum_{i \leq n} (p_{\text{T}}^{\text{jet}})_i + \sum_{i \leq m} (p_{\text{T}}^{\text{lepton}})_i. \tag{5.2}$$

The maximum of the M_{eff} distribution is correlated to the mass scale of the SUSY particles. This feature is not directly used to extract the mass-scale, but SUSY events tend to have higher M_{eff} values compared to the SM processes.

6 For this analysis only the possible overlap of jets with electrons and muons is considered. More objects can be reconstructed from one particle for example by analyses relying on the identification of hadronically decaying tau leptons.

Scalar Sum of Jet Momenta

The scalar sum of the momentum of a number of jets is generally denoted by H_{T}:

$$H_{\mathrm{T}} = \sum_{i \leq n} (p_{\mathrm{T}}^{\mathrm{jet}})_i. \tag{5.3}$$

For the searches of direct sbottom-pair production an upper threshold on additional hadronic activity in the event helps for the background rejection. It is calculated by excluding the leading x jets:

$$H_{\mathrm{T},x} = \sum_{i=x+1}^{n} (p_{\mathrm{T}}^{\mathrm{jet}})_i. \tag{5.4}$$

Transverse Mass

The transverse mass m_{T} of a reconstructed lepton ℓ and the missing transverse momentum is defined as:

$$m_{\mathrm{T}} = \sqrt{2p_{\mathrm{T}}^{\ell} \cdot E_{\mathrm{T}}^{\mathrm{miss}} - 2\mathbf{p}_{\mathrm{T}}^{\ell} \cdot \mathbf{E}_{\mathrm{T}}^{\mathrm{miss}}}. \tag{5.5}$$

The variable can be used to discriminate against $E_{\mathrm{T}}^{\mathrm{miss}}$ contributions arising from $W \to \ell\nu$ decays, as in this case it peaks at the W mass (the so-called Jacobian Peak).[7] Therefore, it provides a handle on the $t\bar{t}$ and W production backgrounds. For the sbottom analyses, it is used for the background estimation in the one-lepton control regions.

Boost Corrected Contransverse Mass

The contransverse mass m_{CT} of two particles v_1 and v_2 is defined in Ref. [116] as:

$$m_{\mathrm{CT}}^2(v_1,v_2) = \left[E_{\mathrm{T}}(v_1) + E_{\mathrm{T}}(v_2)\right]^2 - \left[\mathbf{p}_{\mathrm{T}}(v_1) - \mathbf{p}_{\mathrm{T}}(v_2)\right]^2, \tag{5.6}$$

with $E_{\mathrm{T}} = \sqrt{p_{\mathrm{T}}^2 + m^2}$. For pair-produced particles p where each of them decays into a visible particle v and an invisible particle n, it has an endpoint at:

$$m_{\mathrm{CT}}^{\mathrm{max}} = \frac{m^2(p) - m^2(n)}{m(p)}. \tag{5.7}$$

The m_{CT} quantity is invariant under a longitudinal Lorentz boost. However, it is not invariant under a generic Lorentz boost: if the p_1-p_2-system recoils against upstream objects, for example jets from initial state radiation, the m_{CT} value can exceed the boundary in Eq. (5.7). An exact correction for the boosts is not possible, but a conservative boost correction was proposed in Ref. [117] and is applied to any m_{CT} calculation within this thesis.
The impact of using the m_{CT} variable can be observed in the searches for sbottom-pair production where each sbottom decays via $\tilde{b}_1 \to b\tilde{\chi}_1^0$ (see Chapter 6). The endpoint $m_{\mathrm{CT}}^{\mathrm{max}}(b,b) = \frac{m^2(\tilde{b}) - m^2(\tilde{\chi}_1^0)}{m(\tilde{b})}$ can reach much larger values compared to the SM background, depending on the mass difference between the $\tilde{b}_1$ and $\tilde{\chi}_1^0$. For $t\bar{t}$ events the endpoint is at $m_{\mathrm{CT}}^{\mathrm{max}}(b,b) = \frac{m^2(t) - m^2(W)}{m(t)} \simeq 135$ GeV.

7 $m_{\mathrm{T}} = m_W$ if the lepton and neutrino are emitted in the transverse plane and no other source contributing to $E_{\mathrm{T}}^{\mathrm{miss}}$ than the neutrino is present.

Minimal Azimuthal Distance

The minimal azimuthal distance $\Delta\phi_{\text{min}}$ between n jets and the missing transverse momentum is defined as:

$$\Delta\phi_{\text{min}} = \min\left(|\phi_{\text{jet}_\text{i}} - \phi_{E_\text{T}^\text{miss}}|,...,|\phi_{\text{jet}_\text{n}} - \phi_{E_\text{T}^\text{miss}}|\right). \tag{5.8}$$

It is mainly used to reject QCD multi-jet events, where the E_T^miss is due to mismeasured jets or neutrinos in heavy-flavour jet decays and it is therefore aligned to the direction of one of the jets.

5.6 Background Estimation

There are two types of background sources that need to be considered for the R-parity conserving SUSY searches with no leptons in the final state: the irreducible background processes, with a real E_T^miss component due to neutrinos, as $t\bar{t}$, $W \to \ell\nu$ and $Z \to \nu\nu$ production, and reducible background sources with fake E_T^miss due to mis-measured jets.

Irreducible Backgrounds

The simplest approach to estimate a specific background contribution is to estimate the event yield from dedicated MC samples. As the MC simulation might not fully reproduce the details of the background processes, data-based cross-checks and estimations are mandatory for the main background contributions.

In most of the ATLAS SUSY analyses, the approach to the estimation of the irreducible background processes is relatively simple and corresponds to a semi data-driven method: the shape of the distributions of kinematic quantities is taken from the MC samples, while the final normalisation is obtained from data in a control region (CR). The measured event yield in the CR is converted to the expected event yield in the signal region (SR) via a transfer factor T_f obtained from MC:

$$N_\text{exp}^\text{SR} = T_f \cdot N_\text{data}^\text{CR} = \frac{N_\text{MC}^\text{SR}}{N_\text{MC}^\text{CR}} \cdot N_\text{data}^\text{CR}. \tag{5.9}$$

The CRs are defined such that there is no signal contamination, a high purity and selection efficiency for the background of interest and similar kinematic conditions as in the signal region. They are typically obtained by inverting the cut on any of the background discriminating variables involved, for example the E_T^miss variable. Control regions with one or more leptons were found essential for analyses vetoing leptons like the direct sbottom-pair production searches. Another advantage of this approach is that systematic uncertainties may be reduced as they are correlated in the signal and control region.

An exclusive CR can be defined for each of the dominant backgrounds to estimate each contribution separately. The actual calculation is performed by getting all normalisations in one step with a combined fit of multiple CRs. This way the contamination of different background sources in each CR is automatically taken into account and also CRs with a mixed background composition can be exploited. The statistical setup for the fit is described in Section 5.8.1.

Reducible Backgrounds

A general feature of the reducible background components is that they are caused by rare detector effects for SM processes that have large cross-sections. A sufficient description by

MC samples is therefore often not possible and they need to be estimated completely from data.
A data-driven estimation needs to be applied for the QCD multi-jet background in most of the SUSY analyses. The multi-jet background is usually only a sub-dominant background contribution, as significant $E_{\mathrm{T}}^{\mathrm{miss}}$ is only obtained by heavily mis-measured jets or neutrinos from heavy-flavour jets. A commonly used multi-jet estimation technique for analyses with no leptons is the jet-smearing method, described in Section 5.6.1.

5.6.1 Jet Smearing for Multi-Jet Events

The basic idea for this method is to select a large sample of seed events with a low $E_{\mathrm{T}}^{\mathrm{miss}}$ contribution from data and then smear the jet momenta to obtain a sample of events with large $E_{\mathrm{T}}^{\mathrm{miss}}$. The method is described in detail in Ref. [118] and is summarized here.
The seed events are selected by applying relatively loose single jet triggers and requiring a low $E_{\mathrm{T}}^{\mathrm{miss}}$ significance defined as:

$$S = \frac{E_{\mathrm{T}}^{\mathrm{miss}}}{\sqrt{\sum E_{\mathrm{T}}}}, \tag{5.10}$$

where the sum extends over all transverse clustered and unclustered energies. A low value of S means that the measured jet momenta are close to their true values[8]. In addition some selection criteria, based for example on the number of jets or b-jets, are applied to build a sample resembling the final state addressed in the analysis.
The jets in the seed events are then smeared with a jet response function:

$$R = \frac{p_{\mathrm{T}}^{\mathrm{reco}}}{p_{\mathrm{T}}^{\mathrm{true}}}. \tag{5.11}$$

It is emulating the calorimeter response by comparing the generated momenta $p_{\mathrm{T}}^{\mathrm{true}}$ with the reconstructed jet momenta $p_{\mathrm{T}}^{\mathrm{reco}}$ in MC simulation. The response distribution has mainly a Gaussian shape with small non-Gaussian tails. The shape is corrected using data-based measurements on di-jet and multi-jet events.
The response function depends on the jet flavour and the use of individual response functions instead of one global response function improves the multi-jet estimation in analyses selecting b-jets. In general, a broader tail on the lower side of the response function is caused by the presence of neutrinos in heavy-flavour originated jets.
The seed events are smeared with the response function about 1000 times to generate a significant $E_{\mathrm{T}}^{\mathrm{miss}}$ contribution. Also events where the $E_{\mathrm{T}}^{\mathrm{miss}}$ is coming from multiple mismeasured jets are obtained this way. They correspond to the residual multi-jet events in the signal region that cannot be eliminated by a $\Delta\phi_{\mathrm{min}}$ threshold.
The sample of smeared events can be treated similar to a MC generated sample, but the normalisation needs to be estimated from data. A multi-jet dominated control region is easily obtained by selecting events with low $\Delta\phi_{\mathrm{min}}$.

8 It is required that $S < 0.6$ GeV$^{1/2}$.

5.7 Systematic Uncertainties

Systematic uncertainties on the estimated background processes are evaluated both in terms of experimental uncertainties when reconstructing the events and theory uncertainties for the event generation. For a few uncertainties global values are directly provided. Otherwise the analysis is run separately for each systematic component that is studied, providing the uncertainty in form of a shift in the final event yield. In the combined fit of control regions, the systematic uncertainties are treated as nuisance parameters.

5.7.1 Experimental Uncertainties

Experimental uncertainties are common to all background processes (except for specific multi-jet uncertainties arising from the jet-smearing method). The dominant contributions for the analyses in this thesis come from the uncertainty on the jet energy scale and b-tagging. The experimental uncertainties considered in this thesis are:

Luminosity: The uncertainty on the integrated luminosity depends on the dataset and is usually below ±4% [119].

Pile-up: Uncertainties on the pile-up scaling factors are obtained by varying the average number of interactions per bunch crossing by 10% up and down while performing the pile-up reweighting.[9] They are propagated to uncertainties on the event yield.

JES: The uncertainty on the energy scale of jets is taken into account by shifting the scale up and down by one standard deviation. The modified jet momenta and energies are also passed to the $E_{\mathrm{T}}^{\mathrm{miss}}$ calculation to scale it accordingly.
The energy scale uncertainty depends on the jet p_{T} and η, and it is about ±2% for a central jet of 50 GeV. Additional contributions are considered, which depend on the angular distance to the closest jet and the average quark-gluon composition of the analysed sample. An extra uncertainty on the pile-up energy corrections is included. In total, a ±5% uncertainty is obtained for a 50 GeV jet in the central region. Differences for the energy scale of b-jets were found compared to light jets and an additional contribution of ±2.5% is added for the b-jets[10]. More information on the JES uncertainty can be found in Ref. [98].

JER: The jet momenta are smeared to generate a broader resolution distribution to account for a possibly worse jet energy resolution in data[11]. The smearing is done using a Gaussian distribution with a mean value of 1 and a jet p_{T} and η dependent width.

b-tagging: Uncertainties for the b-tagging scale factors come from the methods described in Section 4.2.3. The b-tagging uncertainties are obtained by varying the scale factors up and down by one standard deviation separately for light-, c- and b-jets, providing three uncorrelated systematic uncertainties[12]. The scale-factor uncertainty for a 50 GeV b-jet is about ±(6-7)%.

9 The ±10% variation is based on the difference of the cross-sections for minimum bias events as predicted by different PYTHIA versions.

10 Here, b-jets refers to the truth flavour of the jet that is stored in the MC samples.

11 The resolution for data compared to MC events was studied for the jet momenta of dijet events using the 2010 dataset [120]. Roughly a 10% worse resolution was observed in data, which is consistent within the estimated systematic uncertainties.

12 In case the scale factors are not applied, which is the case for the sbottom-pair production analysis, the relative scale factor uncertainties can be propagated.

CellOut: Uncertainties for the $E_{\mathrm{x(y)}}^{\mathrm{miss,CellOut}}$ term in the $E_{\mathrm{T}}^{\mathrm{miss}}$ calculation are considered by varying the energy scale for the clusters. The uncertainty on the cluster energy resolution is taken into account independently.

Leptons: Scale factors for the lepton identification efficiencies were found consistent with unity, with the largest discrepancies being below 3%. Therefore, no scale factors are applied and, depending on the analysis, a conservative ±3% uncertainty on the final event yield is assumed or the uncertainty is neglected.
The lepton energy scale and resolution uncertainties are of the order of a fraction of a percent. Its effect was studied by shifting the lepton momenta up and down by 3% for a general class of SUSY analyses with b-jets. The final uncertainty on the event yield was found below ±1% and the uncertainty is therefore neglected.

QCD: Specific uncertainties for the multi-jet background estimated with the jet-smearing method are considered. Variations on the Gaussian width and distribution tails of the response function are applied. Statistical and experimental uncertainties as mentioned above are also taken into account. The uncertainty on the final event yield is large (usually in between ±(50-90)%) and dominated by the tail variations and b-tagging contributions.

5.7.2 Theory Uncertainties

The theory uncertainties are estimated depending on the underlying SM or SUSY process and the generator used to produce the MC samples. Often there is more than one way of addressing one type of uncertainty. A general list of possible contributions and concepts is given here, but it should be noticed that not all of them can be applied for each sample and there may be overlaps between the definitions:

Cross-Section: Two main sources contribute to uncertainties on the cross-sections: PDF uncertainties and uncertainties on the renormalization and factorisation scales. They are computed individually and correlations between the PDF and scale uncertainties are usually neglected.
The PDF sets used in the ATLAS analyses are estimated from data and are provided with uncertainties. A set of 20 to 30 variations, depending of the PDF set, represent the different components of the experimental uncertainties. They are added to an asymmetric total PDF uncertainty.
The scales for the renormalization and factorisation are usually chosen at equal values corresponding to the masses of the primarily produced particles. The uncertainty is then obtained by varying the scales up and down by factors of two.
For samples generated with ALPGEN an additional uncertainty addressing the MLM matching procedure (see Section 2.3.2) can be added.

Generator: As different MC generators tend to produce slightly different results, an uncertainty on the event generation is obtained by the comparison of the results. The relative difference in the final event yield obtained by a independently produced MC sample is taken as the systematic uncertainty.

Initial and Final State Radiation: The phase space for initial state radiation (ISR) is bound by specific parameters which can be varied to estimate the uncertainty. An uncertainty on the final state radiation (FSR) is estimated by modifying the boundary below which no further radiation of the partons is assumed. Limits on the size of these variations

are obtained by a study on the rapidity gaps between jets in $t\bar{t}$ events [121]. Based on these results, separate samples including the maximal allowed variations are produced. The uncertainties are then estimated by comparing event yields obtained from the truth MC information in a simplified analysis.
Depending on the generator, another way of addressing the uncertainty is to examine the impact of varying the number of additional partons in the matrix element.

Parton Shower: Uncertainties for the parton shower modelling are estimated by comparing dedicated samples. Either the showering strength is modified for a given showering model or different implementations for the showering model are compared.

5.8 Interpretation of Results

The final step of any analysis is the statistical interpretation of the results. When no significant deviation from the expected SM background is found in the data, the results are usually interpreted in terms of exclusion limits.
Based on the observed event yields, different hypotheses can be statistically tested by computing the corresponding p-values. The p-value is generally defined as the probability that the observation is, under assumption of the hypothesis H, in equal or better agreement with the prediction of H. If the p-value is found below a given threshold $\hat{p}$, the hypothesis is rejected at a confidence level (CL) of $1-\hat{p}$. Often the p-value is transferred to the significance z, which is defined as the number of standard deviations of a Gaussian distribution such that the integral of the one-sided tail is equal to the p-value ($p = \int_z^\infty 1/\sqrt{2\pi} e^{-x^2/2} \mathrm{d}x$).
The hypotheses of general interest for the search for new physics are the null hypothesis, i.e. the measured data is described by background b only ($H \hat{=} b$), and the signal hypothesis, i.e. the measured data is described by signal and background ($H \hat{=} s+b$). A common convention is to exclude a signal hypotheses if $p < 0.05$, corresponding to $z > 1.64$. For a discovery, the background-only hypothesis must be excluded with $p < 2.87 \cdot 10^{-7}$, corresponding to $z > 5$. In order to optimise the analysis strategy, the expected outcome of the experiment is evaluated by substituting the measurement by the prediction of the assumed hypothesis.
Within this thesis, a generic statistical framework based on a profile likelihood fit is used. It is based on the concepts described in Ref. [122] and is briefly introduced in Section 5.8.1. For the limit calculation, the CLs method as described in Section 5.8.2 is applied. The different modifications of the statistical methods used in this thesis are listed in Section 5.8.3.

5.8.1 Statistical Framework

In case of a simple counting experiment with one signal region selection, the expected number of events is given by $E[n] = \mu s + b$, where s and b are the expected signal and background events and μ is a signal strength parameter allowing for the transition between the background-only, $\mu = 0$, and the nominal signal hypothesis, $\mu = 1$. Both s and b are given by integrating their probability density functions over the allowed range of the signal region, i.e. $s = s_{tot} \int f_s(x;\boldsymbol{\theta}_s)\mathrm{d}x$ and $b = b_{tot} \int f_b(x;\boldsymbol{\theta}_b)\mathrm{d}x$. These may depend on several so-called nuisance parameters, denoted by $\boldsymbol{\theta} = (\boldsymbol{\theta}_s, \boldsymbol{\theta}_b)$. The parameter of interest to make a discovery or an exclusion is the signal strength μ. The likelihood function for this model is given by the Poisson probability:

$$L(\mu,\boldsymbol{\theta}|n) = \frac{\Big(\mu s(\boldsymbol{\theta}_s) + b(\boldsymbol{\theta}_b)\Big)^n}{n!} e^{-\left(\mu s(\boldsymbol{\theta}_s)+b(\boldsymbol{\theta}_b)\right)}. \tag{5.12}$$

It can be easily generalised to consider a measured histogram with several bins, by multiplying the Poisson distributions of the individual bins. A commonly used test statistic is defined via the profile likelihood ratio:

$$q_\mu = -2\ln\frac{L(\mu,\hat{\hat{\boldsymbol{\theta}}})}{L(\hat{\mu},\hat{\boldsymbol{\theta}})}, \tag{5.13}$$

where $\hat{\mu}$ and $\hat{\boldsymbol{\theta}}$ are the values that maximize the unconditional likelihood function and $\hat{\hat{\boldsymbol{\theta}}}$ are the values that maximize the likelihood for a given value μ.[13]
The p-value for a considered μ-hypothesis is obtained from the probability density function of the test statistic $f(q_\mu|\mu)$:

$$p_\mu = \int_{q_{\text{obs}}}^{\infty} f(q_\mu|\mu)\mathrm{d}q_\mu, \tag{5.14}$$

where q_{obs} is the observed value of the test statistic. The $f(q_\mu|\mu)$ distribution can be computed by generating a large number of toy Monte Carlo experiments. An approximation used within this thesis, is to generate only one so-called Asimov dataset that represents the set of toy experiments (see Ref. [122]).
The likelihood function can be extended to take into account additional measurements that constrain the nuisance parameters, referred to as profiling. The nuisance parameters considered in this thesis are the systematic uncertainties described in the previous section. Also the background expectation, denoted by b_{tot} above, can be considered as a nuisance parameter. However, the normalisations for several background components are obtained by adding specific control regions to the likelihood and they are therefore separately denoted here by μ_b. The general idea is to share the background parameters (μ_b and $\boldsymbol{\theta}_b$) among the signal and control regions such that they are mainly constrained by the control regions and have a reduced impact (in terms of uncertainties) in the signal region. In total the likelihood can be written as:

$$L(\mu,\mu_b,\boldsymbol{\theta}|n,\boldsymbol{\theta}^0) = P_{SR}(n|\mu,\mu_b,\boldsymbol{\theta}) \times P_{CR}(n|\mu,\mu_b,\boldsymbol{\theta}) \times P_{sys}(\boldsymbol{\theta}^0|\boldsymbol{\theta}), \tag{5.15}$$

where $P_{SR}(n|\mu,\mu_b,\boldsymbol{\theta})$ is the Poisson probability of the signal region, $P_{CR}(n|\mu,\mu_b,\boldsymbol{\theta})$ denotes the product of the Poisson distributions of all considered control regions and $P_{sys}(\boldsymbol{\theta}^0|\boldsymbol{\theta})$ is typically a product of Gaussian distributions for the systematic uncertainties that are varied around the nominal values $\boldsymbol{\theta}^0$. Ideally, no signal events pass the control region selections. Nevertheless, a possible contamination of signal events can be taken into account via the μ dependence. In case that histograms with multiple bins are considered, the systematic uncertainties can be implemented in different ways depending on the type of the uncertainty:

- Varying the shape of the histogram correlated among the bins but keeping the overall scaling of the histogram.
- Varying the normalisation of the histogram without using the shape information.
- Combining the variations on the shape and normalisation of the histogram.

13 To account for a positive signal strength, q_μ is defined as $q_\mu = -2\ln\frac{L(\mu,\hat{\hat{\boldsymbol{\theta}}})}{L(0,\hat{\hat{\boldsymbol{\theta}}})}$ for negative values of $\hat{\mu}$.

- Varying the shape for each bin separately without considering correlations among the bins.

Most uncertainties are treated by either of the first two prescriptions. It should be noted that the uncertainties can either be assigned to individual background (or signal) components (e.g. theory uncertainties for the top background) or as common uncertainty for all background (and signal) components (e.g. uncertainty on the JES) by sharing the same nuisance parameters. The uncertainties are usually shared among all control and signal regions. Correlations between the nuisance parameters are considered and taken into account when computing the total uncertainties for the final results.

5.8.2 The CLs Method

Upper limits for a given signal model are based on the p-value obtained for the $\mu = 1$ hypothesis ($\hat{=}p_{s+b}$) by requiring:

$$p_{s+b} < \alpha, \tag{5.16}$$

where the threshold is generally set to $\alpha = 0.05$. This procedure, however, excludes also signal models with a limited sensitivity in case of a sufficient downward fluctuation of the number of observed events. A low sensitivity is given when there is hardly any separation of the test statistic of $q_{\mu=1}$ and $q_{\mu=0}$, e.g. if $s \ll b$.
A penalty, based on the p-value of the background-only hypothesis, p_b, is introduced to prevent the exclusion of these models. Instead of excluding models based on the p_{s+b} value, the exclusion is based on the new variable, CLs:

$$\mathrm{CLs} = \frac{p_{s+b}}{1 - p_b} < \alpha. \tag{5.17}$$

In the case of a downward fluctuation of the observed events, the denominator becomes small and the CLs value is increased compared to the p_{s+b} value. In general, more conservative results are provided by the CLs method [123].

5.8.3 Configurations for the Likelihood Fit

Several setups based on the likelihood in Eq. (5.15) are used within this thesis:

Background estimation: A separate determination of the background parameters, using only the control regions and background parameters, is performed to quote the numbers for the estimated background components. A possible signal contamination is neglected for this purpose.

Discovery: Both, signal and control regions are used to determine the p-value of the background-only hypothesis, by evaluating Eq. 5.13 for $\mu = 0$. A possible signal contamination of the control regions is neglected. To state a discovery, the p-value must be below $2.87 \cdot 10^{-7}$.

Model-independent limits: The whole likelihood is used to determine the signal strength μ for which the CLs value passes the threshold of 0.05 without considering a specific signal model. A possible signal contamination of the control regions is neglected. This approach provides a direct limit on the number of maximal allowed signal events. The limit can be translated to a limit on the visible signal cross-section by dividing it by

the integrated luminosity. The visible cross-section σ_{vis} is related to the production cross-section σ via

$$\sigma_{\text{vis}} = \sigma \cdot A \cdot \varepsilon, \tag{5.18}$$

with the signal acceptance A and the selection efficiency ε.

Model-dependent exclusion limits: The signal hypothesis is tested for a given model by evaluating the p-value for $\mu = 1$. The whole likelihood function is used and the signal contributions, as predicted by the model, are given as input. The model is excluded at 95% confidence level (CL) if the corresponding CLs value is found below 0.05. Mostly two-dimensional grids of signal points are used and an exclusion contour line is obtained by interpolating between the signal points. When multiple signal regions are tested, the one providing the best expected limit is chosen for each signal point separately.

The current ATLAS guidelines to produce exclusion limits indicate that all systematic uncertainties apart from the theory uncertainty on the signal cross-section are included in the expected and the nominal observed limits. A one sigma band is added for the signal cross-section uncertainty to the observed limit.

5.9 Current Limits on SUSY Models by the ATLAS Collaboration

A large variety of SUSY searches is performed by the ATLAS collaboration. So far all report good agreement between data and the SM expectation and no evidence for SUSY is yet found. A summary on current mass limits observed by various ATLAS SUSY searches is shown in Fig. 5.4. The full list of published results can be found in Ref. [124].
Here, two recently published analyses are briefly summarised: the no-lepton analysis from the inclusive SUSY searches (5.9.1) and a search for direct neutralino and chargino production from the electroweak production channels (5.9.2). In addition, a short overview of R-parity violating searches is given in Section 5.9.3.

5.9.1 Inclusive Searches: the No-Lepton Channel

A generic search for SUSY is performed by the no-lepton analysis. The production of $\tilde{g}\tilde{g}$, $\tilde{q}\tilde{g}$ and $\tilde{q}\tilde{q}$ pairs, where $\tilde{q}$ refers to squarks from the first two generations, is targeted with a search for final states with multiple jets, $E_{\text{T}}^{\text{miss}}$ and no leptons. The squarks and gluinos are assumed to decay into the LSP, typically via $\tilde{g} \to q\bar{q}\tilde{\chi}_1^0$ and $\tilde{q} \to q\tilde{\chi}_1^0$. Through these decays, at least 2-4 jets are produced and even more jets are expected in cascade decays of heavy particles.
The latest results were obtained analysing 5.8 fb^{-1} of the $\sqrt{s} = 8$ TeV dataset [125]. In total, 12 signal regions with 2-6 jets and harsh M_{eff} thresholds ($M_{\text{eff}} > 1000$ GeV - $M_{\text{eff}} > 1900$ GeV) are explored. The M_{eff} variable is built here from all jets with $p_{\text{T}} > 40$ GeV. The main SM background processes for this analysis are W+jets, Z+jets, $t\bar{t}$, singletop and multi-jet production. They are estimated by a combined fit of four control regions per signal region, one for the W, Z, top and multi-jets backgrounds each.
The SM background expectation is found to be in good agreement with the observed data for all signal regions and the results are interpreted in several SUSY models. Limits obtained for a mSUGRA model with $\tan\beta = 10$, $A_0 = 0$ and $\mu > 0$ are shown in the (m_0,$m_{1/2}$)-plane in Fig. 5.5. Squark and gluino masses up to 1500 GeV are excluded under the assumption of $m_{\tilde{g}} = m_{\tilde{q}}$. In a simplified model with only gluinos and massless neutralinos, gluino masses

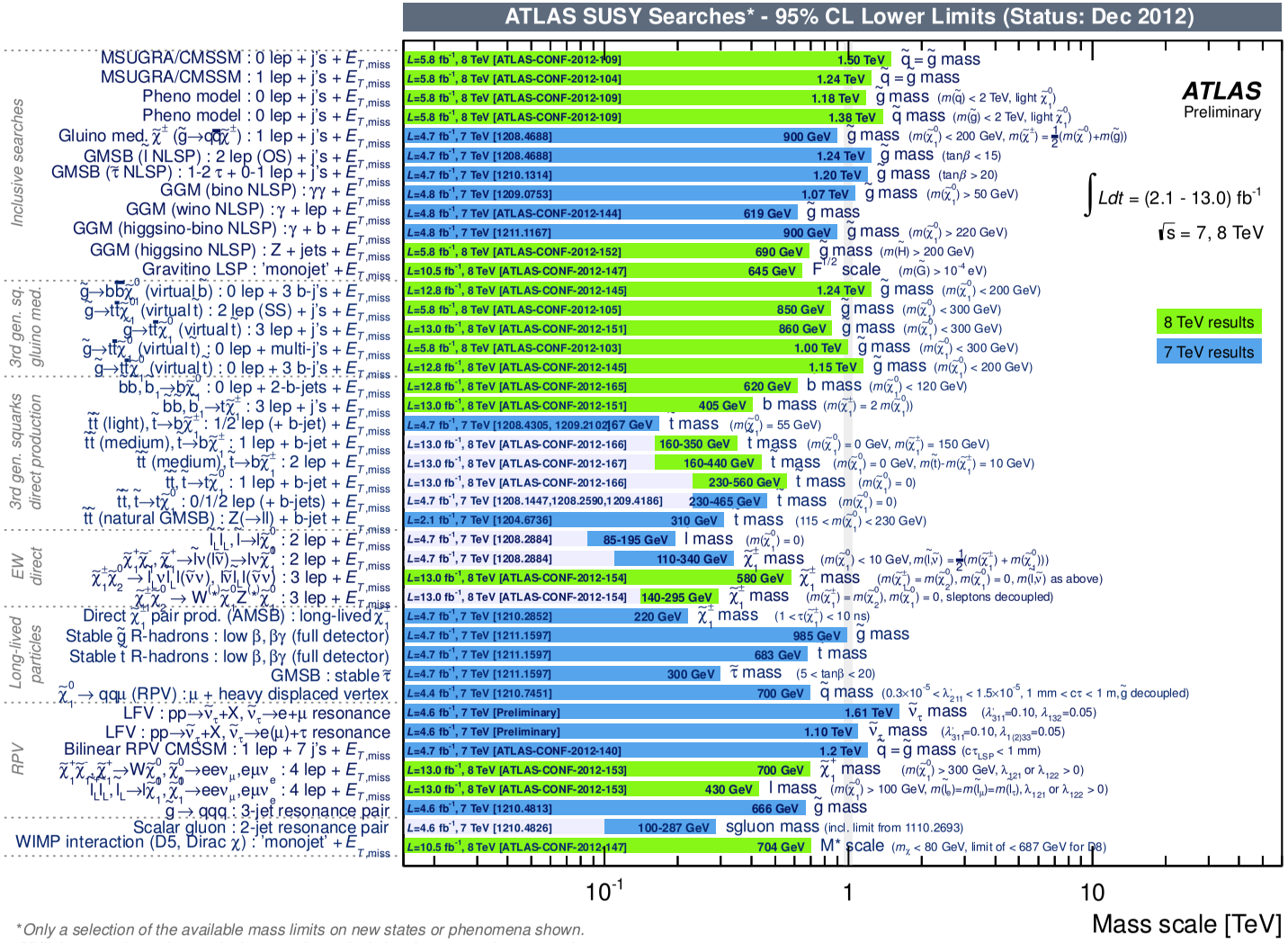

*Only a selection of the available mass limits on new states or phenomena shown.
All limits quoted are observed minus 1σ theoretical signal cross section uncertainty.

Figure 5.4: Summary on the SUSY limits by the ATLAS collaboration [124]. The limits are shown at 95% CL for various SUSY masses exploiting a representative collection from the different fields of SUSY searches. They were performed with an integrated luminosity ranging from 2.1 fb^{-1} up to 13 fb^{-1} of the 2011 (blue) or 2012 (green) dataset. A short description on the SUSY model and the search strategy is given in the left side of the figure. For more details, the number of the corresponding arXiv or conference note publication is given. Note, that some limits shown for the third generation searches will be discussed in detail within this thesis.

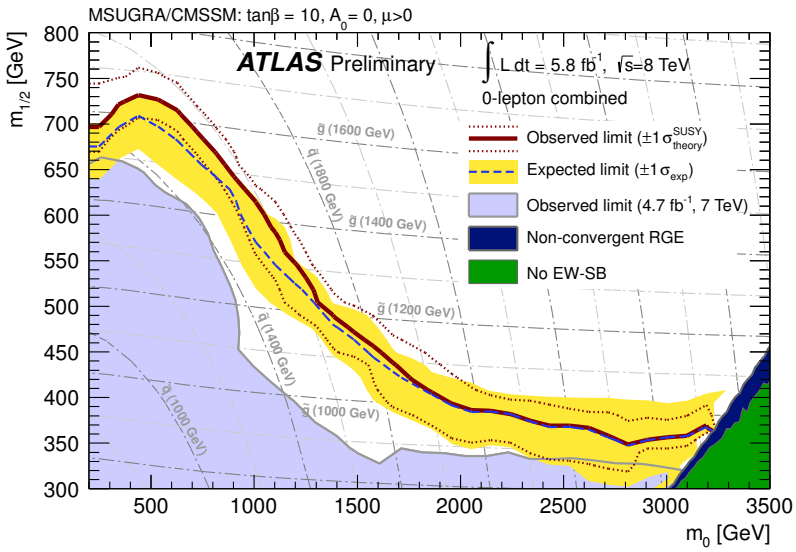

Figure 5.5: Exclusion limit in the (m_0-$m_{1/2}$) mass plane of a mSUGRA model with $\tan\beta = 10$, $A_0 = 0$ and $\mu > 0$. It is obtained by a search channel with no leptons and multiple jets using 5.8 fb^{-1} of the 2012 dataset [125]. The blue dashed line with the yellow band represents the expected limit at 95% CL with its $\pm 1\sigma$ uncertainty, excluding theory uncertainties on the signal. The observed limit is shown as solid red line and the dashed red lines correspond to the variations if theory uncertainties for the signal are applied. In addition, the previous limit for the 2011 dataset and theoretically excluded parameter regions are shown.

up to 1100 GeV can be excluded. Squark masses up to 630 GeV are excluded by a simplified model, where only squarks of the first two generations are produced and decay to massless neutralinos.

5.9.2 Direct Neutralino and Chargino Production

The searches for SUSY particles produced via the electroweak interaction cover SUSY scenarios where the squarks and gluinos are heavy (few TeV). The analysis presented here focuses on the direct production of neutralinos and charginos. The charginos and unstable neutralinos typically decay via sleptons, sneutrinos and massive gauge bosons ($\tilde{\chi}^{\pm} \to l\tilde{\nu}, \nu\tilde{l}, W\tilde{\chi}^0_1$ and $\tilde{\chi}^0_2 \to l\tilde{l}, Z\tilde{\chi}^0_1$), leading to final states with multiple leptons and $E_{\mathrm{T}}^{\mathrm{miss}}$.
A search, looking into final states with three leptons and $E_{\mathrm{T}}^{\mathrm{miss}}$, was published for 13 fb^{-1} of $\sqrt{s} = 8$ TeV data [126]. The dominant production channel is the associated $\tilde{\chi}^{\pm}_1\tilde{\chi}^0_2$ production and three signal regions are explored to cover the different neutralino decay scenarios. The main irreducible background processes are diboson and triboson production, which are mostly estimated from MC. The dominant contribution is the WZ production, which is estimated by a semi data-driven method. Backgrounds with at least one fake lepton are estimated from data and the main contributions come from top quark and Z+jets production.
Also in this case, good agreement of the data and expected SM background yield is observed and the results are interpreted in several scenarios for electroweak production. The exclusion limit for a simplified model, where the $\tilde{\chi}^{\pm}_1$ and $\tilde{\chi}^0_2$ are mass degenerate and decay via sleptons to the LSP, is shown in Fig. 5.6. Mass limits for the $\tilde{\chi}^{\pm}_1$ and $\tilde{\chi}^0_2$ up to 580 GeV are obtained for $m_{\tilde{\chi}^0_1} \sim 0$. If the sleptons are heavy and the gauginos decay via W and Z bosons, masses from 150-300 GeV are excluded for $m_{\tilde{\chi}^0_1} \sim 0$.

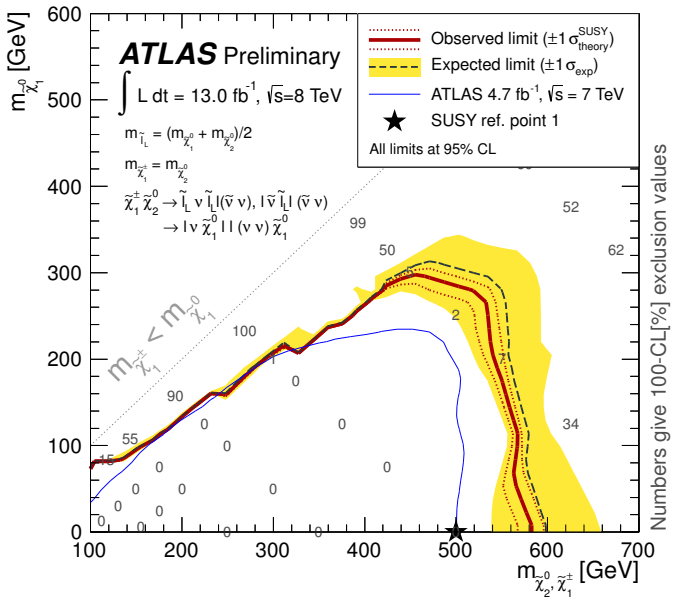

Figure 5.6: Expected and observed exclusion limits at 95% CL for a simplified model with chargino ($\tilde{\chi}_1^{\pm}$) and neutralino ($\tilde{\chi}_2^0$) production, where a decay to the LSP ($\tilde{\chi}_1^0$) via sleptons is assumed. They were obtained by a search channel with three leptons, using 13.0 fb^{-1} of the 2012 dataset [126]. The expected limit with its $\pm 1\sigma$ uncertainty is represented by the black dashed line and the yellow band (excluding signal theory uncertainties). The observed limit is shown as solid red line and the signal theory uncertainty variations as dashed red lines. The percentaged CL values for the signal points and the previous limit obtained with the 2011 dataset are also shown.

5.9.3 R-parity Violating Searches

There is also a number of studies for SUSY models that can violate R-parity. A decay of the LSP to SM particles is possible for these models and three classes of search channels are introduced here:

Long-lived Particles: Different signatures are produced by long-lived SUSY particles. The long lifetime can lead to displaced vertices or hadronization structures inside the detector. A good handle to study displaced vertices is provided by accompanying particles, such as a reconstructed muon which is produced in the decay of a long-lived neutralino [127]. Long-lived particles are are also studied for RPC SUSY models. An example of a RPC study is the search for disappearing tracks, which are produced by long-lived charginos that decay to the LSP [128].

Resonance Searches: Various RPV processes can generate resonance structures in reconstructed mass spectra. An example is the search for a resonance in the $e\mu$, $e\tau$, or $\mu\tau$ mass spectrum which is induced by the decay of a heavy tau sneutrino ($\tilde{\nu}_\tau \to ll'$) [129].

Lepton Number Violation: Final states with multiple leptons can be produced in lepton number violating RPV scenarios. Leptonic neutralino decays that produce final states with at least four reconstructed electrons and muons plus $E_{\mathrm{T}}^{\mathrm{miss}}$ due to neutrinos are studied in Ref. [130].

CHAPTER 6

Searches for Direct Sbottom Pair Production

The direct pair production of sbottoms can play an important role in scenarios where the sbottom is light. For this analysis, a decay of each sbottom to $b\tilde{\chi}_1^0$ is assumed with a branching ratio of 100%.
The analysis was first performed at the end of 2011 based on data corresponding to an integrated luminosity of 2.05 fb^{-1}, collected at a centre-of-mass energy of 7 TeV [131]. A signal region based on selecting events with large m_{CT} was used. In summer 2012, the analysis was updated to the full 2011 dataset, corresponding to an integrated luminosity of 4.7 fb^{-1}, with additional signal regions after a new optimisation of the event selection [132]. The method for the background estimation was also changed from a simple scaling of background normalisations in separate control regions to a combined fit of all the control regions. In fall 2012, the analysis was updated once more using data corresponding to an integrated luminosity of 12.8 fb^{-1}, collected at a centre-of-mass energy of 8 TeV [133]. For this update only small changes were applied to adapt to the $\sqrt{s} = 8$ TeV data. The event selection was not re-optimized and the background estimation method was only slightly changed. All figures and numbers in the following sections are obtained from the latest analysis at $\sqrt{s} = 8$ TeV, unless stated otherwise. Major contributions were made to all parts of this analysis within this thesis, including optimisation studies, the background estimation, estimation of systematic uncertainties and the statistical interpretation of the results. The results published in Ref. [133] are completely based on the results obtained within this thesis.
The dataset and MC samples are briefly described in Section 6.1. The final event selection is discussed in Section 6.2. This section also gives a summary of the selection optimisation that was performed for the 2011 dataset collected at $\sqrt{s} = 7$ TeV. The background estimation is described in Section 6.3, followed by a discussion on the systematic uncertainties in Section 6.4. Finally, the results and their interpretation are presented in Sections 6.5 and 6.6. The results from the sbottom analysis were re-interpreted for a class of SUSY models, where stop-pair production is assumed [134]. A description of the stop interpretation is given in Section 6.7. A short summary for this chapter is added in Section 6.8.

6.1 Data and Monte Carlo Input

This analysis is based on data corresponding to an integrated luminosity of $\mathcal{L} = 14$ fb^{-1} of pp collisions collected in 2012 at $\sqrt{s} = 8$ TeV. The effective luminosity is reduced to 12.8 fb^{-1} once data quality requirements and trigger inefficiencies are considered.
Monte Carlo simulated samples are used in the analysis optimisation studies, for the SM background estimation and for interpreting the results for specific SUSY scenarios. In the

following, a list of MC samples used to describe the relevant SM processes is specified[1]:

Top Pair Production: It is generated with POWHEG interfaced to PYTHIA. The contribution from $t\bar{t}$ events in association with b-jets is taken into account in the showering process.
Separate samples are produced to model the $t\bar{t}$ production in association with W or Z bosons. They are generated with MADGRAPH interfaced to PYTHIA.

Single Top Production: Single top events produced in the t-channel are generated with ACERMC interfaced to PYTHIA. For s-channel events or the associate production with a W boson in the Wt-channel, MC@NLO interfaced to HERWIG and JIMMY for the showering and underlying event simulation is used.

W+jets Production: It is generated with SHERPA. Up to four additional partons are simulated and b-quarks are treated as massive particles while c-quarks are assumed massless. The W production in association with b-jets is in principle relevant for this analysis despite the small cross-section. Separate samples including b-hadrons are used to correctly describe this contribution. To avoid double counting, there is one set of samples filtered for b-hadrons and another set where b-hadrons are vetoed. In addition, separate samples with $p_{\mathrm{T}}(W) > 140$ GeV are used to better describe events with large $E_{\mathrm{T}}^{\mathrm{miss}}$. The resulting double counting for the events with $p_{\mathrm{T}}(W) > 140$ GeV is corrected for by removing those events from the nominal samples[2].

Z+jets Production: The Z+jets events are generated with SHERPA. Separate samples are produced for the production with light jets or jets originating from c- and b-quarks, referred to as hf jets.[3]

Diboson Production: Diboson events are only a minor background in this analysis. They are generated with SHERPA including up to three additional partons.

The $t\bar{t}$, W+jets and Z+jets samples are simulated with ATLFAST-II, while the full detector simulation is used for the other samples. The majority of the samples are generated with the next-to-leading order PDF set CT10 [61]. Only for the $t\bar{t}+W/Z$ and the t-channel single top samples the leading order PDF set CTEQ6L1 [63] is used. A summary on the samples, together with their cross-sections and filter efficiencies, is given in Table 6.1.

Signal samples

The signal samples are produced with MADGRAPH interfaced to PYTHIA[4], using the CTEQ6L1 PDF set. The mass spectrum and branching ratios are calculated with SUSY-HIT [79], and they serve as input for the generation.
A pure production of $\tilde{b}_1\tilde{b}_1$ events and a 100% branching ratio for the $\tilde{b}_1 \to b\tilde{\chi}_1^0$ decay are

1 An introduction of the MC generators is given in Section 2.3.3.

2 The removal is based on the truth information of the generated particles that is stored inside the MC samples.

3 Only the Z + hf jets samples are used for the final results. Not enough events for the Z + light jets samples were generated, leading to large statistical fluctuations in the background estimation. As a normalisation for the total Z contribution is obtained from the control regions, the final Z estimate indirectly includes the contribution from Z + light jets.

4 Previously, when analysing the 2011 dataset, HERWIG++ was used instead, but studies have shown a worse description of the initial state radiation in this case. A correct treatment of the ISR is in particular important as one of the signal regions uses the signature of an ISR jet.

Process	Generator	D.S.	N [10^6]	σ [pb]	pert. order	Filter ϵ
$t\bar{t}$						
$t\bar{t}$ (leptonic)	POWHEG +PYTHIA	AF-II	15	238.06	NNLO [135]	0.543
$t\bar{t} + W$	MADGRAPH +PYTHIA	full	0.8	0.232	NLO [136]	1
$t\bar{t} + Z$	MADGRAPH +PYTHIA	full	0.8	0.208	NLO [137]	1
single top						
s-channel $W \to e\nu$	MC@NLO +H. J.	full	0.2	0.606	NNLO [138]	1
s-channel $W \to \mu\nu$	MC@NLO +H. J.	full	0.2	0.606	NNLO [138]	1
s-channel $W \to \tau\nu$	MC@NLO +H. J.	full	0.2	0.606	NNLO [138]	1
Wt-channel (incl.)	MC@NLO +H. J.	full	2	22.37	NNLO [139]	1
t-channel $W \to e\nu$	ACERMC +PYTHIA	full	0.3	9.464	NNLO [140]	1
t-channel $W \to \mu\nu$	ACERMC +PYTHIA	full	0.3	9.464	NNLO [140]	1
t-channel $W \to \tau\nu$	ACERMC +PYTHIA	full	0.3	9.464	NNLO [140]	1
W + jets						
$W \to e\nu$, b-filter	SHERPA	AF-II	5	12190	NNLO [141]	0.017
$W \to \mu\nu$, b-filter	SHERPA	AF-II	5	12190	NNLO [141]	0.017
$W \to \tau\nu$, b-filter	SHERPA	AF-II	5	12190	NNLO [141]	0.017
$W \to e\nu$, b-veto	SHERPA	AF-II	5	12190	NNLO [141]	0.983
$W \to \mu\nu$, b-veto	SHERPA	AF-II	5	12190	NNLO [141]	0.983
$W \to \tau\nu$, b-veto	SHERPA	AF-II	5	12190	NNLO [141]	0.983
$W(140) \to e\nu$, b-filter	SHERPA	AF-II	0.3	36.7	NNLO [141]	0.066
$W(140) \to \mu\nu$, b-filter	SHERPA	AF-II	0.3	36.7	NNLO [141]	0.066
$W(140) \to \tau\nu$, b-filter	SHERPA	AF-II	0.3	36.7	NNLO [141]	0.066
$W(140) \to e\nu$, b-veto	SHERPA	AF-II	1	36.7	NNLO [141]	0.934
$W(140) \to \mu\nu$, b-veto	SHERPA	AF-II	1	36.7	NNLO [141]	0.934
$W(140) \to \tau\nu$, b-veto	SHERPA	AF-II	0.5	36.7	NNLO [141]	0.934
Z + jets						
$Z \to ee$ + light jets	SHERPA	AF-II	2	1052	NNLO [141]	1
$Z \to \mu\mu$ + light jets	SHERPA	AF-II	2	1052	NNLO [141]	1
$Z \to \tau\tau$ + light jets	SHERPA	AF-II	2	1052	NNLO [141]	1
$Z \to \nu\nu$ + light jets	SHERPA	AF-II	6	5680	NNLO [141]	1
$Z \to ee$ + hf jets	SHERPA	AF-II	5	58.79	NNLO [141]	1
$Z \to \mu\mu$ + hf jets	SHERPA	AF-II	5	58.79	NNLO [141]	1
$Z \to \tau\tau$ + hf jets	SHERPA	AF-II	5	58.79	NNLO [141]	1
$Z \to \nu\nu$ + hf jets	SHERPA	AF-II	27	315.4	NNLO [141]	1
Dibosons						
$WW \to \ell\ell\nu\nu$	SHERPA	full	2.7	5.88	NLO [142]	1
$WZ \to \ell\ell\ell\nu$	SHERPA	full	2.7	10.3	NLO [142]	1
$ZZ \to \ell\ell\ell\ell$	SHERPA	full	1.8	9.70	NLO [142]	1
$ZZ \to \ell\ell\nu\nu$	SHERPA	full	0.9	0.57	NLO [142]	1
$ZV \to eeqq$, V=W/Z	SHERPA	full	0.2	1.70	NLO [142]	1
$ZV \to \mu\mu qq$, V=W/Z	SHERPA	full	0.2	1.70	NLO [142]	1
$ZV \to \tau\tau qq$, V=W/Z	SHERPA	full	0.2	1.70	NLO [142]	1
$WV \to e\nu qq$, V=W/Z	SHERPA	full	0.9	9.56	NLO [142]	1
$WV \to \mu\nu qq$, V=W/Z	SHERPA	full	1.0	9.56	NLO [142]	1
$WV \to \tau\nu qq$, V=W/Z	SHERPA	full	1.0	9.56	NLO [142]	1

Table 6.1: MC samples used to model the different background processes. The process is summarized in the first column ($W(140)$ refers to $p_{\mathrm{T}}(W) > 140$ GeV). The generator and the detector simulation (D.S) used are given in the second and third columns (H. J. = HERWIG JIMMY, full = full detector simulation, AF-II = ATLFAST-II). In addition, the number of generated events N and the cross-sections σ, together with the perturbation order used to calculate them, are shown. The top production cross-sections are evaluated for $m_t = 172.5$ GeV. In the last column, filter efficiencies ε are given for samples where a filter is applied.

assumed. Signal points are generated for sbottom masses ranging from 100 GeV to 1000 GeV and neutralino masses covering the allowed mass range ($m(\tilde{\chi}_1^0) < m(\tilde{b}_1) - m(b)$). The masses of other SUSY particles that are not involved in the production or decay are set to high values to decouple the rest of the SUSY mass spectrum.
The cross-sections are calculated to next-to-leading order (NLO) with PROSPINO [81]. Additional corrections, including NLO supersymmetric QCD calculations and the next-to-leading-logarithmic (NLL) resummation of soft gluon emission, are applied by using the NLL-fast method [143, 144]. The cross-sections are independent of the neutralino mass as, to a very good approximation, only the sbottom mass plays a role in the production process. In Figure 6.1 they are shown together with the positions of the actual signal points. The samples are produced using ATLFAST-II and at least 15000 events are generated per signal point. For the points with large cross-sections more events are generated (about 100000 for $m(\tilde{b}_1) = 100$ GeV and 30000 for $m(\tilde{b}_1) = 400$ GeV).

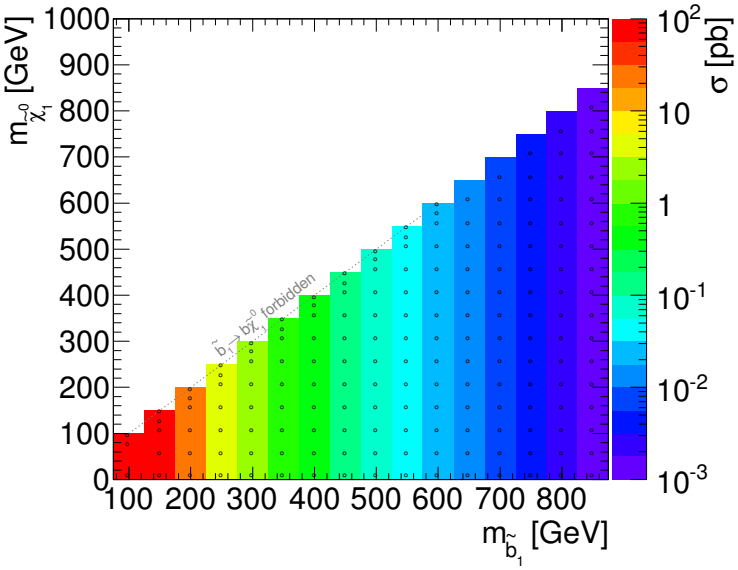

Figure 6.1: Signal cross-sections for sbottom-pair production. The grid points for which events are generated are indicated by the black circles.

6.2 Event Selection

The general topology of a scenario with sbottom-pair production where each sbottom decays via $\tilde{b}_1 \to b\tilde{\chi}_1^0$ is given by a final state with two b-jets, missing transverse momentum, no leptons and low additional hadronic activity. A large dependence of the kinematic properties on the mass difference between the sbottom and neutralino

$$\Delta m = m\left(\tilde{b}_1\right) - m\left(\tilde{\chi}_1^0\right) \tag{6.1}$$

is expected. If the mass-splitting is large, a high energy is released by the sbottom decay that is distributed among the b-quark and neutralino momenta (leading to high p_{T} b-jets and large $E_{\mathrm{T}}^{\mathrm{miss}}$). For small mass-splittings, only a small phase space is available to the $b\tilde{\chi}_1^0$ system and soft b-jets along with low $E_{\mathrm{T}}^{\mathrm{miss}}$ are expected. Three different signal regions are defined to provide sensitivity to the regions of small, medium and large values of Δm:

SR1: Large mass-splitting ($\Delta m > 250$ GeV).

SR2: Intermediate mass-splitting (100 GeV $< \Delta m <$ 250 GeV).

SR3: Small mass-splitting ($\Delta m < 100$ GeV).

The signal region definitions are discussed in detail in Section 6.2.3. In addition, the object definitions used for this analysis (6.2.1), the common preseletion for all signal regions (6.2.2) and a summary on the optimisation study that was performed to define the final selection criteria (6.2.4) are described.

6.2.1 Object Definitions

The object reconstruction is described in detail in Section 4.2. Here, the exact definitions used for the sbottom-pair production analysis are summarised:

Jets: Jets are calibrated using the LCW+JES scheme and are selected if they have $p_{\mathrm{T}} > 20$ GeV and $|\eta| < 2.8$. They are ordered by p_{T}.

b-Jets: b-jets are selected using the MV1 algorithm at a 60% efficiency working point (weight>0.98)[5]. They are required to have $p_{\mathrm{T}} > 30$ GeV and $|\eta| < 2.5$. It should be noted that the b-tagging scaling factors are not applied in this analysis.[6]

Leptons: Electrons are reconstructed following the *medium* selection criteria. They are required to have $p_{\mathrm{T}} > 10$ GeV and $|\eta| < 2.47$. For the muon reconstruction at least one track segment in the muon spectrometer needs to match an inner detector track. They are required to have $p_{\mathrm{T}} > 10$ GeV and $|\eta| < 2.4$.
For the control regions tighter lepton selections are required. The leptons must be isolated and the p_{T} thresholds are raised to 25 GeV for electrons and 20 GeV for muons. In addition, the electrons need to fulfill the *tight* selection criteria.

6.2.2 Preselection

A pure $E_{\mathrm{T}}^{\mathrm{miss}}$ trigger was chosen for the sbottom analysis. It provides the best acceptance compared to other trigger options (for example b-jet or jet+$E_{\mathrm{T}}^{\mathrm{miss}}$ triggers). In contrast to a jet+$E_{\mathrm{T}}^{\mathrm{miss}}$ trigger, it also has the advantage of allowing lower momentum thresholds for the jets. The trigger uses a 40 GeV (45 GeV) $E_{\mathrm{T}}^{\mathrm{miss}}$ threshold at level-1 (level-2) and an event filter threshold of 80 GeV.
For the first 2.1 fb^{-1} of the 2012 dataset only a 90% efficient version of the trigger was available.[7] This reduces the total integrated luminosity of the dataset from 13.0 fb^{-1} to

5 The rejection factors obtained from MC $t\bar{t}$ events are 577, 8 and 23 for light-jets, c-jets and τ-leptons, respectively, for jets selected with $p_{\mathrm{T}} > 20$ GeV and $|\eta| < 2.5$.

6 A worse agreement between MC prediction and data was found in the control regions when applying the scale factors. This can be explained by the fact that the scale factors were obtained under different kinematic conditions than present in this analysis. Nevertheless, multiple checks were performed to validate the background estimation. The relative uncertainties on the scale factors are used, however, in order to estimate the b-tagging uncertainties.

7 The proton bunches are packed in trains which are separated by larger distances than the nominal bunch spacing. The first three bunches in each train were dropped by the early version of the $E_{\mathrm{T}}^{\mathrm{miss}}$-only trigger in order to manage the out-of-time pile-up.

12.8 fb^{-1}.[8] The MC predictions were scaled down accordingly by applying an event weight of 0.9 to a corresponding number of randomly selected events.
The trigger turn-on behaviour as a function of $E_{\mathrm{T}}^{\mathrm{miss}}$ is shown in Fig. 6.2. A plateau value is reached at about 150 GeV. The inefficiency of events selected above the threshold and variations for different data-taking conditions are both below 1% (not taking into account the 10% inefficiency for the first 2.1 fb^{-1}).

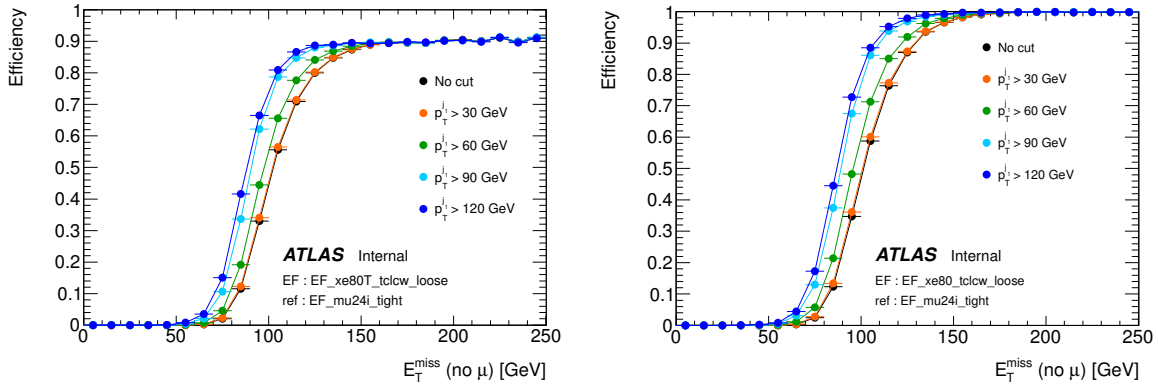

Figure 6.2: Trigger efficiency as a function of an offline $E_{\mathrm{T}}^{\mathrm{miss}}$ threshold [145]. The efficiency was calculated with respect to events selected by a single muon trigger. The left figure shows the 10% inefficient trigger version used for the first 2.1 fb^{-1} of data and the right one the fully efficient version used for the rest. Several distributions with different thresholds for the leading jet transverse momentum are displayed in each figure.

Cleaning criteria to improve the data quality are discussed in Section 5.3. A list summarising the preselection applied for the sbottom-pair production analysis is given in Table 6.2.
A common selection is applied to all signal regions on top of the preselection, including a 150 GeV threshold on $E_{\mathrm{T}}^{\mathrm{miss}}$ to work on the trigger efficiency plateau. Two selection criteria are applied to suppress the QCD multi-jet background. The minimal azimuthal distance $\Delta\phi_{\mathrm{min}}$ between the leading three jets and $E_{\mathrm{T}}^{\mathrm{miss}}$ is required to be larger than 0.4 and the $E_{\mathrm{T}}^{\mathrm{miss}}$ contribution to the effective mass computed from the leading two (three) jets for SR1 and SR2 (SR3) has to be larger than 25%. In addition, the veto on leptons in the final state is common for the three signal regions.

6.2.3 Signal Region Definitions

The three signal regions are defined to gain sensitivity for the different mass-splitting scenarios and are optimized to the specific kinematic topology. All selections require two b-jets, but different momentum thresholds are applied.
The m_{CT} variable was used as starting point for the sbottom analysis as it provides an endpoint at 135 GeV for $t\bar{t}$ events and high endpoints for the signal samples, especially for large Δm (see Section 5.5). It should be noted that non pair-produced backgrounds, like Z+hf, do not have an endpoint and can also contribute for harsh m_{CT} selections. The $t\bar{t}$ endpoint and the use of the m_{CT} variable was motivated in Ref. [117], from where Fig. 6.3a is taken. It is showing the m_{CT} distribution at parton-level for $t\bar{t}$ events for the following selection: ≥ 2 b-jets with $p_{\mathrm{T}} > 50$ GeV, $E_{\mathrm{T}}^{\mathrm{miss}}$ >30 GeV and 2 leptons ($e\mu$) with $p_{\mathrm{T}} > 20$ GeV.

8 The integrated luminosity of 13.0 fb^{-1} corresponds to the effective luminosity when data quality requirements are applied.

Name	Description and Implementation
Data Quality	remove events recorded with mis-functioning detector devices
Trigger	$E_{\mathrm{T}}^{\mathrm{miss}}$ trigger
Vertex Selection	require ≥ 4 tracks pointing to the primary vertex
Dead or Noisy Tile Cells	reject events affected by not-working or noisy tile cells
Corrupted Events	reject noise-burst affected and incomplete events
Forward Calorimeter	reject events affected by technical problems (power supply)
Negative Energy	remove events with negative energy contribution to $E_{\mathrm{T}}^{\mathrm{miss}}$: $f_{\mathrm{CellOut}} < 0.5$ if $E_{\mathrm{T}}^{\mathrm{miss}} > 150$ GeV, else $f_{\mathrm{CellOut}} < \frac{150\ \mathrm{GeV}}{E_{\mathrm{T}}^{\mathrm{miss}}} - 0.5$
Bad Muons	veto events with pre-selected bad muons
Overlap Removal	remove jets within $\Delta R = 0.2$ of an electron remove electrons and muons within $\Delta R = 0.4$ of a jet
Bad Jets	veto events with bad jets that have $p_T > 20$ GeV
Timing	require average jet timing within 5 ns for the selected jets
Jet Charged Fraction	remove events with a selected jet with chf < 0.05 and $\lvert\eta\rvert < 2.0$

Table 6.2: Summary of the event preselection for the sbottom-pair production analysis. "Selected jets" refers to the leading N jets selected by the analysis ($N = 2$ for SR1 and SR2 and $N = 3$ for SR3). The Overlap Removal is not a selection criteria in the sense that events are rejected, but it is included in the list to better understand the status of the reconstructed objects at the current selection step.

The corresponding m_{CT} distribution for $t\bar{t}$ events for reconstructed objects (2 b-jets with $p_{\mathrm{T}} > 60$ GeV, $E_{\mathrm{T}}^{\mathrm{miss}} > 150$ GeV and no leptons) is shown in Fig. 6.3b together with the distributions for two signal points. Even though the $t\bar{t}$ endpoint is smeared out, a good signal-to-background separation can be achieved.

SR1

Especially for large mass-splitting scenarios, a high endpoint in the m_{CT} distribution is expected. Furthermore, the two b-jets can have large transverse momenta from the available phase space of the $\tilde{b}_1 \to b\tilde{\chi}_1^0$ decay.
Two b-jets with $p_{\mathrm{T}} > 130$ GeV for the leading and $p_{\mathrm{T}} > 50$ GeV for the second jet are required. Events with a third jet are rejected if the jet has $p_{\mathrm{T}} > 50$ GeV. The analysis is performed at four different m_{CT} thresholds: 150 GeV, 200 GeV, 250 GeV and 300 GeV.

SR2

The power of a harsh m_{CT} threshold drops for lower mass-splitting values as the m_{CT} endpoint gets lower. In addition, the b-jets are generally softer.
Therefore, two b-jets with $p_{\mathrm{T}} > 60$ GeV are required and the m_{CT} threshold is lowered to 100 GeV. To compensate for the loss in the background rejection due to the looser selection criteria, a harsher $E_{\mathrm{T}}^{\mathrm{miss}}$ threshold of 200 GeV is applied. The background rejection is further improved by vetoing additional hadronic activity in the event via the requirement $H_{\mathrm{T},2} < 50$ GeV.

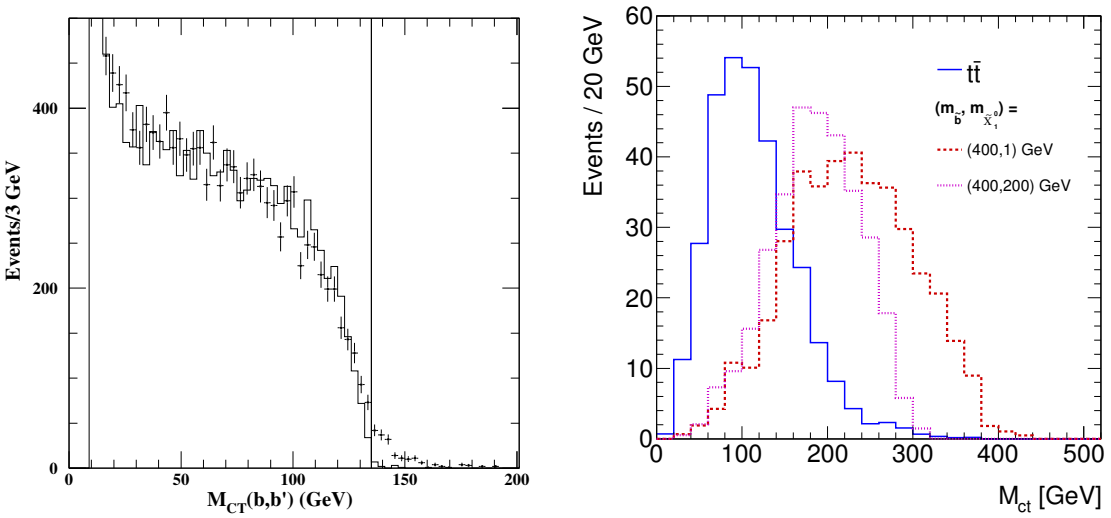

(a) $t\bar{t}$: parton-level **(b)** $t\bar{t}$ and signal: $\tilde{b}_1$-analysis level

Figure 6.3: (a): Distribution of m_{CT} for $t\bar{t}$ events at parton-level (solid line) obtained by Ref. [117]. A simplified detector simulation and reconstruction efficiencies are applied for the histogram with error bars. (b): Distribution of m_{CT} for $t\bar{t}$ events from reconstructed objects at the level of the sbottom analysis. Two signal points with ($m_{\tilde{b}_1}$, $m_{\tilde{\chi}_1^0}$)=(400, 1) GeV and (400, 200) GeV are added.

SR3

For small mass-splittings, the m_{CT} variable looses its discriminating power completely. In addition, only small phase space is available to the b-quarks and neutralinos and soft b-jets and low $E_{\mathrm{T}}^{\mathrm{miss}}$ are therefore expected. To get a handle on those topologies, events are selected where the sbottom-pair system recoils against a high momentum initial state radiation jet. The leading jet is expected to be the ISR jet and is required to have $p_{\mathrm{T}} > 130$ GeV. It is not allowed to be b-tagged and should be back-to-back with the $E_{\mathrm{T}}^{\mathrm{miss}}$ direction. This last feature of the signal is exploited by selecting events where $\Delta\phi\,(E_{\mathrm{T}}^{\mathrm{miss}},\mathrm{jet}_1) > 2.5$. In addition, two b-jets with $p_{\mathrm{T}} > 30$ GeV are required. An upper threshold of 110 GeV is placed on the p_{T} of the leading b-jet. Similar to SR2, additional hadronic activity is reduced by requiring $H_{\mathrm{T},3} < 50$ GeV.
When enough luminosity is available, harsher thresholds can improve the sensitivity. The above selection is therefore denoted as SR3a and an additional signal region, SR3b, is defined on top by increasing the leading jet p_{T} threshold to 150 GeV and the $E_{\mathrm{T}}^{\mathrm{miss}}$ threshold to 200 GeV.

A summary of the signal region definitions is given in Table 6.3.
Three reference signal points with different sbottom-neutralino mass differences are selected, one for each signal region:

- P1: $(m_{\tilde{b}_1}, m_{\tilde{\chi}_1^0}) = (600,1)$ GeV for SR1.
- P2: $(m_{\tilde{b}_1}, m_{\tilde{\chi}_1^0}) = (450,300)$ GeV for SR2.
- P3: $(m_{\tilde{b}_1}, m_{\tilde{\chi}_1^0}) = (300,250)$ GeV for SR3.

The event yields for the three signal points are shown in Tables 6.4-6.6 at different stages of

Description	Signal region			
	SR1	SR2	SR3a	SR3b
Trigger	$E_{\mathrm{T}}^{\mathrm{miss}}$ trigger, $> 99\%$ efficient for $E_{\mathrm{T}}^{\mathrm{miss}} > 150$ GeV			
Event cleaning	Common quality criteria for all SRs			
Lepton veto	No e/μ with $p_{\mathrm{T}} > 10$ GeV			
$E_{\mathrm{T}}^{\mathrm{miss}}$	> 150 GeV	> 200 GeV	> 150 GeV	> 250 GeV
$p_{\mathrm{T}}(\mathrm{jet}_1)$	> 130 GeV	> 60 GeV	> 130 GeV	> 150 GeV
$p_{\mathrm{T}}(\mathrm{jet}_2)$	> 50 GeV	> 60 GeV	> 30 GeV, < 110 GeV	
$p_{\mathrm{T}}(\mathrm{jet}_3)$	veto event if $p_{\mathrm{T}}(\mathrm{jet}_3) > 50$ GeV		> 30 GeV	
$\Delta\phi(E_{\mathrm{T}}^{\mathrm{miss}},\mathrm{jet}_1)$	-		> 2.5	
b-tagging	jet_1 and jet_2 tagged		jet_1 anti-tagged, jet_2 and jet_3 tagged	
$\Delta\phi_{\mathrm{min}}$	> 0.4			
$E_{\mathrm{T}}^{\mathrm{miss}}/M_{\mathrm{eff}}$	> 0.25			
m_{CT}	$> 150, 200, 250, 300$ GeV	> 100 GeV	-	
$H_{\mathrm{T},x}$	-	< 50 GeV, $x = 2$	< 50 GeV, $x = 3$	

Table 6.3: Summary of the event selection criteria for the three signal regions SR1, SR2 and SR3. SR3 is split into two sub-selections, SR3a and SR3b. The jets are sorted by their transverse momenta.

the event selections for the three signal regions. It can be seen, that in each case the relative selection efficiency is better for the associated signal point than for the other two points. The relative composition of the SM background in the signal regions is shown in Table 6.7.

6.2.4 Optimisation Studies

For the results published in summer 2012, various studies have been performed to maximize the sensitivity for the sbottom-pair production analysis. A short summary of the optimisation procedures is given here, but it should be noted that all figures shown in this section were obtained for the 7 TeV analysis.[9]
The performance of different selection setups is compared by computing the signal significance for each point of the signal grid. As the full and accurate process of the limit calculation is not necessary for this purpose, a rough estimation of the significance via

$$z = \frac{s}{\sqrt{b + \sigma^2(b)}}, \tag{6.2}$$

with the expected signal yield s and background yield b is performed. The systematic uncertainty on the background yield $\sigma(b)$ includes the dominant uncertainties (JES and b-tagging) and rough estimations for the theoretical uncertainties of the individual SM processes. Minor

9 The main differences compared to the 8 TeV analysis arise from a change in the cross-sections and the fact that different MC generators were used.

Selection (SR1)	P3	P2	P1	SM
Initial	2.6e+04	2.2e+03	3.2e+02	
Preselection + e/μ veto	7.1e+03	1.5e+03	2.9e+02	
$E_{\mathrm{T}}^{\mathrm{miss}} > 150$ GeV	3.5e+03	1.1e+03	2.7e+02	
$p_{\mathrm{T}}(\mathrm{jet}_1) > 130$ GeV	2.4e+03	7.6e+02	2.6e+02	
$p_{\mathrm{T}}(\mathrm{jet}_2) > 50$ GeV	1.9e+03	6.7e+02	2.5e+02	
veto if $p_{\mathrm{T}}(\mathrm{jet}_3) > 50$ GeV	8.6e+02	3.1e+02	1.1e+02	
$\Delta\phi_{\mathrm{min}}$	6.6e+02	2.8e+02	93	
$E_{\mathrm{T}}^{\mathrm{miss}}/M_{\mathrm{eff}}$	6.6e+02	2.7e+02	84	
b-tagging	9.9	84	24	
$m_{\mathrm{CT}} > 100$	4.3	79	23	
$m_{\mathrm{CT}} > 150$	2.5	58	22	187
$m_{\mathrm{CT}} > 200$	0.90	21	19	76
$m_{\mathrm{CT}} > 250$	0.33	1.3	16	26
$m_{\mathrm{CT}} > 300$	0	0	13	8

Table 6.4: Expected event yields for the three reference signal points at different stages of the event selection for SR1. The numbers are normalised assuming an integrated luminosity of 12.8 fb^{-1}. For comparison, the event yields for the total expected SM background are given for the signal regions.

Selection (SR2)	P3	P2	P1	SM
Initial	2.6e+04	2.2e+03	3.2e+02	
Preselection + e/μ veto	7.1e+03	1.5e+03	2.9e+02	
$E_{\mathrm{T}}^{\mathrm{miss}} > 150$ GeV	3.5e+03	1.1e+03	2.7e+02	
$p_{\mathrm{T}}(\mathrm{jet}_1) > 60$ GeV	3.4e+03	1.0e+03	2.6e+02	
$p_{\mathrm{T}}(\mathrm{jet}_2) > 60$ GeV	2.1e+03	8.3e+02	2.5e+02	
veto if $p_{\mathrm{T}}(\mathrm{jet}_3) > 50$ GeV	8.9e+02	3.9e+02	1.0e+02	
$\Delta\phi_{\mathrm{min}}$	7.2e+02	3.6e+02	91	
$E_{\mathrm{T}}^{\mathrm{miss}}/M_{\mathrm{eff}}$	7.2e+02	3.6e+02	82	
b-tagging	11	1.1e+02	24	
$H_{\mathrm{T},2} < 50$ GeV	3.3	79	15	
$m_{\mathrm{CT}} > 100$ GeV	0.84	76	15	
$E_{\mathrm{T}}^{\mathrm{miss}} > 200$ GeV	0.27	41	14	94

Table 6.5: Expected event yields for the three reference signal points at different stages of the event selection for SR2. The numbers are normalised assuming an integrated luminosity of 12.8 fb^{-1}. For comparison, the event yield for the total expected SM background is given for the signal region.

Selection (SR3)	P3	P2	P1	SM
Initial	2.6e+04	2.2e+03	3.2e+02	
Preselection + e/μ veto	7.1e+03	1.5e+03	2.9e+02	
$p_{\mathrm{T}}(\mathrm{jet}_1) > 130$	3.4e+03	1.0e+03	2.8e+02	
$p_{\mathrm{T}}(\mathrm{jet}_2) > 30$	3.0e+03	8.6e+02	2.5e+02	
$p_{\mathrm{T}}(\mathrm{jet}_3) > 30$	2.5e+03	6.9e+02	2.1e+02	
$E_{\mathrm{T}}^{\mathrm{miss}} > 150$ GeV	1.8e+03	5.2e+02	1.9e+02	
$\Delta\phi_{\mathrm{min}}$	1.4e+03	4.5e+02	1.7e+02	
$E_{\mathrm{T}}^{\mathrm{miss}}/M_{\mathrm{eff}}$	1.4e+03	4.3e+02	1.5e+02	
jet_1 anti-tagged	1.3e+03	2.6e+02	76	
b-tagging ($\mathrm{jet}_{2,3}$)	1.1e+02	37	5.1	
$p_{\mathrm{T}}(\mathrm{jet}_2) < 110$ GeV	90	13	0.39	
$H_{\mathrm{T},3} < 50$ GeV	58	6.9	0.032	197
$E_{\mathrm{T}}^{\mathrm{miss}} > 250$ GeV	23	4.3	0.024	
$p_{\mathrm{T}}(\mathrm{jet}_1) > 150$ GeV	23	3.7	0.024	26

Table 6.6: Expected event yields for the three reference signal points at different stages of the event selection for SR3. The numbers are normalised assuming an integrated luminosity of 12.8 fb^{-1}. The two additional thresholds applied for SR3b are separated from the SR3a selection by the horizontal line. For comparison, the event yields for the total expected SM background are given for the signal regions.

Selection		SM total	Top	Z	W	Other	QCD
SR1	$m_{\mathrm{CT}} > 150$ GeV	187	26%	44%	21%	3%	6%
	$m_{\mathrm{CT}} > 200$ GeV	76	25%	45%	21%	5%	3%
	$m_{\mathrm{CT}} > 250$ GeV	26	31%	46%	19%	5%	1%
	$m_{\mathrm{CT}} > 300$ GeV	8	23%	50%	16%	9%	0%
SR2		94	17%	62%	16%	4%	1%
SR3	a	197	74%	11%	11%	2%	2%
	b	26	58%	19%	15%	6%	0%

Table 6.7: Relative background composition in the signal regions. The $t\bar{t}$ and single top processes are included in "Top". "Others" comprises the diboson and $t\bar{t} + W/Z$ processes. For reference, the total number of expected background events is given in the second column. The event yields are estimated from the MC samples except for the multi-jet contribution, which is estimated from data as explained later.

backgrounds are neglected in this study. When multiple selections or thresholds are compared, the one giving the highest significance value is chosen. The final set of selections is defined as a compromise of the optimal significance across the whole plane and the complexity of the analysis.

A general set of studies was performed for all signal regions, which included changing the b-tagging operation point to different values and testing the thresholds for the QCD rejecting $\Delta\phi_{\mathrm{min}}$ and $E_{\mathrm{T}}^{\mathrm{miss}}/M_{\mathrm{eff}}$ selections. In the following more details are given for the choice of the specific signal region selections as presented in the previous section.

SR1

For SR1 it was tested if other kinematic variables than m_{CT} would provide a better expected discovery reach. The transverse mass, computed from $E_{\mathrm{T}}^{\mathrm{miss}}$ and the momenta of the b-jets, and α_{T} as defined in Ref. [146][10] were tested but a similar or worse performance compared to that achieved with m_{CT} was observed.
In addition, different thresholds for the m_{CT} selection were tried. In general a higher threshold is found optimal with increasing luminosity and decreasing systematic uncertainties. In the end a set of thresholds ($m_{\mathrm{CT}} > 150, 200, 250$ GeV) was kept to reach a large parameter space. For the 8 TeV analysis, a new threshold at 300 GeV was added. The result of a comparison of different m_{CT} thresholds for the SR1 selection is shown in Fig. 6.4 as a function of $m_{\tilde{b}_1}$ and $m_{\tilde{\chi}_1^0}$.

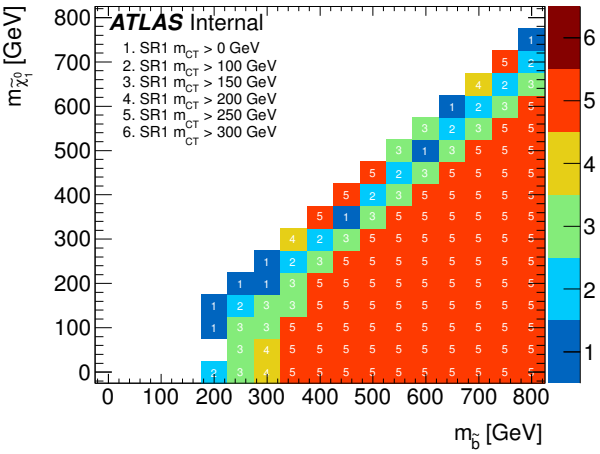

Figure 6.4: Selection that yields the highest significance for each signal point in the sbottom-neutralino mass plane for SR1 using different m_{CT} thresholds. The corresponding selections are listed in the legend. All selection criteria for SR1 except the final m_{CT} selection are applied as baseline selection.

SR2

To study the performance of the SR2 selection, a baseline selection with $E_{\mathrm{T}}^{\mathrm{miss}} > 150$ GeV and two b-jets with $p_{\mathrm{T}} > 60$ GeV was used. The distributions of various kinematic and topological variables after applying the baseline selection were studied for further separation power. They include the number of (b-)jets, the jet momenta, the invariant mass and angular separation of the two b-jets and standard SUSY variables like $E_{\mathrm{T}}^{\mathrm{miss}}$, m_{CT}, M_{eff} and H_{T}. Special emphasis was given on the additional hadronic activity in the event. A harsh veto on additional jets in the event provides a good background separation, but a similar effect can be obtained by placing an upper threshold on the sum of additional jet momenta $H_{\mathrm{T},2}$ which is found more robust under pile-up.
The best discrimination power was obtained by adding a low m_{CT} threshold, an upper threshold on $H_{\mathrm{T},2}$ and a harsher $E_{\mathrm{T}}^{\mathrm{miss}}$ threshold. The $H_{\mathrm{T},2}$ and $E_{\mathrm{T}}^{\mathrm{miss}}$ distributions, before applying the additional selection criteria on any of the two variables, are shown in Fig. 6.5. The results of a study comparing multiple combinations of $H_{\mathrm{T},2}$ and $E_{\mathrm{T}}^{\mathrm{miss}}$ thresholds on top of the baseline plus $m_{\mathrm{CT}} > 100$ GeV selection are displayed in Fig. 6.6a.

10 The α_{T} variable is calculated from the ratio of the momentum of the second leading jet and the invariant mass of the two leading jets.

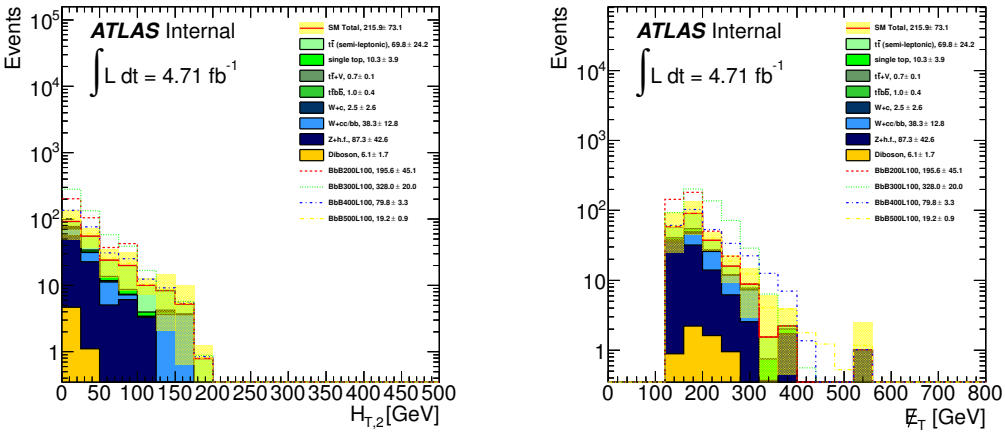

(a) $H_{\mathrm{T},2}$ **(b)** $E_{\mathrm{T}}^{\mathrm{miss}}$

Figure 6.5: Kinematic distributions for SR2 after applying the baseline selection as described in the text and $m_{\mathrm{CT}} > 100$ GeV. The (a) $H_{\mathrm{T},2}$ and (b) $E_{\mathrm{T}}^{\mathrm{miss}}$ distributions are shown for the expected MC background and several signal points for $m(\tilde{\chi}_1^0) = 100$ GeV and $200 \leq m(\tilde{b}_1) \leq 500$ GeV.

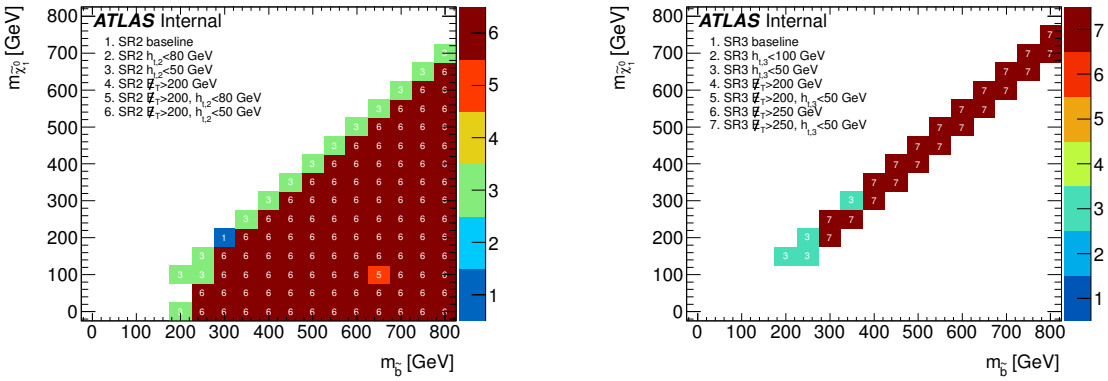

(a) SR2 selections **(b)** SR3 selections

Figure 6.6: Selection that yields the highest significance for each signal point in the sbottom-neutralino mass plane for (a) SR2 and (b) SR3. The corresponding selections are listed in the legends. A set of $H_{\mathrm{T,x}}$ (where $x = 2$ for SR2 and $x = 3$ for SR3) and $E_{\mathrm{T}}^{\mathrm{miss}}$ selections are placed on top of the respective baseline selection. For SR2, a $m_{\mathrm{CT}} > 100$ GeV threshold is included in the baseline selection (compared to the definition in the text). For SR3, the baseline selection used at this point contains all final selection criteria of SR3a except the one on $H_{\mathrm{T},3}$. Only signal points with a small mass-splitting are shown for SR3 because for other points no events survive the selections.

SR3

Similar tests as for SR2 were performed for SR3. In Figure 6.6b, the results of testing different $E_{\mathrm{T}}^{\mathrm{miss}}$ and $H_{\mathrm{T},3}$ thresholds are shown. It can be seen that two sets of thresholds are optimal for different parameter regions. Therefore, two sub-selections, namely SR3a and SR3b, were chosen. A further investigation on SR3b revealed that even a better performance was obtained by increasing the threshold on the momentum of the leading jet to 150 GeV. Special attention was given to a theory study based on an ISR selection with just one b-jet [147]. However, a worse performance was found for a single b-jet analysis.

The significances obtained for all different signal regions were compared and in Fig. 6.7 the selection that yields the highest significance is shown in the sbottom-neutralino mass plane. As expected, SR1 is optimal for signal points with a large mass-splitting and the harshest m_{CT} selection ($m_{\mathrm{CT}} > 250$ GeV) is chosen for most of the points. In contrast, SR3 is optimal for the very small mass-splittings, while the region in between is covered by SR2.

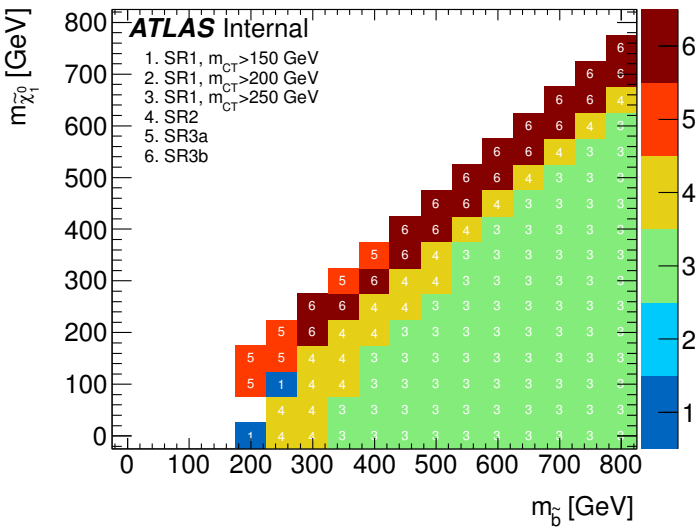

Figure 6.7: Selection that yields the highest significance for each signal point in the sbottom-neutralino mass plane for the finally selected signal regions, including the different m_{CT} thresholds for SR1 and the two sub-selections for SR3. The selections are listed in the legend.

6.3 Background Estimation

The main background contributions for this analysis come from top production, Z+hf jets and W+hf jets processes. Thereby, the Z contribution is completely dominated by $Z \to \nu\nu$ events. The W contribution is smaller in comparison and dominated by events where the lepton is either a hadronically decaying tau or an electron or muon that is not reconstructed or out of acceptance. A combined fit is performed to estimate the main background normalisations from control regions (CRs). The setup and results of the fit are summarised in Section 6.3.2.
Sub-dominant background contributions from diboson and $t\bar{t} + W/Z$ processes are estimated directly from MC simulation. They are grouped together to a contribution called *Others* in the following. Multi-jet events from QCD production processes are only a minor contribution but need to be estimated via a data driven jet-smearing method, which is described in Section 6.3.1.

6.3.1 Multi-jet Estimation

The jet-smearing method is described in Section 5.6. For this analysis, two different approaches for the jet smearing are compared: using a common response function (RF) for all jets or using two different response functions depending on the jet flavour (separating light jets and b-jets).
Multi-jet enriched control regions, used to extract the normalisation, are obtained by apply-

ing all selection criteria of Table 6.3 up to the $E_{\mathrm{T}}^{\mathrm{miss}}/M_{\mathrm{eff}}$ criteria, but inverting the $\Delta\phi_{\mathrm{min}}$ selection. For SR3 the SR3a thresholds are applied, since SR3b is a subset of it. For all SM contributions, other than multi-jet production, pure MC predictions are used. In Table 6.8 the data and MC estimates are given for the three CRs associated with SR1, SR2 and SR3. The multi-jet estimates from this table are used to normalise the multi-jet samples. As an example, the full $\Delta\phi_{\mathrm{min}}$ distribution is shown in Fig. 6.8 for SR1 after applying the normalisation.

CR	Data	non-QCD MC	QCD est.
CR1	858	85	773
CR2	105	15	90
CR3	374	45	329

Table 6.8: Contributions to the multi-jet control regions (CR1, CR2 and CR3 are the CRs associated to SR1, SR2 and SR3, respectively). The signal region selections up to the $E_{\mathrm{T}}^{\mathrm{miss}}/M_{\mathrm{eff}}$ requirement are applied, but the $\Delta\phi_{\mathrm{min}}$ threshold is reversed: $\Delta\phi_{\mathrm{min}} < 0.4$. The "non-QCD MC" column refers to all other SM contributions, which are estimated from MC. The QCD estimations (QCD est.) are obtained by subtracting the non-QCD MC contributions from the observed data events.

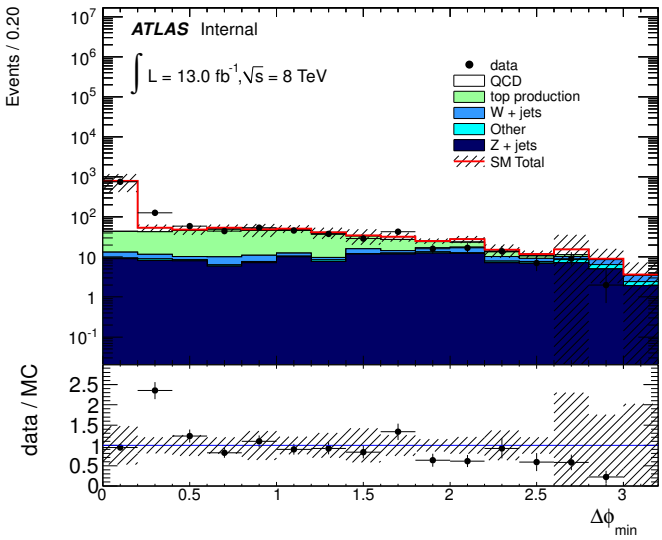

Figure 6.8: Distribution of $\Delta\phi_{\mathrm{min}}$ for SR1 before applying a $\Delta\phi_{\mathrm{min}}$ threshold. The first two bins correspond to the control region and the multi-jet normalisation is taken from here. The inclusive jet-smearing function is applied.

In Figure 6.9, the m_{CT} and leading jet p_{T} distributions are shown for the multi-jet enriched CRs, separately for both smearing approaches as defined above. A multi-jet overestimation for large m_{CT} values is observed for the common RF. This is due to an overestimation of the contribution from under-fluctuations of light-flavoured jets in events where the $b\bar{b}$ pair is emitted against the mis-measured light jet. Other kinematic distributions, like the leading jet p_{T}, are mostly well described. The smearing functions for the flavour dependent approach were not studied with as much detail as the common RF and small discrepancies are observed for several kinematic distributions. In particular, the multi-jet contribution for large m_{CT}

values is underestimated in this case. A reasonable agreement is again found for the leading jet p_{T} distributions. It was decided to take the average of the two approaches as the final multi-jet estimation. The difference is assigned as systematic uncertainty, which roughly amounts to 100% for all signal regions.
The multi-jet contributions to the signal regions are provided in Table 6.9 for both approaches concerning the smearing function and the averaged result. For all signal regions, the common RF yields a larger multi-jet contribution than the flavour dependent RF.

SR		Common RF	Flavour dep. RF	Average
SR1	$m_{\mathrm{CT}} > 150$ GeV	23.0	0.4	11.7
	$m_{\mathrm{CT}} > 200$ GeV	3.9	0.0	1.9
	$m_{\mathrm{CT}} > 250$ GeV	0.5	0.0	0.3
	$m_{\mathrm{CT}} > 300$ GeV	0.02	0.0	0.01
SR2		1.3	0.0	0.6
SR3	a	7.0	1.8	4.4
	b	0.0	0.0	-

Table 6.9: Multi-jet background contribution expected in each signal region. Results are shown for a common jet response function in the second and a flavour dependent jet response function in the third column. The average of both is used as final estimate and is given in the last column.

6.3.2 Combined Background Fit

The normalisations of the dominant background contributions are obtained from data by a simultaneous fit of multiple control regions, as discussed in Section 5.8.1. All CRs are based on a similar baseline selection as the corresponding signal region but with the modified requirement of one or two leptons[11]. Three regions are used for SR1 to estimate the normalisations of the top, Z and W background processes. For SR2 and SR3, only two regions are used to obtain the top and Z normalisations from the fit, while the W normalisation is taken from MC.[12]
The general definitions of the control regions are:

CR1L: The one-lepton CR is dominated by top and W events. It is based on a final state with exactly one electron or muon. The m_{T} variable is used to ensure working in a top and W dominated environment. Residual multi-jet events are removed by requiring $m_{\mathrm{T}} > 40$ GeV and a possible signal contamination is resolved by requiring $m_{\mathrm{T}} < 100$ GeV. The upper threshold also enhances the relative contribution of W events compared to the total yield (dominated by top-pair production) to 5-15%. For SR1 a further enhancement of the W background to about 25% is achieved by requiring $m_{\mathrm{CT}} > 150$ GeV.

CR2L: The two-lepton CR is designed to be dominated by Z events. Events with either two electrons or two muons are selected. The Z background is enhanced by selecting events

11 Lepton refers to an electron or muon in this section, disregarding tau leptons. The tight lepton selection criteria are applied.

12 Several attempts were made to define a third, W enriched, CR for SR2 and SR3, but none provided a satisfactory selection efficiency for W events allowing to isolate them from top events.

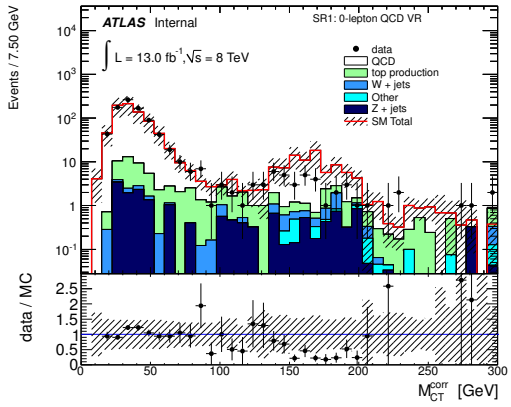

(a) CR1: m_{CT} for common RF

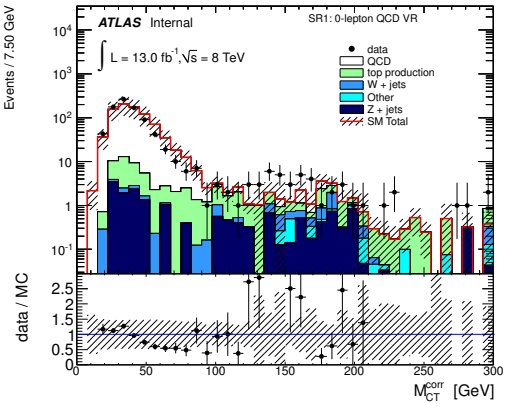

(b) CR1: m_{CT} for flavour dep. RF

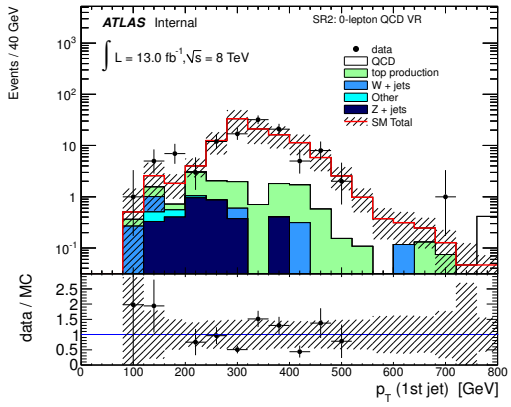

(c) CR2: $p_{\mathrm{T}}(\mathrm{jet}_1)$ for common RF

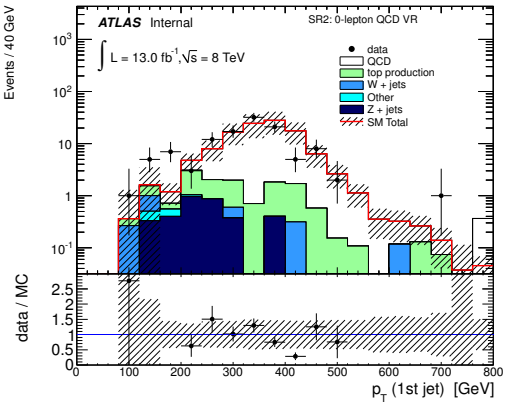

(d) CR2: $p_{\mathrm{T}}(\mathrm{jet}_1)$ for flavour dep. RF

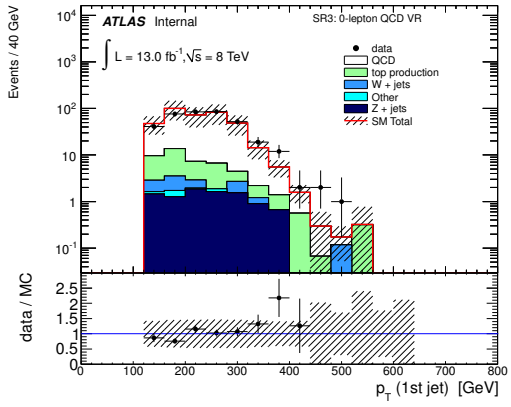

(e) CR3: $p_{\mathrm{T}}(\mathrm{jet}_1)$ for common RF

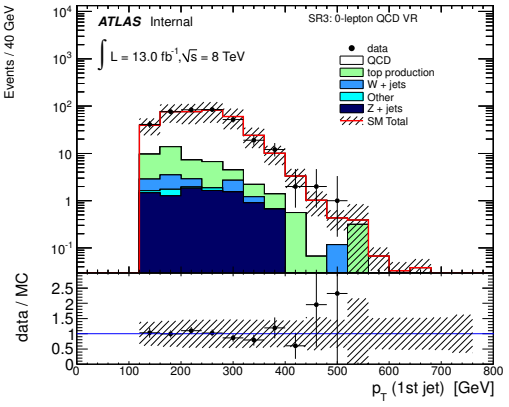

(f) CR3: $p_{\mathrm{T}}(\mathrm{jet}_1)$ for flavour dep. RF

Figure 6.9: Kinematic distributions for the multi-jet control regions. The m_{CT} distributions are shown for the CR associated with SR1 and the p_{T} of the leading jet for CR2 and CR3. For each case, the distribution obtained with a common smearing function is shown on the left and the same distribution obtained with separate functions for light and b-jets is shown on the right. A normalisation for the multi-jet contribution as described in the text is applied.

with an invariant di-lepton mass around the Z mass peak: the invariant mass of the two leptons $m_{\ell\ell}$ is required to satisfy $75 < m_{\ell\ell} < 105$ GeV. A further enhancement of Z events is achieved by a tight threshold on the p_{T} of the leading lepton ($p_{\mathrm{T}} > 90$ GeV). The relative Z contribution to the total event yield is raised from below 50% to above 70% by this.
Furthermore, the momenta of the leptons are vectorially added to $E_{\mathrm{T}}^{\mathrm{miss}}$ to emulate the most important Z contribution, where the Z decays to neutrinos.

CR2LDF: A pure sample of $t\bar{t}$ events is selected with a CR based on the selection of two leptons with different flavour. Exactly one electron and one muon are required. A threshold on the invariant mass of the $e\mu$ pair is set ($m_{\ell\ell} > 50$ GeV) to reduce possible fake-lepton background processes.

Lepton triggers are used for all control regions. For CR1L and CR2LDF, events triggered by isolated leptons are selected, while di-lepton triggers are applied for CR2L. A summary on the triggers used is given in Table 6.10 together with the minimal thresholds that ensure working on the trigger efficiency plateaus. The leptons are generally selected with $p_{\mathrm{T}}(e,\mu) >$ (25,20) GeV and an additional threshold at 25 GeV is added for the muon in CR1L. A matching of the selected leptons to the trigger objects is required. For CR2LDF, either the electron or muon needs to be matched to the corresponding trigger. It should be noted that the CR1L and CR2L selections are separately applied to electron and muon events and both contributions are added in the end. Apart from the trigger, the same preselection as for the signal regions is applied.

Channel	Trigger description	Required offline threshold
1-electron	isolated e with $p_{\mathrm{T}} > 24$ GeV or e with $p_{\mathrm{T}} > 60$ GeV	$p_{\mathrm{T}}(e) > 25$ GeV
1-muon	isolated μ with $p_{\mathrm{T}} > 24$ GeV or μ with $p_{\mathrm{T}} > 36$ GeV	$p_{\mathrm{T}}(\mu) > 25$ GeV
2-electron	ee with $p_{\mathrm{T}} > (12, 12)$ GeV	$p_{\mathrm{T}}(e,e) > (20,20)$ GeV
2-muon	$\mu\mu$ with $p_{\mathrm{T}} > (18, 8)$ GeV	$p_{\mathrm{T}}(\mu,\mu) > (20,10)$ GeV
1-e, 1-μ	1-e or 1-μ trigger	$p_{\mathrm{T}}(e/\mu) > (25)$ GeV

Table 6.10: Triggers used for the different control regions. The trigger momentum thresholds in the second row correspond to the event filter. The last row shows the threshold at the trigger efficiency plateau is reached [148].

The control regions should be populated by events with similar kinematic properties as those in the signal regions for the investigated background process, which can be achieved by applying similar kinematic thresholds. However, some thresholds need to be lowered or completely removed to guarantee a sufficient selection efficiency for the background of interest. The multi-jet based selections on $\Delta\phi_{\mathrm{min}}$ and $E_{\mathrm{T}}^{\mathrm{miss}}/M_{\mathrm{eff}}$ are specific for the no-lepton selections and are not applied. In the current analysis, the contribution from multi-jet events to the

leptonic control regions is neglected.[13] The specific selections used for the different signal regions are explained in the following.

SR1

The three control regions are used for SR1 to estimate the top, Z and W normalisation. The $E_{\mathrm{T}}^{\mathrm{miss}}$ threshold is lowered to 100 GeV for all control regions and the leading jet p_{T} is lowered to 50 GeV for CR2L to ensure that enough events pass the selection. The lowest m_{CT} threshold of 150 GeV is applied for CR1L, while it is lowered to 75 GeV for CR2LDF and completely removed for CR2L. Finally, the corresponding m_{T} or $m_{\ell\ell}$ selections are added as described above. The selections are summarised in Table 6.11. Distributions of several kinematic variables for CR1L, CR2L and CR2LDF before correcting the background normalisation with the fit results are shown in Figs. 6.10, 6.11 and 6.12, respectively.

CR1L_SR1	CR2L_SR1	CR2LDF_SR1
exactly one lepton e or μ	exactly two leptons ee or $\mu\mu$	exactly two leptons $e\mu$
$p_{\mathrm{T}}(\mathrm{jet}_1) > 130$ GeV $p_{\mathrm{T}}(\mathrm{jet}_2) > 50$ GeV	$p_{\mathrm{T}}(\mathrm{jet}_1) > 50$ GeV $p_{\mathrm{T}}(\mathrm{jet}_2) > 50$ GeV	$p_{\mathrm{T}}(\mathrm{jet}_1) > 130$ GeV $p_{\mathrm{T}}(\mathrm{jet}_2) > 50$ GeV
no third jet with $p_{\mathrm{T}} > 50$ GeV		
$E_{\mathrm{T}}^{\mathrm{miss}} > 100$ GeV	$E_{\mathrm{T}}^{\mathrm{miss}}$ (lepton-corrected) > 100 GeV	$E_{\mathrm{T}}^{\mathrm{miss}} > 100$ GeV
jet_1 and jet_2 b-tagged		
$m_{\mathrm{CT}} > 150$ GeV	—	$m_{\mathrm{CT}} > 75$ GeV
40 GeV $< m_{\mathrm{T}} <$ 100 GeV —	75 GeV $< m_{\ell\ell} <$ 105 GeV $p_{\mathrm{T}} > 90$ GeV for leading lepton	$m_{\ell\ell}$ >50 GeV —

Table 6.11: Definition of the control regions adopted for SR1. The trigger and event cleaning selections are described in the text and are applied beforehand.

SR2

Only two control regions are used for SR2. The W normalisation is therefore taken from the MC simulation and the CR2LDF region is removed from the fit to avoid overconstraining. The exact definitions of the CR1L and CR2L selections for SR2 are given in Table 6.12. The m_{CT} and $H_{\mathrm{T},2}$ requirements are completely dropped and the $E_{\mathrm{T}}^{\mathrm{miss}}$ threshold is lowered to 120 GeV for CR1L and 100 GeV for CR2L. The thresholds for both jets are lowered to 50 GeV for CR2L and as a result the definition of CR2L_SR2 is identical to CR2L_SR1. Distributions of several kinematic variables for the one-lepton CR are shown in Fig. 6.13.

13 Non-prompt leptons arising from heavy quark decays, photon conversions or misidentified jets can in principle cause a contamination from multi-jet events. These contributions were studied for the results published in summer and they were found below 1% for the one-lepton CR and below 1‰ for the two-lepton CR.

CR1L_SR2	CR2L_SR2
exactly one lepton e or μ	exactly two leptons ee or $\mu\mu$
$p_{\mathrm{T}}(\mathrm{jet}_1) > 60$ GeV $p_{\mathrm{T}}(\mathrm{jet}_2) > 60$ GeV	$p_{\mathrm{T}}(\mathrm{jet}_1) > 50$ GeV $p_{\mathrm{T}}(\mathrm{jet}_2) > 50$ GeV
no third jet with $p_{\mathrm{T}} > 50$ GeV	
$E_{\mathrm{T}}^{\mathrm{miss}} > 120$ GeV	$E_{\mathrm{T}}^{\mathrm{miss}}$ (lepton-corrected)> 100 GeV
jet_1 and jet_2 b-tagged	
40 GeV $< m_{\mathrm{T}} < 100$ GeV —	75 GeV $< m_{ll} < 105$ GeV $p_{\mathrm{T}} > 90$ GeV for leading lepton

Table 6.12: Definition of the control regions adopted for SR2. The trigger and event cleaning selections are described in the text and are applied beforehand.

SR3

Also for SR3, the CR2LDF selection is removed from the fit and the W normalisation is taken from MC simulation. The same control regions are used for SR3a and SR3b. They are defined in Table 6.13. Following the ISR-jet selection, the leading jet is required not to be b-tagged and the p_{T} threshold is set to 130 GeV for CR1L and 50 GeV for CR2L. As for the SR definition, two additional b-tagged jets of 30 GeV are required. The upper threshold on the momentum of the leading b-jet is applied in CR1L but omitted for CR2L. The $H_{\mathrm{T},3}$ requirement is removed from both selections and the $E_{\mathrm{T}}^{\mathrm{miss}}$ threshold is lowered to 120 GeV in CR1L and 100 GeV in CR2L. Distributions of several kinematic variables for the CR1L and CR2L selections for SR3 are shown in Figs. 6.14 and 6.15

CR1L_SR3	CR2L_SR3
exactly one lepton e or μ	exactly two leptons ee or $\mu\mu$
≥ 3 jets ($p_{\mathrm{T}} > 30$ GeV)	
$p_{\mathrm{T}}(\mathrm{jet}_1) > 130$ GeV	$p_{\mathrm{T}}(\mathrm{jet}_1) > 50$ GeV
$E_{\mathrm{T}}^{\mathrm{miss}} > 120$ GeV	$E_{\mathrm{T}}^{\mathrm{miss}}$ (lepton-corrected)> 100 GeV
jet_1 anti-tagged, jet_2 and jet_3 b-tagged	
$p_{\mathrm{T}}(\mathrm{jet}_2) < 110$ GeV	—
40 GeV $< m_{\mathrm{T}} < 100$ GeV —	75 GeV $< m_{ll} < 105$ GeV $p_{\mathrm{T}} > 90$ GeV for leading lepton

Table 6.13: Definition of the control regions adopted for SR3. The trigger and event cleaning selections are described in the text and are applied beforehand.

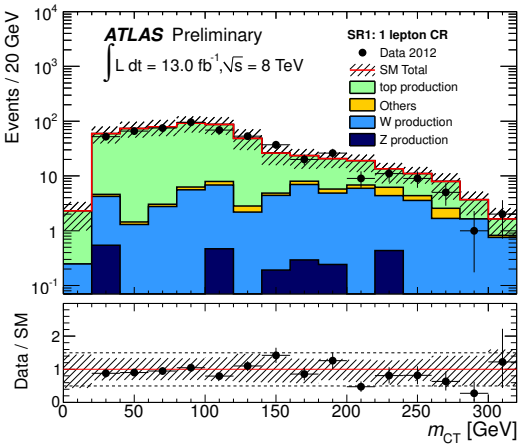

(a) m_{CT}

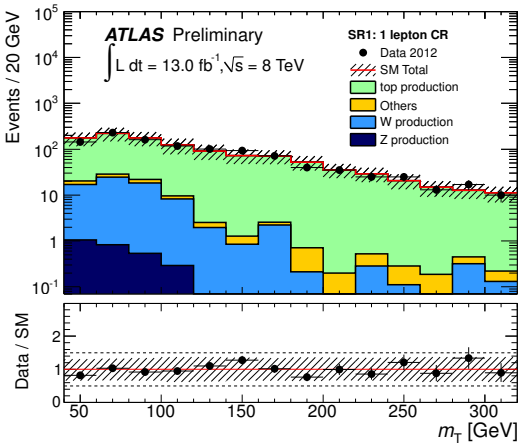

(b) m_{T}

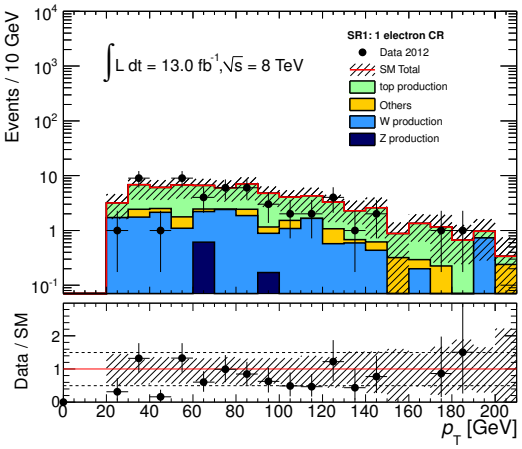

(c) $p_{\mathrm{T}}(e)$ for electron events

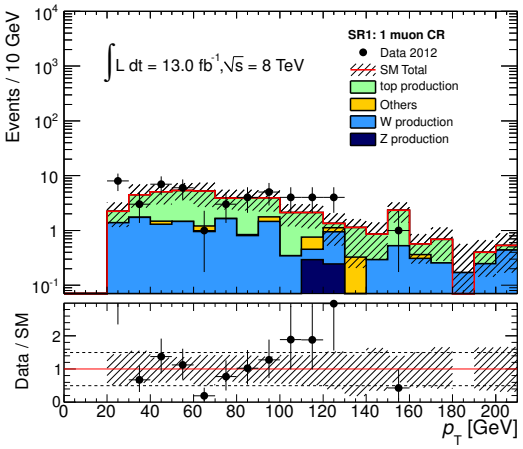

(d) $p_{\mathrm{T}}(\mu)$ for muon events

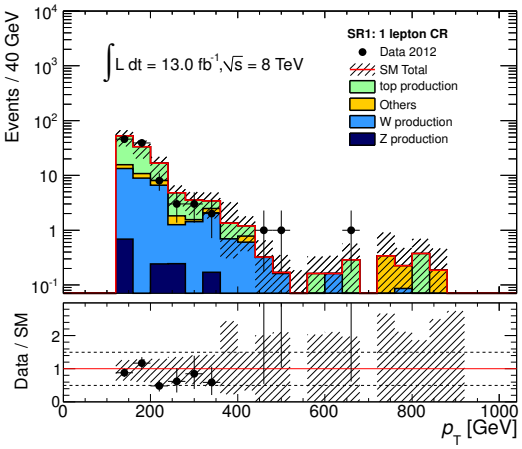

(e) $p_{\mathrm{T}}(\mathrm{jet}_1)$

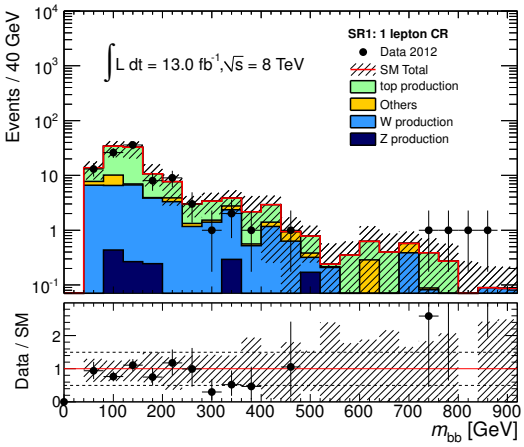

(f) m_{bb}

Figure 6.10: Distributions of kinematic variables (m_{CT}, m_{T}, $p_{\mathrm{T}}(e)$, $p_{\mathrm{T}}(\mu)$, $p_{\mathrm{T}}(\mathrm{jet}_1)$, m_{bb}) for CR1L_SR1 before the background fit. The m_{T} distribution is shown before applying the m_{T} and m_{CT} selections and the m_{CT} distribution before applying the m_{CT} selection. The lepton p_{T} distributions are shown separately for events with one electron and one muon. The error bands include statistical and systematic uncertainties.

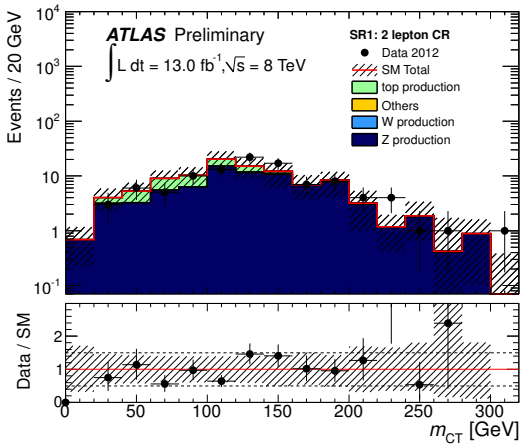

(a) m_{CT}

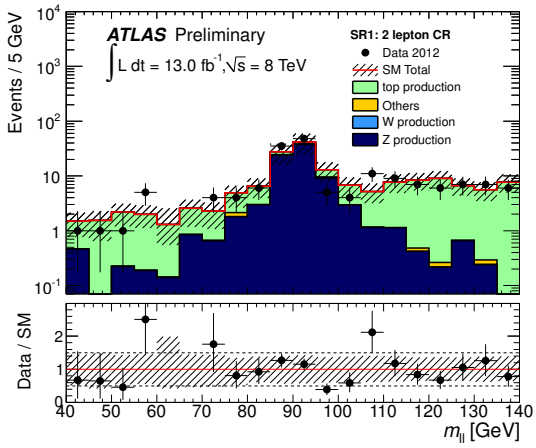

(b) $m_{\ell\ell}$

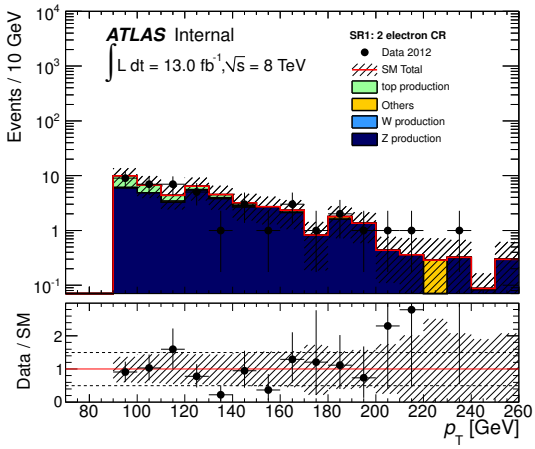

(c) $p_{\mathrm{T}}(e_1)$ for electron events

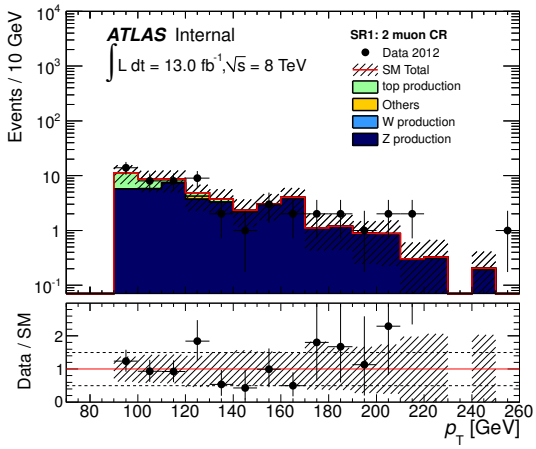

(d) $p_{\mathrm{T}}(\mu_1)$ for muon events

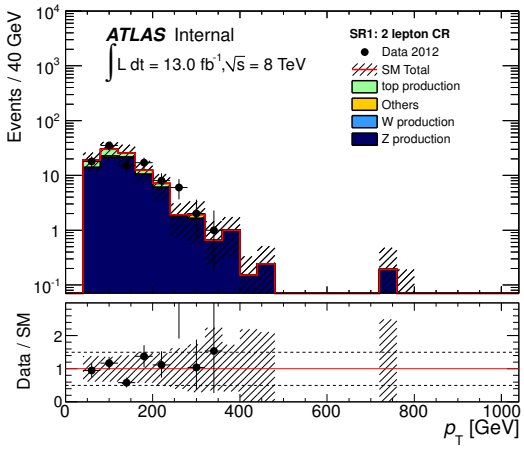

(e) $p_{\mathrm{T}}(\mathrm{jet}_1)$

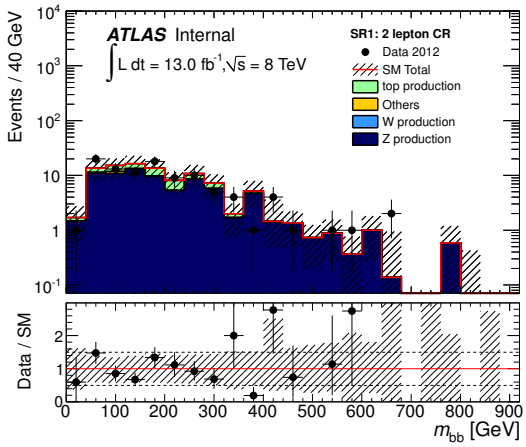

(f) m_{bb}

Figure 6.11: Distributions of kinematic variables (m_{CT}, $m_{\ell\ell}$, $p_{\mathrm{T}}(e_1)$, $p_{\mathrm{T}}(\mu_1)$, $p_{\mathrm{T}}(\mathrm{jet}_1)$, m_{bb}) for CR2L_SR1 before the background fit. The $m_{\ell\ell}$ distribution is shown before applying the $m_{\ell\ell}$ selection. The distributions of the leading electron and muon p_{T} are shown separately for events with two electrons and two muons. The error bands include statistical and systematic uncertainties.

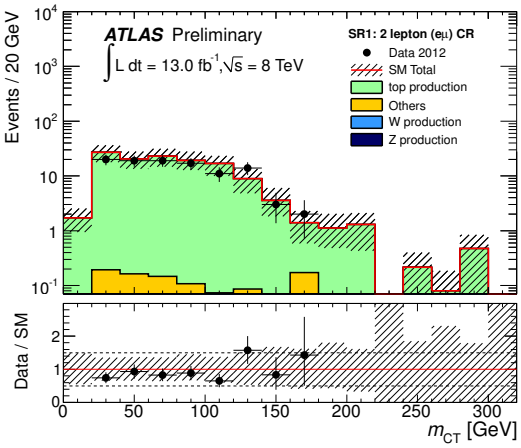

(a) m_{CT}

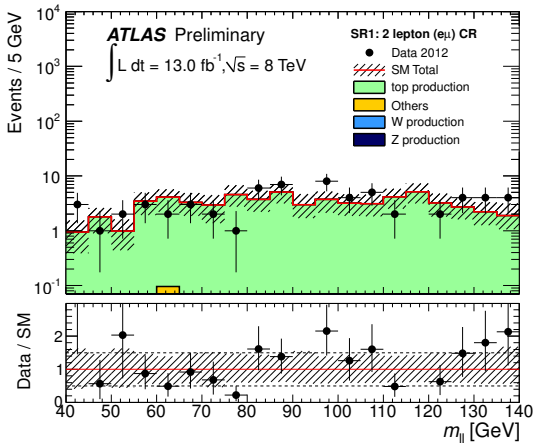

(b) $m_{e\mu}$

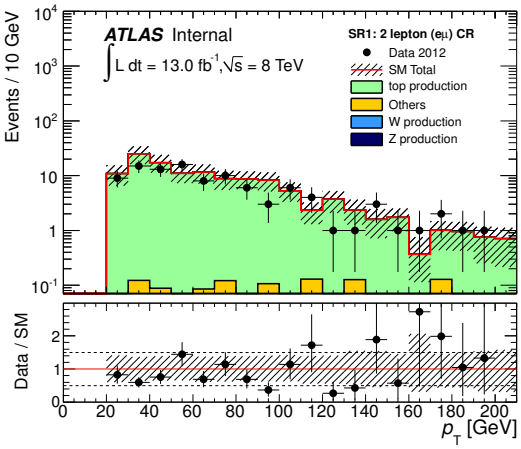

(c) $p_{\mathrm{T}}(e)$

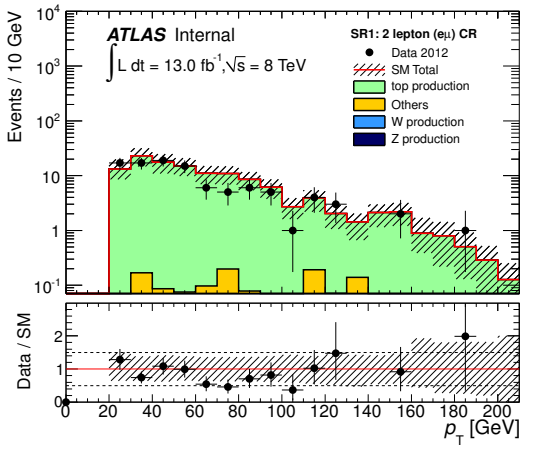

(d) $p_{\mathrm{T}}(\mu)$

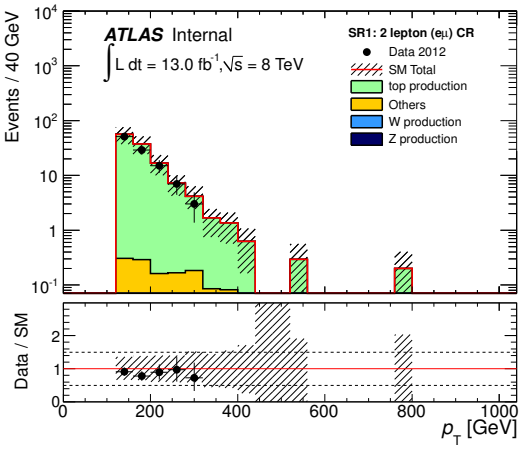

(e) $p_{\mathrm{T}}(\mathrm{jet}_1)$

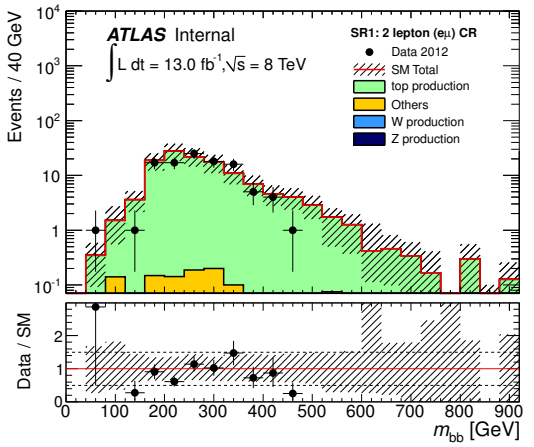

(f) m_{bb}

Figure 6.12: Distributions of kinematic variables (m_{CT}, $m_{e\mu}$, $p_{\mathrm{T}}(e)$, $p_{\mathrm{T}}(\mu)$, $p_{\mathrm{T}}(\mathrm{jet}_1)$, m_{bb}) for CR2LDF_SR1 before the background fit. The distributions are shown before applying the $m_{\mathrm{CT}} > 75$ GeV and $m_{\ell\ell} > 50$ GeV selections. The error bands include statistical and systematic uncertainties.

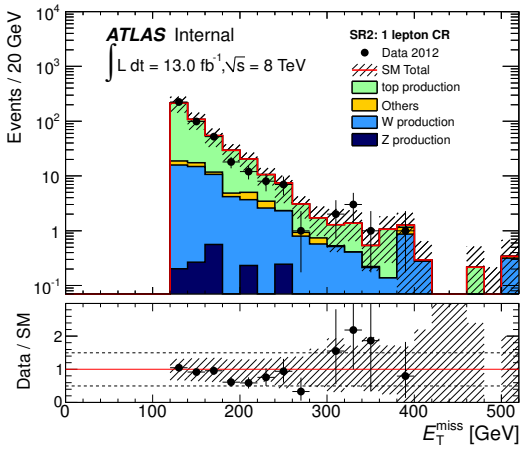

(a) $E_{\mathrm{T}}^{\mathrm{miss}}$

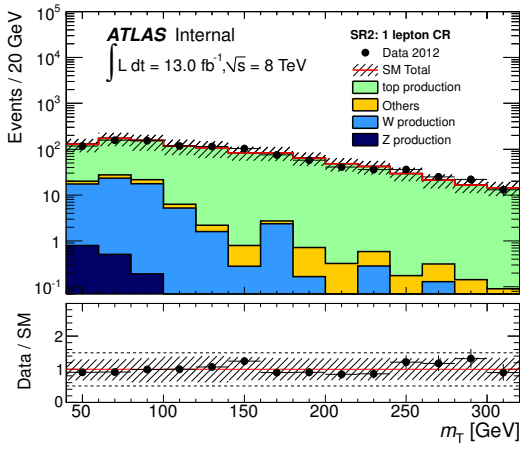

(b) m_{T}

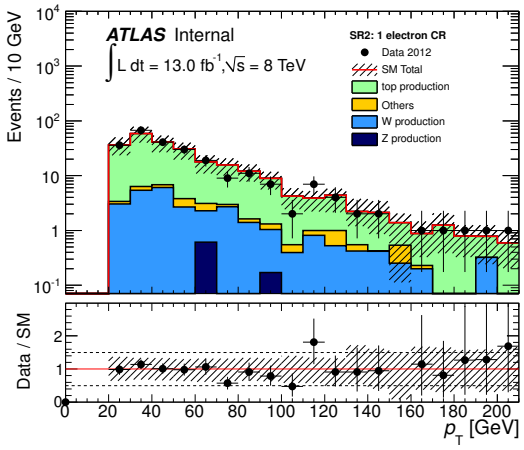

(c) $p_{\mathrm{T}}(e)$ for electron events

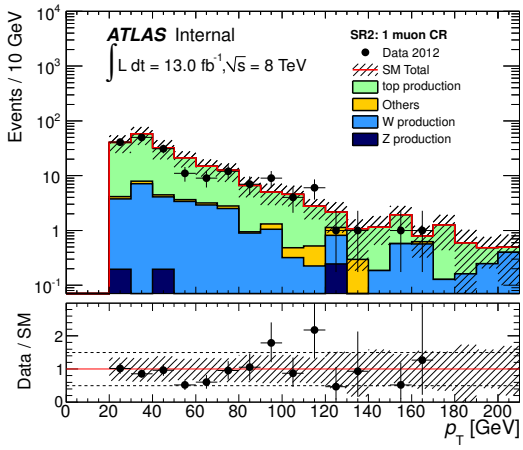

(d) $p_{\mathrm{T}}(\mu)$ for muon events

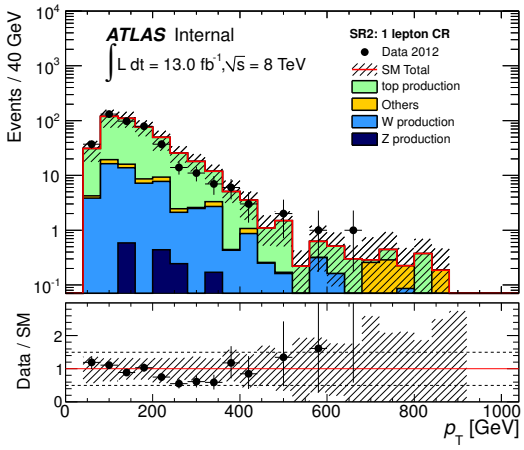

(e) $p_{\mathrm{T}}(\mathrm{jet}_1)$

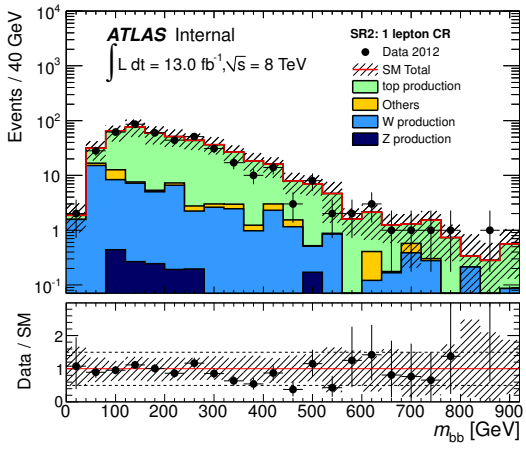

(f) m_{bb}

Figure 6.13: Distributions of kinematic variables ($E_{\mathrm{T}}^{\mathrm{miss}}$, m_{T}, $p_{\mathrm{T}}(e)$, $p_{\mathrm{T}}(\mu)$, $p_{\mathrm{T}}(\mathrm{jet}_1)$, m_{bb}) for CR1L_SR2 before the background fit. The m_{T} distribution is shown before applying the m_{T} selection. The lepton p_{T} distributions are shown separately for events with one electron and one muon. The error bands include statistical and systematic uncertainties.

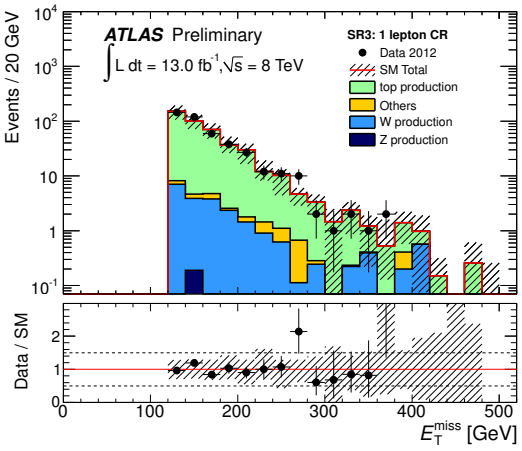

(a) $E_{\mathrm{T}}^{\mathrm{miss}}$

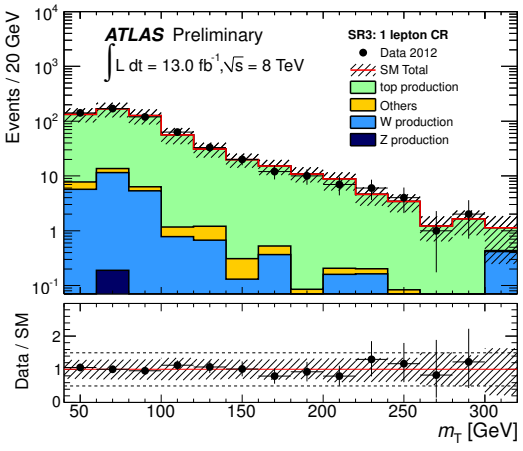

(b) m_{T}

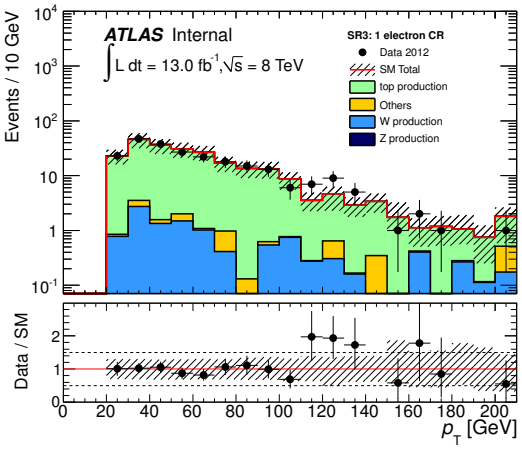

(c) $p_{\mathrm{T}}(e)$ for electron events

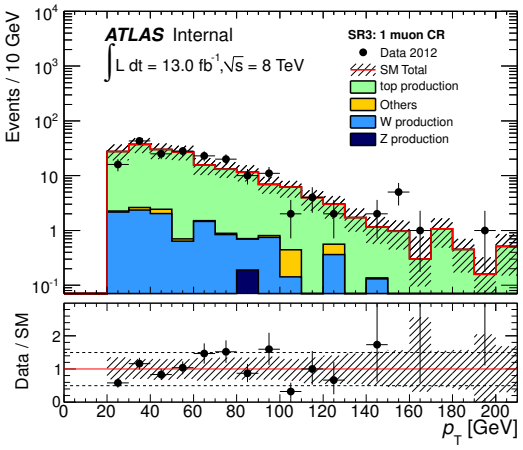

(d) $p_{\mathrm{T}}(\mu)$ for muon events

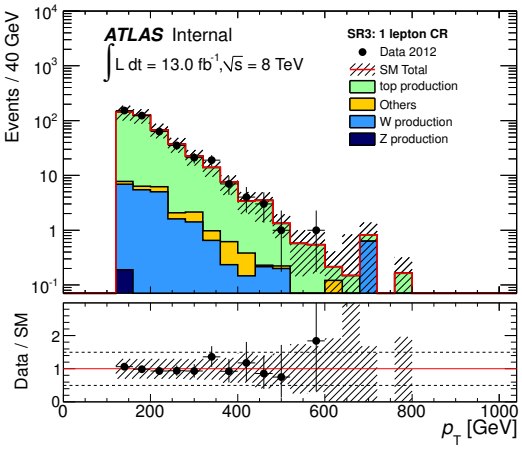

(e) $p_{\mathrm{T}}(\mathrm{jet}_1)$

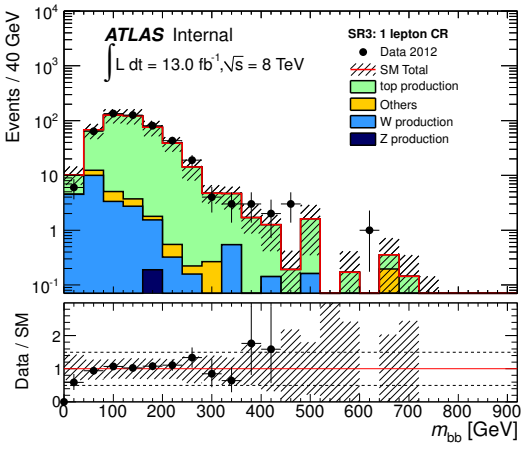

(f) m_{bb}

Figure 6.14: Distributions of kinematic variables ($E_{\mathrm{T}}^{\mathrm{miss}}$, m_{T}, $p_{\mathrm{T}}(e)$, $p_{\mathrm{T}}(\mu)$, $p_{\mathrm{T}}(\mathrm{jet}_1)$, m_{bb}) for CR1L_SR3 before the background fit. The m_{T} distribution is shown before applying the upper selection on m_{T}. The lepton p_{T} distributions are shown separately for events with one electron and one muon. The error bands include statistical and systematic uncertainties.

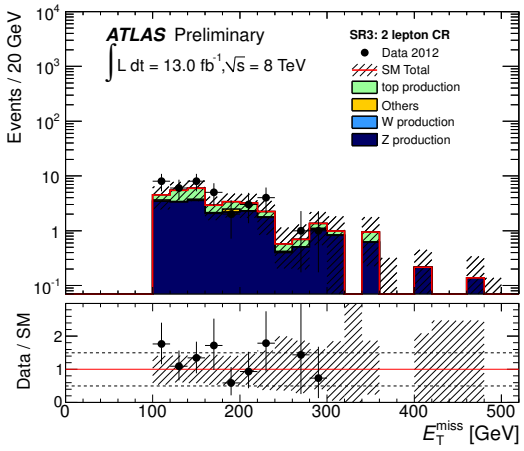

(a) $E_{\mathrm{T}}^{\mathrm{miss}}$

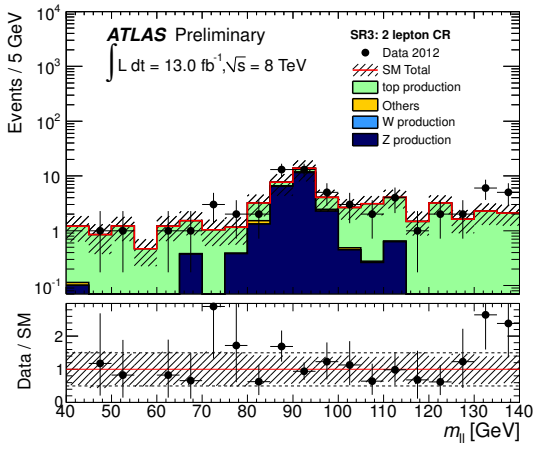

(b) $m_{\ell\ell}$

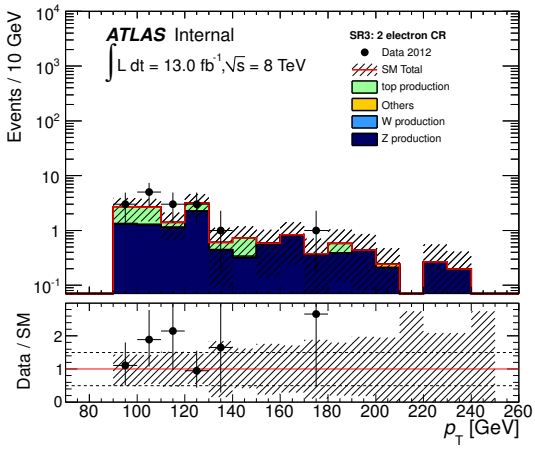

(c) $p_{\mathrm{T}}(e_1)$ for electron events

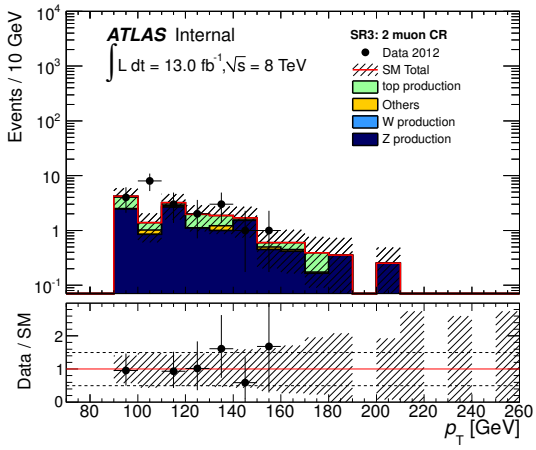

(d) $p_{\mathrm{T}}(\mu_1)$ for muon events

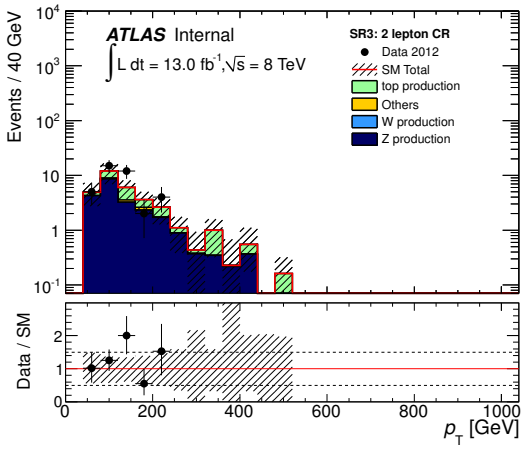

(e) $p_{\mathrm{T}}(\mathrm{jet}_1)$

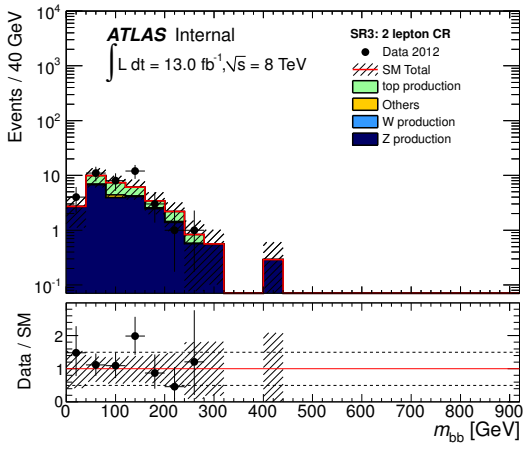

(f) m_{bb}

Figure 6.15: Distributions of kinematic variables ($E_{\mathrm{T}}^{\mathrm{miss}}$, $m_{\ell\ell}$, $p_{\mathrm{T}}(e_1)$, $p_{\mathrm{T}}(\mu_1)$, $p_{\mathrm{T}}(\mathrm{jet}_1)$, m_{bb}) for CR2L_SR3 before the background fit. The $m_{\ell\ell}$ distribution is shown before applying the $m_{\ell\ell}$ selection. The distributions of the leading electron and muon p_{T} are shown separately for events with two electrons and two muons. The error bands include statistical and systematic uncertainties.

The normalisation factors obtained by the fit are summarized in Table 6.14. They are consistent with 1 within their uncertainties, with the trend of reducing the top and W contributions and increasing the Z contribution, especially for SR3. The results obtained in the different control regions for the SM backgrounds are shown in Table 6.15. The fitted SM event yields are compatible with the MC expectations before applying the fit. Experimental as well as theoretical uncertainties are provided as input to the fit. They are further described in Section 6.4.

Factor	SR1	SR2	SR3
μ_{Top}	0.92 ± 0.32	0.93 ± 0.36	1.00 ± 0.42
μ_Z	1.04 ± 0.26	1.04 ± 0.31	1.24 ± 0.45
μ_W	0.73 ± 0.57	—	—

Table 6.14: Normalisation factors μ_{Top}, μ_Z and μ_W obtained by the background fit on the dedicated control regions for the three signal regions.

Validation of the Fit Results

Several validation regions are investigated to check the reliability of the fit results. A validation region with no leptons, labelled as VR0L, is added for each SR by inverting the threshold on one of the kinematic variables, but otherwise applying the SR definition. For SR1 and SR2, $m_{\text{CT}} < 100$ GeV is required. To increase the selection efficiency, the $E_{\text{T}}^{\text{miss}}$ threshold is lowered to 150 GeV for SR2. The $H_{\text{T,3}}$ selection is reverted for SR3 ($H_{\text{T,3}} > 50$ GeV) and the selection criteria on the jets are reduced to require exactly two b-jets.[14]
Another VR with no leptons is used to verify the QCD multi-jet background estimation. The selections are based on the VR0L selections, but with reverted $\Delta\phi_{\text{min}}$ thresholds ($\Delta\phi_{\text{min}} < 0.4$)[15]. Other changes compared to the VR0L selection are a tighter $E_{\text{T}}^{\text{miss}}$ threshold for SR2 ($E_{\text{T}}^{\text{miss}}$ >200 GeV) and the complete removal of the $H_{\text{T,3}}$ requirement for SR3. For SR2 and SR3, also the CR2LDF selection is used as validation region.
Special care is taken of the b-tagging stability by adding a VR with exactly one b-jet for each signal and control region. Apart from the b-jet multiplicity, the same selection as for the corresponding SR or CR is applied.
The fitted SM background expectations are found to be in agreement with the observed data events for all validation regions. The exact results are presented in Appendix C. The $E_{\text{T}}^{\text{miss}}$ distributions for the no-lepton validation regions are shown in Fig. 6.16. Good agreement between the SM expectation and data is observed.

6.4 Systematic Uncertainties

Theoretical and experimental uncertainties, as described in Section 5.7, are considered for the SM backgrounds. For the fit described in the previous section, the experimental uncertainties

14 The ISR-criteria for the leading jet and the upper threshold for the leading b-jet are removed from the SR3 validation region selection.

15 Although the same procedure on reverting the $\Delta\phi_{\text{min}}$ threshold is applied, the multi-jet VR selections are different from the multi-jet control regions used in the previous section as they are based on the VR0L selections.

Channel	SR1 Control Regions			SR2 Control Regions		SR3 Control Regions	
	CR1L	CR2L	CR2LDF	CR1L	CR2L	CR1L	CR2L
Observed events	104	102	51	428	102	430	38
Fitted SM events	104.0 ± 11.0	102.0 ± 10.9	51.0 ± 7.5	428.0 ± 24.1	102.0 ± 11.1	430.1 ± 69.5	38.0 ± 7.9
Fitted Top events	70.0 ± 16.2	17.8 ± 4.3	50.2 ± 7.5	358.9 ± 30.6	18.0 ± 4.0	402.3 ± 69.4	9.2 ± 3.3
Fitted Z events	1.5 ± 0.4	81.8 ± 11.7	—	1.6 ± 0.4	81.6 ± 11.8	0.2 ± 0.4	27.8 ± 9.0
Fitted W events	24.9 ± 19.3	—	—	56.9 ± 15.8	—	22.4 ± 6.3	—
Fitted Others events	7.7 ± 4.0	2.4 ± 1.3	0.8 ± 0.5	10.6 ± 5.9	2.4 ± 1.3	5.2 ± 2.9	1.0 ± 0.6
MC exp. SM events	119.2	100.3	55.2	456.0	100.3	427.8	32.6
MC exp. Top events	75.9	19.3	54.4	386.8	19.3	400.1	9.2
MC exp. Z events	1.4	78.5	—	1.5	78.5	0.2	22.4
MC exp. W events	34.2	—	—	57.0	—	22.3	—
MC exp. Others events	7.7	2.4	0.8	10.7	2.4	5.2	1.0

Table 6.15: Results of the background fit in the control regions exploited for SR1, SR2 and SR3. The MC expectation before applying the fit and the number of fitted background events are shown separately for the different background contributions. The uncertainties provided by the fit account for experimental and theoretical uncertainties. When no value is given, less than 0.01 events are expected.

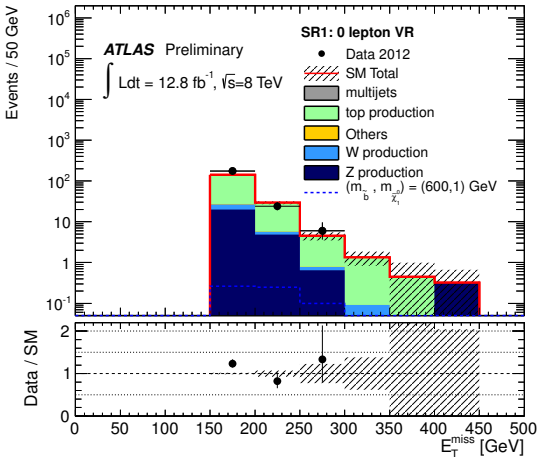

(a) SR1: no-lepton VR

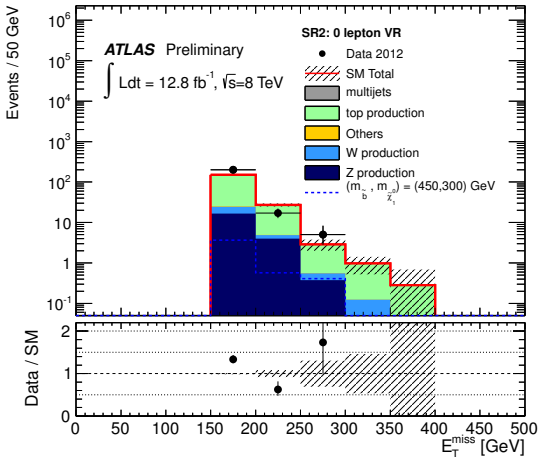

(b) SR2: no-lepton VR

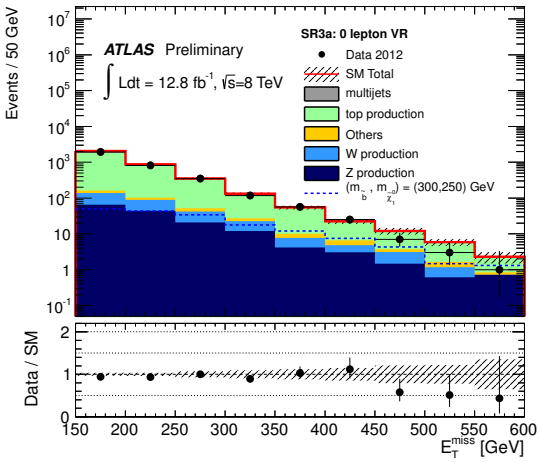

(c) SR3: no-lepton VR

Figure 6.16: Distributions of $E_{\mathrm{T}}^{\mathrm{miss}}$ for the no-lepton validation regions for each signal region. The fit results are applied and the error bands include both detector and theoretical systematic uncertainties. For each VR, the distribution for the associated reference signal point is also shown (see Section 6.2.3).

are considered to be fully correlated among the background contributions, while the theory uncertainties are treated individually per background process.
The experimental uncertainties include the b-tagging (separated for b-, c- and light jets), JES, JER, Pile-up[16] and $E_{\mathrm{T}}^{\mathrm{miss,CellOut}}$ (separated into an energy scale and an energy resolution contribution) uncertainties. Uncertainties on the luminosity measurement are taken to be $\pm 3.9\%$, following the same method as detailed in Ref. [119].

16 For SR2 and SR3, a more conservative pile-up uncertainty is applied than what is obtained by the procedure described in Section 5.7. A $\pm 10\%$ variation of the final event yields is considered, based on additional studies that were performed to explicitly check the pile-up dependence of the third jet veto and H_{T} selections.

For the background specific uncertainties, the following variations are considered:

Top: Three types of variations are considered for the top background. The generator uncertainty is evaluated by comparing the event yields predicted by the POWHEG sample to those of a sample generated with the MC@NLO generator. Uncertainties on the parton shower and hadronisation modelling are estimated by comparing POWHEG interfaced to PYTHIA with POWHEG interfaced to HERWIG and JIMMY. The ISR and FSR uncertainty is addressed by a comparison of ACERMC samples with stronger and weaker parton showering strength. Kinematic distributions obtained for the different samples are shown in Fig. 6.17. The relative uncertainties that are obtained for the signal and control regions are provided in Table 6.16. All uncertainties are estimated on pure $t\bar{t}$ events, but are applied to the whole top background (including single top production).

W/Z: For the W+jets and Z+jets backgrounds, generator uncertainties are estimated by comparing the SHERPA samples to samples generated with ALPGEN. Variations of scales related to the matching scheme and the functional form and absolute scale of the strong coupling constant are summarised as scale uncertainties. They are estimated from the ALPGEN samples.[17] The relative uncertainties that are obtained for the signal and control regions are shown in Table 6.17 for the Z and in Table 6.18 for the W background.

Others: The contributions from diboson and $t\bar{t}$ $+W/Z$ events are small and no dedicated estimation of different theory uncertainties is performed. Uncertainties for the $t\bar{t}$ $+W$ ($t\bar{t}$ $+Z$) NLO cross-sections are provided in Refs. [136,137] and amount to ±30% (±50%). A conservative uncertainty of ±50% is assigned to the contribution of the Others backgrounds.

QCD: A 100% uncertainty is assumed for the multi-jet background for all signal regions.

The uncertainties described above, and in particular the theory uncertainties given in Tables 6.16-6.18, are provided as input to the background fit. The absolute uncertainties on the event yields that are obtained after applying the fit are shown in Table 6.19 for all signal regions. They are split among the different contributions described above and the uncertainties for the background normalisation factors and statistical uncertainties are also shown. It should be noted though, that correlations among the contributions are not readable from the table, but need to be taken into account when adding the uncertainties. Statistical uncertainties due to the limited size of the MC samples are only considered by the fit if they are larger than 5%, which is the case only for SR3b.

Signal Uncertainties

When extracting exclusion limits, the same experimental uncertainties as for the SM background processes are applied to the signal samples. The dominant contributions come from the b-tagging and JES uncertainties. The effects of the b-tagging uncertainties on the signal event yields are about ±28% for SR1 and SR2 and ±(10-20)% for SR3. In Figure 6.18, the relative uncertainties on the event yields are shown in the sbottom-neutralino mass plane for SR1 ($m_{\mathrm{CT}} > 150$ GeV) and SR3a. The effects of the JES uncertainties are small for

17 Common scale factors to reweight the ALPGEN samples for the different variations were derived within the SUSY group and are applied here.

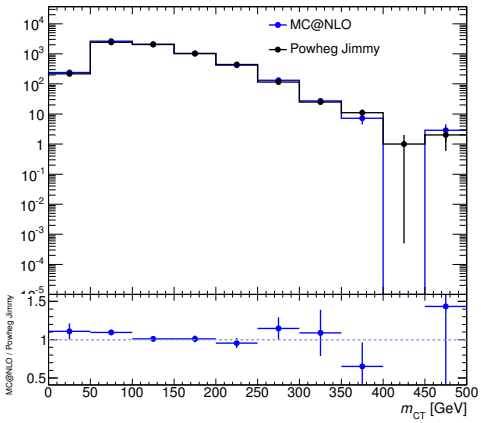

(a) SR1: POWHEG vs. MC@NLO

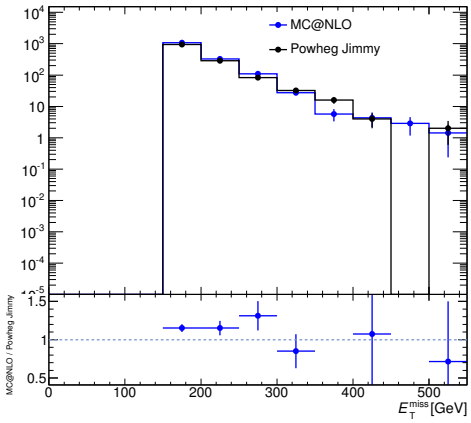

(b) SR3a: POWHEG vs. MC@NLO

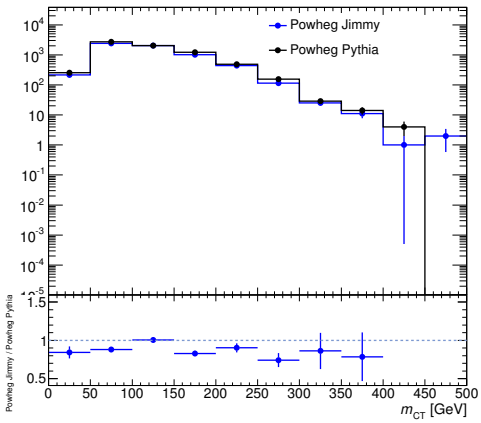

(c) SR1: PYTHIA vs. HERWIG + JIMMY

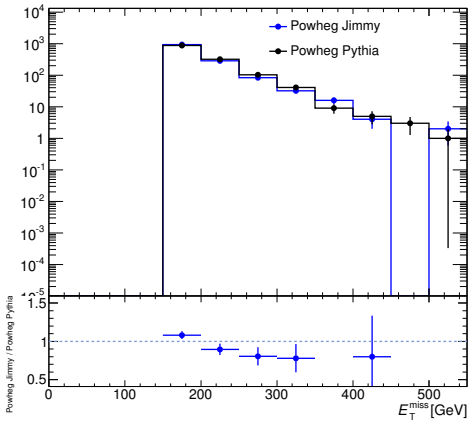

(d) SR3a: PYTHIA vs. HERWIG + JIMMY

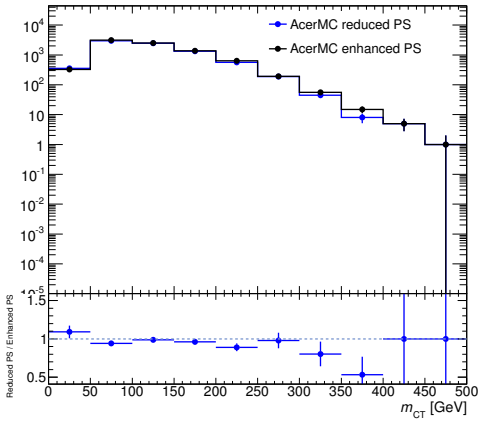

(e) SR1: enhanced PS vs. reduced PS (ACERMC)

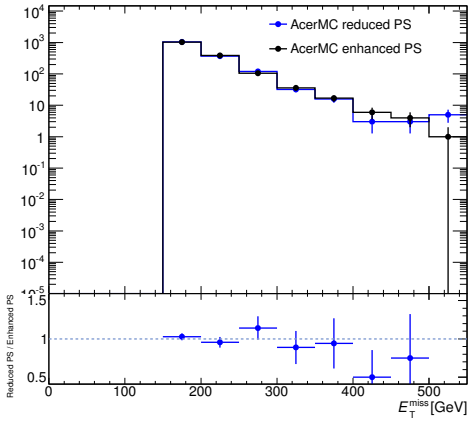

(f) SR3a: enhanced PS vs. reduced PS (ACERMC)

Figure 6.17: Distributions of m_{CT} for SR1 (left) and $E_{\mathrm{T}}^{\mathrm{miss}}$ for SR3a for the different samples used to estimate the $t\bar{t}$ theory uncertainties. A comparison of different generators (POWHEG vs. MC@NLO), parton showering models (PYTHIA vs. HERWIG+JIMMY) and ISR/FSR contributions (ACERMC with enhanced PS vs. ACERMC with reduced PS) is presented. The lower insets show the ratio between the two compared samples. The last bin includes the overflow and uncertainties are purely statistical.

Selection	Top Theory Uncertainty [%]		
	Generator	Parton Shower	ISR/FSR
SR1, $m_{CT} > 150$ GeV	$\pm 0.9 \pm 1.5$	$\pm 8.0 \pm 1.4$	$\pm 3.2 \pm 1.5$
SR1, $m_{CT} > 200$ GeV	$\pm 2.0 \pm 2.6$	$\pm 6.6 \pm 2.4$	$\pm 5.3 \pm 2.4$
SR1, $m_{CT} > 250/300$ GeV	$\pm 5.0 \pm 5.3$	$\pm 11.9 \pm 4.1$	$\pm 4.3 \pm 4.4$
SR2	$\pm 3.9 \pm 2.8$	$\pm 4.3 \pm 2.8$	$\pm 2.4 \pm 2.6$
SR3a	$\pm 8.4 \pm 1.9$	$\pm 0.5 \pm 1.5$	$\pm 0.7 \pm 1.8$
SR3b	$\pm 5.0 \pm 5.8$	$\pm 6.6 \pm 5.1$	$\pm 1.8 \pm 5.5$
CR1L_SR1	$\pm 0.6 \pm 2.4$	$\pm 4.4 \pm 5.9$	$\pm 12.6 \pm 4.6$
CR1L_SR2	$\pm 2.0 \pm 2.8$	$\pm 0.5 \pm 7.8$	$\pm 15.5 \pm 5.6$
CR1L_SR3	$\pm 15.1 \pm 5.4$	$\pm 6.6 \pm 10.0$	$\pm 0.7 \pm 8.8$
CR2L_SR1	$\pm 1.1 \pm 0.9$	$\pm 3.0 \pm 1.3$	$\pm 1.2 \pm 1.3$
CR2L_SR2	$\pm 1.7 \pm 1.6$	$\pm 1.8 \pm 2.1$	$\pm 2.7 \pm 2.1$
CR2L_SR3	$\pm 2.5 \pm 1.4$	$\pm 4.6 \pm 2.2$	$\pm 9.0 \pm 2.1$

Table 6.16: Relative systematic theory uncertainties for top-pair production for the signal regions and the one- and two-lepton control regions. The errors correspond to the statistical uncertainties on the systematic uncertainties. The uncertainties are used as input to the fit (the values for the one-lepton control region are used for the CR2LDF selections).

Selection	Z Theory Uncertainty [%]	
	Generator	Scale
SR1 ($m_{CT} > 150$ GeV)	± 7	± 12
SR2	± 6	± 12
SR3a and SR3b	± 7	± 12
CR2L_SR1, CR2LDF_SR1, CR2L_SR2	± 6	± 12
CR2L_SR3	± 16	± 14

Table 6.17: Relative theoretical uncertainties for the Z+jets background for the signal and two-lepton control regions (the Z contribution to the one-lepton control regions is negligible). The uncertainties are used as input to the fit.

most signal points in SR1 and SR2 ($< \pm 6\%$), but get larger for small mass-splitting points ($\pm$(20-40)%). For SR3, fluctuations from $\sim \pm 1\%$ to $\sim \pm 30\%$ are observed throughout the signal grid. The relative JES uncertainties on the event yields for SR1 ($m_{CT} > 150$ GeV) and SR3a are shown in the sbottom-neutralino mass plane in Fig. 6.19.
The theory uncertainties on the signal cross-sections include effects from using different PDF sets and variations on the factorisation and renormalization scales (see Section 5.7)[18]. They are about $\pm 15\%$ for moderate sbottom masses ($m(\tilde{b}_1) < 600$ GeV) and rise to approximately $\pm 20\%$ for higher sbottom masses ($m(\tilde{b}_1) \approx 800$ GeV).

18 Detailed information on the calculation of the signal cross-sections and their theoretical uncertainties is given in Ref. [149].

Selection	W Theory Uncertainty [%]	
	Generator	Scale
SR1 ($m_{\mathrm{CT}} > 150$ GeV)	±3	±8
SR2	±8	±9
SR3a and SR3b	±8	±9

Table 6.18: Relative theoretical uncertainties for the W+jets background for the signal regions. Large statistical fluctuations were observed for the control regions. Therefore, the values from the corresponding signal regions are used for the control regions. The uncertainties are used as input to the fit.

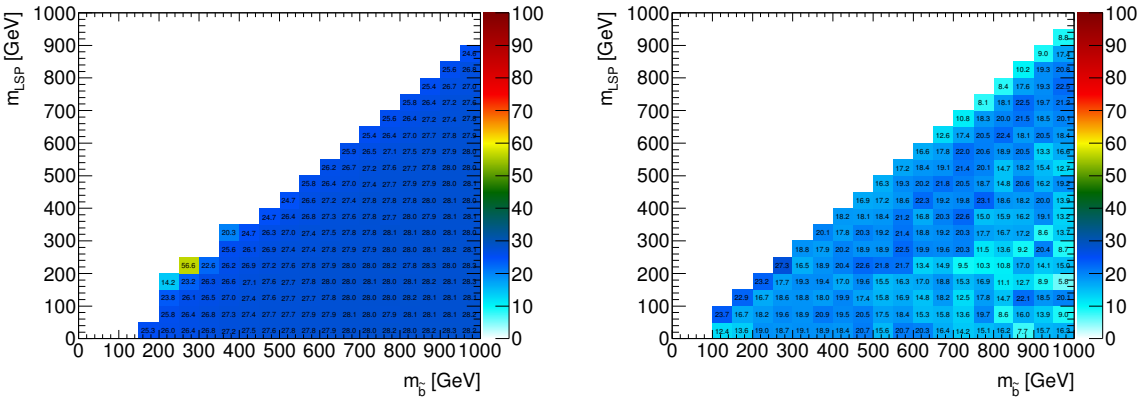

(a) SR1 ($m_{\mathrm{CT}} > 150$ GeV) **(b)** SR3a

Figure 6.18: Effects of the b-tagging systematic uncertainties on the signal event yields in the sbottom-neutralino mass plane for (a) SR1 ($m_{\mathrm{CT}} > 150$ GeV) and (b) SR3a. The values (in percent) obtained after applying the full event selection are shown.

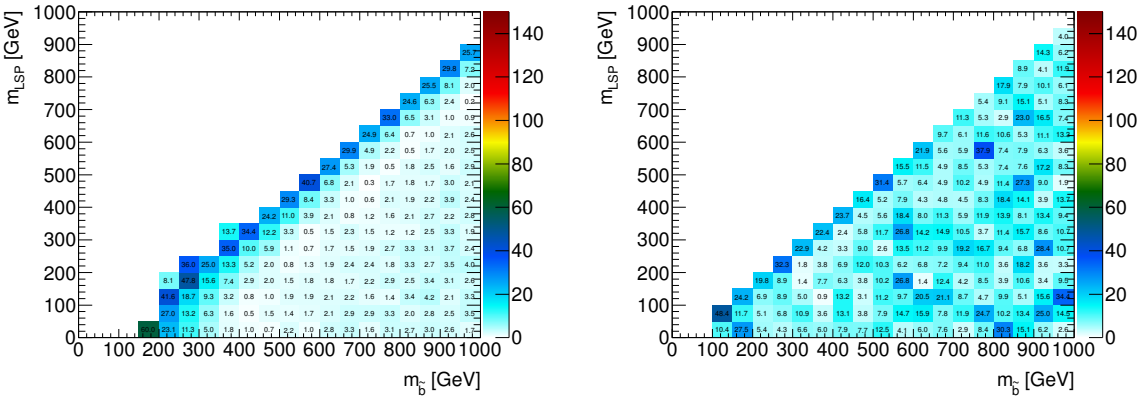

(a) SR1 ($m_{\mathrm{CT}} > 150$ GeV) **(b)** SR3a

Figure 6.19: Effects of the JES uncertainty on the signal event yields in the sbottom-neutralino mass plane for (a) SR1 ($m_{\mathrm{CT}} > 150$ GeV) and (b) SR3a. The values (in percent) obtained after applying the full event selection are shown.

Uncertainty	SR1, m_{CT} selection [GeV]				SR2	SR3	
	150	200	250	300		SR3a	SR3b
Total	25.52	10.68	3.65	1.74	11.17	34.89	5.04
Experimental Uncertainties							
b-tagging (b-jets)	26.58	11.14	4.09	1.24	21.45	33.06	4.85
b-tagging (c-jets)	12.58	6.20	2.11	0.65	4.19	4.96	0.41
b-tagging (light jets)	1.80	0.68	0.43	0.11	0.63	1.10	0.01
JES	22.10	9.28	2.61	1.23	11.03	15.73	2.76
JER	4.27	1.34	1.15	0.37	3.70	8.92	1.31
Pile-up	0.46	0.03	0.09	0.30	9.49	19.87	2.72
$E_{\mathrm{T}}^{\mathrm{miss,CellOut}}$ (scale)	1.12	0.49	0.17	0.17	0.00	0.51	0.24
$E_{\mathrm{T}}^{\mathrm{miss,CellOut}}$ (resolution)	0.33	0.10	0.00	0.00	0.19	0.65	0.21
Theory Uncertainties							
Top (generator)	0.83	0.56	0.36	0.08	0.60	11.87	0.77
Top (parton shower)	3.56	1.47	0.79	0.19	0.64	0.34	0.98
Top (ISR/FSR)	1.91	0.94	0.33	0.08	0.36	1.14	0.28
W (generator)	0.79	0.33	0.11	0.03	1.14	1.85	0.33
W (scale)	2.11	0.89	0.28	0.07	1.30	1.94	0.34
Z (generator)	5.08	2.13	0.72	0.24	3.02	1.84	0.45
Z (scale)	9.86	4.13	1.40	0.46	6.68	3.22	0.79
Others	2.90	2.07	0.67	0.36	2.00	1.93	0.78
QCD	11.87	2.00	0.25	0.01	0.64	4.53	—
Uncertainties on the Normalisation Factors							
μ_{Top}	15.79	6.11	2.47	0.58	5.94	60.81	6.30
μ_W	22.34	9.44	3.01	0.77	—	—	—
μ_Z	21.75	9.11	3.10	1.03	18.01	9.81	2.42
Statistical Uncertainties							
Statistical (MC)	—	—	—	—	—	—	2.76

Table 6.19: Absolute uncertainties on the event numbers after the background fit for each of the signal regions. Correlations between the individual uncertainties need to be taken into account to obtain the total uncertainty. Statistical uncertainties for the MC samples are only considered in the fit when they are above 5%. See text for a more detailed description on the uncertainties.

6.5 Results

In the previous sections, the signal regions have been defined and a detailed estimation of background processes with systematic uncertainties has been performed. In this section, the results obtained in the various signal regions are presented.
The observed and expected SM background event yields are shown in Table 6.20 for all signal regions. The values for the expected background yields are estimated by the combined fit[19] and the errors include statistical and systematic uncertainties. In general, a good agreement of the observed event yields with the expected SM event yields is obtained within the quoted uncertainties, indicating no evidence for a possible contribution of SUSY events. The only deviation is found for SR1 with $m_{\mathrm{CT}} > 250$ GeV where a slight down fluctuation of the data events is observed. The relative systematic uncertainties on the total SM event yields are found within ±(14-23)% for SR1, ±12% for SR2 and ±(17-18)% for SR3. As expected, the dominant SM background contribution for SR1 and SR2 comes from Z production, followed by contributions from top and W production. For SR3, the top background contribution is dominant, followed by contributions from Z and W production.

Channel	SR1, m_{CT} selection				SR2	SR3	
	150 GeV	200 GeV	250 GeV	300 GeV		SR3a	SR3b
Observed	**172**	**66**	**16**	**8**	**104**	**207**	**21**
SM Total	176 ± 25	71 ± 11	25 ± 4	7.4 ± 1.7	95 ± 11	203 ± 35	27 ± 5
Top	45 ± 13	17 ± 6	7 ± 3	1.6 ± 0.6	15 ± 4	146 ± 40	15 ± 5
Z	85 ± 15	36 ± 6	12 ± 2	4.0 ± 0.9	60 ± 9	27 ± 9	7 ± 2
W	28 ± 23	12 ± 10	4 ± 3	1 ± 1	15 ± 5	22 ± 7	4 ± 1
Others	6 ± 3	4 ± 2	1.4 ± 0.8	0.7 ± 0.4	4 ± 2	4 ± 2	1.5 ± 0.9
Multi-jet	12 ± 12	2 ± 2	0.2 ± 0.2	0.01 ± 0.01	0.6 ± 0.6	4 ± 4	—

Table 6.20: Numbers of observed events and predicted background events for each signal region. Uncertainties include statistical and systematic uncertainties together.

For each SR, one specific distribution is shown after applying the fit results: the m_{CT} distribution for SR1 in Fig. 6.20 and the $E_{\mathrm{T}}^{\mathrm{miss}}$ distributions for SR2 and SR3 in Figs. 6.21 and Fig. 6.22, respectively. In the 250-300 GeV range of the m_{CT} distribution for SR1 the down fluctuation of data events as mentioned above is visible. More distributions of kinematic variables for the signal regions are shown in Figs. 6.23 and 6.24. Also the various kinematic distributions for the observed data events and expected SM background contributions agree well within the estimated uncertainties.

19 The numbers for the multi-jet contribution are obtained from data via the jet-smearing method and are provided as input to the fit along with the MC simulation for the other backgrounds.

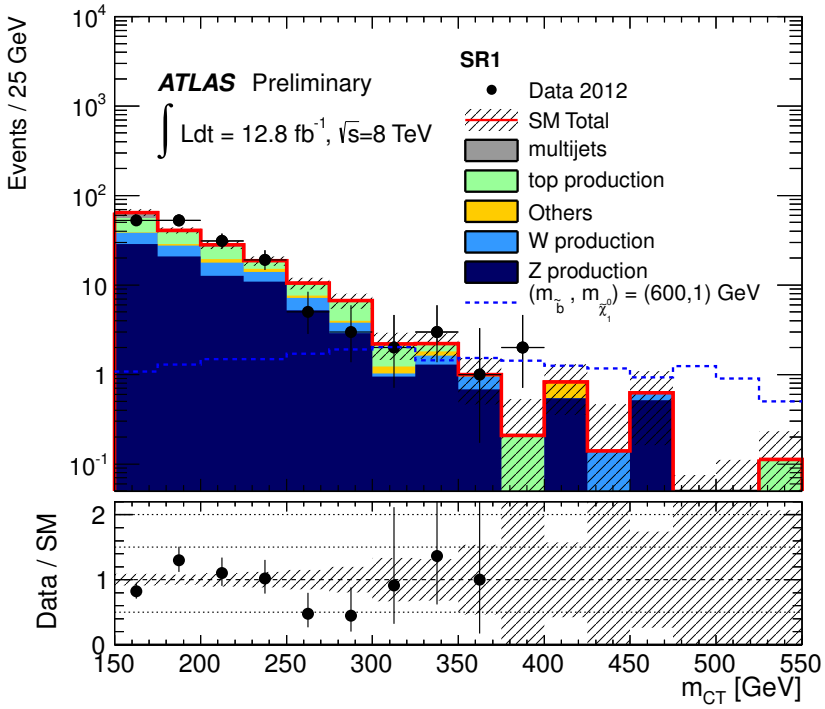

Figure 6.20: Distribution of m_{CT} for SR1 after the loosest selection on m_{CT} ($m_{\mathrm{CT}} > 150$ GeV). The shaded band includes both detector and theoretical systematic uncertainties. The backgrounds and uncertainties are normalised to the values determined by the fit. As reference, the distribution for the signal point at $m(\tilde{b}_1) = 600$ GeV and $m(\tilde{\chi}_1^0) = 1$ GeV is included.

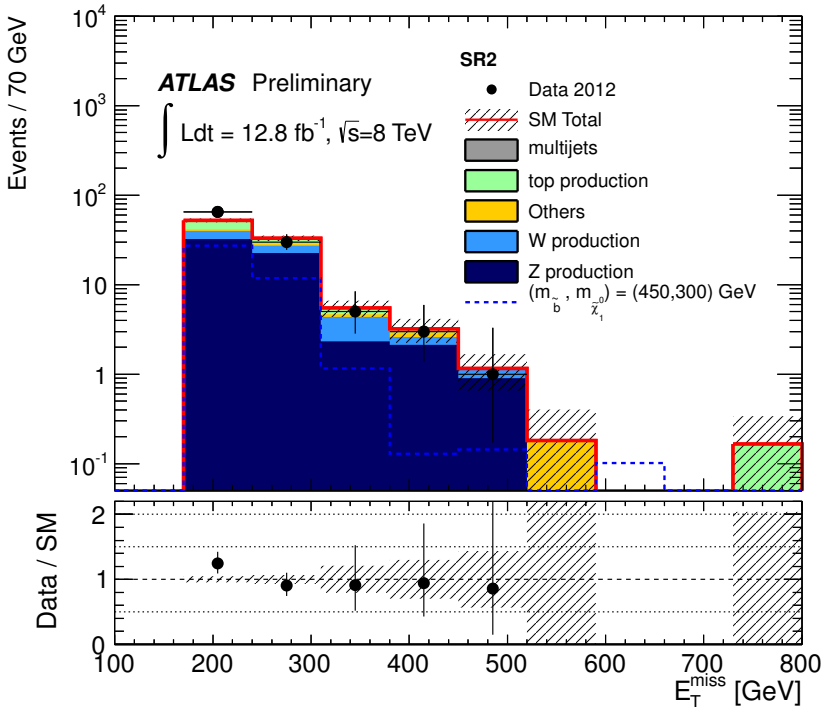

Figure 6.21: Distribution of $E_{\mathrm{T}}^{\mathrm{miss}}$ for SR2. The shaded band includes both detector and theoretical systematic uncertainties. The backgrounds and uncertainties are normalised to the values determined by the fit. As reference, the distribution for the signal point at $m(\tilde{b}_1) = 450$ GeV and $m(\tilde{\chi}_1^0) = 300$ GeV is included.

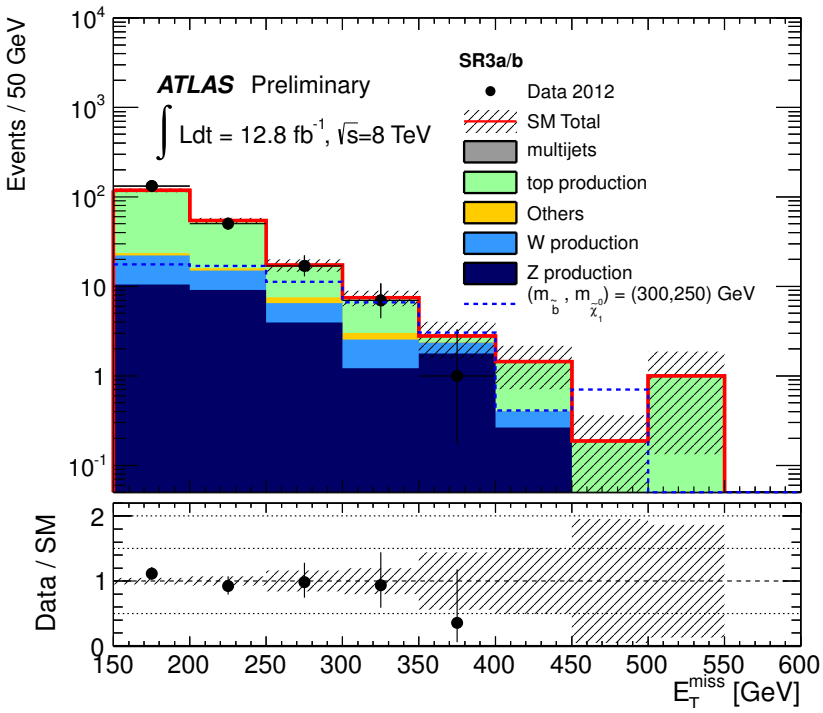

Figure 6.22: Distribution of $E_{\mathrm{T}}^{\mathrm{miss}}$ for SR3 (applying the looser selection of SR3a). The shaded band includes both detector and theoretical systematic uncertainties. The backgrounds and uncertainties are normalised to the values determined by the fit. As reference, the distribution for the signal point at $m(\tilde{b}_1) = 300$ GeV and $m(\tilde{\chi}_1^0) = 250$ GeV is included.

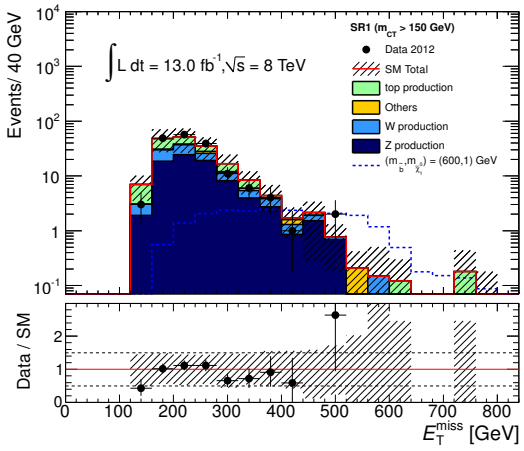

(a) SR1 ($m_{\mathrm{CT}} > 150$ GeV): $E_{\mathrm{T}}^{\mathrm{miss}}$

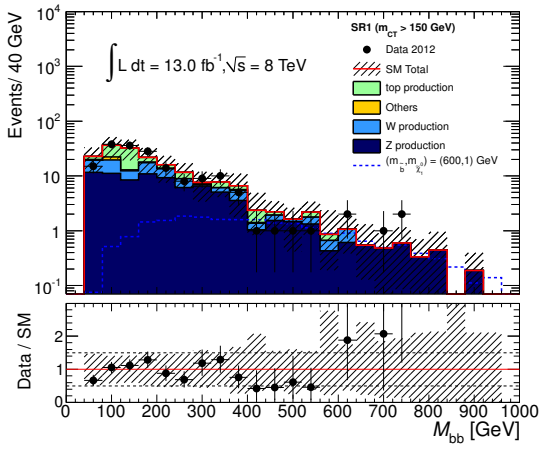

(b) SR1 ($m_{\mathrm{CT}} > 150$ GeV): m_{bb}

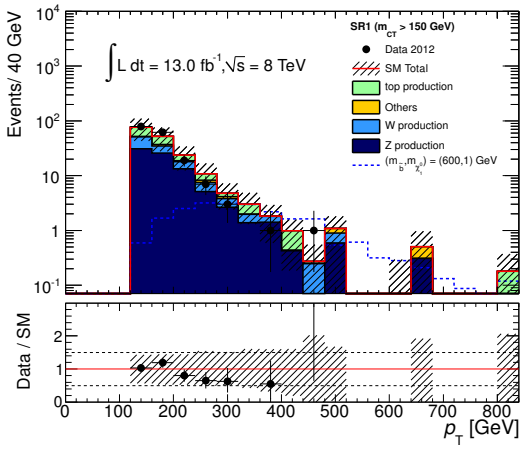

(c) SR1 ($m_{\mathrm{CT}} > 150$ GeV): $p_{\mathrm{T}}(\mathrm{jet}_1)$

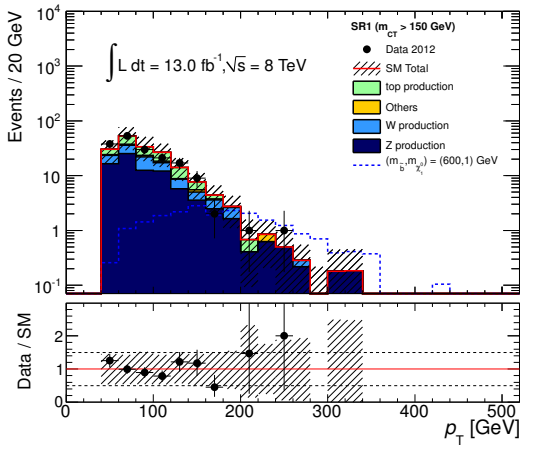

(d) SR1 ($m_{\mathrm{CT}} > 150$ GeV): $p_{\mathrm{T}}(\mathrm{jet}_2)$

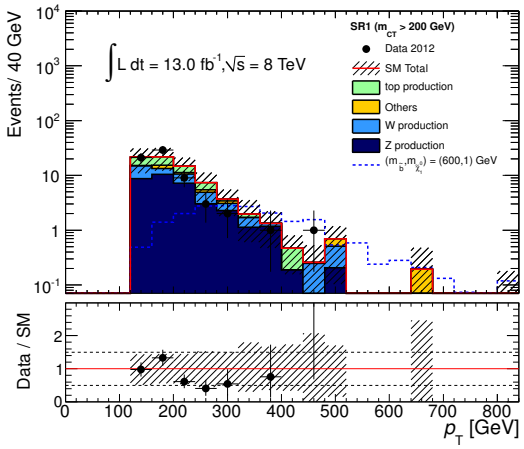

(e) SR1 ($m_{\mathrm{CT}} > 200$ GeV): $p_{\mathrm{T}}(\mathrm{jet}_1)$

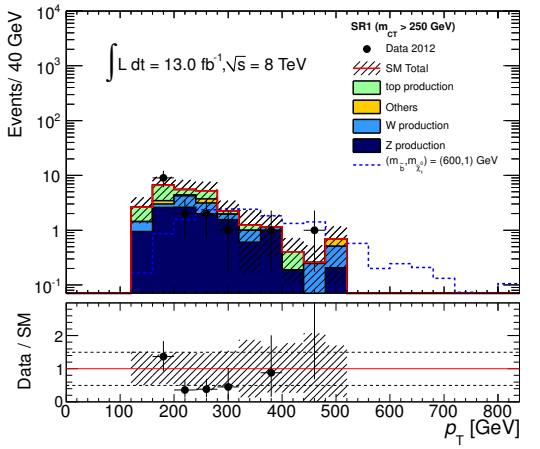

(f) SR1 ($m_{\mathrm{CT}} > 250$ GeV): $p_{\mathrm{T}}(\mathrm{jet}_1)$

Figure 6.23: Distributions of several kinematic distributions for SR1 ($E_{\mathrm{T}}^{\mathrm{miss}}$, m_{bb}, $p_{\mathrm{T}}(\mathrm{jet}_1)$, $p_{\mathrm{T}}(\mathrm{jet}_2)$ for $m_{\mathrm{CT}} > 150$ GeV and $p_{\mathrm{T}}(\mathrm{jet}_1)$ for $m_{\mathrm{CT}} > 200$, 250 GeV) without applying the fit results. The error bands include statistical and systematic uncertainties (without considering correlations). The distributions for the reference signal point associated with SR1 are also shown.

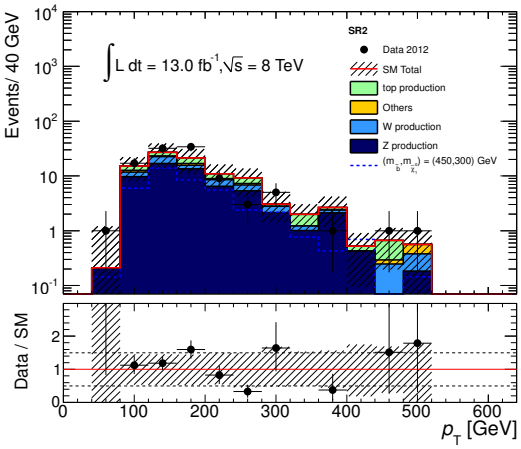

(a) SR2: $p_{\mathrm{T}}(\mathrm{jet}_1)$

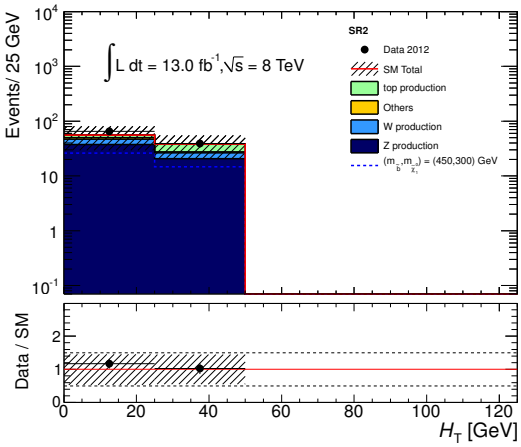

(b) SR2: $H_{\mathrm{T},2}$

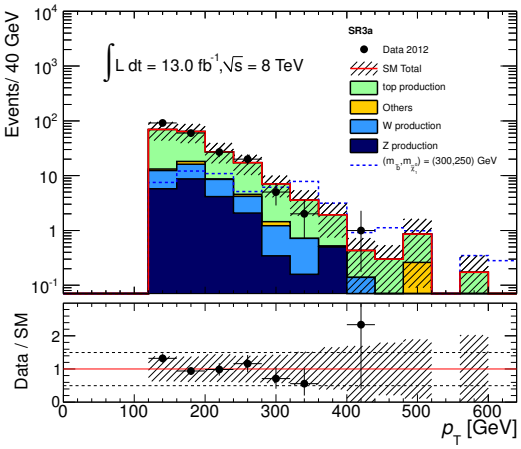

(c) SR3a: $p_{\mathrm{T}}(\mathrm{jet}_1)$

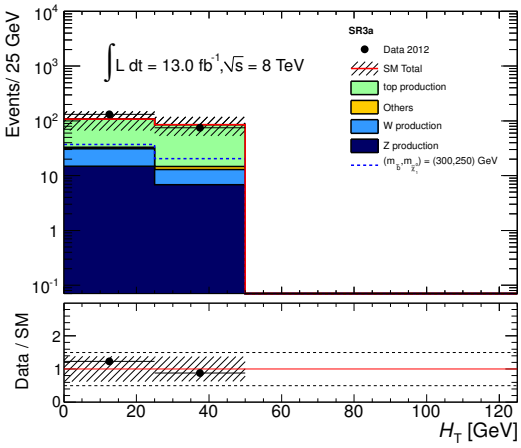

(d) SR3a: $H_{\mathrm{T},3}$

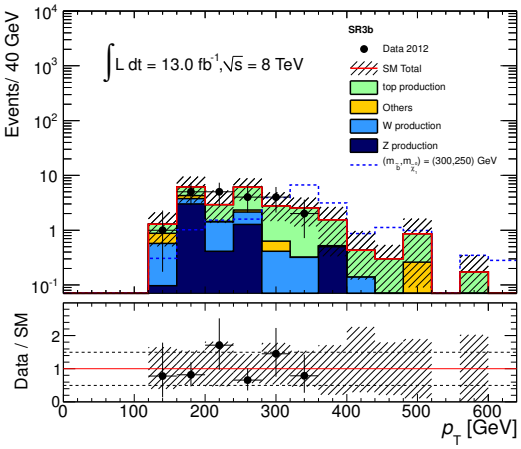

(e) SR3b: $p_{\mathrm{T}}(\mathrm{jet}_1)$

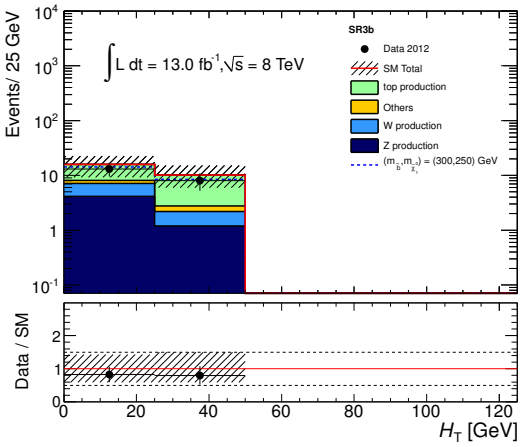

(f) SR3b: $H_{\mathrm{T},3}$

Figure 6.24: Distributions of $p_{\mathrm{T}}(\mathrm{jet}_1)$ and $H_{\mathrm{T},x}$ for SR2, SR3a and SR3b without applying the fit results. The error bands include statistical and systematic uncertainties (without considering correlations). The distributions for the reference signal points (associated to the respective SR) are also shown.

6.6 Interpretation of the Results

As discussed in the previous section, a good agreement between the SM expectation and data observation is found for all signal regions. This means that no evidence for a contribution of supersymmetric processes is observed. Nevertheless, the results contain valuable information allowing to set constraints on the expected signal contributions. Upper limits can be set on the allowed number of generic signal events and for the specific signal models considering $\tilde{b}_1\tilde{b}_1$ production where the sbottom decays via $\tilde{b}_1 \to b\tilde{\chi}_1^0$ with a 100% branching ratio.
The direct limits on the maximal number of allowed signal events and the corresponding visible cross-sections σ_{vis}, as defined in Section 5.8.3, are given for all signal regions in Table 6.21 together with the expected and observed event yields. These numbers can be used to test if a specific signal model is excluded in consideration of the efficiency and acceptance ($\sigma_{\text{vis}} = \sigma \cdot A \cdot \varepsilon$).

Signal region	SM total	Data	UL on BSM event yield		UL on σ_{vis} [fb]	
			expected	observed	expected	observed
SR1 ($m_{\text{CT}} > 150$ GeV)	176 ± 25	172	55	54	4.2	4.1
SR1 ($m_{\text{CT}} > 200$ GeV)	71 ± 11	66	25	22	1.9	1.7
SR1 ($m_{\text{CT}} > 250$ GeV)	25 ± 4	16	12.5	7.9	0.96	0.61
SR1 ($m_{\text{CT}} > 300$ GeV)	7.4 ± 1.7	8	7.5	8.0	0.58	0.62
SR2	95 ± 11	104	32	39	2.5	3.0
SR3a	203 ± 35	207	54	54	4.2	4.2
SR3b	27 ± 5	21	13.1	9.6	1.0	0.74

Table 6.21: Expected and observed event yields with the corresponding Upper Limits (UL) at 95% CL on generic beyond SM (BSM) signal yields and visible cross-sections σ_{vis} for all the signal regions defined. The uncertainties on the background event yields include statistical and systematic uncertainties.

Exclusion limits for the considered model ($\tilde{b}_1\tilde{b}_1$ production where $\tilde{b}_1 \to b\tilde{\chi}_1^0$ with a 100% branching ratio) are calculated in the sbottom-neutralino mass plane. The are presented in Fig. 6.25 for SR1 and Fig. 6.26 for SR2 and SR3. For SR1, the excluded parameter regions significantly extend the previous limit, set by the ATLAS experiment for 2.05 fb^{-1}, to scenarios with larger sbottom masses. However, this selection is not sensitive to the very compressed scenarios with a small neutralino-sbottom mass-splitting. This tendency is increased by the harsher m_{CT} thresholds of 250 GeV and 300 GeV which provide the best limits for large sbottom masses.[20] The SR2 selection covers a region of medium mass-splittings, as it was designed to. However, a similar region is also excluded by the SR1 selection with the loosest m_{CT} threshold ($m_{\text{CT}} > 150$ GeV). As expected, the SR3a and SR3b selections exclude regions for the compressed scenarios but have no sensitivity for the regions with large mass-splittings and sbottom masses. The harsher selection criteria applied for SR3b result in a larger uncertainty for the expected limit. However, the observed limit is slightly better than the one obtained with SR3a.

20 The small down fluctuation of the data events for the SR1 selection with $m_{\text{CT}} > 250$ GeV (see previous section) results in a better observed limit compared to the expected limit.

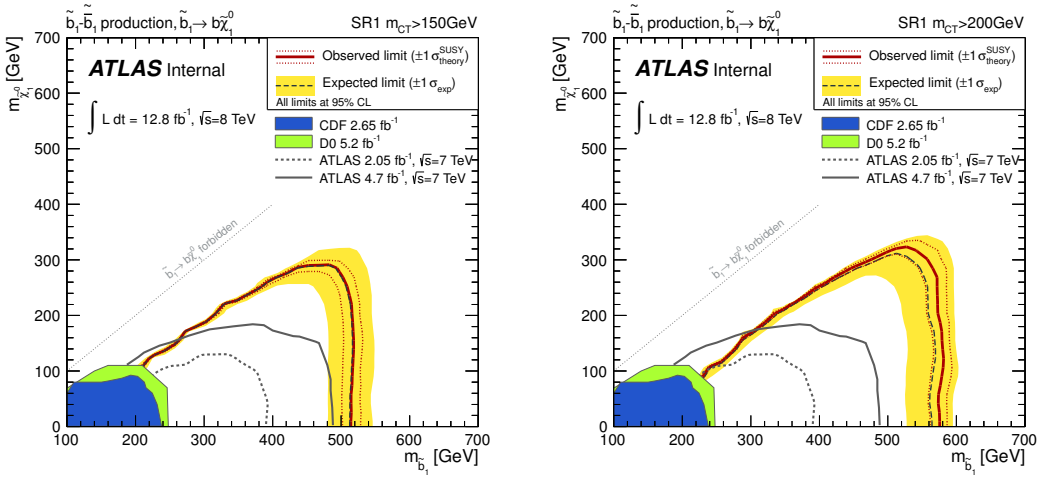

(a) $m_{\mathrm{CT}} > 150$ GeV

(b) $m_{\mathrm{CT}} > 200$ GeV

(c) $m_{\mathrm{CT}} > 250$ GeV

(d) $m_{\mathrm{CT}} > 300$ GeV

Figure 6.25: Exclusion limit at 95% CL in the sbottom-neutralino mass plane for SR1 applying the different m_{CT} thresholds. For each plot, the black, dashed line shows the expected limit if theory uncertainties on the signal are neglected. The yellow band corresponds to the ± 1 σ Gaussian equivalent uncertainty on the expected limit. The red solid line shows the nominal observed limit, while the red dashed line corresponds to its variation if theory uncertainties on the signal are taken into account. Previous limits set by the ATLAS [131, 132], CDF [150] and D0 [151] experiments are also shown.

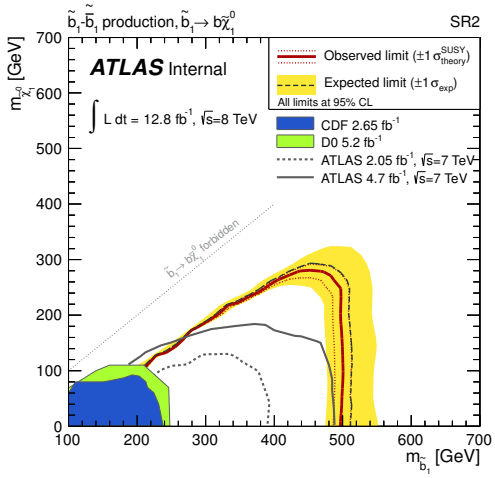

(a) SR2

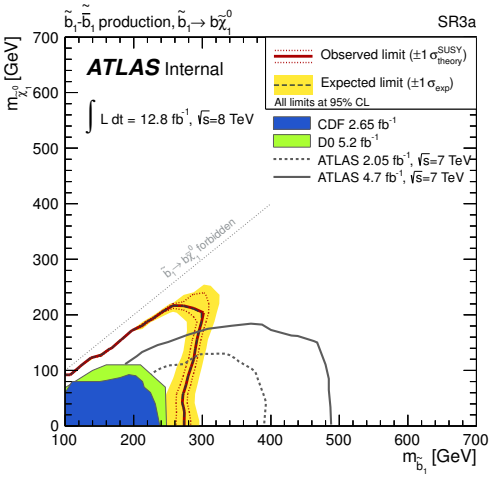

(b) SR3a

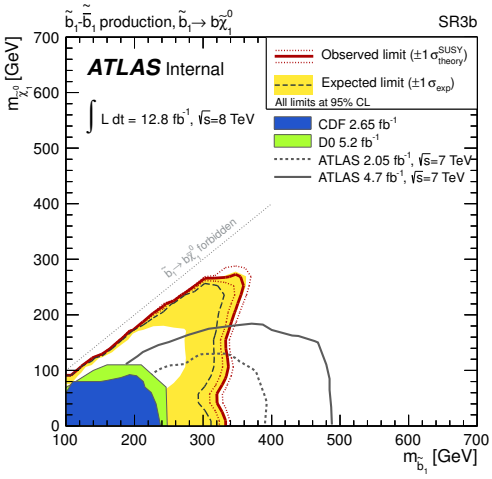

(c) SR3b

Figure 6.26: Exclusion limit at 95% CL in the sbottom-neutralino mass plane for SR2, SR3a and SR3b. For each plot, the black, dashed line shows the expected limit if theory uncertainties on the signal are neglected. The yellow band corresponds to the ± 1 σ Gaussian equivalent uncertainty on the expected limit. The red solid line shows the nominal observed limit, while the red dashed line corresponds to its variation if theory uncertainties on the signal are taken into account. Previous limits set by the ATLAS [131, 132], CDF [150] and D0 [151] experiments are also shown.

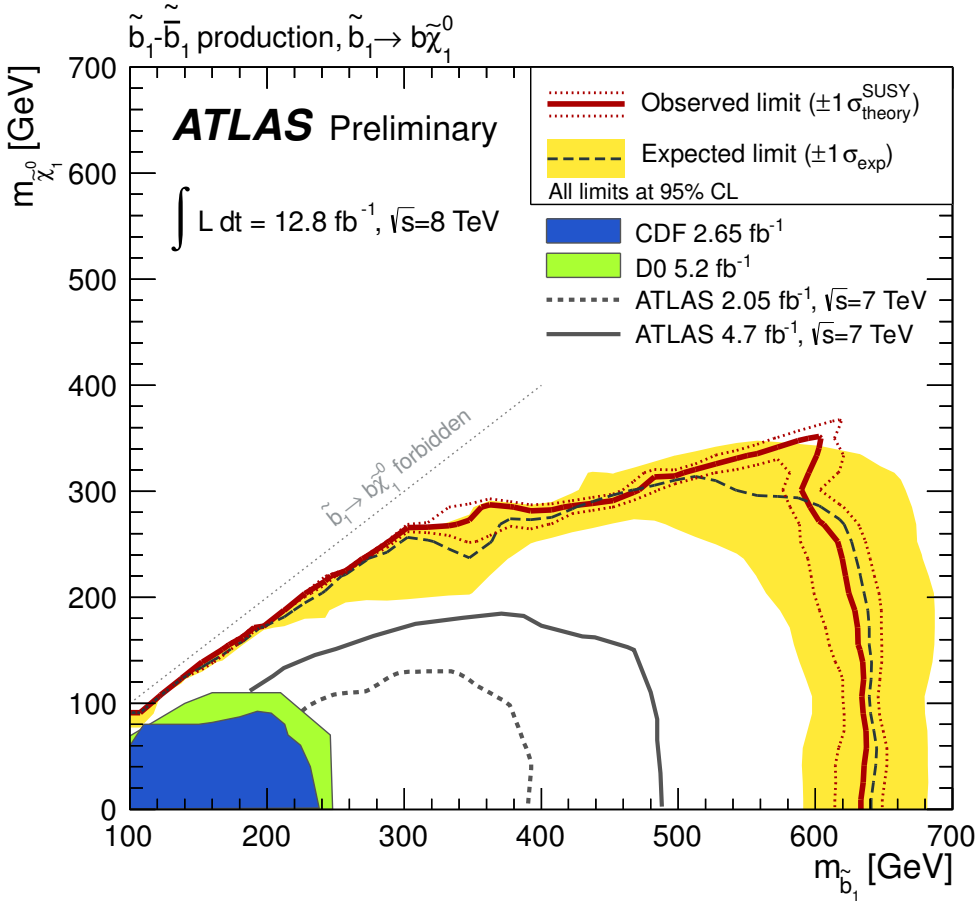

Figure 6.27: Exclusion limit at 95% CL in the sbottom-neutralino mass plane, obtained by taking the signal region which gives the best expected exclusion limit in each point. The black, dashed line with yellow band shows the expected limit with its $\pm 1\ \sigma$ Gaussian equivalent uncertainty, if theory uncertainties on the signal are neglected. The red solid line shows the nominal observed limit, while the red dashed lines correspond to its variation if theory uncertainties on the signal are taken into account. Previous limits set by the ATLAS [131, 132], CDF [150] and D0 [151] experiments are also included.

The final exclusion limit is obtained from the combination of all signal regions by selecting the one giving the best expected exclusion limit for each signal point separately.[21] It is shown in Fig. 6.27. A significant extension compared to the previous limits set by the ATLAS, D0 and CDF experiments is achieved. Due to the complementary structure of the signal regions, the limit is extended both to larger sbottom masses (SR1) and compressed scenarios (SR3). Sbottom masses up to 620 GeV are excluded at 95% CL for massless neutralinos and neutralino masses up to 320 GeV are excluded for sbottom masses around 550 GeV. Mass differences between the sbottom and neutralino above 40 GeV are excluded for $m_{\tilde{\chi}_1^0} < 300$ GeV. A gain of about 50 GeV to 100 GeV compared to the results obtained in summer 2012 [132] is reached.

21 The definition of SR3 is orthogonal to SR1 and SR2. Therefore, a statistical combination of SR1 with SR3 and SR2 with SR3 is in principle possible. However, the gain compared to considering the signal regions standalone is expected to be small as SR3 is only contributing for very small mass-splittings in which case neither SR1 nor SR2 provide a significant sensitivity.

The signal region giving the best expected exclusion limit for each considered signal point is shown in Fig. 6.28a. A difference compared to the expectations presented in the selection optimisation study (see Section 6.2.4, Fig. 6.7) is observed. The optimal selection for large mass-splittings is still SR1 and points with $\Delta m \leq 40$ GeV are dominated by SR3, but for medium mass-splittings a large contribution comes from SR1 with a moderate m_{CT} threshold, while SR2 hardly contributes. The differences may be caused by changes in the systematic uncertainties and it should be kept in mind, that the optimisation study was performed with a lower integrated luminosity and centre-of-mass energy. The CLs values obtained for each signal point are mapped in Fig. 6.28b.

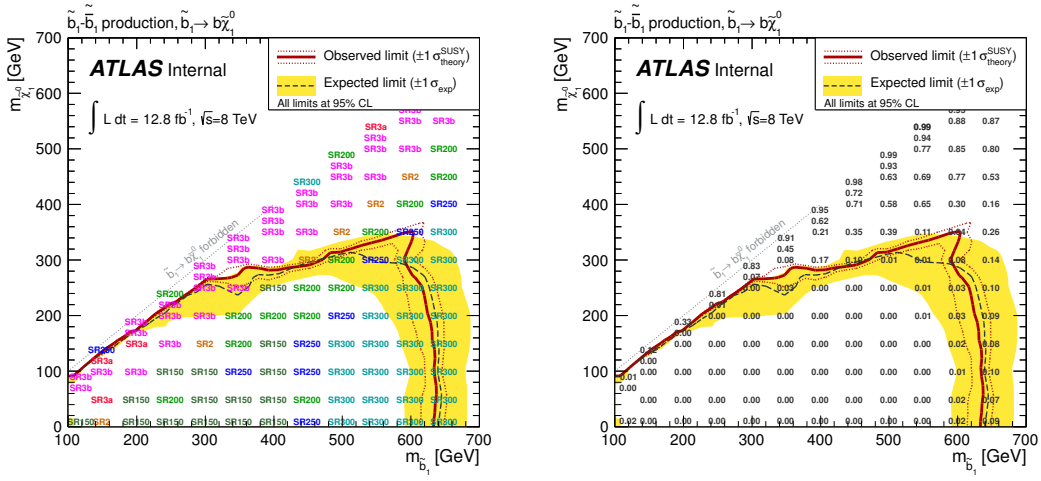

(a) Best signal region

(b) CLs values

Figure 6.28: Selected signal region per point (a) and observed CLs values using the nominal signal cross-sections (b). The signal regions denoted by SR150, SR200, SR250 and SR300 correspond to SR1 with the respective m_{CT} threshold. The bottom line of entries is moved up by 10 GeV, while the leftmost column is shifted to the right by 20 GeV to provide a better visibility in both figures.

6.7 Re-interpreting the Sbottom Results on Stop Models

In natural SUSY scenarios, the lightest neutralino and chargino are almost pure higgsinos and therefore nearly degenerate in mass. Therefore, the analysis described in this chapter can be sensitive also to direct stop-pair production, when the stop decays via:

$$\tilde{t}_1 \to b\tilde{\chi}_1^{\pm}, \tag{6.3}$$

$$\tilde{\chi}_1^{\pm} \to W^*\tilde{\chi}_1^0 \to f f'\tilde{\chi}_1^0, \tag{6.4}$$

where f and f' correspond to fermions produced by the W^* decay. In fact, if the chargino-neutralino mass splitting ($\Delta m(\tilde{\chi}_1^{\pm},\tilde{\chi}_1^0) = m_{\tilde{\chi}_1^{\pm}} - m_{\tilde{\chi}_1^0}$) is small, the W^* is very soft and its decay products might not be reconstructed. The final state signature is therefore identical to the signature investigated so far for the sbottom-pair production. A drop in the selection efficiencies is expected for larger $\Delta m(\tilde{\chi}_1^{\pm},\tilde{\chi}_1^0)$ values, when the fermions start to pass the reconstruction thresholds.

Two sets of stop samples are produced, one with $\Delta m(\tilde{\chi}_1^{\pm},\tilde{\chi}_1^0) = 5$ GeV and one with $\Delta m(\tilde{\chi}_1^{\pm},\tilde{\chi}_1^0) = 20$ GeV. A few signal points with $\Delta m(\tilde{\chi}_1^{\pm},\tilde{\chi}_1^0) = 10$ GeV are added to study the selection efficiencies at intermediate scenarios. No signal points are produced for $m_{\tilde{\chi}_1^{\pm}} < 100$ GeV, since chargino masses up to 103.5 GeV are excluded by LEP [152].
The samples are generated with MADGRAPH interfaced to PYTHIA and the CTEQ6L1 PDF set is used. The cross-sections are the same as the ones for corresponding sbottom signal points with $m_{\tilde{t}_1} = m_{\tilde{b}_1}$ (see Ref. [143]) and the same theory uncertainties are assumed. The fast simulation ATLFAST-II is used and at least 10000 events are generated per signal point (∼100000 events for $m_{\tilde{t}_1} \leq 300$ GeV, ∼30000 events for $m_{\tilde{t}_1} = 450$ GeV and ∼15000 events for $m_{\tilde{t}_1} = 600$ GeV).
A comparison of the stop and sbottom signal samples is provided in Section 6.7.1 and the new interpretation of the sbottom results for the stop models are presented in Section 6.7.2.

6.7.1 Comparison of the Stop and Sbottom Signals

Differences between the sbottom and stop results are expected for the selection acceptances. In particular, the veto on leptons and additional jets can be affected by the additional fermions produced in the stop decays.
The selection efficiencies for SR1 are compared for three stop signal points ($\Delta m(\tilde{\chi}_1^{\pm},\tilde{\chi}_1^0) = 5, 10, 20$ GeV) and the corresponding sbottom signal point ($m_{\tilde{t}_1} = m_{\tilde{b}_1} = 500$ GeV, $m_{\tilde{\chi}_1^0} = 300$ GeV) in Table 6.22. The efficiency for the lepton veto is decreasing for the stop models with increasing $\Delta m(\tilde{\chi}_1^{\pm},\tilde{\chi}_1^0)$, as expected. In addition, a drop in efficiency is observed for the harsh m_{CT} thresholds. In contrast, the veto on a third jet with $p_{\mathrm{T}} > 50$ GeV, as well as all other selection steps, have a similar selection efficiency for all samples. The p_{T} distribution and the number of leptons are shown for the signal points mentioned above in Fig. 6.29.
The $H_{\mathrm{T},x}$ distributions for $\tilde{t}_1\tilde{t}_1$ and $\tilde{b}_1\tilde{b}_1$ production are shown in Fig. 6.30 for SR2 and SR3. The $\Delta m(\tilde{\chi}_1^{\pm},\tilde{\chi}_1^0) = 5$ GeV and 20 GeV stop signals are compared to the sbottom signal for $m_{\tilde{t}_1} = m_{\tilde{b}_1} = 600$ GeV, $m_{\tilde{\chi}_1^0} = 100$ GeV for SR2 and $m_{\tilde{t}_1} = m_{\tilde{b}_1} = 500$ GeV, $m_{\tilde{\chi}_1^0} = 450$ GeV for SR3. A difference in the shape is visible, but the impact on the selection efficiency is small for $\Delta m(\tilde{\chi}_1^{\pm},\tilde{\chi}_1^0) = 5$ GeV (within a few percent), while efficiency drops up to 50% are found for larger $\Delta m(\tilde{\chi}_1^{\pm},\tilde{\chi}_1^0)$.

6.7.2 Interpretation for Stop Models

Exclusion limits for the stop signal models are derived in the stop-neutralino mass plane. They are shown in Fig. 6.31 for the two considered scenarios with $\Delta m(\tilde{\chi}_1^{\pm},\tilde{\chi}_1^0) = 5$ GeV and $\Delta m(\tilde{\chi}_1^{\pm},\tilde{\chi}_1^0) = 20$ GeV. For each signal point, the selection which provides the best expected sensitivity is chosen. In case of the scenario with $\Delta m(\tilde{\chi}_1^{\pm},\tilde{\chi}_1^0) = 5$ GeV, stop masses up to 580 GeV are excluded at 95% CL for $m_{\tilde{\chi}_1^0} = 100$ GeV and neutralino masses up to 300 GeV are excluded for $m_{\tilde{t}_1} = 500$ GeV. The sensitivity is reduced for the very compressed scenarios with a small neutralino-stop mass-splitting. As expected, a smaller region in the ($m_{\tilde{t}_1}$-$m_{\tilde{\chi}_1^0}$) plane is excluded for $\Delta m(\tilde{\chi}_1^{\pm},\tilde{\chi}_1^0) = 20$ GeV. In this case, the limit on the stop mass is lowered to 480 GeV for $m_{\tilde{\chi}_1^0} = 100$ GeV and the neutralino mass limit to 250 GeV for $m_{\tilde{t}_1} = 480$ GeV. In addition, the observed upper limits on the signal cross-sections are given in Fig. 6.32 for all signal points considered.
A summary of the sbottom and stop exclusion limits is shown in Fig. 6.33. Only a slight degradation of the stop limits compared to the corresponding sbottom limits is observed for the scenario with $\Delta m(\tilde{\chi}_1^{\pm},\tilde{\chi}_1^0) = 5$ GeV, while a significant reduction of the excluded region is visible for the scenario with $\Delta m(\tilde{\chi}_1^{\pm},\tilde{\chi}_1^0) = 20$ GeV.

Selection	Sbottom		Stop, $\Delta m(\tilde{\chi}_1^{\pm},\tilde{\chi}_1^0)$ =					
			5 GeV		10 GeV		20 GeV	
	rel.	abs.	rel.	abs.	rel.	abs.	rel.	abs.
Preselection	91%	91%	89%	89%	87%	87%	86%	86%
e/μ veto	99%	90%	98%	87%	94%	82%	84%	72%
$E_{\mathrm{T}}^{\mathrm{miss}}$ >150	77%	70%	75%	66%	74%	60%	71%	51%
$\geq$2 jets	99%	69%	99%	65%	100%	60%	100%	51%
$p_T(\mathrm{jet}_1) > 130$ GeV	85%	59%	83%	54%	84%	50%	82%	42%
$p_T(\mathrm{jet}_2) > 50$ GeV	91%	53%	92%	50%	91%	46%	90%	38%
third jet veto	48%	26%	47%	23%	48%	22%	45%	17%
$\Delta\phi_{\mathrm{min}} > 0.4$	89%	23%	89%	21%	88%	19%	84%	14%
$E_{\mathrm{T}}^{\mathrm{miss}}/m_{\mathrm{eff}} > 0.25$	97%	22%	98%	20%	98%	19%	98%	14%
b-tagging	35%	7.6%	33%	6.7%	34%	6.4%	33%	4.5%
$m_{\mathrm{CT}} > 100$ GeV	94%	7.2%	93%	6.2%	94%	6.0%	96%	4.3%
$m_{\mathrm{CT}} > 150$ GeV	85%	6.1%	84%	5.2%	81%	4.9%	79%	3.4%
$m_{\mathrm{CT}} > 200$ GeV	66%	4.0%	62%	3.2%	58%	2.8%	56%	1.9%
$m_{\mathrm{CT}} > 250$ GeV	38%	1.5%	37%	1.2%	30%	0.9%	29%	0.6%

Table 6.22: Relative and absolute selection efficiencies for SR1 evaluated for a sbottom signal point ($m_{\tilde{b}_1}$ = 500 GeV, $m_{\tilde{\chi}_1^0}$ = 300 GeV), and three stop signal points with $\Delta m(\tilde{\chi}_1^{\pm},\tilde{\chi}_1^0)$ = 5 GeV, 10 GeV and 20 GeV ($m_{\tilde{t}_1}$ = 500 GeV, $m_{\tilde{\chi}_1^0}$ = 300 GeV). The relative efficiencies (rel.) are computed with respect to the previous selection step, while the absolute efficiencies (abs.) are calculated with respect to the initial number of events.

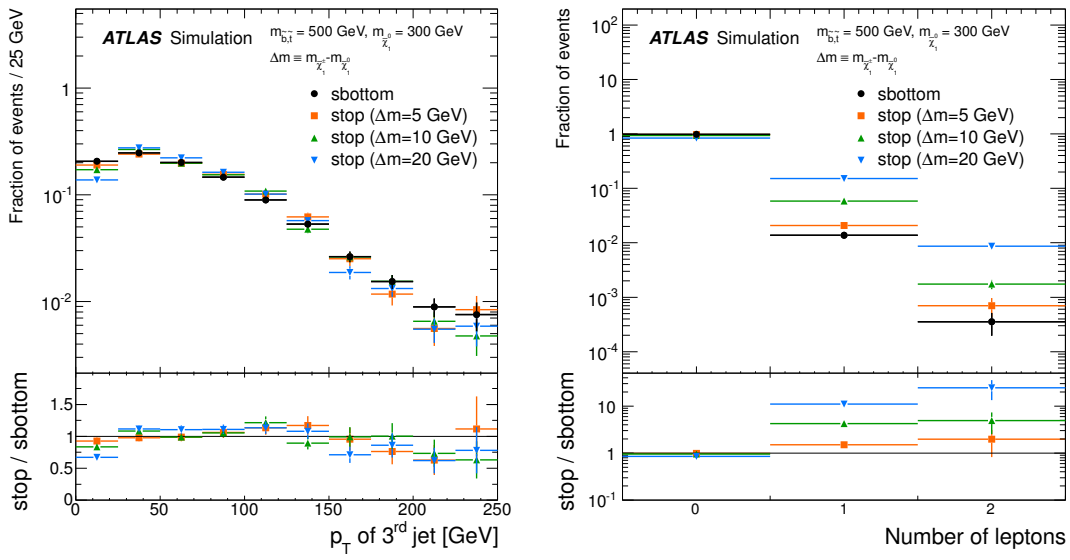

(a) $p_{\mathrm{T}}(\mathrm{jet}_3)$ **(b)** Number of leptons (e/μ)

Figure 6.29: Distributions of (a) $p_{\mathrm{T}}(\mathrm{jet}_3)$ and (b) the number of leptons for the sbottom sample and the stop samples with $\Delta m(\tilde{\chi}_1^{\pm},\tilde{\chi}_1^0) = 5$ GeV, 10 GeV and 20 GeV for signal points with $m_{\tilde{b}_1/\tilde{t}_1} = 500$ GeV and $m_{\tilde{\chi}_1^0} = 300$ GeV for SR1. The distributions are normalised to unit area and the overflow is included in the last bin. The ratios, shown in the lower panels, are obtained by dividing the distributions for the stop samples by the distributions for the sbottom sample. The error bars correspond to the statistical uncertainties of the signal samples. The distribution of the p_{T} of the third leading jet is shown before applying the veto on the third jet and the distribution of the number of leptons is shown after applying the preselection.

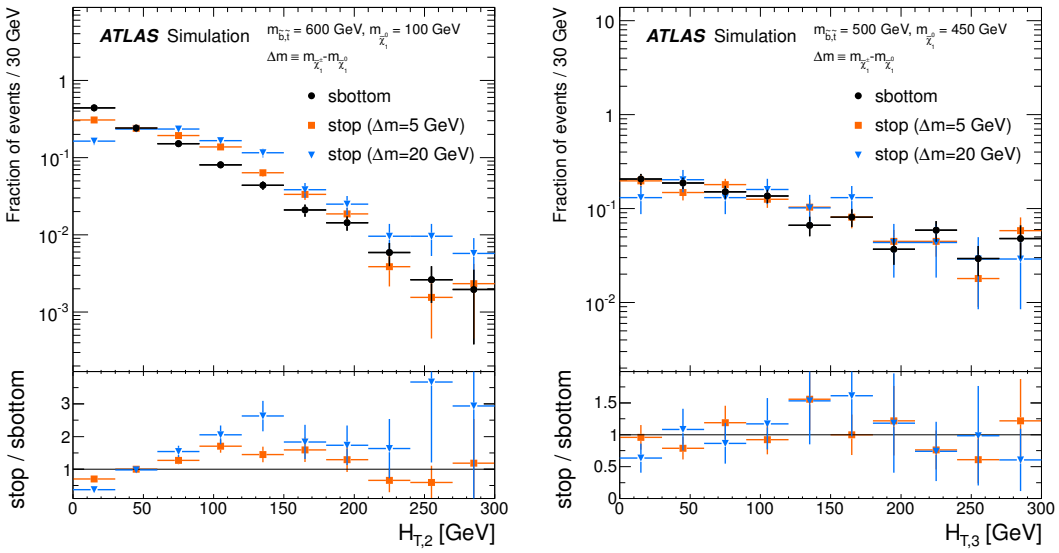

(a) SR2: $H_{\mathrm{T},2}$ **(b)** SR3: $H_{\mathrm{T},3}$

Figure 6.30: Distributions of $H_{\mathrm{T},x}$ for the sbottom sample and the stop samples with $\Delta m(\tilde{\chi}_1^{\pm},\tilde{\chi}_1^0) = 5$ GeV and 20 GeV for (a) SR2 ($m_{\tilde{b}_1/\tilde{t}_1} = 600$ GeV, $m_{\tilde{\chi}_1^0} = 100$ GeV) and (b) SR3 ($m_{\tilde{b}_1/\tilde{t}_1} = 500$ GeV, $m_{\tilde{\chi}_1^0} = 450$ GeV). The distributions are shown before applying the $H_{\mathrm{T},x}$ thresholds. They are normalised to unit area and the overflow is included in the last bin. The ratios, shown in the lower panels, are obtained by dividing the distributions for the stop samples by the distributions for the sbottom sample. The error bars correspond to the statistical uncertainties of the signal samples.

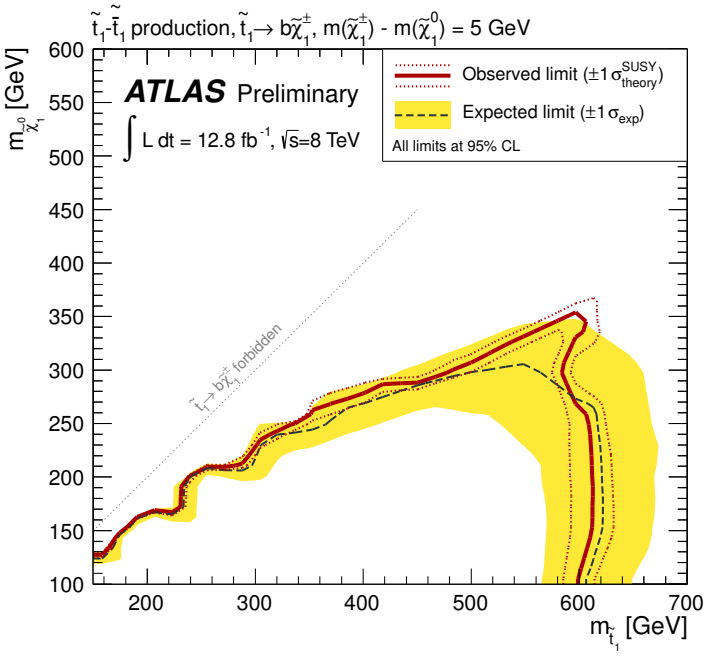

(a) $\Delta m(\tilde{\chi}_1^{\pm},\tilde{\chi}_1^0) = 5$ GeV

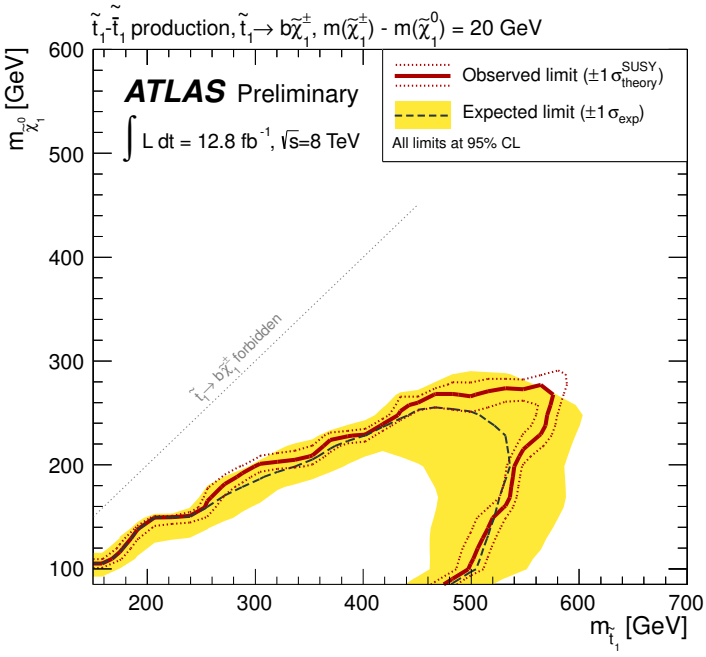

(b) $\Delta m(\tilde{\chi}_1^{\pm},\tilde{\chi}_1^0) = 20$ GeV

Figure 6.31: Expected and observed 95% CL exclusion limits in the stop-neutralino mass plane for stop models with (a) $\Delta m(\tilde{\chi}_1^{\pm},\tilde{\chi}_1^0) = 5$ GeV and (b) $\Delta m(\tilde{\chi}_1^{\pm},\tilde{\chi}_1^0) = 20$ GeV. The black, dashed lines with yellow bands show the expected limits with their ± 1 σ Gaussian equivalent uncertainty, if theory uncertainties on the signal are neglected. The red solid lines show the nominal observed limits, while the red dashed lines correspond to their variations if theory uncertainties on the signal are taken into account.

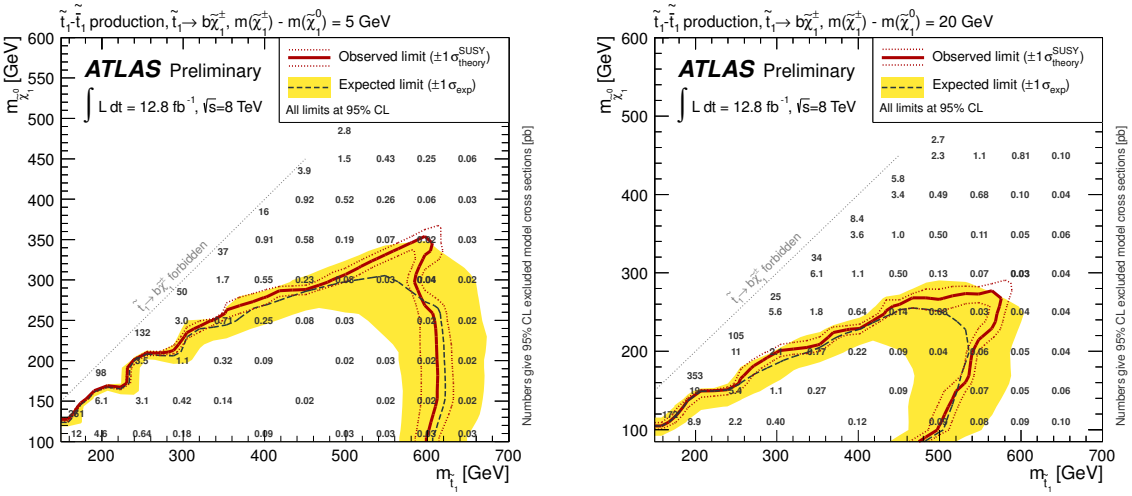

(a) $\Delta m(\tilde{\chi}_1^\pm, \tilde{\chi}_1^0) = 5$ GeV **(b)** $\Delta m(\tilde{\chi}_1^\pm, \tilde{\chi}_1^0) = 20$ GeV

Figure 6.32: Observed upper limits on the signal cross-sections for (a) $\Delta m(\tilde{\chi}_1^\pm, \tilde{\chi}_1^0) = 5$ GeV and (b) $\Delta m(\tilde{\chi}_1^\pm, \tilde{\chi}_1^0) = 20$ GeV in the $(m_{\tilde{t}_1}\text{-}m_{\tilde{\chi}_1^0})$ plane, for all signal points considered. The numbers are given in pb and are overlaid to the corresponding exclusion limits (see Fig. 6.31). For clarity, numbers of the first column (bottom row) are shifted to the right (upwards, only for $\Delta m(\tilde{\chi}_1^\pm, \tilde{\chi}_1^0) = 5$ GeV) by 10 GeV.

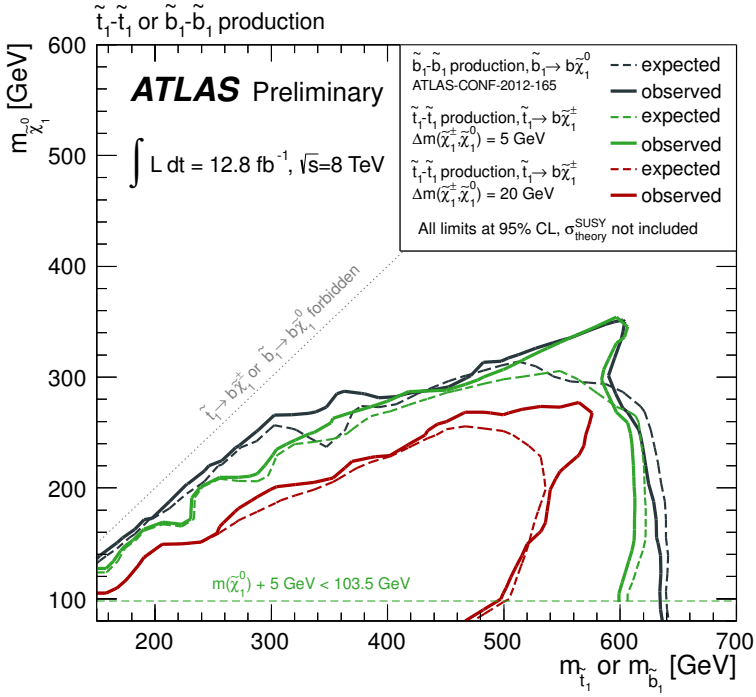

Figure 6.33: Expected and observed 95% CL exclusion limits on sbottom-pair production in the $(m_{\tilde{b}_1}\text{-}m_{\tilde{\chi}_1^0})$ plane, together with the expected and observed 95% CL exclusion limits for stop-pair production in the $(m_{\tilde{t}_1}\text{-}m_{\tilde{\chi}_1^0})$ plane for $\Delta m = 5$ GeV and 20 GeV. The theory uncertainty on the signal is not shown.

6.8 Summary

A search for pair-produced sbottom quarks is presented in this chapter. It is assumed that both sbottom quarks decay directly to a neutralino and a b-quark, leading to a final state with two b-jets and $E_{\mathrm{T}}^{\mathrm{miss}}$. Three signal regions, adapted to small, medium and large sbottom-neutralino mass-splitting scenarios, are exploited.
The results, obtained with the $\sqrt{s} = 8$ TeV dataset for an integrated luminosity of 12.8 fb^{-1}, are presented and no evidence for pair-produced sbottom quarks is found. The background contributions, estimated with a combined fit of control regions, are in good agreement with the observed data yields in all signal regions. Exclusion limits are calculated in the sbottom-neutralino mass plane for the sbottom SUSY models ($\tilde{b}_1\tilde{b}_1$ production where $\tilde{b}_1 \to b\tilde{\chi}_1^0$ with a 100% branching ratio). The following mass constraints are derived at 95% CL:

- $m_{\tilde{b}_1} > 620$ GeV for $m_{\tilde{\chi}_1^0} \simeq 0$
- $m_{\tilde{\chi}_1^0} > 320$ GeV for $m_{\tilde{b}_1} \simeq 550$ GeV
- $\Delta m(\tilde{b}_1, \tilde{\chi}_1^0) < 40$ GeV for $m_{\tilde{\chi}_1^0} < 300$ GeV.

The assumption on the 100% branching ratio for the $\tilde{b}_1 \to b\tilde{\chi}_1^0$ decay is justified for SUSY scenarios where the $\tilde{b}_1 \to t\tilde{\chi}_1^\pm$ decay is suppressed, as for example if $m_{\tilde{b}_1} < m_{\tilde{\chi}_1^\pm} + m_t$ or if the $\tilde{b}_1$ is mostly $\tilde{b}_R$ and the chargino is wino dominated.

The results are re-interpreted in stop models with a similar event topology ($\tilde{t}_1\tilde{t}_1$ production with $\tilde{t}_1 \to b\tilde{\chi}_1^\pm \to bW^*\tilde{\chi}_1^0 \to bff'\tilde{\chi}_1^0$ for small $\Delta m(\tilde{\chi}_1^\pm,\tilde{\chi}_1^0)$, such that the fermionic decay products are not reconstructed). The model assumptions are justified for scenarios where the higgsino mass parameter μ is small compared to the bino and wino mass parameters M_1 and M_2. In this case, the $\tilde{\chi}_1^0$ and $\tilde{\chi}_1^\pm$ masses are almost degenerate and both of the order of μ. Scenarios of this type are favoured by naturalness arguments (see Section 2.2). The mass limits depend strongly on the value of $\Delta m(\tilde{\chi}_1^\pm,\tilde{\chi}_1^0)$ and the following results are obtained at 95% CL:

- $\Delta m(\tilde{\chi}_1^\pm,\tilde{\chi}_1^0) = 5$ GeV:
  - $m_{\tilde{t}_1} > 580$ GeV for $m_{\tilde{\chi}_1^0} \simeq 100$ GeV
  - $m_{\tilde{\chi}_1^0} > 300$ GeV for $m_{\tilde{t}_1} \simeq 500$ GeV
- $\Delta m(\tilde{\chi}_1^\pm,\tilde{\chi}_1^0) = 20$ GeV:
  - $m_{\tilde{t}_1} > 480$ GeV for $m_{\tilde{\chi}_1^0} \simeq 100$ GeV
  - $m_{\tilde{\chi}_1^0} > 250$ GeV for $m_{\tilde{t}_1} \simeq 480$ GeV.

The exclusion limits obtained by this analysis provide a significant contribution to the stop searches by the ATLAS collaboration. A summary of ATLAS searches for stop-pair production with 4.7 fb^{-1} of $\sqrt{s} = 7$ TeV or 13 fb^{-1} of $\sqrt{s} = 8$ TeV data is shown in Fig. 6.34. The analysis performed in this thesis covers a large region of the parameter space for large stop masses (excluded region shown in mint green). However, it should be stressed, that the limit is only valid for a small chargino-neutralino mass-splitting ($\Delta m(\tilde{\chi}_1^\pm,\tilde{\chi}_1^0) = 5$ GeV).

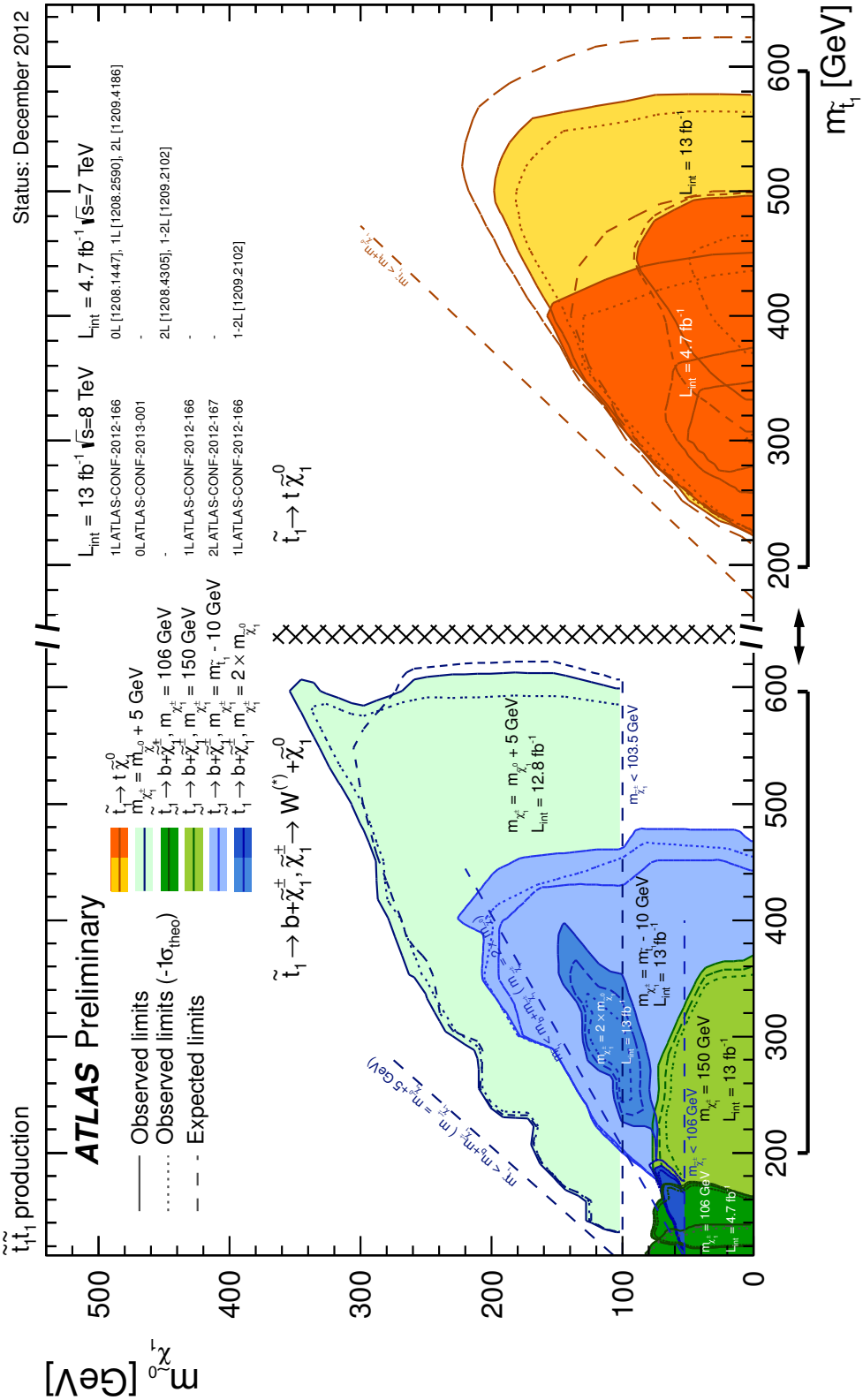

Figure 6.34: Summary on exclusion limits for direct stop-pair production by the ATLAS collaboration [124]. The limits are shown at 95% CL in the stop-neutralino mass plane for different search channels. For each search channel, the expected (dashed), observed (solid) and observed with 1σ down fluctuation of the signal cross-sections (dotted) limits are shown. The underlying SUSY models are summarised in the legend. Two main decay modes for the stop are considered: the direct decay to the neutralino ($\tilde{t}_1 \to t + \tilde{\chi}_1^0$) on the right and a decay via a chargino ($\tilde{t}_1 \to b\tilde{\chi}_1^\pm$ with $\tilde{\chi}_1^\pm \to W^{(*)}\tilde{\chi}_1^0$) on the left. The limit observed by the analysis presented in this chapter is shown in mint green for $\Delta m(\tilde{\chi}_1^\pm, \tilde{\chi}_1^0) = 5$ GeV.

CHAPTER 7

Searches for Gluino-Mediated Sbottom Production

Besides the direct production, sbottom quarks can also be produced in the decay chains of primary produced gluinos. Also for the gluino-mediated sbottom production, a 100% branching ratio is assumed for the $\tilde{b}_1 \to b\tilde{\chi}_1^0$ decay. Therefore, the topologies of the gluino-mediated and direct production have similar final states with b-jets, $E_{\mathrm{T}}^{\mathrm{miss}}$ and no leptons.
First results for SUSY searches with b-jets were published with the 2010 dataset [153]. A generic event selection with at least one b-jet, $\geq$ 2 additional jets, moderate $E_{\mathrm{T}}^{\mathrm{miss}}$ ($E_{\mathrm{T}}^{\mathrm{miss}} > 100$ GeV) and a harsh M_{eff} threshold ($M_{\mathrm{eff}} > 600$ GeV) was used to exclude models with $\tilde{g}\tilde{g}$ production where the gluinos decay via $\tilde{g} \to b\tilde{b}_1$ and a corresponding fraction of events with direct $\tilde{b}_1\tilde{b}_1$ production.[1] The analysis was first updated using data from the 2011 dataset corresponding to an integrated luminosity of 0.83 fb^{-1} [154], where the number of signal region selections was increased to four (with either ≥ 1 or ≥ 2 b-jets and $M_{\mathrm{eff}} > 500$ GeV or 700 GeV). Another update using data corresponding to an integrated luminosity of 2.05 fb^{-1} was performed at the end of 2011 [155]. All non-QCD background predictions were previously taken from MC and a data-driven $t\bar{t}$ estimation was added for this update. Main contributions within this thesis were made for the background estimation, in particular the validation of the background estimation via an alternative method. More details and results for this analysis are presented in Section 7.1.
A general revision of the gluino-mediated sbottom production was performed for the full 2011 dataset [156], corresponding to an integrated luminosity of 4.7 fb^{-1}. A combined analysis was designed to cover also the gluino-mediated stop production, which was previously considered in a separate one-lepton analysis [153, 155, 157]. It was found, that also the stop production channel can be covered by a no-lepton analysis, if a high jet multiplicity is required. In addition, the re-optimisation of the signal regions led to selections with at least three b-jets. The gluino-mediated three b-jets analysis was updated using data corresponding to an integrated luminosity of 12.8 fb^{-1} from the 2012 dataset, collected at $\sqrt{s} = 8$ TeV [158]. Main contributions to this analysis were made for the background estimation and in particular the estimation of various sources of systematic uncertainties. Details and results for this analysis are presented in Section 7.2.
A summary on the analyses for gluino-mediated sbottom (and stop) production is given in Section 7.3.

1 The fraction of $\tilde{b}_1\tilde{b}_1$ compared to $\tilde{g}\tilde{g}$ events depends on the mass splitting between the gluino and sbottom. For large mass splittings, the production of $\tilde{b}_1\tilde{b}_1$ becomes dominant.

7.1 Early Searches for Gluino-Mediated Sbottom Production

This section focuses on the gluino-mediated production of sbottom quarks, where the sbottoms decay via $\tilde{b}_1 \to b\tilde{\chi}_1^0$. The latest results obtained with data corresponding to an integrated luminosity of 2.05 fb^{-1} are presented.
In the following subsections, the input samples (7.1.1), the event selection (7.1.2), the background estimation (7.1.3), systematic uncertainties (7.1.4) and the results (7.1.5) are described.

7.1.1 Data and Monte Carlo Input

The dataset used for this analysis includes the first $\mathcal{L} = 2.05 \pm 0.07$ fb^{-1} of data collected in 2011 at $\sqrt{s} = 7$ TeV.[2]
The relevant expected SM background processes are shorty described in the following:

Top Production: The $t\bar{t}$ and single top samples are simulated with the MC@NLO generator, interfaced to HERWIG for the fragmentation and hadronisation and JIMMY for the underlying event. The top mass is set to 172.5 GeV and the next-to-leading order PDF set CTEQ6.6 [62] is used.
A separate sample is produced to model the $t\bar{t}$ production in association with b-jets. It is generated with ALPGEN interfaced to HERWIG and JIMMY, using the CTEQ6L1 [63] leading order PDF set.

W/Z+jets Production: The W+jets and Z+jets events are generated with ALPGEN, interfaced to HERWIG and JIMMY for the showering and underlying event simulation. Samples with up to five additional partons are generated (the last one being inclusive). For the associated production with c- and b-quarks, separate samples, denoted as Wbb, Wc, Wcc and Zbb, are produced. This introduces an overlap between the nominal and the additional samples as no heavy-flavour matching is applied by the ALPGEN generator.[3] The events are sorted into heavy-flavour and light-flavour samples based on the truth information of the partons, also removing the overlap between the different samples. Scale factors of 1.63 ± 0.76 (Wbb, Wcc) and 1.11 ± 0.35 (Wc) are applied on top of the nominal normalisation, as discussed in Ref. [159]. No additional scaling is needed for the Zbb events [160]. The leading order PDF set CTEQ6L1 [63] is used for the ALPGEN samples.

Diboson Production: WW, WZ and ZZ samples are produced with HERWIG and the CTEQ6L1 PDF set. It is a minor background for this analysis.

All samples are simulated with the full ATLAS detector simulation. The cross-sections for the various processes are summarized in Table 7.1.

Signal Samples
Results of this analysis are interpreted in a phenomenological MSSM model, a simplified model (Gbb) and SO(10) models:

2 Data collected in 2010 is not added as is was taken under different conditions (for example the trigger setup changed) and would not add much luminosity to the total dataset.

3 For example, an event with a W, two b-quarks and one additional parton can be included in both the $W+3$ partons sample (where the $b\bar{b}$ pair is produced by the parton shower) and the Wbb+1 parton sample.

Process	σ [nb]	Perturbative order	Generator
$t\bar{t}$	0.164	NLO + NNLL [161]	MC@NLO
single top	0.037	NLO + NNLL [161]	MC@NLO
$t\bar{t}$+$b\bar{b}$	0.9×10^{-3}	LO [74]	ALPGEN
$W \to \ell\nu$ +jets	31.4	NNLO [162]	ALPGEN
$Z \to \ell\ell$ +jets	3.20	NNLO [162]	ALPGEN
$Z \to \nu\nu$ +jets	5.82	NNLO [162]	ALPGEN
Diboson	7.1×10^{-2}	NLO [142, 163]	HERWIG

Table 7.1: Cross-sections for the relevant SM backgrounds with the perturbation order they are calculated to. In addition, the generator used to simulate the events is given in the last column. All three lepton flavours are included in the vector boson samples ($\ell = e, \mu, \tau$).

Gluino-sbottom: A phenomenological MSSM scenario, where only gluinos and sbottom quarks can be produced. The $\tilde{b}_1$ is assumed to be the lightest squark and its mass is below the gluino mass ($m_{\tilde{g}} > m_{\tilde{b}_1} > m_{\tilde{\chi}_1^0}$). The masses of other squarks are above the gluino mass and the neutralino mass is fixed at 60 GeV. For this mass hierarchy, the gluino decays to $b\tilde{b}_1$ with a 100% branching ratio and the sbottom to $b\tilde{\chi}_1^0$. A grid of signal points is produced in the ($m_{\tilde{g}}$, $m_{\tilde{b}_1}$) plane.

Gbb: A simplified model for gluino-pair production, where the gluinos decay to $b\bar{b}\tilde{\chi}_1^0$ via an off-shell sbottom ($\tilde{b}_1^{(*)} \to b\tilde{\chi}_1^0$). The $\tilde{b}_1$ is the lightest squark, but has a larger mass than the gluino ($m_{\tilde{b}_1} > m_{\tilde{g}} > m_{\tilde{\chi}_1^0}$, $m_{\tilde{b}_1} = 1$ TeV). A grid of signal points is produced in the ($m_{\tilde{g}}$, $m_{\tilde{\chi}_1^0}$) plane, providing complementary information to the Gluino-Sbottom model, where the neutralino mass is fixed.

SO(10): SUSY GUT based on SO(10), as described in Section 2.2.4. Two configurations are used for this analysis, a HS and a DR3 model. For both models, parameters that allow for Yukawa coupling unification are chosen. The parameters for the HS model are: $m_{16}(1,2,3) = 10000$ GeV, $m_{10} = 12054$ GeV, $M_D = 3287$ GeV, $A_0 = -19947$, $\tan\beta = 50.4$ and $\mu > 0$. The parameters for the DR3 model are: $m_{16}(1,2) = 11806$ GeV, $m_{16}(3) = 10840$ GeV, $m_{10} = 13903$ GeV, $M_D = 1851$ GeV, $A_0 = -22786$, $\tan\beta = 50$ and $\mu > 0$. In both cases $m_{1/2}$ is the only free parameter, that is varied to scan over the gluino mass (in the range allowing Yukawa coupling unification).

The mass spectra and branching ratios are calculated with SUSYHIT [79] for the Gluino-Sbottom and Gbb models and ISASUSY [80] for SO(10). The signal samples are generated with HERWIG++, using the CTEQ6.6M PDF set [164]. Cross-sections at NLO are calculated with PROSPINO [81]. A summary of the signal samples is shown in Table 7.2.

7.1.2 Event Selection

The final states of the SUSY scenarios investigated in this analysis include four b-jets and large $E_{\mathrm{T}}^{\mathrm{miss}}$ due to two neutralinos:

Model	Generator	Main parameters	Main processes
Gluino-Sbottom (Pheno. MSSM)	SUSYHIT	$m_{\tilde{g}}$, $m_{\tilde{b}_1}$ $m_{\tilde{\chi}_1^0}$ =60 GeV	$\tilde{g}\tilde{g}$, $\tilde{b}\tilde{b}$, $\tilde{g}\tilde{b}$ $\tilde{g} \to b\tilde{b}_1$, $\tilde{b} \to b\tilde{\chi}_1^0$
Gbb (Simplified Model)	SUSYHIT	$m_{\tilde{g}}$, $m_{\tilde{\chi}_1^0}$ $m_{\tilde{g}} < m_{\tilde{b}_1}$	$\tilde{g}\tilde{g}$ $\tilde{g} \to b\bar{b}\tilde{\chi}_1^0$
HS model (SO(10))	ISASUSY	$m_{\tilde{g}}$ tanβ=50.4, m_{16}=10 TeV, $\mu > 0$	$\tilde{g}\tilde{g}$, $\tilde{\chi}_2^0\tilde{\chi}_1^\pm$ $\tilde{g} \to b\bar{b}\tilde{\chi}_2^0$
DR3 model (SO(10))	ISASUSY	$m_{\tilde{g}}$ tanβ=50, m_{16} ∼11 TeV, $\mu > 0$	$\tilde{g}\tilde{g}$, $\tilde{\chi}_2^0\tilde{\chi}_1^\pm$ $\tilde{g} \to b\bar{b}\tilde{\chi}_1^0$

Table 7.2: Summary of signal samples considered in this analysis. The generator refers to the mass-spectrum calculation.

- Gluino-Sbottom: $\tilde{g}\tilde{g}$ production[4] with $\tilde{g} \to b\tilde{b}_1$, $\tilde{b}_1 \to b\tilde{\chi}_1^0$.
- Gbb: $\tilde{g}\tilde{g}$ production with $\tilde{g} \to b\bar{b}\tilde{\chi}_1^0$.
- SO(10): $\tilde{g}\tilde{g}$ production with $\tilde{g} \to b\bar{b}\tilde{\chi}_2^0$ or $\tilde{g} \to b\bar{b}\tilde{\chi}_1^0$.

The signal regions are based on the b-jet multiplicity and the M_{eff} variable built by the three leading jets, which were found to be the best performing variables in terms of separating the signal and background contributions while allowing for a suitable background estimation. The different steps for the event selection, including the object definitions and preselection, are described in the following.

Object Definitions

The object reconstruction follows the methods described in Section 4.2. The exact definitions used for the gluino-mediated analysis are:

Jets: Jets are calibrated with the EM+JES calibration scheme and are required to have $p_{\text{T}} > 20$ GeV and $|\eta| < 2.8$.

b-Jets: The JetFitterCombNN algorithm is used to identify b-jets. They are selected at a 60% efficiency working point (weight> 2)[5] and are required to have $p_{\text{T}} > 50$ GeV and $|\eta| < 2.5$.

Leptons: Electrons are selected following the *medium* criteria and are required to have $p_{\text{T}} > 20$ GeV and $|\eta| < 2.47$. Muons are identified if a match between the inner detector track and at least one track segment in the muon spectrometer is obtained. They are required to have $p_{\text{T}} > 10$ GeV and $|\eta| < 2.4$.
Tighter lepton selections are applied for the control regions, where a lepton is required.

4 Also sbottom-pair production is included in this model, but this analysis focuses on the gluino-mediated signatures, while the $\tilde{b}_1\tilde{b}_1$ production is specifically targeted by the analysis presented in the previous chapter.

5 The 60% efficiency is obtained for a $t\bar{t}$ MC sample. The corresponding rejection factors are 378, 8 and 28 for light-jets, c-jets and τ-leptons.

The isolation criteria are applied, the p_{T} thresholds raised to 25/20 GeV (e/μ) and the electrons must fulfill the *tight* criteria.

The identified jets and leptons are sorted by their transverse momentum.

Preselection

A Jet+$E_{\mathrm{T}}^{\mathrm{miss}}$ trigger is used to select the events for this analysis. At event filter level, a jet with p_{T} greater than 75 GeV and $E_{\mathrm{T}}^{\mathrm{miss}}$ greater than 45 GeV is required. The trigger turn-on characteristics are shown in Fig. 7.1 for data and $t\bar{t}$ MC events as a function of $E_{\mathrm{T}}^{\mathrm{miss}}$. The efficiency plateau is reached at $E_{\mathrm{T}}^{\mathrm{miss}} > 130$ GeV for events with at least one jet with $p_{\mathrm{T}} > 130$ GeV.
The data quality criteria applied for the gluino-mediated analysis are summarized in Table 7.3 (see Section 5.3 for a detailed description).

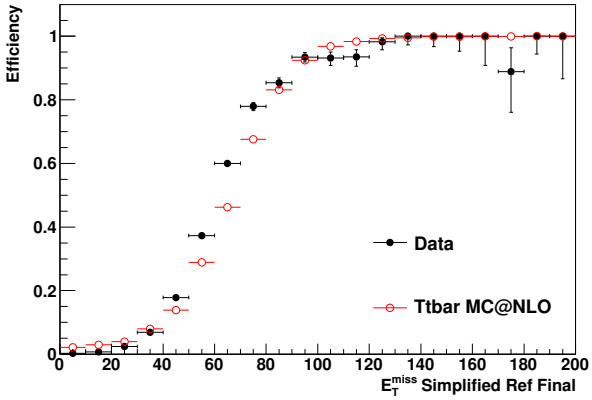

Figure 7.1: Trigger efficiency for the Jet+$E_{\mathrm{T}}^{\mathrm{miss}}$ trigger as a function of an offline $E_{\mathrm{T}}^{\mathrm{miss}}$ threshold for data and $t\bar{t}$ MC events. It is calculated with respect to a single jet trigger and at least one jet with $p_{\mathrm{T}} > 130$ GeV is required to ensure working on the efficiency plateau of the jet trigger.

In addition to the trigger and data quality selections, the following requirements are added to the event preselection. Events with at least one electron or muon are removed. To ensure working on the trigger efficiency plateau, one jet with $p_{\mathrm{T}} > 130$ GeV and $E_{\mathrm{T}}^{\mathrm{miss}} > 130$ GeV are required. Two additional jets of 50 GeV are required and enter the M_{eff} calculation together with the leading jet. Multi-jet background contributions are reduced by requiring $\Delta\phi_{\mathrm{min}} > 0.4$ for the three leading jets and $E_{\mathrm{T}}^{\mathrm{miss}}/M_{\mathrm{eff}} > 0.25$.

Signal Region Definition

The kinematic properties of the considered final states depend on the mass difference of the primary produced gluinos and the neutralinos. For large mass splittings, the average momenta of the final state objects are larger. The M_{eff} variable is used as final discriminating variable in the signal region selections. Its distribution is shown in Fig. 7.2 for various signal points of the Gbb grid. Only tiny differences are observed by signal points with the same mass splitting, while the M_{eff} distribution is shifted to higher values with increasing $\Delta m(\tilde{g},\tilde{\chi}_1^0)$. Different M_{eff} thresholds are used for the signal region definitions.
An optimisation of the event selection was carried out for the results obtained with the data corresponding to an integrated luminosity of 0.83 fb^{-1} [154], by varying the b-jet multiplicity, the $E_{\mathrm{T}}^{\mathrm{miss}}$ threshold and the M_{eff} threshold. It was also tested, if better results are obtained by replacing the M_{eff} threshold by a H_{T} threshold. Four signal regions with at least one or two

Name	Description and Implementation
Data Quality	remove events recorded with mis-functioning detector devices
Trigger	Jet+$E_{\mathrm{T}}^{\mathrm{miss}}$ trigger
Vertex Selection	require ≥ 4 tracks pointing to the primary vertex
Corrupted Events	reject noise-burst affected events
LAr hole	remove events with large $E_{\mathrm{T}}^{\mathrm{miss}}$ fraction due to LAr hole
Overlap Removal	remove jets within $\Delta R = 0.2$ of an electron remove electrons and muons within $\Delta R = 0.4$ of a jet
Bad Jets	veto events with bad jets that have $p_T > 20$ GeV
Jet Charged Fraction	remove events if any selected jet has chf < 0.05 and $\lvert\eta\rvert < 2.0$

Table 7.3: Summary of the event preselection for the gluino-mediated sbottom analysis. "Selected jets" refers to the leading three jets. The Overlap Removal is not a selection criteria in the sense that events are rejected, but it is included in the list to better understand the status of the reconstructed objects at the current selection step.

b-jets and $M_{\mathrm{eff}} > 500$ GeV or 700 GeV were found to provide an optimal sensitivity throughout the different signal scenarios. For this analysis, a harsher M_{eff} threshold of 900 GeV is added as the dataset considerably increased.
The selection efficiency highly depends on the SUSY scenario. The efficiency increases from about 1% for $\Delta m(\tilde{g},\tilde{\chi}_1^0) = 200$ GeV to 45% with increasing mass splitting for the Gbb

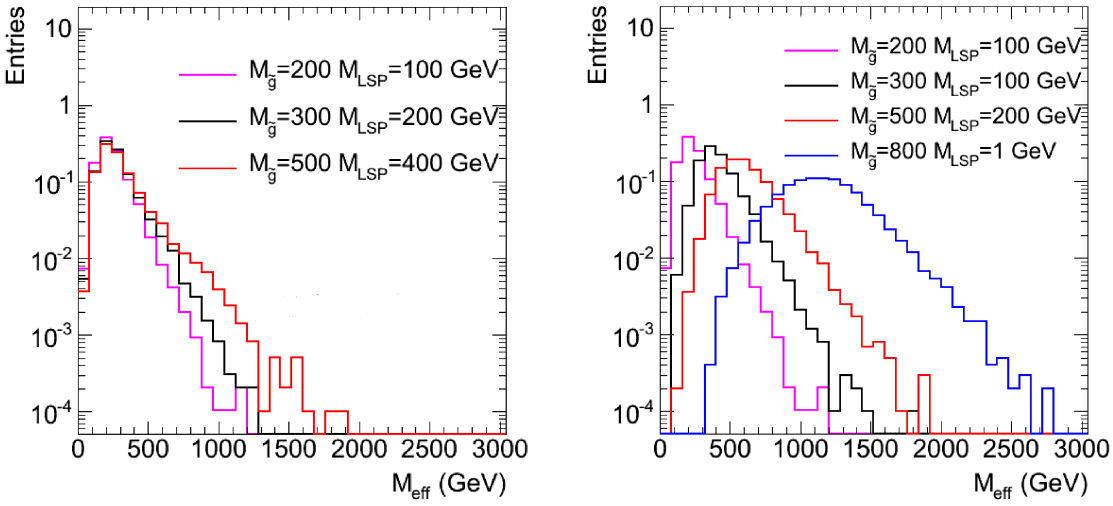

(a) $\Delta m(\tilde{g},\tilde{\chi}_1^0) = \text{const.}$ **(b)** 100 GeV $< \Delta m(\tilde{g},\tilde{\chi}_1^0) <$ 800 GeV

Figure 7.2: Distribution of M_{eff} for various Gbb signal points with (a) a constant gluino-neutralino mass splitting and (b) a varying mass splitting. The distributions are normalized to unity.

model. For the Gluino-Sbottom model, efficiencies around 5-50% are found for the sensitive parameter region. The efficiencies for both models are shown in Fig. 7.3, separately for the loosest and harshest selection thresholds.
In Figure 7.4 it is shown, which selection provides the best expected sensitivity for the Gbb signal grid. It is based on a simplified $S/\sqrt{B}$ significance calculation, where the background B is estimated from MC. The $2b$-jets selection is found best performing for most signal points, while the $1b$-jet selection only contributes for points with very small mass splitting.
A summary of the event selections with one b-jet (SR0-1b) and two b-jets (SR0-2b) is given in Table 7.4.

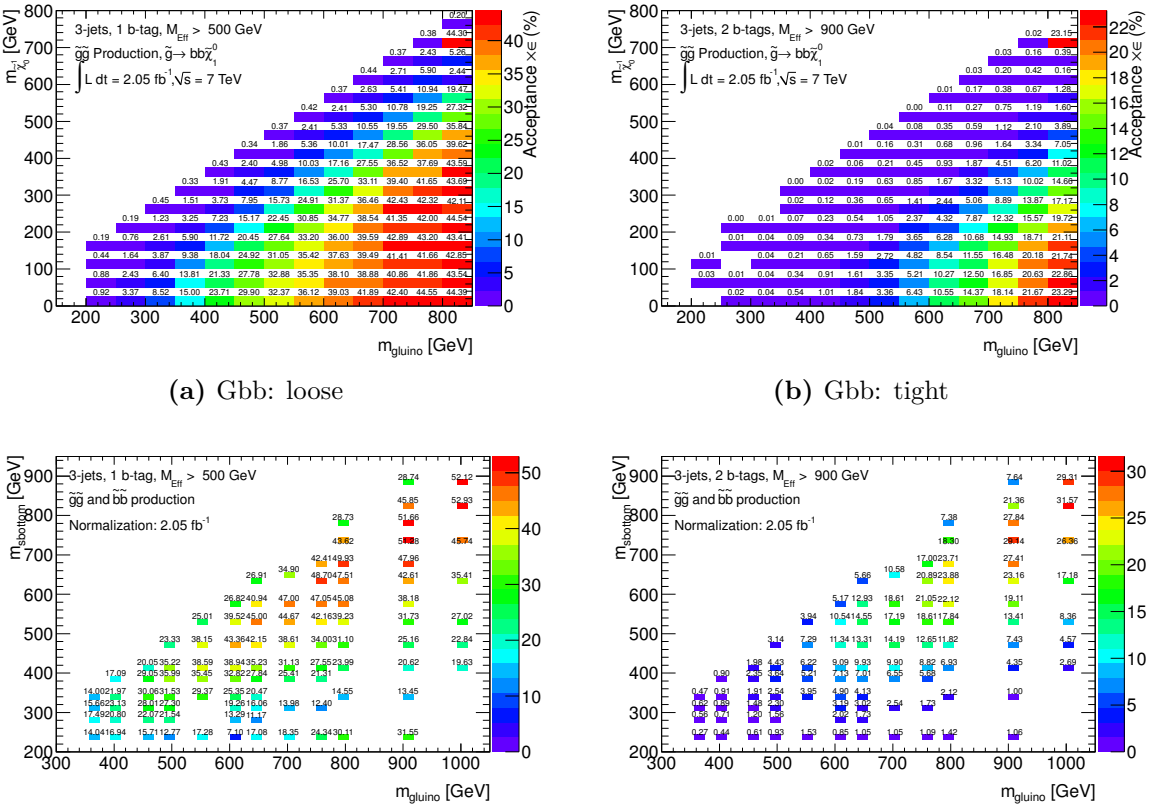

(a) Gbb: loose

(b) Gbb: tight

(c) Gluino-Sbottom: loose

(d) Gluino-Sbottom: tight

Figure 7.3: Selection efficiencies in percent for the Gbb model in the $(m_{\tilde{g}}$-$m_{\tilde{\chi}_1^0})$ plane and the Gluino-Sbottom model in the $(m_{\tilde{g}}$-$m_{\tilde{b}_1})$ plane for the loose and tight signal region selections. The loose selection refers to $\geq 1b$-jet, $M_{\text{eff}} > 500$ GeV and the tight selection refers to $\geq 2b$-jets, $M_{\text{eff}} > 900$ GeV.

7.1.3 Background Estimation

The dominant SM background process in the gluino-mediated signal regions is top production. It is followed by contributions from W and Z boson production in association with heavy-flavour jets. The W and Z backgrounds contribute about 30% to SR0-1b and 10% to SR0-2b. The top normalisation is estimated via a semi data-driven method, while the W and Z backgrounds are estimated directly from MC. Also the sub-dominant diboson contributions are estimated from MC. A validation of the background estimation is presented at the end

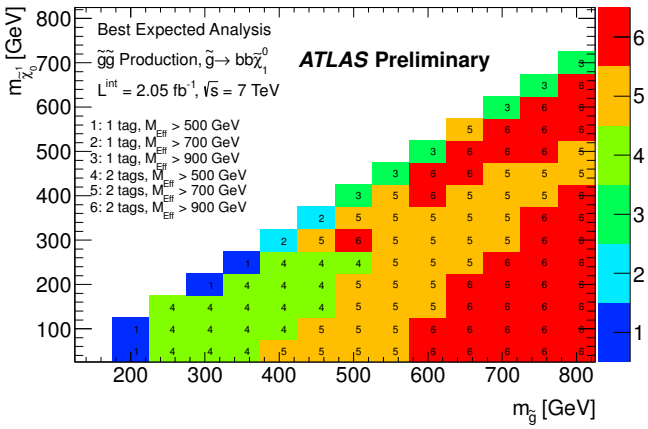

Figure 7.4: Optimal expected signal region for the Gbb model in the ($m_{\tilde{g}}$-$m_{\tilde{\chi}_1^0}$) plane. The selection, as listed in the legend, providing the highest expected significance is choosen per signal point.

Description	Signal region	
	SR0-1b	SR0-2b
Trigger	Jet+$E_{\mathrm{T}}^{\mathrm{miss}}$ trigger	
Data Quality	Apply event cleaning	
Leptons	No e/μ with $p_{\mathrm{T}} > (20/10)$ GeV	
$E_{\mathrm{T}}^{\mathrm{miss}}$	> 130 GeV	
Jets	≥ 3 jets with $p_{\mathrm{T}} > 50$ GeV, $p_{\mathrm{T}}(\mathrm{jet}_1) > 130$ GeV	
QCD Rejection	$\Delta\phi_{\mathrm{min}} > 0.4$, $E_{\mathrm{T}}^{\mathrm{miss}}/M_{\mathrm{eff}} > 0.25$	
b-tagging	$\geq 1b$-jet	$\geq 2b$-jet
M_{eff}	$> 500, 700, 900$ GeV	$> 500, 700, 900$ GeV

Table 7.4: Summary of the gluino-mediated event selections. The jets are sorted by their transverse momentum.

of this section. Multi-jet production is a minor background for this analysis and estimated via the jet-smearing method.

Estimation of the Multi-Jet Background

The seed events for the jet-smearing method are collected from data by applying single jet triggers. Different trigger thresholds are used to ensure that enough events for the different kinematic regimes are selected. In addition, the seed events are required to have three reconstructed jets with $p_{\mathrm{T}} > 30$ GeV and one b-jet with $p_{\mathrm{T}} > 20$ GeV.
Separate response functions are constructed and used for b-jets and light jets (including all jets that are not b-tagged).

A special treatment needs to be applied to estimate the effect of events affected by the LAr hole. The energy loss due to the hole causes additional mis-measurements that are taken into account by a separate response function, obtained from a MC sample of $t\bar{t}$ events where the hole is implemented in the simulation process. It is applied to an appropriate fraction of seed events, for which the direction of one of the jets is shifted to point into the hole.
The smeared events are normalized in a multi-jet control region with a reverted $\Delta\phi_{\text{min}}$ threshold ($\Delta\phi_{\text{min}} < 0.4$). Otherwise the signal region selection is applied up to the b-tagging (missing the M_{eff} thresholds). The normalisation is done separately for events with one and two b-jets and for the LAr hole affected events. In Figure 7.5, the $E_{\text{T}}^{\text{miss}}$ and M_{eff} distributions are shown for the multi-jet control region with one b-jet. The event yields obtained for the signal regions are given in Table 7.5. It can be seen, that the relative contribution of LAr hole affected events is of the order of a few percent.

Selection		Nominal	LAr hole	Total
SR0-1b (M_{eff})	500 GeV	48.7	1.0	49.7
	700 GeV	3.8	0.2	4.0
	900 GeV	0.4	0.04	0.44
SR0-2b (M_{eff})	500 GeV	14.0	0.5	14.5
	700 GeV	1.3	0.04	1.34
	900 GeV	0.2	0.01	0.21

Table 7.5: Estimate of the multi-jet background from the jet-smearing method for the gluino-mediated signal regions. The contributions from nominal events and LAr hole affected events are shown separately.

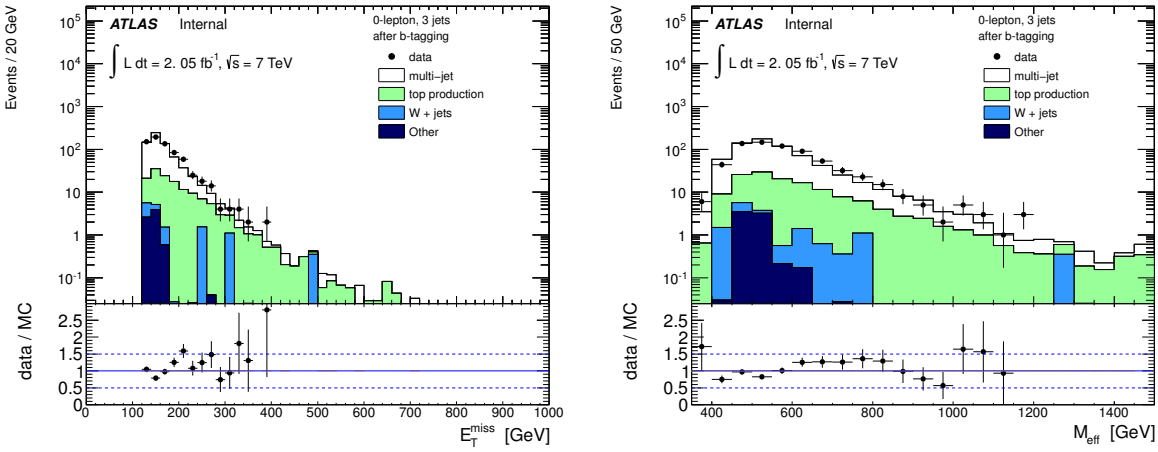

(a) $E_{\text{T}}^{\text{miss}}$ **(b)** M_{eff}

Figure 7.5: Distributions of (a) $E_{\text{T}}^{\text{miss}}$ and (b) M_{eff} for the multi-jet control region with $\Delta\phi_{\text{min}} < 0.4$ and $\geq 1b$-jet. The non-QCD processes are taken from MC.

Estimation of the Top Background

A semi data-driven method is used to estimate the dominant SM background process. The statistical framework described in Section 5.8.1 was not yet available when performing this analysis. Therefore, a stand-alone approach is employed here.

The normalisation of events from the production of top quarks is obtained from a control region with one electron or muon. The events are selected by a single lepton trigger and the tight lepton selection criteria are applied. Otherwise the same preselection and jet and $E_{\mathrm{T}}^{\mathrm{miss}}$ thresholds as for the signal regions are applied: at least three jets with $p_{\mathrm{T}} > 130, 50, 50$ GeV and $E_{\mathrm{T}}^{\mathrm{miss}} > 130$ GeV. Two control regions are defined with either one b-jet (CR0-1) or two b-jets (CR0-2) to account for the different signal region selections. A medium M_{eff} threshold of $M_{\mathrm{eff}} > 600$ GeV is applied for both. In addition, it is required that 40 GeV $< m_{\mathrm{T}} <$ 100 GeV to reduce a possible signal contamination. A summary on the control region selections is given in Table 7.6.

Description	Control region	
	CR0-1	CR0-2
Trigger	Single lepton trigger	
Data Quality	Apply event cleaning	
Leptons	one e or μ with $p_{\mathrm{T}} > 25$ or 20 GeV	
$E_{\mathrm{T}}^{\mathrm{miss}}$	> 130 GeV	
Jets	≥ 3 jets with $p_{\mathrm{T}} > 50$ GeV, $p_{\mathrm{T}}(\mathrm{jet}_1) > 130$ GeV	
Signal Contamination	40 GeV $< m_{\mathrm{T}} <$ 100 GeV	
b-tagging	$\geq 1b$-jet	$\geq 2b$-jets
M_{eff}	> 600 GeV	

Table 7.6: Summary of the control regions used to estimate the top background. The jets are sorted by their transverse momentum.

The contributions from $t\bar{t}$, single top and $t\bar{t} + b\bar{b}$ production are summed together to the total top contribution which is normalized by the control regions. The contamination of W and Z events is estimated from MC. Other contributions include the diboson and multi-jet background and are found to contribute less than 1% to the control regions. While the diboson background is estimated from MC, a data-driven method needs to be applied for the multi-jet background[6].

The $E_{\mathrm{T}}^{\mathrm{miss}}$ and M_{eff} distributions for the CR0-1 and CR0-2 selections are shown in Fig. 7.6 and Fig. 7.7, separately for events with one electron and events with one muon. The number

6 The multi-jet background is dominated by "fake" leptons, that are either produced by photon conversion and heavy-flavour decays or identified wrongly by the lepton reconstruction. The probability to reconstruct a fake lepton is estimated in a multi-jet enriched control region (low $E_{\mathrm{T}}^{\mathrm{miss}}$) and used to assess the multi-jet contribution. More details on the method can be found in Ref. [165].

of top events in the signal region is estimated following Eq. (5.9):

$$N_{\mathrm{SR}}^{\mathrm{Top}} = T_f(N_{\mathrm{CR}}^{\mathrm{data}} - N_{\mathrm{CR}}^{\mathrm{non-Top}}), \tag{7.1}$$

where the number of non-top background events $N_{\mathrm{CR}}^{\mathrm{non-Top}}$ is subtracted from the observed events $N_{\mathrm{CR}}^{\mathrm{data}}$ in the control regions and the transfer factor is given by the MC top event yields ($T_f = N_{\mathrm{SR}}^{\mathrm{MC,Top}}/N_{\mathrm{CR}}^{\mathrm{MC,Top}}$). The event yields for the control regions are given in Table 7.7. The numbers are separated into events with one electron and events with one muon and the sum of both contributions is used as input for Eq. (7.1). As a result, the data-driven and MC based top event yields agree for the signal regions with one b-jet (normalisation obtained from data ~ 1). The event yield is shifted up by about 30% for the signal regions with two b-jets for the data-driven approach, which can be explained by imperfect b-tagging scaling factors. In both cases, a reduction of the systematic uncertainties, as discussed in the next section, is obtained with the data-driven method.

Control Region	Top	W/Z	Other	Total	Data
CR0-1 (e)	187	48	1	235 ± 45	217
CR0-1 (μ)	146	22	1	169 ± 45	177
CR0-2 (e)	53	2	0.1	55 ± 20	64
CR0-2 (μ)	42	3	0.1	45 ± 17	62

Table 7.7: Expected background and observed data event yields for the top control regions, separated for events with one electron and one muon. The multi-jet and diboson contributions are included in "Others". The uncertainty for the total SM prediction includes only experimental systematic uncertainties (dominated by JES and b-tagging uncertainties).

Validation

Several validation regions are defined to cross-check the background estimation. The top background estimation is in particular validated in selections similar to the control region selections, but with a low value of M_{eff} ($M_{\mathrm{eff}} < 600$ GeV) and either small m_{T} (40 GeV $< m_{\mathrm{T}} < 100$ GeV) or large m_{T} ($m_{\mathrm{T}} > 100$ GeV). In Table 7.8, results for the control and validation region with two b-jets are given separately for electron and muon events. Only statistical uncertainties are included, but good agreement between the SM expectation and observed event yields is obtained for all selections.

A second validation is performed by a combined fit of multiple control regions. The general idea is based on extracting global normalisations for the SM backgrounds from different control regions that allow separating the SM contributions.[7]

The top, W and Z normalizations are obtained from CRs with different b-jet and lepton multiplicities: the b-jet multiplicity allows to separate top from W/Z events. In addition, a different lepton multiplicity is expected for the W and Z events. In total six control regions with either no leptons or one lepton and $0,1,\geq 2$ b-jets are exploited. For the no-lepton CRs, the M_{eff} threshold is reverted ($M_{\mathrm{eff}} < 500$ GeV) to avoid signal contamination, while 40 GeV $< m_{\mathrm{T}} < 100$ GeV and $M_{\mathrm{eff}} > 600$ GeV is requested for the leptonic CRs. The MC

7 It is the same idea that is used for the background estimation of later analyses, like the sbottom-pair production analysis. However, here the fit is performed stand-alone.

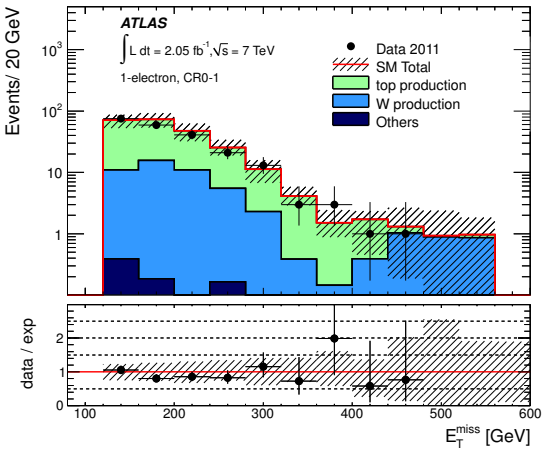

(a) 1-electron: $E_{\mathrm{T}}^{\mathrm{miss}}$

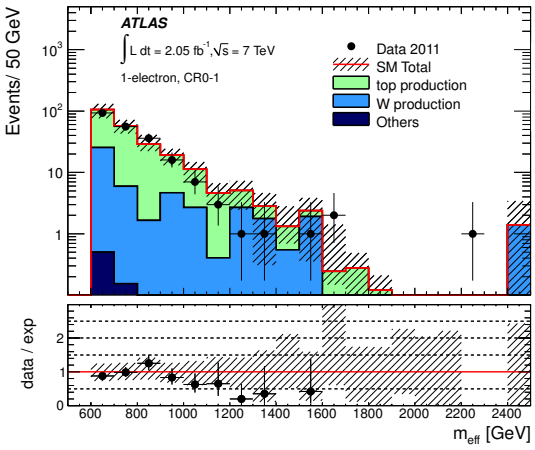

(b) 1-electron: M_{eff}

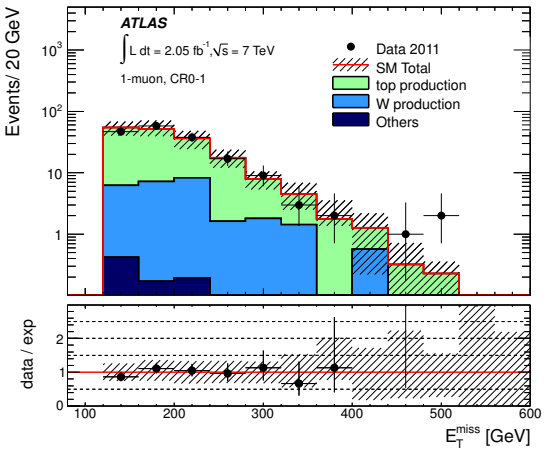

(c) 1-muon: $E_{\mathrm{T}}^{\mathrm{miss}}$

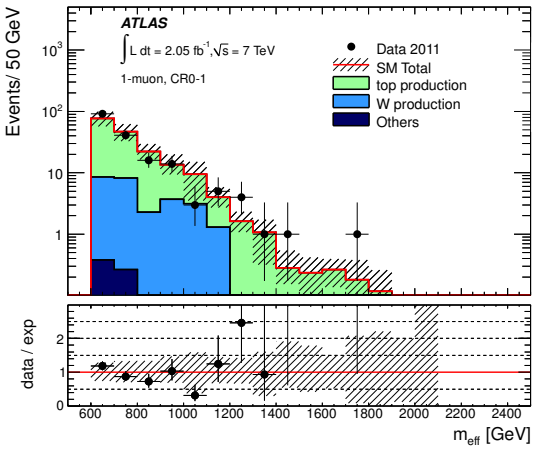

(d) 1-muon: M_{eff}

Figure 7.6: Distributions of $E_{\mathrm{T}}^{\mathrm{miss}}$ and M_{eff} in the top control regions with one b-jet (CR0-1). The distributions are shown separately for events with one electron and events with one muon. The Z, diboson and multi-jet contributions are included in "Others". The uncertainty bands include experimental and theoretical uncertainties for the SM backgrounds.

and data event yields for the control regions are filled into one histogram, such that each bin corresponds to one CR. A template fit is performed with MC templates for the SM backgrounds to extract the scaling factors s_{Top}, s_W and s_Z giving the optimal agreement with the measured data distribution. The estimated values are $s_{\mathrm{Top}} = 1.11 \pm 0.05$, $s_W = 0.80 \pm 0.06$ and $s_Z = 0.93 \pm 0.17$ with a reduced chi-square value of 0.25. The CR distribution is shown together with the fit result in Fig. 7.8. The SM prediction for the signal regions is given by $N_{\mathrm{SM}}^{\mathrm{exp}} = s_W \cdot N_W^{\mathrm{SM}} + s_Z \cdot N_Z^{\mathrm{SM}} + s_{\mathrm{Top}} \cdot N_{\mathrm{Top}}^{\mathrm{SM}}$.
Systematic uncertainties for the JES and b-tagging are evaluated with pseudo experiments. A data distribution is emulated by adding the nominal MC templates for the SM processes, using the normalisation obtained from MC. About 10000 pseudo experiments are generated by applying independent Poissonian fluctuations for each of the control regions. The pseudo experiments are fitted with the nominal and shifted MC templates, and the systematic uncer-

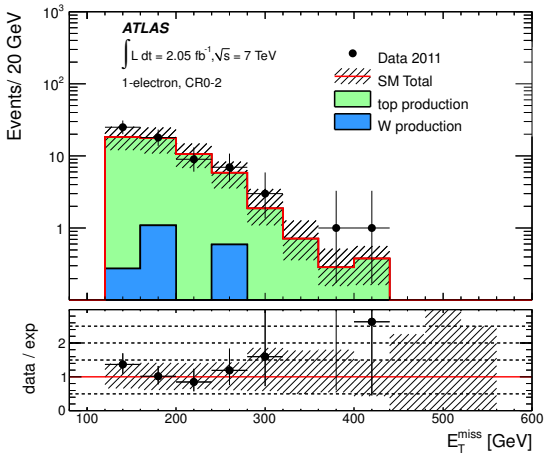

(a) 1-electron: $E_{\mathrm{T}}^{\mathrm{miss}}$

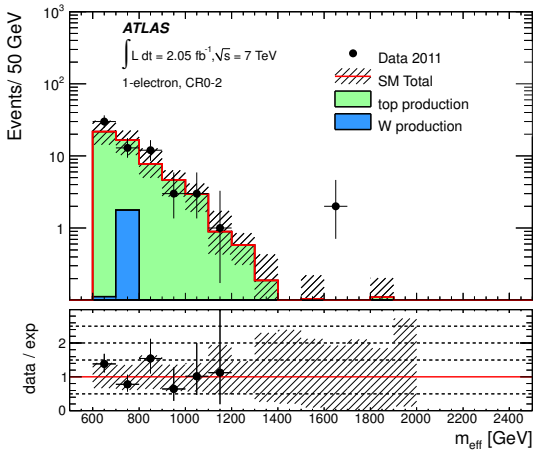

(b) 1-electron: M_{eff}

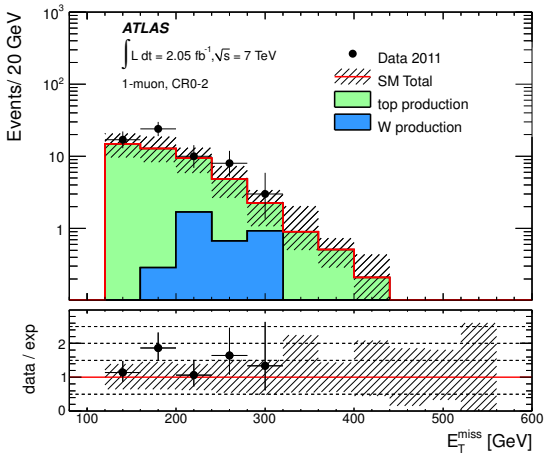

(c) 1-muon: $E_{\mathrm{T}}^{\mathrm{miss}}$

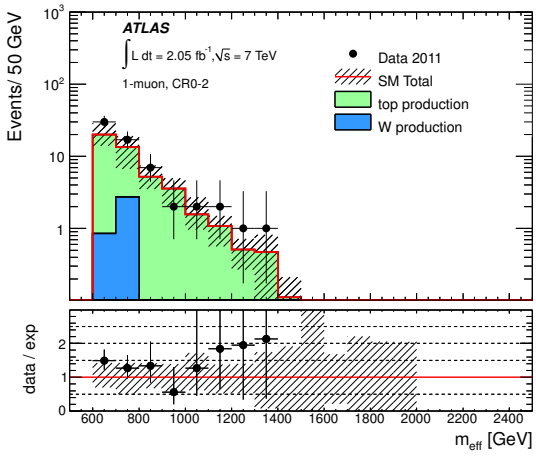

(d) 1-muon: M_{eff}

Figure 7.7: Distributions of $E_{\mathrm{T}}^{\mathrm{miss}}$ and M_{eff} in the top control regions with two b-jets (CR0-2). The distributions are shown separately for events with one electron and events with one muon. The Z, diboson and multi-jet contributions are included in "Others". The uncertainty bands include experimental and theoretical uncertainties for the SM backgrounds.

tainty is obtained from the relative difference of the mean values of the nominal and shifted fit results. A correlation of the JES uncertainty for the CR and SR selections leads to a reduced uncertainty on the final event yields, while the b-tagging uncertainties are only partly reduced for the top background.
In general, good agreement with the results from the nominal background estimation is achieved.

7.1.4 Systematic Uncertainties

The systematic uncertainties on the final event yields include the experimental and theoretical uncertainties as introduced in Section 5.7. For the MC based estimates (W/Z) they are computed directly, but for the top background the uncertainties on the transfer factor need to be calculated and propagated accordingly.

Selection	SM prediction	data
1-electron		
CR0-2	70 ± 8	64
VR (low m_{T})	40 ± 7	37
VR (high m_{T})	10 ± 3	13
1-muon		
CR0-2	56 ± 8	62
VR (low m_{T})	43 ± 7	39
VR (high m_{T})	12 ± 3	15

Table 7.8: The total SM expectation (after the data-driven determination of the top background) and the observed event yields for the control and validation regions with 2 b-jets. The quoted errors only includes statistical uncertainties.

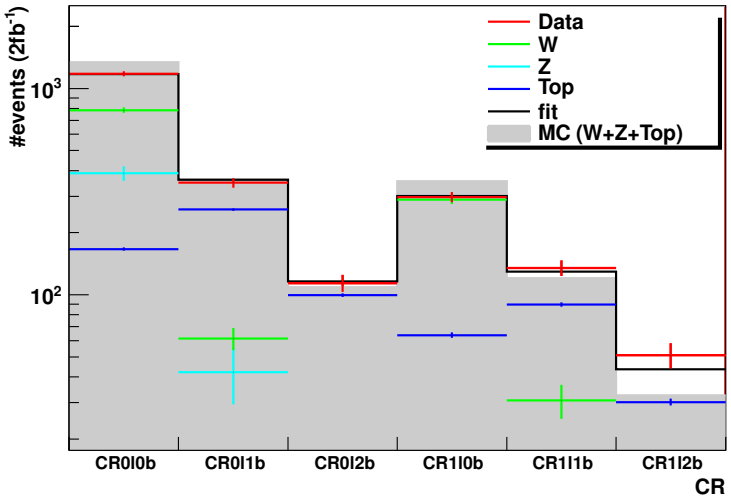

Figure 7.8: Distribution of the event yields in the CRs for the combined background fit. The first three bins contain the CRs with no leptons and 0, 1, ≥ 2 b-jets and the last the bins contain the corresponding CRs with a lepton. The distribution of the total SM background as obtained after the fit is shown as black line.

The dominant experimental uncertainties arise from the imperfect knowledge of the JES and the b-tagging efficiencies. The relative uncertainties on the final event yields amount to $\pm$(20-30)% (JES) and $\pm$10/30% (b-tagging SR0-1b/SR0-2b) for a MC based top estimation. Other experimental uncertainties, including the uncertainties on the JER, the lepton identification efficiencies and the luminosity measurement, are found to be negligibly small.
The background process dependent uncertainties are given in the following:

Multi-jet

Different sources for systematic uncertainties for the multi-jet background estimate are investigated. They include uncertainties arising from statistical uncertainties for the normalisation and seed event selection, uncertainties on the shape of the response function and possible biases in the seed event selection. The relative uncertainty on the multi-jet event yield ranges

from ±(50-70)% in the different signal regions. When the experimental uncertainties are included a total uncertainty of ±(70-100)% is obtained for the multi-jet background.

Top

Theoretical uncertainties for the top background are evaluated for $t\bar{t}$ events and then also applied for single top events which roughly amount to ±10% of the top background for the selections considered within this chapter. A ±100% uncertainty is assumed for the minor contribution of $t\bar{t} + b\bar{b}$ events.
Generator uncertainties for the $t\bar{t}$ background are obtained by comparing the MC@NLO event yields to event yields obtained for POWHEG and ALPGEN samples. The POWHEG comparison shows the effect of using a different NLO calculation and the ALPGEN comparison is sensitive to uncertainties related to the presence of additional jets. Uncertainties on the parton showers are obtained by comparing two sets of POWHEG samples, using either HERWIG or PYTHIA for the showering. ISR and FSR uncertainties are evaluated with specific ACERMC samples.
When computing the transfer factors for the top-background estimation, the theoretical uncertainties are dominating the transfer factor uncertainties. Values of ±(11-35)% are obtained, while the experimental uncertainties are found below ∼ ±5%. In Table 7.9, the relative theoretical uncertainties on the top-event yields in the signal regions are shown together with the statistical and different experimental uncertainty contributions.

Signal region		JES+JER	b-tagging	Lepton	Theory	Other	Total
SR0-1b (M_{eff})	500 GeV	4%	3%	2%	11%	10%	15%
	700 GeV	3%	3%	2%	20%	10%	22%
	900 GeV	3%	4%	2%	35%	11%	37%
SR0-2b (M_{eff})	500 GeV	3%	3%	2%	15%	11%	19%
	700 GeV	3%	4%	2%	20%	10%	22%
	900 GeV	3%	2%	2%	30%	12%	32%

Table 7.9: Relative uncertainties for the top background estimated by the semi data-driven method for the six signal regions. Statistical uncertainties on the event yields in the control regions and systematic uncertainties on the non-top contributions are included in "Other". The total uncertainty is given in the last column.

W* and *Z

The uncertainty for the W and Z production in association with b-jets is taken from the additional normalisation factors introduced in Section 7.1.1. A ±50% uncertainty is obtained for W events and a ±100% uncertainty is assumed for Z events.
For the W and Z production in association with light jets, the uncertainty is evaluated by varying the relative cross-sections of samples with a different number of outgoing partons and comparing ALPGEN samples with different parameter settings, as for example the renormalization and factorisation scales. It is evaluated for the SR0-1b selection before applying any M_{eff} threshold and roughly amounts to ±30%.

7.1.5 Results and Interpretation

In this section, the final results obtained for the analysis considering gluino-mediated sbottom production for $\mathcal{L} = 2.05$ fb^{-1} are presented.
The expected and observed event yields for all signal regions are shown in Table 7.10. Good agreement between the observed event yields and the SM expectation is obtained for all selections. As expected, the background is dominated by top production for all signal regions. The large contribution is also given by the $W + Z$ background in the signal region with $1b$-jet (about 25-40% of the total background). For the signal region with $2b$-jets, the contribution from $W + Z$ events is found below 10%.
In Figure 7.9, the M_{eff} and $E_{\text{T}}^{\text{miss}}$ distributions are shown for the $1b$-jet and $2b$-jet signal regions. The distributions for the observed data events are well described by the distributions for the expected SM background.

Channel	≥ 1 b-jet, M_{eff} threshold			≥ 2 b-jets, M_{eff} threshold		
	500 GeV	700 GeV	900 GeV	500 GeV	700 GeV	900 GeV
Observed	1112	197	34	299	43	8
SM Total	1000 ± 180	190 ± 50	39 ± 14	316 ± 72	54 ± 11	9.8 ± 3.2
Top	705 ± 110	119 ± 26	22 ± 8	272 ± 65	47 ± 10	8.5 ± 3
$W + Z$	248 ± 150	67 ± 42	16 ± 11	23 ± 15	4.5 ± 3	0.8 ± 1
Other	53 ± 21	7.3 ± 4.7	1.5 ± 1	21 ± 12	2.8 ± 1.7	0.5 ± 0.4

Table 7.10: Expected and observed event yields for all signal regions. The "Other" background component includes the multi-jet contribution, obtained by the jet-smearing method, and diboson predictions. The top-background estimate is obtained by the semi data-driven approach.

As no deviation from the SM expectation is observed, first model independent limits and then exclusion limits[8] for the different signal models are calculated. The upper limits on the maximal allowed number of signal events and the corresponding visible cross-sections σ_{vis}, as defined in Section 5.8.3, are given in Table 7.11.
The exclusion limit for the phenomenological MSSM ($\tilde{g}\tilde{g}$ and $\tilde{b}_1\,\tilde{b}_1$ production with $\tilde{g} \to b\tilde{b}_1$ and $\tilde{b}_1 \to b\tilde{\chi}_1^0$) is shown in the ($m_{\tilde{g}}$-$m_{\tilde{b}_1}$) plane in Fig. 7.10. It is obtained by choosing the selection which returns the best expected exclusion limit for each signal point. Gluino masses up to 900 GeV are excluded for $m_{\tilde{b}_1} < 800$ GeV. The limit obtained by the sbottom-pair production analysis with the same dataset is included in the figure and it can be seen that complementary results are obtained by the gluino-mediated search. The limit extends well beyond previous limits set by the ATLAS, CDF and D0 experiments.
The exclusion limit for the Gbb model is shown in the ($m_{\tilde{g}}$-$m_{\tilde{\chi}_1^0}$) plane in Fig. 7.11, together with the upper limits on the signal cross-sections. For this model, gluino masses up to 900 GeV are excluded for $m_{\tilde{\chi}_1^0} < 300$ GeV.
Limits for the SO(10) SUSY scenarios are calculated in combination with the results obtained

8 Remark: the signal theory uncertainties are directly included together with all other uncertainties in the limit calculation within this section.

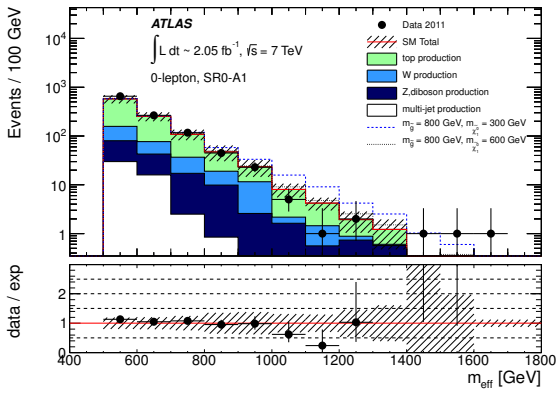

(a) SR0-1b: M_{eff}

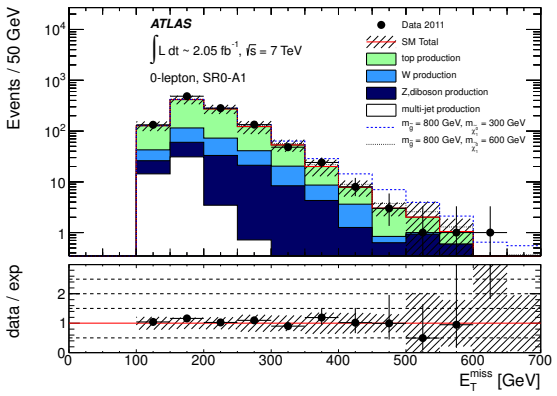

(b) SR0-1b: $E_{\mathrm{T}}^{\mathrm{miss}}$

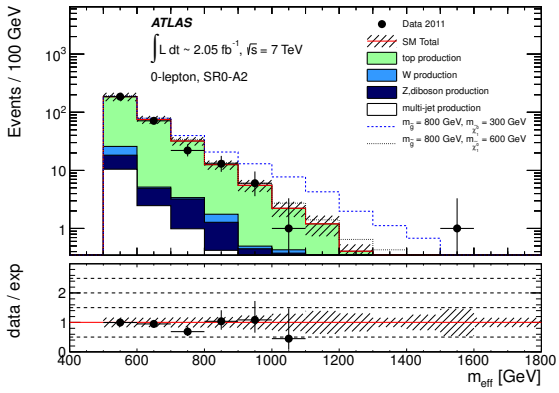

(c) SR0-2b: M_{eff}

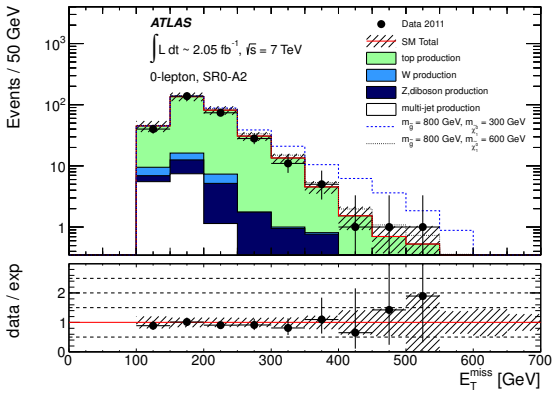

(d) SR0-2b: $E_{\mathrm{T}}^{\mathrm{miss}}$

Figure 7.9: Distributions of M_{eff} and $E_{\mathrm{T}}^{\mathrm{miss}}$ for the signal regions with one b-jet (top) and two b-jets (bottom), with the lowest M_{eff} threshold applied ($M_{\mathrm{eff}} > 500$ GeV). The distributions for two reference signal points from the Gbb model are also shown ($m_{\tilde{g}} = 800$ GeV and $m_{\tilde{\chi}_1^0} = 300/600$ GeV).

by the one-lepton channel, which is published together with this analysis in Ref. [155].[9] The limits are shown in Fig. 7.12 as a function of the gluino mass. They are dominated by the results from the no-lepton analysis for low gluino masses, while the one-lepton analysis becomes dominant for heavy gluinos because decay modes involving top quarks become more relevant. Gluino masses up to 650 GeV (620 GeV) are excluded for the DR3 (HS) model. This excludes the most favoured signal ranges, as the degree of Yukawa coupling unification decreases with increasing gluino mass.[10]

9 The one-lepton analysis focuses on stop production and is based on a similar event selection but with a lepton requirement instead of the lepton veto.

10 The degree of coupling unification is given by the quantity $R = \max(f_t,f_b,f_\tau)/\min(f_t,f_b,f_\tau)$ for the t, b and τ Yukawa couplings f_t, f_b and f_τ. The deviation of R from unity raises above a few percent for $m_{\tilde{g}} > 500$ GeV for both models considered.

Signal region		UL on BSM event yield		UL on σ_{vis} [fb]	
		observed	expected	observed	expected
SR0-1b (M_{eff})	500 GeV	580	520	283	254
	700 GeV	133	133	65	65
	900 GeV	31.6	34.6	15.4	16.9
SR0-2b (M_{eff})	500 GeV	124	134	61	66
	700 GeV	29.6	31.0	14.4	15.0
	900 GeV	8.9	10.3	4.3	5.0

Table 7.11: Upper Limits (UL) at 95% CL on generic beyond SM (BSM) signal yields and the visible cross-sections σ_{vis} for the gluino-mediated signal regions with at least one or two b-jets. Systematic uncertainties on the SM backgrounds are included.

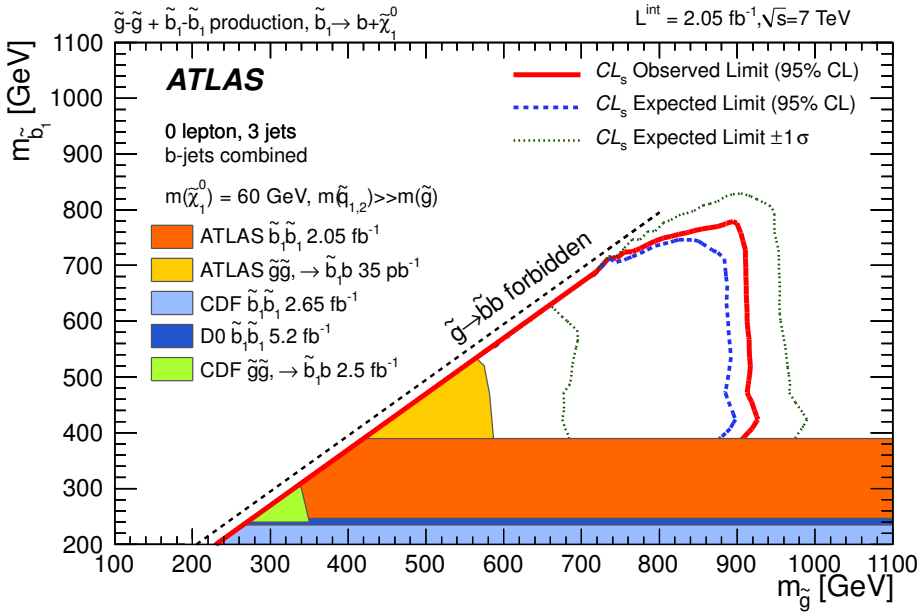

Figure 7.10: Observed and expected 95% CL exclusion limits for the Gluino-Sbottom phenomenological MSSM in the ($m_{\tilde{g}}$-$m_{\tilde{b}_1}$) plane. The solid red line corresponds to the observed limit and the dashed blue with dotted green lines to the expected limit with its $\pm 1\sigma$ uncertainties. For each scenario, the signal region providing the best expected limit is chosen. Previous limits from the ATLAS [153] and CDF [166] experiments for the same decay topology are also included. In addition, limits for the direct sbottom-pair production from the CDF [150], D0 [151] and ATLAS [131] experiments are shown.

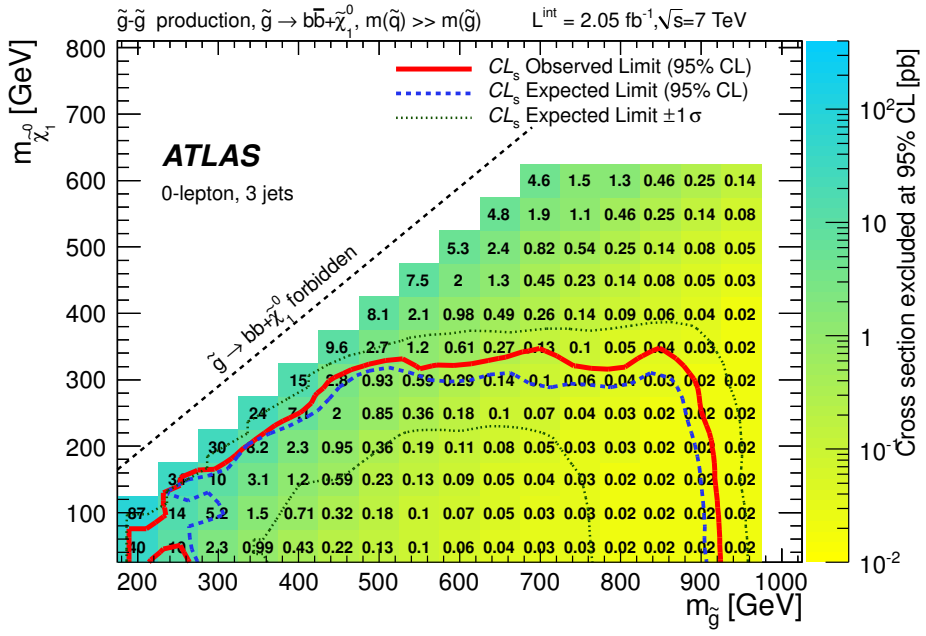

Figure 7.11: Observed and expected 95% CL exclusion limits for the Gbb model in the ($m_{\tilde{g}}$-$m_{\tilde{\chi}_1^0}$) plane. The solid red line corresponds to the observed limit and the dashed blue with dotted green lines to the expected limit with its $\pm 1\sigma$ uncertainties. The numbers give the observed upper limits on the signal cross-sections in pb. For each scenario, the signal region selection providing the best expected limit is chosen.

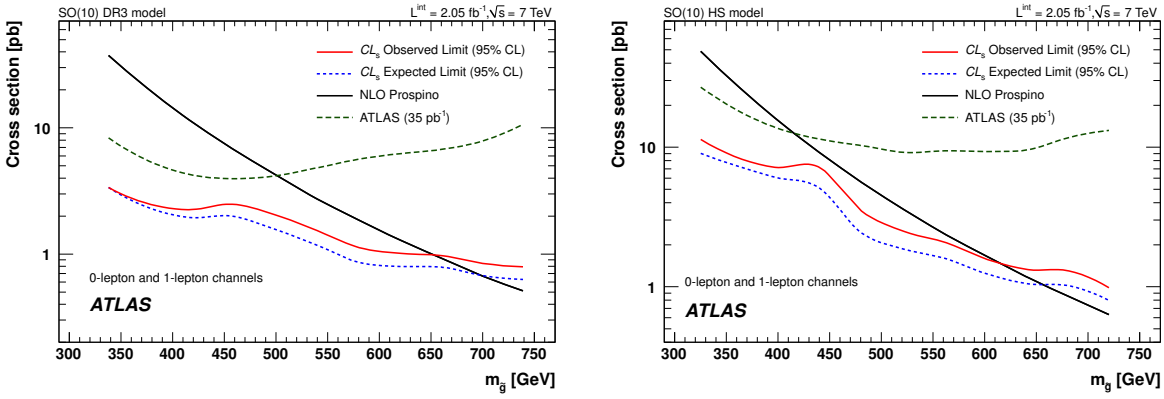

(a) DR3 model **(b)** HS model

Figure 7.12: Observed and expected 95% CL exclusion limits for the (a) DR3 and (b) HS scenarios for a SO(10) GUT. The observed limits (solid red) and expected limits (dashed blue) are provided as upper limits on the signal cross-section as a function of the gluino mass. For each signal point, the selection providing the best expected limit is chosen, also including signal regions with one lepton [155]. The theoretical NLO signal cross-sections (solid black) are calculated with PROSPINO [81]. Previous observed limits obtained for $\mathcal{L} = 35$ pb^{-1} are also shown [153].

7.2 The Three *b*-jets Analysis

A new approach to the gluino-mediated searches for light third generation squarks is accomplished with the three b-jets analysis. It focuses on models, where the gluinos decay via off-shell sbottom or stop quarks. It should be noted that the latest results presented here are published with the same dataset as the sbottom analysis presented in the previous chapter. Thus, many commonalities are found, for example in the preselection and MC input.
In the following subsections, a short summary is given on the input samples (7.2.1), the event selection (7.2.2), the background estimation (7.2.3), systematic uncertainties (7.2.4) and the results (7.2.5).

7.2.1 Data and Monte Carlo Input

Data corresponding to the first 14.0 fb^{-1} of integrated luminosity collected at $\sqrt{s} = 8$ TeV are used for this analysis. The effective luminosity is reduced to 12.8 fb^{-1} by data quality requirements and the chosen trigger. For the SM processes, the same MC samples are used as described in Section 6.1 for the sbottom analysis.
The results of this analysis are interpreted in two signal grids. Both are based on gluino-pair production and each gluino decays to the LSP either through an off-shell sbottom quark (Gbb model) or an off-shell stop quark (Gtt model):

- Gbb: $\tilde{g} \to b\bar{b}\tilde{\chi}_1^0$, $m_{\tilde{b}_1} > m_{\tilde{g}}$
- Gtt: $\tilde{g} \to t\bar{t}\tilde{\chi}_1^0$, $m_{\tilde{t}_1} > m_{\tilde{g}}$

Masses of all other sparticles are set to be above the TeV scale. The signal samples are produced in the gluino-neutralino mass plane. They are generated with HERWIG++, using the CTEQ6L1 PDF set [63]. About 20000 events are produced per signal point with the fast simulation ATLFAST-II in case of the Gbb model and the full detector simulation in case of the Gtt model. The cross-sections are calculated to next-to-leading order precision with PROSPINO and next-to-leading-logarithmic corrections are added for the resummation of soft gluon emission [81, 144, 167–169].

7.2.2 Event Selection

Final states with large $E_{\mathrm{T}}^{\mathrm{miss}}$ and four b-jets are expected for the models considered in this analysis. The event selection is based on reconstructing at least three b-jets and applying a harsh threshold of the effective mass. Two classes of signal regions are defined, one optimised for the Gbb models and the other optimised for the Gtt models. The object definitions, preselection and signal region selections are described in the following.

Object Definition

The methods and thresholds used to identify the objects, based on Section 4.2, are:

Jets: Jets are calibrated with the LCW+JES calibration scheme and are required to have $p_{\mathrm{T}} > 20$ GeV and $|\eta| < 2.8$. The selected jets are sorted by their transverse momentum.

b-Jets: The MV1 algorithm is used to identify b-jets. They are selected at a 75% efficiency working point[11] and are required to have $p_{\mathrm{T}} > 20$ GeV and $|\eta| < 2.5$.[12]

Leptons: Electrons are selected following the *medium* criteria and are required to have $p_{\mathrm{T}} > 20$ GeV and $|\eta| < 2.47$. Muons are identified if a match between the inner detector track and at least one track segment in the muon spectrometer is obtained. They are required to have $p_{\mathrm{T}} > 10$ GeV and $|\eta| < 2.4$.

Preselection

The events are selected with the same $E_{\mathrm{T}}^{\mathrm{miss}}$ trigger as described in Section 6.2.2 for the sbottom-pair production analysis. Also the event cleaning follows closely the one summarised in Table 6.2 of the sbottom analysis.[13]
A $E_{\mathrm{T}}^{\mathrm{miss}}$ threshold of 200 GeV and a p_{T} threshold of 90 GeV for the leading jet is applied to all selections (assuring being in the trigger plateau). Even though leptons can be expected for the Gtt models, where four top quarks are produced, a lepton veto is applied to all signal regions.[14] Two requirements are added to reduce the multi-jet events: $\Delta\phi_{\mathrm{min}} > 0.4$ and $E_{\mathrm{T}}^{\mathrm{miss}}/M_{\mathrm{eff}} > 0.2$. Both variables, $\Delta\phi_{\mathrm{min}}$ and M_{eff}, are calculated from the four leading jets.

Signal Regions

Events are selected that have at least three b-jets with $p_{\mathrm{T}} > 30$ GeV. Two sets of signal regions are defined to achieve a high sensitivity for the Gbb as well as the Gtt models. They are classified by the minimal number of requested jets with $p_{\mathrm{T}} > 50$ GeV:

- SR4: ≥ 4 jets (Gbb model)
- SR6: ≥ 6 jets (Gtt model)

Final states with four jets are expected for the Gbb model, while additional jets from the top quark decays are expected for the Gtt model. The sensitivity of the SR4 selection is enhanced by raising the p_{T} threshold of the b-jets to 50 GeV. The event selections are completed by harsh M_{eff} thresholds. The M_{eff} variable is computed from the four leading jets for the SR4 selection, while all jets with $p_{\mathrm{T}} > 30$ GeV are included in the M_{eff} calculation for the SR6 selection. A loose (L), medium (M) and tight (T) M_{eff} threshold is defined for each selection class. In general, a better sensitivity is achieved with the tight selection for high gluino masses and large gluino-neutralino mass splittings. The looser selections provide a better sensitivity for small $\Delta m(\tilde{g},\tilde{\chi}_1^0)$, as softer jets and lower $E_{\mathrm{T}}^{\mathrm{miss}}$ values are expected. A summary on the signal regions is given in Table 7.12.

7.2.3 Background Estimation

The dominant reducible background for this analysis is $t\bar{t}$+jet production where the third b-jet can arise from misidentifying one of the W decay products. Another major contribu-

11 The working point is defined such that a 75% efficiency is obtained for a $t\bar{t}$ MC sample. The corresponding rejection factors are 58, 4 and 8 for light-jets, c-jets and τ-leptons.

12 In contrast to the sbottom-pair production analysis, the b-tagging scaling factors are applied in this analysis.

13 A small difference exists for the Jet Charged Fraction requirement: here, events are rejected if any of the two leading jets with $p_{\mathrm{T}} > 100$ GeV and $|\eta| < 2.0$ either has chf<0.02 or it has chf<0.05 and the electromagnetic energy fraction is greater than 0.9.

14 In the optimisation study, a similar sensitivity was found for selections based on a high jet multiplicity (≥ 6 jets) and a lepton veto as for selections requiring a lepton.

Description	Signal region	
	SR4-L,M,T	SR6-L,M,T
Trigger	$E_{\mathrm{T}}^{\mathrm{miss}}$ trigger	
Data Quality	Apply event cleaning	
Leptons	No e/μ with $p_{\mathrm{T}} > (20/10)$ GeV	
$E_{\mathrm{T}}^{\mathrm{miss}}$	> 200 GeV	
QCD Rejection	$\Delta\phi_{\mathrm{min}} > 0.4$, $E_{\mathrm{T}}^{\mathrm{miss}}/M_{\mathrm{eff}} > 0.2$	
Jets	$p_{\mathrm{T}}(\mathrm{jet}_1) > 90$ GeV	
	≥ 4 jets with $p_{\mathrm{T}} > 50$ GeV	≥ 6 jets with $p_{\mathrm{T}} > 50$ GeV
b-tagging	$\geq 3b$-jets	
	$p_{\mathrm{T}}(b\text{-jets}) > 50$ GeV	$p_{\mathrm{T}}(b\text{-jets}) > 30$ GeV
M_{eff}	> 900, 1100, 1300 GeV	> 1100, 1300, 1500 GeV

Table 7.12: Summary of the event selections for the three b-jets analysis. The jets are sorted by their transverse momentum. The M_{eff} variable for the final threshold is calculated from the four leading jets (all jets with $p_{\mathrm{T}} > 50$ GeV) for SR4 (SR6).

tion is given by the irreducible process of $t\bar{t}$ production in association with b-jets, which contributes up to 25% of the total background. The $t\bar{t}$ MC sample is produced inclusive with respect to the $t\bar{t} + b/b\bar{b}$ contribution and the truth information of the MC sample is assessed to separate the $t\bar{t} + b/b\bar{b}$ events from the remaining reducible part. While the reducible $t\bar{t}$ background is estimated with a control region, the $t\bar{t} + b/b\bar{b}$ normalisation is taken from MC. Additional reducible background components are single top, $t\bar{t} + W/Z$, diboson and W/Z production in association with heavy-flavour jets. They amount to 10-20% of the total background and are estimated directly from the MC samples. The multi-jet background is studied with the jet-smearing method, but negligible contributions are found for all signal regions (no events pass the selection criteria) and the top control regions ($< 1\%$).

Estimation of the Top Background

The reducible $t\bar{t}$ background is estimated from a control region with exactly two b-jets. Two CR selections are defined, one adapted for SR4 (CR4) and one adapted for SR6 (CR6). The selection of the corresponding signal region is applied apart from the b-jet requirement and relaxed $E_{\mathrm{T}}^{\mathrm{miss}}$ and M_{eff} thresholds. The $E_{\mathrm{T}}^{\mathrm{miss}}$ threshold is reduced to 150 GeV and the M_{eff} threshold to 500 GeV for CR4 and 600 GeV for CR6. In Figure 7.13, the $E_{\mathrm{T}}^{\mathrm{miss}}$ and M_{eff} distributions are shown for the two CRs.

The $t\bar{t}$ background estimation is implemented as a profile likelihood fit, as described in Section 5.8.1. The overall $t\bar{t}$ normalisation is the only free parameter and systematic uncertainties are treated as nuisance parameters.

The fit results are extrapolated to validation regions to cross-check the background estimation. Two validation regions, located kinematically between the corresponding SR and CR, are exploited: one with a reduced $E_{\mathrm{T}}^{\mathrm{miss}}$ selection (150 GeV $< E_{\mathrm{T}}^{\mathrm{miss}} < 200$ GeV, $M_{\mathrm{eff}} > 500$ GeV (VR4-1) or $M_{\mathrm{eff}} > 600$ GeV (VR6-1)) and one with a reduced M_{eff} selection ($E_{\mathrm{T}}^{\mathrm{miss}} > 200$ GeV,

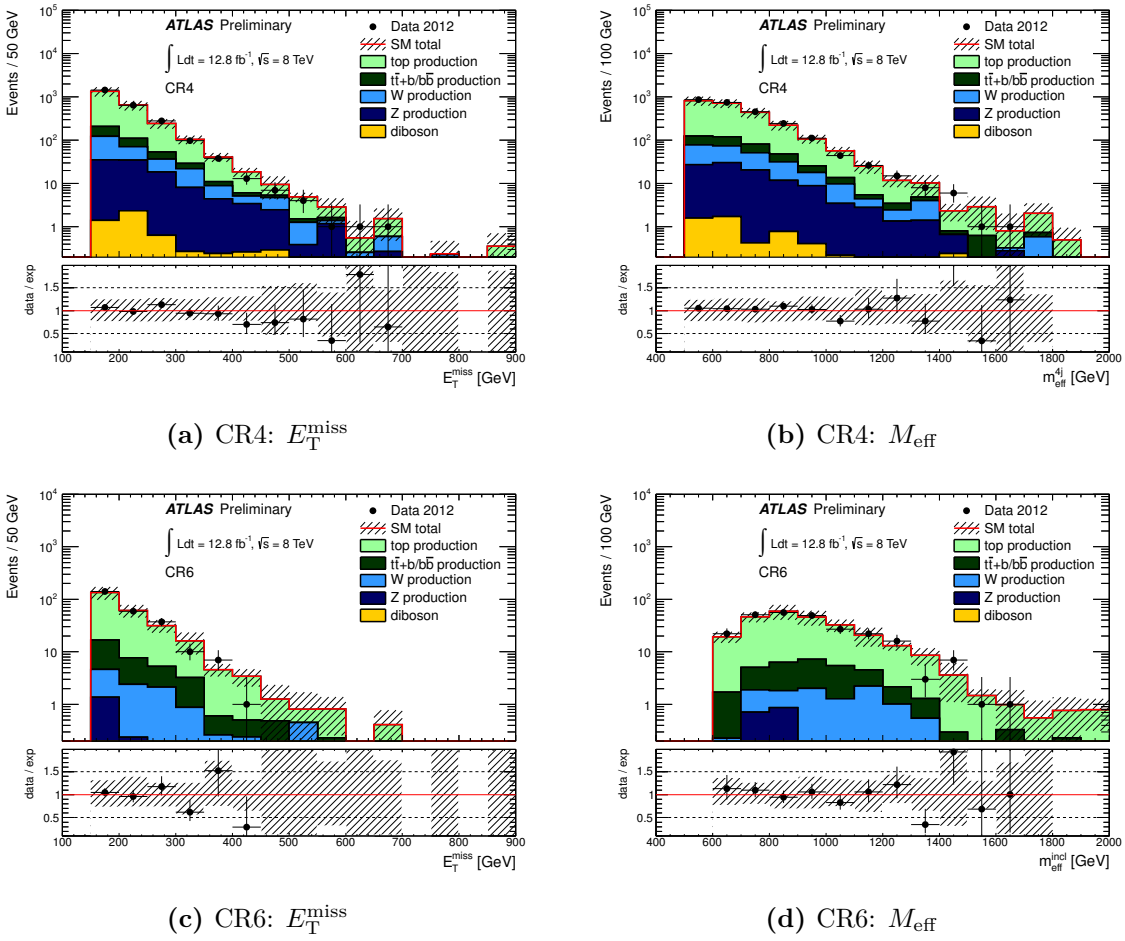

(a) CR4: $E_{\mathrm{T}}^{\mathrm{miss}}$ **(b)** CR4: M_{eff}

(c) CR6: $E_{\mathrm{T}}^{\mathrm{miss}}$ **(d)** CR6: M_{eff}

Figure 7.13: Distributions of $E_{\mathrm{T}}^{\mathrm{miss}}$ and M_{eff} for the CR4 and CR6 control regions before reweighting the $t\bar{t}$ contribution. The error bands include statistical and experimental systematic uncertainties. The reducible $t\bar{t}$, $t\bar{t}+W/Z$ and single top processes are included in "top production".

500 GeV $< M_{\mathrm{eff}} <$ 900 (VR4-2) or 600 GeV $< M_{\mathrm{eff}} <$ 1100 (VR6-2)) compared to the SR selection. Results obtained for the control and validation regions associated with SR4 and SR6 are given in Table 7.13 and 7.14, respectively. The expected SM event yields are found in agreement with the observed event yields for all validation regions.

7.2.4 Systematic Uncertainties

Experimental and theoretical uncertainties are investigated and added as nuisance parameters in the profile likelihood fit for the background estimation. The experimental uncertainties are dominated by the JES, JER and b-tagging uncertainties. Additional uncertainties are included for the pile-up reweighting, the energy scale and resolution of the $E_{\mathrm{T}}^{\mathrm{miss,CellOut}}$ term and the luminosity measurement.
Several effects for the MC modelling are investigated for the reducible $t\bar{t}$ background component. The generator choice is evaluated by comparing the POWHEG event yields to event yields obtained with samples generated with ALPGEN. The nominal POWHEG samples, interfaced to PYTHIA, are compared to samples generated with POWHEG interfaced to JIMMY and HERWIG to assess the parton shower uncertainty. ISR and FSR uncertainties

Channel	CR4	VR4-1	VR4-2
Observed events	2518	249	158
Total background events	2518 ± 80	291 ± 50	176 ± 30
(MC prediction)	(2400 ± 700)	(280 ± 100)	(170 ± 60)
$t\bar{t}$ + jets events	1936 ± 200	217 ± 40	126 ± 24
(MC prediction)	(1800 ± 600)	(210 ± 70)	(120 ± 40)
$t\bar{t} + b/b\bar{b}$ events	155 ± 150	46 ± 46	25 ± 25
single top events	125 ± 45	12 ± 5	8 ± 3
$t\bar{t} + W/Z$ events	28 ± 15	3 ± 2	4 ± 2
W/Z events	269 ± 120	12 ± 7	13 ± 8
diboson events	5 ± 3	–	–
Gbb: $(m_{\tilde{g}}, m_{\tilde{\chi}_1^0}) = (1000, 600)$ GeV	39 ± 16	12 ± 2	29 ± 5
Gbb: $(m_{\tilde{g}}, m_{\tilde{\chi}_1^0}) = (1200, 1)$ GeV	8.9 ± 5.5	0.1 ± 0.1	0.1 ± 0.1

Table 7.13: Expected and observed event yields obtained for CR4 and the validation regions associated with CR4. For the $t\bar{t}$ and total SM predictions, the nominal MC expectation is given in addition to the result from the background fit. The expectations for two Gbb signal points, one with small and one with large $\Delta m(\tilde{g},\tilde{\chi}_1^0)$, are also given. Statistical plus systematic uncertainties are shown (for the signal points no theoretical uncertainties are included).

Channel	CR6	VR6-1	VR6-2
Observed events	255	52	34
Total background events	255 ± 20	55 ± 15	32 ± 9
(MC prediction)	(255 ± 100)	(55 ± 26)	(32 ± 17)
$t\bar{t}$ + jets events	205 ± 30	35 ± 8	20 ± 5
(MC prediction)	(205 ± 80)	(35 ± 16)	$(20 \pm 11$)
$t\bar{t} + b/b\bar{b}$ events	24 ± 24	16 ± 16	9 ± 9
single top events	10 ± 4	2 ± 1	1 ± 1
$t\bar{t} + W/Z$ events	5 ± 3	1 ± 1	1 ± 1
W/Z events	11 ± 6	1 ± 1	2 ± 1
diboson events	–	–	–
Gtt: $(m_{\tilde{g}}, m_{\tilde{\chi}_1^0}) = (1000, 400)$ GeV	15 ± 5	5.9 ± 0.6	8.6 ± 0.8
Gtt: $(m_{\tilde{g}}, m_{\tilde{\chi}_1^0}) = (1200, 1)$ GeV	3.6 ± 1.6	0.2 ± 0.1	0.1 ± 0.1

Table 7.14: Expected and observed event yields obtained for CR6 and the validation regions associated with CR6. For the $t\bar{t}$ and total SM predictions, the nominal MC expectation is given in addition to the result from the background fit. The expectations for two Gtt signal points, one with small and one with large $\Delta m(\tilde{g},\tilde{\chi}_1^0)$, are also given. Statistical plus systematic uncertainties are shown (for the signal points no theoretical uncertainties are included).

are estimated from dedicated ACERMC samples. Also for single top events, ACERMC samples are used to assess the ISR and FSR uncertainties. A ±100% uncertainty is assumed for the $t\bar{t} + b/b\bar{b}$ contribution and a ±50% uncertainty for the $t\bar{t} + W/Z$ events.
For the W and Z production, uncertainties were evaluated in detail for the 2011 data results [156] and a ±60% (±100%) uncertainty is assumed for W (Z) production in association with b-jets.
Theoretical uncertainties for the signal samples include uncertainties on the PDF set and renormalisation and factorisation scales [149]. They amount to ±15% for $m_{\tilde{g}} \sim 200$ GeV and increase to ±40% for $m_{\tilde{g}} \sim 1400$ GeV. Experimental uncertainties for the signal samples are dominated by JES and b-tagging uncertainties and sum up to values of ±(2-25)%.

7.2.5 Results and Interpretation

In this section, the results obtained for the three b-jet analysis are summarised. The observed and expected background event yields are shown in Table 7.15 for the SR4 and Table 7.16 for the SR6 selections. The expected event yields for two representative signal points are also given. Good agreement between the observed and expected SM event yields is observed for all signal regions. The contribution of the reducible top background is dominant for all signal regions. The $E_{\mathrm{T}}^{\mathrm{miss}}$ and M_{eff} distributions are shown in Fig. 7.14 for the SR4-L and SR6-L selections. The distributions for the expected background events agree with the distributions for the data events within their uncertainties.
Since no deviation from the SM expectation is observed, direct limits on the number of generic signal events and the corresponding visible cross-sections are calculated for all signal regions. The results are given in Table 7.17.
Exclusion limits for the Gbb and Gtt signal models, as introduced in Section 7.2.1, are presented in Fig. 7.15 in the ($m_{\tilde{g}}$-$m_{\tilde{\chi}_1^0}$) plane. For the Gbb model, gluino masses up to 1240 GeV are excluded for massless neutralinos and neutralino masses up to 570 GeV are excluded for $m_{\tilde{g}} \sim 1100$ GeV. For the Gtt model, gluino masses up to 1150 GeV are excluded for $m_{\tilde{\chi}_1^0} < 200$ GeV and neutralino masses up to 440 GeV are excluded for $m_{\tilde{g}} \sim 1100$ GeV. At very low gluino-neutralino mass splittings, no sensitivity is achieved for the Gbb model as soft jets and very low $E_{\mathrm{T}}^{\mathrm{miss}}$ are expected. A gain of about 250 GeV is obtained for both models compared to the previous results published with the 2011 dataset [156].

Channel	SR4-L	SR4-M	SR4-T
Observed events	38	8	4
Total background events	46 ± 10	10.7 ± 2.9	2.9 ± 1.0
(MC prediction)	(44 ± 17)	(10.3 ± 4.6)	(2.7 ± 1.3)
$t\bar{t}$ + jets events	30 ± 6	7.0 ± 1.8	2.4 ± 0.9
(MC prediction)	(29 ± 11)	(6.6 ± 2.5)	(2.3 ± 1.1)
$t\bar{t} + b/b\bar{b}$ events	8.1 ± 8.3	2.5 ± 2.5	0.1 ± 0.2
single top events	3.5 ± 1.3	0.4 ± 0.5	0.2 ± 0.1
$t\bar{t} + W/Z$ events	1.4 ± 0.8	0.5 ± 0.3	0.2 ± 0.1
W/Z events	2.6 ± 1.9	0.4 ± 0.6	–
diboson events	–	–	–
Gbb: $(m_{\tilde{g}}, m_{\tilde{\chi}_1^0}) = (1000, 600)$ GeV	30 ± 7	11 ± 3	3.8 ± 1.3
Gbb: $(m_{\tilde{g}}, m_{\tilde{\chi}_1^0}) = (1200, 1)$ GeV	17 ± 2	17 ± 2	15 ± 2

Table 7.15: Predicted SM background and observed event yield for the signal regions with four jets. For the $t\bar{t}$ and total SM predictions, the nominal MC expectation is given in addition to the result from the background fit. The expectations for two Gbb signal points, one with small and one with large $\Delta m(\tilde{g},\tilde{\chi}_1^0)$, are also given. Statistical plus systematic uncertainties are shown (for the signal points no theoretical uncertainties are included).

Channel	SR6-L	SR6-M	SR6-T
Observed events	20	4	2
Total background events	18 ± 6	6.3 ± 2.4	2.2 ± 1.3
(MC prediction)	(18 ± 9)	(6.3 ± 3.4)	(2.2 ± 1.8)
$t\bar{t}$ + jets events	12 ± 4	4.3 ± 1.9	1.7 ± 1.0
(MC prediction)	(12 ± 6)	(4.3 ± 2.4)	(1.7 ± 1.5)
$t\bar{t} + b/b\bar{b}$ events	4.6 ± 5.0	1.3 ± 1.4	0.2 ± 0.3
single top events	0.6 ± 0.3	0.4 ± 0.2	0.2 ± 0.1
$t\bar{t} + W/Z$ events	0.8 ± 0.4	0.3 ± 0.2	0.1 ± 0.1
W/Z events	0.1 ± 0.1	–	–
diboson events	–	–	–
Gtt: $(m_{\tilde{g}}, m_{\tilde{\chi}_1^0}) = (1000, 400)$ GeV	18 ± 3	8.8 ± 2.2	3.6 ± 1.2
Gtt: $(m_{\tilde{g}}, m_{\tilde{\chi}_1^0}) = (1200, 1)$ GeV	8.2 ± 0.4	7.8 ± 0.5	6.8 ± 0.6

Table 7.16: Predicted SM background and observed event yields for the signal regions with six jets. For the $t\bar{t}$ and total SM predictions, the nominal MC expectation is given in addition to the result from the background fit. The expectations for two Gtt signal points, one with small and one with large $\Delta m(\tilde{g},\tilde{\chi}_1^0)$, are also given. Statistical plus systematic uncertainties are shown (for the signal points no theoretical uncertainties are included).

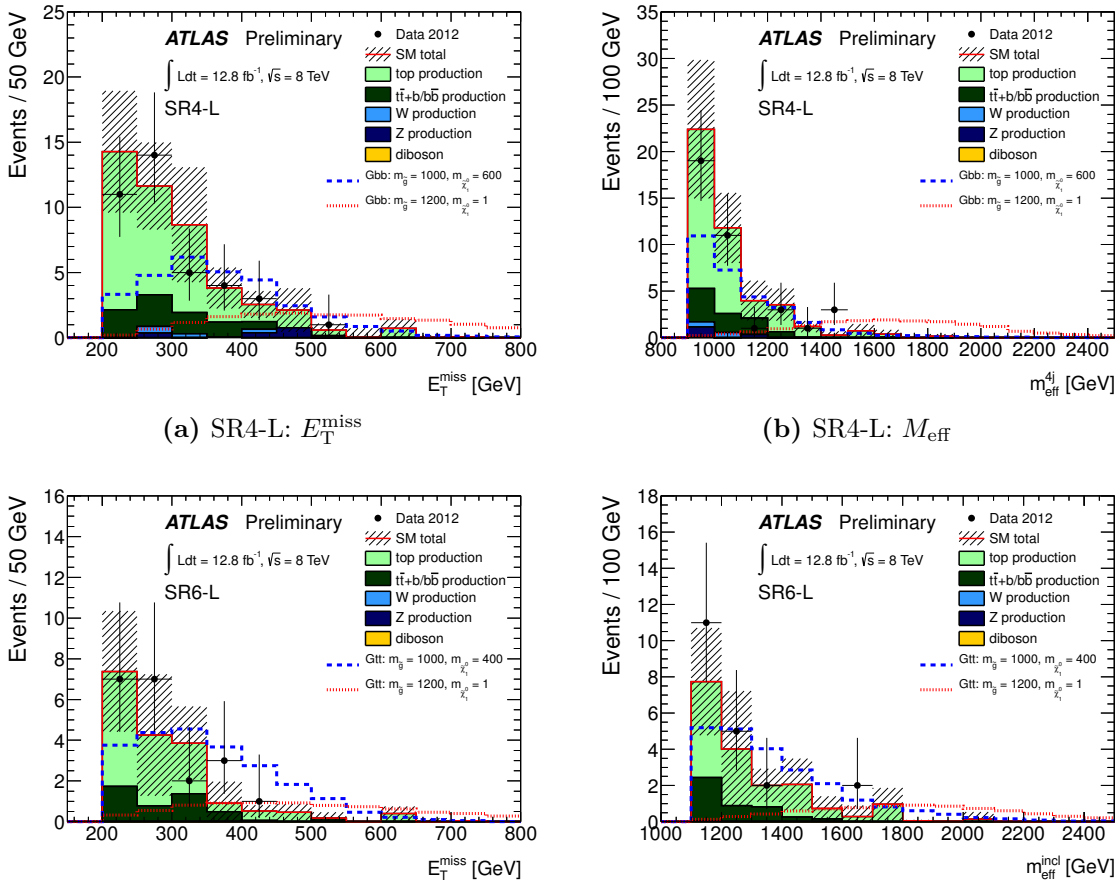

(a) SR4-L: $E_{\mathrm{T}}^{\mathrm{miss}}$ **(b)** SR4-L: M_{eff}

(c) SR6-L: $E_{\mathrm{T}}^{\mathrm{miss}}$ **(d)** SR6-L: M_{eff}

Figure 7.14: Distributions of $E_{\mathrm{T}}^{\mathrm{miss}}$ and M_{eff} the SR4-L and SR6-L signal regions. The SM expectations are shown before applying the background fit. The error bands include statistical and experimental systematic uncertainties. Two Gbb (Gtt) signal points are overlaid in the SR4-L (SR6-L) plots, one with small and one with large $\Delta m(\tilde{g},\tilde{\chi}_1^0)$.

Signal Region	UL on BSM event yield		UL on σ_{vis} [fb]	
	observed	expected	observed	expected
SR4-L	17.9	$20.5^{+8.0}_{-5.2}$	1.4	1.6
SR4-M	7.6	$8.8^{+3.5}_{-2.1}$	0.59	0.69
SR4-T	6.5	$5.0^{+2.2}_{-1.1}$	0.51	0.39
SR6-L	17.0	$15.5^{+6.2}_{-3.8}$	1.3	1.2
SR6-M	5.9	$6.6^{+2.8}_{-1.5}$	0.46	0.52
SR6-T	5.1	$4.6^{+1.9}_{-0.6}$	0.40	0.36

Table 7.17: Observed and expected upper limits (UL) at 95% CL on the number of signal events and the visible cross-section σ_{vis} for all signal regions. The systematic uncertainties on the SM background estimation are included.

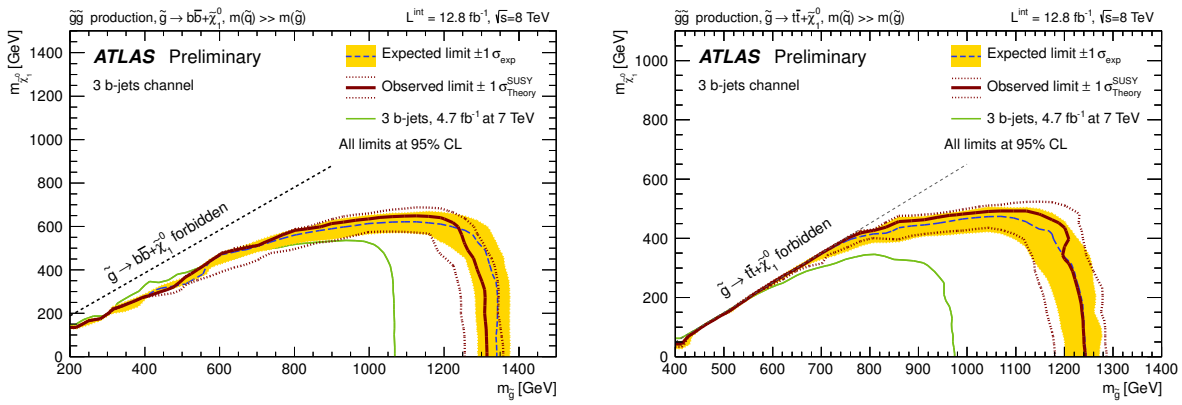

(a) Gbb **(b)** Gtt

Figure 7.15: Expected and observed exclusion limits for the (a) Gbb and (b) Gtt model in the ($m_{\tilde{g}}$-$m_{\tilde{\chi}_1^0}$) plane at 95% CL. The dashed blue lines with yellow bands show the expected limits with their $\pm 1\sigma$ uncertainty. Theoretical uncertainties for the signal are not included in the expected limits. The nominal observed limits are indicated by the solid red lines, while the dashed red lines show the observed limits if theoretical uncertainties for the signal are taken into account. For each signal point, the selection providing the best expected limit is chosen. For reference, the previous limits obtained with the 2011 dataset are also shown [156].

7.3 Summary for the Gluino-Mediated Sbottom Production

In this chapter, the production of gluino pairs is investigated, where a decay of the gluinos to the LSP via a sbottom quark is assumed. Two analysis are presented, the first published with data corresponding to an integrated luminosity of 2.05 fb^{-1} of the 2011 dataset and the second published with data corresponding to an integrated luminosity of 12.8 fb^{-1} of the 2012 dataset. In the latter case, also the gluino-mediated stop production is included. For both analyses, good agreement between the predicted SM event yields and the observed data events is obtained.
The $\mathcal{L} = 2.05$ fb^{-1} analysis is based on selections with at least one or two b-jets and harsh M_{eff} thresholds. The results are interpreted in a phenomenological MSSM model (Gluino-Sbottom), a simplified model (Gbb) and two SO(10) scenarios (DR3 and HS). The following limits are obtained at 95% CL:

- $m_{\tilde{g}} > 900$ GeV for $m_{\tilde{b}_1} < 800$ GeV (Gluino-Sbottom)
- $m_{\tilde{g}} > 900$ GeV for $m_{\tilde{\chi}_1^0} < 300$ GeV (Gbb)
- $m_{\tilde{g}} > 650$ GeV (DR3)
- $m_{\tilde{g}} > 620$ GeV (HS)

The event selection is adapted to require at least three b-jets for the $\mathcal{L} = 12.8$ fb^{-1} analysis. The results are interpreted in simplified models with gluino-mediated sbottom (Gbb) and stop (Gtt) production. Signal regions with at least four jets are optimised for the Gbb models, while selections with at least six jets are used for the Gtt models. The following limits are obtained at 95% CL:

- $m_{\tilde{g}} > 1240$ GeV for $m_{\tilde{\chi}_1^0} = 0$, $m_{\tilde{\chi}_1^0} > 570$ GeV for $m_{\tilde{g}} \sim 1100$ GeV (Gbb)
- $m_{\tilde{g}} > 1150$ GeV for $m_{\tilde{\chi}_1^0} < 200$ GeV, $m_{\tilde{\chi}_1^0} > 440$ GeV for $m_{\tilde{g}} \sim 1100$ GeV (Gtt)

The limits for the Gbb model are significantly improved by the updated analysis.
In general, complementary results to the sbottom-pair production analysis are provided by the gluino-mediated searches.

CHAPTER 8

Summary

Several analyses targeting the possible production of third generation squarks in the ATLAS detector are presented. The main focus is set on the search for the supersymmetric partner of the bottom quark, the sbottom particle. Scenarios with stop production are considered in cases where similar final state topologies are expected.

An enhanced production of the third generation squarks at the LHC is characteristic for supersymmetric extensions of the Standard Model that provide a natural solution of the hierarchy problem because the stop and sbottom particles are required to be light compared to other SUSY particles. The analyses are performed within the context of R-parity conserving SUSY scenarios, where the lightest supersymmetric particle is stable. In the exploited models, the lightest neutralino is assumed to be the LSP, which provides a good candidate for dark matter.
Two different scenarios for the sbottom and stop production are considered, the direct pair production and the gluino-mediated production in case of light gluinos. In general, the final state topologies are based on b-jets (coming from the sbottom or stop decays), missing transverse momentum (coming from the LSPs that leave the detector undetected) and a veto on leptons (a focus is set on scenarios where no leptons occur in the decay chains).
For the direct sbottom-pair production scenarios, a 100% branching ratio for the $\tilde{b}_1 \to b\tilde{\chi}_1^0$ decay is assumed and exactly two b-jets are expected in the final state. A similar topology is provided by models considering direct stop-pair production, where the stop decays via a chargino to the neutralino in case of small chargino-neutralino mass differences, $\tilde{t}_1 \to b\tilde{\chi}_1^\pm \to bW^*\tilde{\chi}_1^0 \to bf\bar{f}\tilde{\chi}_1^0$, such that the additional fermions are not reconstructed.
Several models are considered for the gluino-mediated production. The main scenarios assume gluino-pair production, and a subsequent decay of the gluinos to the LSP via sbottom or stop particles, which can be on- or off-shell ($\tilde{g} \to b\tilde{b}_1^{(*)} \to b\bar{b}\tilde{\chi}_1^0$ or $\tilde{g} \to t\tilde{t}_1^{(*)} \to t\bar{t}\tilde{\chi}_1^0$). For these models, the final states have exactly four b-jets. Additional jets from the top decays are expected in models for gluino-mediated stop production.
For each analysis, specific signal-region selections are exploited to gain sensitivity for the different parameter configurations of the considered scenarios. Dedicated methods are applied to ensure a robust estimation of the Standard Model background contributions. A fundamental strategy is based on extracting the normalisations for the main background contributions from data using control regions. For all analyses good agreement between the observed data event yields and the predicted Standard Model contributions is found and the results are used to set upper limits on the SUSY signals. The exclusion limits obtained at 95% CL by the different analyses are summarised in the following.

The results presented for the direct sbottom- and stop-pair production are based on data corresponding to an integrated luminosity of 12.8 fb^{-1}, collected in pp collisions at $\sqrt{s} = 8$ TeV. For scenarios with sbottom-pair production, where each sbottom decays via $\tilde{b}_1 \to b\tilde{\chi}_1^0$ with a 100% BR, sbottom masses up to 620 GeV are excluded for massless neutralinos. Neutralino masses up to 320 GeV are excluded for $m_{\tilde{b}_1} \simeq 550$ GeV. The limits obtained for scenarios with stop-pair production, where $\tilde{t}_1 \to b\tilde{\chi}_1^{\pm} \to bW^*\tilde{\chi}_1^0 \to bf\bar{f}\tilde{\chi}_1^0$ with 100% BR is assumed, highly depend on the chargino-neutralino mass splitting. For $\Delta m(\tilde{\chi}_1^{\pm},\tilde{\chi}_1^0) = 5$ GeV, stop masses up to 580 GeV are excluded for $m_{\tilde{\chi}_1^0} \simeq 100$ GeV. The limit is lowered to 480 GeV for $\Delta m(\tilde{\chi}_1^{\pm},\tilde{\chi}_1^0) = 20$ GeV.

For the gluino-mediated production, two analyses are presented. The first is based on selections with at least one or two b-jets and uses data corresponding to an integrated luminosity of 2.05 fb^{-1}, collected in pp collisions at $\sqrt{s} = 7$ TeV. For models considering $\tilde{g}\tilde{g}$ and $\tilde{b}_1\tilde{b}_1$ production with subsequent $\tilde{g} \to b\bar{b}\tilde{b}_1$ and $\tilde{b}_1 \to b\tilde{\chi}_1^0$ decays, gluino masses up to 900 GeV are excluded for $m_{\tilde{b}_1} < 800$ GeV and $m_{\tilde{\chi}_1^0} = 60$ GeV. For scenarios based on the decays via off-shell sbottoms ($\tilde{g} \to b\bar{b}\tilde{\chi}_1^0$ with 100% BR), gluino masses up to 900 GeV are excluded for $m_{\tilde{\chi}_1^0} < 300$ GeV. Additional interpretations of the results are presented for SO(10) GUT scenarios, excluding gluino masses up to 650 (620) GeV for models assuming D-term (Higgs) splitting.
The second analysis is based on selections with at least three b-jets. The results are presented for data corresponding to an integrated luminosity of 12.8 fb^{-1}, collected in pp collisions at $\sqrt{s} = 8$ TeV. Gluino masses up to 1240 GeV are excluded for models considering the decays via off-shell sbottoms ($\tilde{g}\tilde{g}$ production with $\tilde{g} \to b\bar{b}\tilde{\chi}_1^0$ with 100% BR) in case of massless neutralinos. Neutralino masses up to 570 GeV are excluded for $m_{\tilde{g}} \simeq 1100$ GeV. For scenarios considering the decays via off-shell stops ($\tilde{g}\tilde{g}$ production with $\tilde{g} \to t\bar{t}\tilde{\chi}_1^0$ with 100% BR), gluino masses up to 1150 GeV are excluded for $m_{\tilde{\chi}_1^0} < 200$ GeV.

The results presented in this thesis give an outstanding contribution to the SUSY search effort by the ATLAS collaboration. Together with the results from searches for first and second generation squarks, the direct stop production and the electroweak SUSY production, these results exclude large regions of the SUSY parameter space. Nevertheless, given the huge number of possible SUSY configurations, there are still many scenarios that could not yet be tested with the available data. In the coming years, the LHC is expected to operate at higher centre-of-mass energies of 13-14 TeV and collect data up to an integrated luminosity of about 300 fb^{-1}. This will open new search possibilities, providing sensitivity to the scenarios that are currently out of reach.

Bibliography

[1] UA1 Collaboration, G. Arnison et al.: *Experimental Observation of Isolated Large Transverse Energy Electrons with Associated Missing Energy at $\sqrt{s}$ =540 GeV.* Phys. Lett. B122 (1983) 103–116 (Cited on page 1)

[2] UA2 Collaboration, M. Banner et al.: *Observation of Single Isolated Electrons of High Transverse Momentum in Events with Missing Transverse Energy at the CERN $\bar{p}p$ Collider.* Phys. Lett. B122 (1983) 476–485 (Cited on page 1)

[3] UA1 Collaboration, G. Arnison et al.: *Experimental Observation of Lepton Pairs of Invariant Mass Around 95 GeV/c^2 at the CERN SPS Collider.* Phys. Lett. B126 (1983) 398–410 (Cited on page 1)

[4] UA2 Collaboration, P. Bagnaia et al.: *Evidence for $Z^0 \to e^+e^-$ at the CERN $\bar{p}p$ Collider.* Phys. Lett. B129 (1983) 130–140 (Cited on page 1)

[5] CDF Collaboration, F. Abe et al.: *Observation of Top Quark Production in $\bar{p}p$ Collisions.* Phys. Rev. Lett. 74 (1995) 2626 (Cited on page 1)

[6] DØ Collaboration, S. Abachi et al.: *Observation of the Top Quark.* Phys. Rev. Lett. 74 (1995) 2632 (Cited on page 1)

[7] ATLAS Collaboration, G. Aad et al.: *Observation of a new particle in the search for the Standard Model Higgs boson with the ATLAS detector at the LHC.* Phys. Lett. B716 (2012) 1–29 (Cited on pages 1 and 5)

[8] CMS Collaboration, S. Chatrchyan et al.: *Observation of a new boson at a mass of 125 GeV with the CMS experiment at the LHC.* Phys. Lett. B716 (2012) 30–61 (Cited on pages 1 and 5)

[9] F. Halzen and A. Martin: *Quarks and Leptons.* John Wiley & Sons, 1984 (Cited on page 3)

[10] M. E. Peskin and D. V. Schroeder: *An Introduction to Quantum Field Theory.* Westview Press, 1995 (Cited on page 3)

[11] ATLAS Collaboration, G. Aad et al.: *Search for down-type fourth generation quarks with the ATLAS detector in events with one lepton and hadronically decaying W bosons.* Phys. Rev. Lett. 109 (2012) 032001 (Cited on page 4)

[12] ATLAS Collaboration, G. Aad et al.: *Search for same-sign top-quark production and fourth-generation down-type quarks in pp collisions at $\sqrt{s}$ = 7 TeV with the ATLAS detector.* JHEP 04 (2012) 069 (Cited on page 4)

[13] ALEPH Collaboration, DELPHI Collaboration, L3 Collaboration, OPAL Collaboration, SLD Collaboration, LEP Electroweak Working Group, SLD Electroweak and Heavy Flavour Groups: *Precision Electroweak Measurements on the Z Resonance.* Phys. Rep. 427 (2006) 257 (Cited on page 4)

[14] Particle Data Group, J. Beringer et al.: *Review of Particle Physics.* Phys. Rev. D86 (2012) 010001 (Cited on pages 4 and 45)

[15] Particle Data Group, J. Beringer et al.: *Review of Particle Physics: 13. Neutrino mass, mixing, and oscillations.* Phys. Rev. D86 (2012) 010001 (Cited on pages 4 and 7)

[16] ATLAS Collaboration: *Combined measurements of the mass and signal strength of the Higgs-like boson with the ATLAS detector using up to 25 fb^{-1} of proton-proton collision data.* CERN, Geneva, Mar 2013 (ATLAS-CONF-2013-014) (Cited on page 5)

[17] CMS Collaboration: *Combination of standard model Higgs boson searches and measurements of the properties of the new boson with a mass near 125 GeV.* CERN, Geneva, 2012 (CMS-PAS-HIG-12-045) (Cited on page 5)

[18] S. Glashow: *Partial Symmetries of Weak Interactions.* Nucl. Phys. 22 (1961) 579–588 (Cited on pages 5 and 8)

[19] S. Weinberg: *A Model of Leptons.* Phys. Rev. Lett. 19 (1967) 1264–1266 (Cited on pages 5 and 8)

[20] A. Salam: *Weak and Electromagnetic Interactions.* Svartholm: Elementary Particle Theory, Proceedings Of The Nobel Symposium Held 1968 At Lerum, Sweden (1968) (Cited on pages 5 and 8)

[21] E. Noether: *Invariante Variationsprobleme.* Nachr. d. König. Gesellsch. d. Wiss. zu Göttingen, Math-phys. Klasse (1918) 235–257 (Cited on page 5)

[22] M. Kobayashi and T. Maskawa: *CP-Violation in the Renormalizable Theory of Weak Interaction.* Progress of Theoretical Physics 49 (1973) 652–657 (Cited on page 7)

[23] P. W. Higgs: *Broken Symmetries and the Masses of Gauge Bosons.* Phys. Rev. Lett. 13 (1964) 508–509 (Cited on page 9)

[24] F. Englert and R. Brout: *Broken Symmetry and the Mass of Gauge Vector Mesons.* Phys. Rev. Lett. 13 (1964) 321–323 (Cited on page 9)

[25] G. Guralnik, C. Hagen and T. Kibble: *Global Conservation Laws and Massless Particles.* Phys. Rev. Lett. 13 (1964) 585–587 (Cited on page 9)

[26] S. Martin: *A Supersymmetry Primer.* arXiv:hep-ph/9709356, 1997 (Cited on pages 11, 13, 15, 20, and 54)

[27] M. E. Peskin: *Supersymmetry in Elementary Particle Physics.* arXiv:0801.1928 [hep-ph], 2008 (Cited on page 11)

[28] Planck Collaboration, P. Ade et al.: *Planck 2013 results. XVI. Cosmological parameters.* arXiv:1303.5076 [astro-ph.CO], 2013 (Cited on page 13)

[29] D. B. Cline: *Recent results on the low mass dark matter WIMP controversy: 2011.* arXiv:1109.1799 [astro-ph.CO], 2011 (Cited on page 13)

[30] A. Einstein: *Die Grundlage der allgemeinen Relativitätstheorie.* Annalen der Physik 49 7 (1916) 50 (Cited on page 13)

[31] J. Wess and B. Zumino: *Supergauge transformations in four dimensions.* Nucl. Phys. B70 (1974) 39 – 50 (Cited on page 14)

[32] R. Haag, J. T. Lopuszanski and M. Sohnius: *All possible generators of supersymmetries of the S-matrix.* Nucl. Phys. B88 (1975) 257–274 (Cited on page 14)

[33] H. D. Politzer and S. Wolfram: *Bounds on particle masses in the Weinberg-Salam model.* Phys. Lett. B82 (1979) 245 (Cited on page 16)

[34] L. Maiani, G. Parisi and R. Petronzio: *Bounds on the number and masses of quarks and leptons.* Nucl. Phys. B136 (1978) 115 (Cited on page 16)

[35] F. Riva, C. Biggio and A. Pomarol: *Is the 125 GeV Higgs the superpartner of a neutrino?* JHEP 02 (2013) 081 (Cited on page 17)

[36] T. Hebbeker: *Can the sneutrino be the lightest supersymmetric particle?* Phys. Lett. B470 (1999) 259–262 (Cited on page 17)

[37] A. Djouadi, J. Kneur and G. Moultaka: *SuSpect: A Fortran Code for the Supersymmetric and Higgs Particle Spectrum in the MSSM.* Comp. Phys. Comm. 176 (2007) 426 (Cited on page 19)

[38] J. Alwall, P. Schuster and N. Toro: *Simplified Models for a First Characterization of New Physics at the LHC.* Phys. Rev. D79 (2009) 075020 (Cited on page 19)

[39] A. H. Chamseddine, R. Arnowitt and P. Nath: *Locally Supersymmetric Grand Unification.* Phys. Rev. Lett. 49 (1982) 970 (Cited on page 19)

[40] R. Barbieri, S. Ferrara and C. A. Savoy: *Gauge Models with Spontaneously Broken Local Supersymmetry.* Phys. Lett. B119 (1982) 343 (Cited on page 19)

[41] L. J. Hall, J. D. Lykken and S. Weinberg: *Supergravity as the Messenger of Supersymmetry Breaking.* Phys. Rev. D27 (1983) 2359–2378 (Cited on page 19)

[42] N. Ohta: *Grand Unified Theories Based on Local Supersymmetry.* Prog. Theor. Phys. 70 (1983) 542 (Cited on page 19)

[43] G. L. Kane, C. F. Kolda, L. Roszkowski and J. D. Wells: *Study of constrained minimal supersymmetry.* Phys. Rev. D49 (1994) 6173–6210 (Cited on page 19)

[44] M. Dine and W. Fischler: *A Phenomenological Model of Particle Physics Based on Supersymmetry.* Phys. Lett. B110 (1982) 227 (Cited on page 19)

[45] L. Alvarez-Gaume, M. Claudson and M. B. Wise: *Low-Energy Supersymmetry.* Nucl. Phys. B207 (1982) 96 (Cited on page 19)

[46] C. R. Nappi and B. A. Ovrut: *Supersymmetric Extension of the SU(3) x SU(2) x U(1) Model.* Phys. Lett. B113 (1982) 175 (Cited on page 19)

[47] M. Dine and A. E. Nelson: *Dynamical supersymmetry breaking at low-energies.* Phys. Rev. D48 (1993) 1277–1287 (Cited on page 19)

[48] M. Dine, A. E. Nelson and Y. Shirman: *Low-energy dynamical supersymmetry breaking simplified.* Phys. Rev. D51 (1995) 1362–1370 (Cited on page 19)

[49] M. Dine, A. E. Nelson, Y. Nir and Y. Shirman: *New tools for low-energy dynamical supersymmetry breaking.* Phys. Rev. D53 (1996) 2658–2669 (Cited on page 19)

[50] H. Baer, S. Kraml, A. Lessa and S. Sekmen: *Testing Yukawa-unified SUSY during year 1 of LHC: the role of multiple b-jets, dileptons and missing E_T.* JHEP 02 (2010) 055 (Cited on pages 19 and 21)

[51] H. Fritzsch and P. Minkowski: *Unified Interactions of Leptons and Hadrons.* Annals of Physics 93 (1975) 193 (Cited on page 21)

[52] M. Papucci, J. T. Ruderman and A. Weiler: *Natural SUSY Endures.* JHEP 09 (2012) 035 (Cited on pages 22 and 23)

[53] J. M. Campbell, J. Huston and W. Stirling: *Hard Interactions of Quarks and Gluons: A Primer for LHC Physics.* Rept. Prog. Phys. 70 (2007) 89 (Cited on page 24)

[54] T. Gleisberg et al.: *SHERPA 1.α, a Proof-of-Concept Version.* JHEP 02 (2004) 056 (Cited on pages 25 and 28)

[55] J. C. Collins, D. E. Soper and G. F. Sterman: *Factorization of Hard Processes in QCD.* Adv. Ser. Direct. High Energy Phys. 5 (1988) 1–91 (Cited on page 24)

[56] V. Gribov and L. Lipatov: *Deep inelastic e p scattering in perturbation theory.* Sov. J. Nucl. Phys. 15 (1972) 438–450 (Cited on page 25)

[57] G. Altarelli and G. Parisi: *Asymptotic Freedom in Parton Language.* Nucl. Phys. B126 (1977) 298 (Cited on page 25)

[58] Y. L. Dokshitzer: *Calculation of the Structure Functions for Deep Inelastic Scattering and e+ e- Annihilation by Perturbation Theory in Quantum Chromodynamics.* Sov. Phys. JETP 46 (1977) 641–653 (Cited on page 25)

[59] H1 Collaboration, ZEUS Collaboration, V. Radescu: *HERA Precision Measurements and Impact for LHC Predictions.* arXiv:1107.4193 [hep-ex], 2011 (Cited on page 25)

[60] A. Martin, W. Stirling, R. Thorne and G. Watt: *Parton distributions for the LHC.* Eur. Phys. J. C63 (2009) 189–285 (Cited on pages 25 and 26)

[61] H.-L. Lai, M. Guzzi, J. Huston, Z. Li, P. M. Nadolsky et al.: *New parton distributions for collider physics.* Phys. Rev. D82 (2010) 074024 (Cited on pages 25 and 74)

[62] P. M. Nadolsky et al.: *Implications of CTEQ global analysis for collider observables.* Phys. Rev. D78 (2008) 013004 (Cited on pages 25 and 126)

[63] J. Pumplin, D. Stump, J. Huston, H. Lai, P. M. Nadolsky et al.: *New generation of parton distributions with uncertainties from global QCD analysis.* JHEP 07 (2002) 012 (Cited on pages 25, 74, 126, and 144)

[64] S. Catani, F. Krauss, R. Kuhn and B. Webber: *QCD matrix elements + parton showers.* JHEP 11 (2001) 063 (Cited on page 26)

[65] M. L. Mangano, M. Moretti, F. Piccinini and M. Treccani: *Matching matrix elements and shower evolution for top-quark production in hadronic collisions.* JHEP 01 (2007) 013 (Cited on page 26)

[66] B. Andersson, G. Gustafson, G. Ingelman and T. Sjöstrand: *Parton Fragmentation and String Dynamics.* Phys. Rep. 97 (1983) 31 (Cited on page 27)

[67] B. R. Webber: *A QCD model for jet fragmentation including soft gluon interference.* Nucl. Phys. (1984) 492 – 528 (Cited on page 27)

[68] ATLAS Collaboration, G. Aad et al.: *Measurements of underlying-event properties using neutral and charged particles in pp collisions at 900 GeV and 7 TeV with the ATLAS detector at the LHC.* Eur. Phys. J. C71 (2011) 1636 (Cited on page 27)

[69] ATLAS Collaboration: *Charged particle multiplicities in p p interactions at $\sqrt{s}$ = 0.9 and 7 TeV in a diffractive limited phase-space measured with the ATLAS detector at the LHC and new PYTHIA6 tune.* CERN, Geneva, Jul 2010 (ATLAS-CONF-2010-031) (Cited on page 27)

[70] T. Sjöstrand, S. Mrenna and P. Skands: *PYTHIA 6.4 physics and manual.* JHEP 05 (2006) 026 (Cited on page 27)

[71] G. Corcella et al.: *HERWIG 6: An event generator for hadron emission reactions with interfering gluons (including supersymmetric processes).* JHEP 01 (2001) 010 (Cited on page 27)

[72] J. Butterworth, J. Forshaw and M. Seymour: *Multiparton interactions in photoproduction at HERA.* Z. Phys. C72 (1996) 637–646 (Cited on page 27)

[73] M. Bahr, S. Gieseke, M. Gigg, D. Grellscheid, K. Hamilton et al.: *Herwig++ Physics and Manual.* Eur. Phys. J. C58 (2008) 639–707 (Cited on page 27)

[74] M. Mangano et al.: *ALPGEN, a generator for hard multiparton processes in hadronic collisions.* JHEP 07 (2003) 001 (Cited on pages 28 and 127)

[75] J. Alwall, M. Herquet, F. Maltoni, O. Mattelaer and T. Stelzer: *MadGraph 5 : Going Beyond.* JHEP 06 (2011) 128 (Cited on page 28)

[76] B. P. Kersevan and E. Richter-Was: *The Monte Carlo event generator AcerMC version 2.0 with interfaces to PYTHIA 6.2 and HERWIG 6.5.* arXiv:hep-ph/0405247 [hep-ph], 2004 (Cited on page 28)

[77] S. Frixione and B. Webber: *Matching NLO QCD computations and parton shower simulations.* JHEP 06 (2002) 029 (Cited on page 28)

[78] S. Frixione and others: *Matching NLO QCD computations with parton showers simulations: the POWHEG method.* JHEP 11 (2007) 070 (Cited on page 28)

[79] A. Djouadi, M. M. Muhlleitner and M. Spira: *Decays of Supersymmetric Particles: the program SUSY-HIT (SUspect-SdecaY-Hdecay-InTerface).* Acta Phys. Polon. B38 (2007) 635–644 (Cited on pages 28, 74, and 127)

[80] F. E. Paige, S. D. Protopopescu, H. Baer and X. Tata: *ISAJET 7.69: A Monte Carlo event generator for pp, anti-p p, and e+e- reactions.* arXiv:hep-ph/0312045 [hep-ph], 2003 (Cited on pages 28, 127, and 169)

[81] W. Beenakker, R. Hopker, M. Spira and P. Zerwas: *Squark and gluino production at hadron colliders.* Nucl. Phys. B492 (1997) 51–103 (Cited on pages 28, 54, 76, 127, 143, 144, and 170)

[82] C. Lefèvre: *The CERN accelerator complex. Complexe des accélérateurs du CERN.* `http://cdsweb.cern.ch/record/1260465`. Version: Dec 2008. – Accessed: 21/01/2013 (Cited on page 32)

[83] L. Evans and P. Bryant: *LHC Machine.* JINST 3 (2008) S08001 (Cited on page 32)

[84] ATLAS Collaboration, G. Aad et al.: *The ATLAS Experiment at the CERN Large Hadron Collider.* JINST 3 (2008) S08003 (Cited on pages 33, 34, 36, and 37)

[85] M. Capeans, G. Darbo, K. Einsweiller, M. Elsing, T. Flick, M. Garcia-Sciveres, C. Gemme, H. Pernegger, O. Rohne and R. Vuillermet: *ATLAS Insertable B-Layer Technical Design Report.* CERN, Geneva, Sep 2010 (CERN-LHCC-2010-013. ATLAS-TDR-019) (Cited on page 34)

[86] A. B. Poy, H. Boterenbrood, H. J. Burckhart, J. Cook, V. Filimonov, S. Franz, O. Gutzwiller, B. Hallgren, V. Khomutnikov, S. Schlenker and F. Varela: *The detector control system of the ATLAS experiment.* JINST 3 (2008) P05006 (Cited on page 38)

[87] GEANT4 Collaboration, S. Agostinelli et al.: *GEANT4: A Simulation toolkit.* Nucl. Instrum. Meth. A506 (2003) 250–303 (Cited on page 39)

[88] J. Allison, K. Amako, J. Apostolakis, H. Araujo, P. Dubois et al.: *Geant4 developments and applications.* IEEE Trans. Nucl. Sci. 53 (2006) 270 (Cited on page 39)

[89] ATLAS Collaboration, M. Beckingham, M. Duehrssen, E. Schmidt, M. Shapiro, M. Venturi, J. Virzi, I. Vivarelli, M. Werner, S. Yamamoto and T. Yamanaka: *The simulation principle and performance of the ATLAS fast calorimeter simulation FastCaloSim.* CERN, Geneva, Oct 2010 (ATL-PHYS-PUB-2010-013) (Cited on page 39)

[90] P. Calafiura, W. Lavrijsen, C. Leggett, M. Marino and D. Quarrie: *The athena control framework in production, new developments and lessons learned.* Proceedings: Computing in High-Energy Physics 2004 (2005) 456–458 (Cited on page 39)

[91] ATLAS Collaboration: *Luminosity Public Results.* `https://twiki.cern.ch/twiki/bin/view/AtlasPublic/LuminosityPublicResults`. – Accessed: 21/01/2013 (Cited on page 42)

[92] ATLAS Collaboration: *Data Quality.* `https://twiki.cern.ch/twiki/bin/view/AtlasPublic/RunStatsPublicResults2010`. – Accessed: 21/01/2013 (Cited on page 42)

[93] ATLAS Collaboration: *Performance of the ATLAS Inner Detector Track and Vertex Reconstruction in the High Pile-Up LHC Environment.* CERN, Geneva, Mar 2012 (ATLAS-CONF-2012-042) (Cited on page 43)

[94] M. Cacciari, G. Salam and G. Soyez: *The anti-k_t jet clustering algorithm.* JHEP 04 (2008) 063 (Cited on page 43)

[95] W. Lampl, S. Laplace, D. Lelas, P. Loch, H. Ma, S. Menke, S. Rajagopalan, D. Rousseau, S. Snyder and G. Unal: *Calorimeter Clustering Algorithms: Description and Performance*. CERN, Geneva, Apr 2008 (ATL-LARG-PUB-2008-002. ATL-COM-LARG-2008-003) (Cited on page 43)

[96] G. C. Blazey, J. R. Dittmann, S. D. Ellis, V. D. Elvira, K. Frame et al.: *Run II jet physics*. arXiv:hep-ex/0005012, 2000 (Cited on page 44)

[97] R. Wigmans: *Calorimetry: Energy Measurement in Particle Physics*. Oxford University Press, 2000 (Cited on page 44)

[98] ATLAS Collaboration: *Jet energy measurement with the ATLAS detector in proton-proton collisions at* $\sqrt{s} = 7$ *TeV*. arXiv:1112.6426 [hep-ex], 2011 (Cited on pages 44 and 63)

[99] ATLAS Collaboration: *In-situ jet energy scale and jet shape corrections for multiple interactions in the first ATLAS data at the LHC*. CERN, Geneva, Mar 2011 (ATLAS-CONF-2011-030) (Cited on page 44)

[100] ATLAS Collaboration: *Performance of the ATLAS Secondary Vertex b-tagging Algorithm in 7 TeV Collision Data*. CERN, Geneva, Jul 2010 (ATLAS-CONF-2010-042) (Cited on page 45)

[101] ATLAS Collaboration: *Calibrating the b-Tag Efficiency and Mistag Rate in 35* pb^{-1} *of Data with the ATLAS Detector*. CERN, Geneva, Jun 2011 (ATLAS-CONF-2011-089) (Cited on page 45)

[102] ATLAS Collaboration: *Commissioning of the ATLAS high-performance b-tagging algorithms in the 7 TeV collision data*. CERN, Geneva, Jul 2011 (ATLAS-CONF-2011-102) (Cited on page 45)

[103] ATLAS Collaboration: *Measurement of the b-tag Efficiency in a Sample of Jets Containing Muons with 5* fb^{-1} *of Data from the ATLAS Detector*. CERN, Geneva, Mar 2012 (ATLAS-CONF-2012-043) (Cited on pages 46 and 47)

[104] ATLAS Collaboration: *Measurement of the Mistag Rate with 5* fb^{-1} *of Data Collected by the ATLAS Detector*. CERN, Geneva, Mar 2012 (ATLAS-CONF-2012-040) (Cited on page 47)

[105] ATLAS Collaboration: *Expected electron performance in the ATLAS experiment*. CERN, Geneva, Apr 2011 (ATL-PHYS-PUB-2011-006) (Cited on page 48)

[106] ATLAS Collaboration, G. Aad et al.: *Electron performance measurements with the ATLAS detector using the 2010 LHC proton-proton collision data*. Eur. Phys. J. C72 (2012) 1–46 (Cited on page 48)

[107] ATLAS Collaboration: *Electron identification efficiency dependence on pileup*. `https://atlas.web.cern.ch/Atlas/GROUPS/PHYSICS/EGAMMA/PublicPlots/20110512/EfficiencyPileup/ATL-COM-PHYS-2011-1636`. – Accessed: 08/03/2013 (Cited on page 48)

[108] ATLAS Collaboration: *Electron efficiency measurements in early 2012 data*. `https://atlas.web.cern.ch/Atlas/GROUPS/PHYSICS/EGAMMA/PublicPlots/`

20120611/ElectronEfficiency2012/ATL-COM-PHYS-2011-783. – Accessed: 08/03/2013 (Cited on page 48)

[109] ATLAS Collaboration, G. Aad et al.: *Expected Performance of the ATLAS Experiment: Detector, Trigger and Physics.* arXiv:0901.0512 [hep-ex], 2008 (Cited on pages 48, 171, and 173)

[110] ATLAS Collaboration: *Muon reconstruction efficiency in reprocessed 2010 LHC proton-proton collision data recorded with the ATLAS detector.* CERN, Geneva, Apr 2011 (ATLAS-CONF-2011-063) (Cited on page 49)

[111] ATLAS Collaboration: *Muon Momentum Resolution in First Pass Reconstruction of pp Collision Data Recorded by ATLAS in 2010.* CERN, Geneva, Mar 2011 (ATLAS-CONF-2011-046) (Cited on page 49)

[112] ATLAS Collaboration, G. Aad et al.: *Performance of missing transverse momentum reconstruction in proton-proton collisions at $\sqrt{s} = 7$ TeV with ATLAS.* Eur. Phys. J. C72 (2012) 1844 (Cited on page 50)

[113] ATLAS Collaboration: *Performance of Missing Transverse Momentum Reconstruction in ATLAS with 2011 Proton-Proton Collisions at sqrts = 7 TeV.* CERN, Geneva, Jul 2012 (ATLAS-CONF-2012-101) (Cited on pages 50 and 51)

[114] ATLAS Collaboration: *Etmiss performance under high pile conditions in 2012 data.* https://twiki.cern.ch/twiki/bin/view/AtlasPublic/JetEtmissApproved2012EtmissWithPileup. – Accessed: 22/01/2013 (Cited on pages 50 and 51)

[115] ATLAS Collaboration: *Trigger Public Results.* https://twiki.cern.ch/twiki/bin/view/AtlasPublic/MissingEtTriggerPublicResults. – Accessed: 26/04/2013 (Cited on page 56)

[116] D. Tovey: *On measuring the masses of pair-produced semi-invisibly decaying particles at hadron colliders.* JHEP 04 (2008) 034 (Cited on page 60)

[117] G. Polesello and D. Tovey: *Supersymmetric particle mass measurement with the boost-corrected contransverse mass.* JHEP 03 (2010) 030 (Cited on pages 60, 78, and 80)

[118] ATLAS Collaboration, G. Aad et al.: *Search for squarks and gluinos with the ATLAS detector in final states with jets and missing transverse momentum using 4.7 fb^{-1} of $\sqrt{s} = 7$ TeV proton-proton collision data.* arXiv:1208.0949 [hep-ex], 2012 (Cited on page 62)

[119] ATLAS Collaboration: *Luminosity Determination in pp Collisions at $\sqrt{s} = 7$ TeV using the ATLAS Detector in 2011.* CERN, Geneva, Aug 2011 (ATLAS-CONF-2011-116) (Cited on pages 63 and 101)

[120] ATLAS Collaboration, G. Aad et al.: *Jet energy resolution in proton-proton collisions at $\sqrt{s} = 7$ TeV recorded in 2010 with the ATLAS detector.* Eur. Phys. J. C73 (2013) 2306 (Cited on page 63)

[121] ATLAS Collaboration, G. Aad et al.: *Measurement of $t\bar{t}$ production with a veto on additional central jet activity in pp collisions at $\sqrt{s} = 7$ TeV using the ATLAS detector.* Eur. Phys. J. C72 (2012) 2043 (Cited on page 65)

[122] G. Cowan, K. Cranmer, E. Gross and O. Vitells: *Asymptotic formulae for likelihood-based tests of new physics.* Eur. Phys. J. C71 (2011) 1–19 (Cited on pages 65 and 66)

[123] A. L. Read: *Presentation of search results: the CLs technique.* J. Phys. G28 (2002) 2693 (Cited on page 67)

[124] ATLAS Collaboration: *Supersymmetry Public Results.* `https://twiki.cern.ch/twiki/bin/view/AtlasPublic/SupersymmetryPublicResults`. – Accessed: 19/02/2013 (Cited on pages 68, 69, and 124)

[125] ATLAS Collaboration: *Search for squarks and gluinos with the ATLAS detector using final states with jets and missing transverse momentum and 5.8 fb^{-1} of $\sqrt{s}$=8 TeV proton-proton collision data.* CERN, Geneva, Aug 2012 (ATLAS-CONF-2012-109) (Cited on pages 68 and 70)

[126] ATLAS Collaboration: *Search for direct production of charginos and neutralinos in events with three leptons and missing transverse momentum in 13.0 fb-1 of pp collisions at $\sqrt{s}$=8 TeV with the ATLAS detector.* CERN, Geneva, Nov 2012 (ATLAS-CONF-2012-154) (Cited on pages 70 and 71)

[127] ATLAS Collaboration, G. Aad et al.: *Search for long-lived, heavy particles in final states with a muon and multi-track displaced vertex in proton-proton collisions at $\sqrt{s} = 7$ TeV with the ATLAS detector.* Phys. Lett. B719 (2013) 280 – 298 (Cited on page 71)

[128] ATLAS Collaboration, G. Aad et al.: *Search for direct chargino production in anomaly-mediated supersymmetry breaking models based on a disappearing-track signature in pp collisions at $\sqrt{s} = 7$ TeV with the ATLAS detector.* JHEP 01 (2013) 131 (Cited on page 71)

[129] ATLAS Collaboration, G. Aad et al.: *Search for a heavy narrow resonance decaying to $e\mu$, $e\tau$, or $\mu\tau$ with the ATLAS detector in $\sqrt{s} = 7$ TeV pp collisions at the LHC.* arXiv:1212.1272 [hep-ex], 2012 (Cited on page 71)

[130] ATLAS Collaboration: *Search for Supersymmetry in events with four or more leptons in 13 fb^{-1} pp collisions at $\sqrt{s} = 8$ TeV with the ATLAS detector.* CERN, Geneva, Nov 2012 (ATLAS-CONF-2012-153) (Cited on page 71)

[131] ATLAS Collaboration, G. Aad et al.: *Search for Scalar Bottom Quark Pair Production with the ATLAS Detector in pp Collisions at $\sqrt{s} = 7$ TeV.* Phys. Rev. Lett. 108 (2012) 181802 (Cited on pages 73, 113, 114, 115, and 142)

[132] ATLAS Collaboration: *Search for scalar bottom pair production in final states with missing transverse momentum and two b-jets in pp collisions at $\sqrt{s}$=7 TeV with the ATLAS Detector.* CERN, Geneva, Aug 2012 (ATLAS-CONF-2012-106) (Cited on pages 73, 113, 114, and 115)

[133] ATLAS Collaboration: *Search for direct sbottom production in event with two b-jets using 12.8 fb^{-1} of pp collisions at $\sqrt{s} = 8$ TeV with the ATLAS Detector.* CERN, Geneva, Dec 2012 (ATLAS-CONF-2012-165) (Cited on page 73)

[134] ATLAS Collaboration: *Search for direct stop production in events with missing transverse momentum and two b-jets using 12.8 fb^{-1} of pp collisions at $\sqrt{s} = 8$ TeV with the ATLAS detector.* CERN, Geneva, Jan 2013 (ATLAS-CONF-2013-001) (Cited on page 73)

[135] M. Aliev, H. Lacker, U. Langenfeld, S. Moch, P. Uwer et al.: *HATHOR: HAdronic Top and Heavy quarks crOss section calculatoR.* Comput. Phys. Commun. 182 (2011) 1034–1046 (Cited on page 75)

[136] J. M. Campbell and R. K. Ellis: *$t\bar{t}W^{+-}$ production and decay at NLO.* JHEP 07 (2012) 052 (Cited on pages 75 and 102)

[137] M. Garzelli, A. Kardos, C. Papadopoulos and Z. Trocsanyi: *$t\ \bar{t}\ W^{+-}$ and $t\ \bar{t}\ Z$ Hadroproduction at NLO accuracy in QCD with Parton Shower and Hadronization effects.* JHEP 11 (2012) 056 (Cited on pages 75 and 102)

[138] N. Kidonakis: *NNLL resummation for s-channel single top quark production.* Phys. Rev. D81 (2010) 054028 (Cited on page 75)

[139] N. Kidonakis: *Two-loop soft anomalous dimensions for single top quark associated production with a W- or H-.* Phys. Rev. D82 (2010) 054018 (Cited on page 75)

[140] N. Kidonakis: *Next-to-next-to-leading-order collinear and soft gluon corrections for t-channel single top quark production.* Phys. Rev. D83 (2011) 091503 (Cited on page 75)

[141] S. Catani, L. Cieri, G. Ferrera, D. d. Florian and M. Grazzini: *Vector boson production at hadron colliders: A Fully exclusive QCD calculation at NNLO.* Phys. Rev. Lett. 103 (2009) 082001 (Cited on page 75)

[142] J. Campbell, R. Ellis and C. Williams: *Vector boson pair production at the LHC.* JHEP 07 (2011) 018 (Cited on pages 75 and 127)

[143] W. Beenakker et al.: *Supersymmetric top and bottom squark production at hadron colliders.* JHEP 08 (2010) 098 (Cited on pages 76 and 117)

[144] W. Beenakker, S. Brensing, M. Kramer, A. Kulesza, E. Laenen et al.: *Squark and Gluino Hadroproduction.* Int. J. Mod. Phys. A26 (2011) 2637–2664 (Cited on pages 76 and 144)

[145] A. Marzin: *With the courtesy of Antoine Marzin, University of Oklahoma (US).* 2012 (Cited on page 78)

[146] L. Randall and D. Tucker-Smith: *Dijet Searches for Supersymmetry at the LHC.* Phys. Rev. Lett. 101 (2008) 221803 (Cited on page 84)

[147] E. Alvarez and Y. Bai: *Reach the Bottom Line of the Sbottom Search.* JHEP 08 (2012) 003 (Cited on page 85)

[148] ATLAS Collaboration: *Search for Supersymmetry in final states with two same-sign leptons, jets and missing transverse momentum with the ATLAS detector in pp collisions at $\sqrt{s} = 8$ TeV.* CERN, Geneva, Aug 2012 (ATLAS-CONF-2012-105) (Cited on page 90)

[149] M. Kramer, A. Kulesza, R. v. d. Leeuw, M. Mangano, S. Padhi et al.: *Supersymmetry production cross sections in pp collisions at $\sqrt{s} = 7$ TeV.* arXiv:1206.2892 [hep-ph], 2012 (Cited on pages 104 and 149)

[150] CDF Collaboration, T. Aaltonen et al.: *Search for the Production of Scalar Bottom Quarks in $p\bar{p}$ collisions at $\sqrt{s} = 1.96$ TeV.* Phys. Rev. Lett. 105 (2010) 081802 (Cited on pages 113, 114, 115, and 142)

[151] DØ Collaboration, V. M. Abazov et al.: *Search for scalar bottom quarks and third-generation leptoquarks in pp^- bar collisions at $\sqrt{s} = 1.96$ TeV.* Phys. Lett. B693 (2010) 95–101 (Cited on pages 113, 114, 115, and 142)

[152] LEPSUSYWG, ALEPH, DELPHI, L3 and OPAL experiments: *Notes LEPSUSYWG/01-03.1 and 04-01.1.* `http://lepsusy.web.cern.ch/lepsusy/Welcome.html`. – Accessed 05/03/2013 (Cited on page 117)

[153] ATLAS Collaboration, G. Aad et al.: *Search for supersymmetry in pp collisions at $\sqrt{s} = 7$ TeV in final states with missing transverse momentum and b-jets.* Phys. Lett. B701 (2011) 398–416 (Cited on pages 125, 142, and 143)

[154] ATLAS Collaboration: *Search for supersymmetry in pp collisions at $\sqrt{s} = 7$ TeV in final states with missing transverse momentum, b-jets and no leptons with the ATLAS detector.* CERN, Geneva, Jul 2011 (ATLAS-CONF-2011-098) (Cited on pages 125 and 129)

[155] ATLAS Collaboration, G. Aad et al.: *Search for supersymmetry in pp collisions at $\sqrt{s} = 7$ TeV in final states with missing transverse momentum and b-jets with the ATLAS detector.* Phys. Rev. D85 (2012) 112006 (Cited on pages 125, 141, and 143)

[156] ATLAS Collaboration, G. Aad et al.: *Search for top and bottom squarks from gluino pair production in final states with missing transverse energy and at least three b-jets with the ATLAS detector.* Eur. Phys. J. C72 (2012) 2174 (Cited on pages 125, 149, and 152)

[157] ATLAS Collaboration: *Search for supersymmetry in pp collisions at $\sqrt{s} = 7$TeV in final states with missing transverse momentum, b-jets and one lepton with the ATLAS detector.* CERN, Geneva, Sep 2011 (ATLAS-CONF-2011-130) (Cited on page 125)

[158] ATLAS Collaboration: *Search for gluino pair production in final states with missing transverse momentum and at least three b-jets using 12.8 fb^{-1} of pp collisions at $\sqrt{s} = 8$ TeV with the ATLAS Detector.* CERN, Geneva, Nov 2012 (ATLAS-CONF-2012-145) (Cited on page 125)

[159] ATLAS Collaboration, G. Aad et al.: *Measurement of the cross section for the production of a W boson in association with b-jets in pp collisions at $\sqrt{s} = 7$ TeV with the ATLAS detector.* Phys. Lett. B707 (2012) 418–437 (Cited on page 126)

[160] ATLAS Collaboration, G. Aad et al.: *Measurement of the cross-section for b-jets produced in association with a Z boson at $\sqrt{s}$=7 TeV with the ATLAS detector.* Phys. Lett. B706 (2011) 295–313 (Cited on page 126)

[161] S. Moch and P. Uwer: *Theoretical status and prospects for top-quark pair production at hadron colliders.* Phys. Rev. D78 (2008) 034003 (Cited on page 127)

[162] K. Melnikov and F. Petriello: *Electroweak gauge boson production at hadron colliders through $\mathcal{O}(\alpha_s^2)$.* Phys. Rev. D74 (2006) 114017 (Cited on pages 127 and 170)

[163] J. Campbell, J. Ellis and R. Keith: *An update on vector boson pair production at hadron colliders.* Phys. Rev. D60 (1999) 113006 (Cited on page 127)

[164] D. Stump et al.: *Inclusive jet production, parton distributions, and the search for new physics.* JHEP 10 (2003) 046 (Cited on page 127)

[165] ATLAS Collaboration, G. Aad et al.: *Measurement of the $W \to \ell\nu$ and $Z/\gamma^* \to \ell\ell$ production cross sections in proton-proton collisions at $\sqrt{s} = 7$ TeV with the ATLAS detector*. JHEP 12 (2010) 060 (Cited on page 134)

[166] CDF Collaboration, T. Aaltonen et al.: *Search for Gluino-Mediated Sbottom Production in $p\bar{p}$ Collisions at $\sqrt{s} = 1.96$ TeV*. Phys. Rev. Lett. 102 (2009) 221801 (Cited on page 142)

[167] A. Kulesza and L. Motyka: *Threshold resummation for squark-antisquark and gluino-pair production at the LHC*. Phys. Rev. Lett. 102 (2009) 111802 (Cited on page 144)

[168] A. Kulesza and L. Motyka: *Soft gluon resummation for the production of gluino-gluino and squark-antisquark pairs at the LHC*. Phys. Rev. D80 (2009) 095004 (Cited on page 144)

[169] W. Beenakker, S. Brensing, M. Kramer, A. Kulesza, E. Laenen et al.: *Soft-gluon resummation for squark and gluino hadroproduction*. JHEP 12 (2009) 041 (Cited on page 144)

[170] ATLAS Collaboration: *Discovery Potential for Supersymmetry with b-jet Final States with the ATLAS detector*. CERN, Geneva, Apr 2009 (ATL-PHYS-PUB-2009-075) (Cited on pages 169 and 171)

[171] CMS Collaboration, G. Bayatian et al.: *CMS Physics Technical Design Report, Volume II: Physics Performance*. J. Phys. G34 (2007) 995–1579 (Cited on page 173)

[172] U. Bitenc, S. D'Auria, M. Fehling-Kaschek, D. Hoffmann, O. Pisano, S. Roe, S. Schlenker, C. Tsarouchas and S. Winkelmann: *ATLAS Detector Control System Data Viewer*. – Internal communication (Cited on pages 189 and 190)

[173] Google Developers: *GWT API Reference*. `https://developers.google.com/web-toolkit/doc/latest/RefGWTClassAPI`. – Accessed: 31/05/2013 (Cited on page 190)

[174] Mozilla Developer Network: *Asynchronous JavaScript + XML*. `https://developer.mozilla.org/en-US/docs/AJAX`. – Accessed: 31/05/2013 (Cited on page 190)

[175] JFree.org, D. Gilbert and T. Morgner: *JFreeChart*. `http://www.jfree.org/jfreechart`. – Accessed: 31/05/2013 (Cited on page 191)

APPENDIX A

Search for a $h \to b\bar{b}$ Resonance in SUSY

In this appendix, a strategy for a search for $b\bar{b}$ resonances in final states with supersymmetric particles is described. Such resonances might appear in the decays of Higgs bosons in cascade decays of SUSY particles. It should be stressed that the study was performed in form of a feasibility study before the data taking of the LHC started. All results presented are based purely on Monte Carlo simulation for a centre-of-mass energy of $\sqrt{s} = 10$ TeV and 14 TeV.

The study is performed for different mSUGRA scenarios, where the presence of b-jets in the SUSY decay cascades is enhanced for large values of $\tan\beta$ (see Section 2.2.5). In addition, b-jets may also result from decays of SUSY particles into a Higgs boson, which subsequently decays into a pair of b-jets. The event selection is based on the inclusive SUSY searches with final states with b-jets and missing transverse energy, as described in Ref. [170].
A profile likelihood approach is used to estimate the significance of a possible signal on top of the background from Standard Model and SUSY processes. Although the focus is set on the Higgs boson production in the SUSY decay chain, the method is more general and can be applied to other resonance searches as well.
In the following sections, the exploited Monte Carlo samples are presented (A.1), the object definitions and event selections are summarised (A.2), and the Higgs content in different mSUGRA parameter configurations is discussed (A.3). The actual method to extract the signal significance for a $b\bar{b}$ resonance is presented in Section A.4, together with the results for specific mSUGRA scenarios and a discussion of sources of systematic uncertainties. The conclusions are presented in Section A.5.

A.1 Monte Carlo Samples

All samples are produced assuming a centre-of-mass energy of 10 TeV. Results for $\sqrt{s} =$ 14 TeV are obtained by an appropriate scaling, as described in Section A.4.2.

Signal

The signal samples are generated with HERWIG, interfaced to ISASUSY [80] for the particle spectrum, and simulated with ATLFAST-II. The mSUGRA model is assumed and two grids in the (m_0 - $m_{1/2}$) plane with $A_0 = 0$, $\mu > 0$ and $\tan\beta = 10$ and 50 are used, in order to explore different SUSY decay chains. Next-to-leading order cross-sections are calculated with

PROSPINO[1] [81] and shown in Fig. A.1. For each signal point, a Monte Carlo sample of 30000 events is produced.

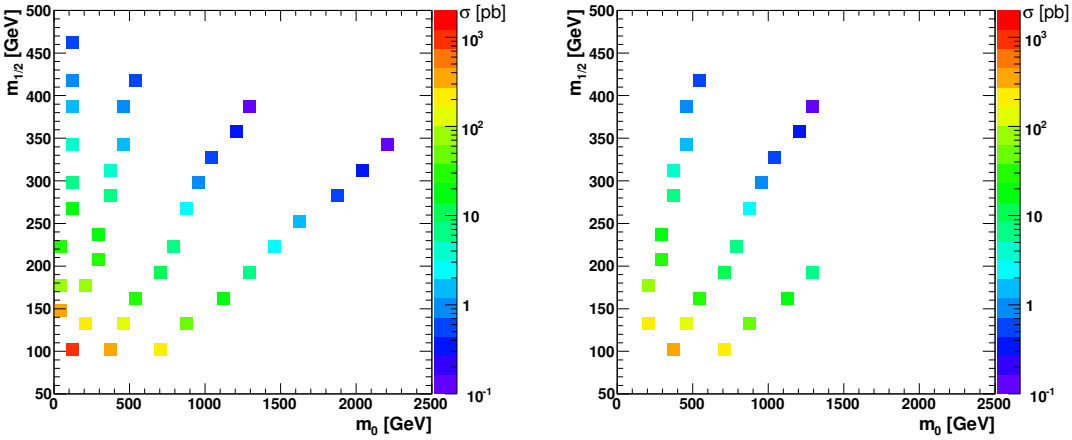

Figure A.1: Cross-sections at NLO (in pb) for the mSUGRA signal points in the (m_0-$m_{1/2}$) plane for $\tan\beta = 10$ (left) and $\tan\beta = 50$ (right), assuming $A_0 = 0$ and $\mu > 0$.

Throughout this analysis, four signal points are used as benchmark points for different regions of the parameter space, as indicated in Table A.1. In addition, the mSUGRA signal point named SU9 ($m_0 = 300$ GeV, $m_{1/2} = 425$ GeV, $A_0 = 20$ GeV, $\tan\beta = 20$, $\mu > 0$) is also taken as reference.

Point	m_0 [GeV]	$m_{1/2}$ [GeV]
230_170	230	170
770_228	770	228
1170_356	1170	356
430_345	430	345

Table A.1: Values of m_0 and $m_{1/2}$ for the reference mSUGRA points. Other parameters are $A_0 = 0$, $\mu > 0$. Both values of $\tan\beta$ ($\tan\beta = 10$ and 50) are considered.

SM Background

The expected signature consists of a high jet multiplicity, $E_{\mathrm{T}}^{\mathrm{miss}}$ and b-jets. Only the most relevant backgrounds are considered. They include top-pair production, inclusive production of W and Z bosons and multi-jet QCD production processes. The full detector simulation is used for all background samples.

Top Pair Production: $t\bar{t}$ events are generated with MC@NLO interfaced to HERWIG and JIMMY. Both the fully hadronic decay mode, where both W bosons decay hadronically, as well as the semi-leptonic decay modes, where at least one W boson decays leptonically, are considered.

W/Z+jets Production: Events for the W and Z production are generated with ALPGEN. The cross-sections are normalised to the NNLO prediction of the FEWZ [162] program.

Multi-jet Processes: Multi-jet events from QCD processes are generated with ALPGEN. Due to the large cross-section, the samples are generated in different p_{T} ranges for

1 For simplicity, only gluino and squark production processes are considered in the calculation.

each parton final state configuration. Since the heavy-flavour content of the multi-jet samples is limited to gluon-splitting processes ($g \to b\bar{b}$), a dedicated production of $b\bar{b}$ events was performed ($p_{\mathrm{T}}(b) > 20$ GeV and $\Delta R(b\bar{b}) > 0.7$), given the importance of b-jets for the analysis considered. The double counting introduced is neglected in the present analysis. All multi-jet samples are normalised to LO cross-sections.

A.2 Event Selection

The object definitions and event selection follow the prescription established in Ref. [170], which was published assuming a centre-of-mass of 14 TeV. Small adaptions are implemented to account to the $\sqrt{s} = 10$ TeV scenario.

Object Definitions

The object reconstruction is described in detail in Section 4.2. Here, a summary of the exact definitions for the $h \to b\bar{b}$ analysis is given:

Jets: Jets are reconstructed using a cone algorithm with cone size 0.4. They are selected if they have $p_{\mathrm{T}} > 20$ GeV and $|\eta| < 2.5$.

b-Jets: b-jets are selected using the IP3DSV1 algorithm at a 50% efficiency working point (weight>6.75). They are required to have $p_{\mathrm{T}} > 20$ GeV and $|\eta| < 2.5$. Since this is a pure MC study, no b-tagging scaling factors are applied.[2]

Leptons: Electrons are reconstructed following the *medium* selection criteria. Muons are reconstructed with the STACO algorithm. Both electrons and muons are required to be isolated and have $p_{\mathrm{T}} > 10$ GeV and $|\eta| < 2.5$.

Trigger

Due to the rich final state topology of SUSY events and the relatively strong selection criteria applied in this analysis, the trigger efficiency is expected to be above 95% if a trigger involving multi-jets and $E_{\mathrm{T}}^{\mathrm{miss}}$ is considered. The results presented in the following are not corrected for any trigger efficiency losses.

Nominal Event Selection

The event selection is based on large jet multiplicities and high $E_{\mathrm{T}}^{\mathrm{miss}}$ values, that were found to be powerful discriminators against the major SM background processes [170]. The following requirements are imposed for the nominal event selection:

1. $\geq$4 jets with $p_{\mathrm{T}} > 40$ GeV;
2. $p_{\mathrm{T}}(\mathrm{jet}_1) > 80$ GeV;
3. $E_{\mathrm{T}}^{\mathrm{miss}} > 80$ GeV;
4. $E_{\mathrm{T}}^{\mathrm{miss}} > 0.2\ M_{\mathrm{eff}}$;[3]
5. $S_{\mathrm{T}} > 0.2$;[4]

2 The b-jets are corrected for muons by adding muons found within a cone of $\Delta R = 0.4$. The p_{T} of the b-jets is additionally corrected for neutrinos, see Ref. [109].

3 Here, M_{eff} is defined as the scalar sum of the missing transverse energy and the transverse momenta of the four leading jets and isolated leptons: $M_{\mathrm{eff}} = E_{\mathrm{T}}^{\mathrm{miss}} + \sum_{i=1}^{4}(\mathrm{jet}_i) + \sum p_{\mathrm{T}}(\mathrm{lepton})$.

4 The transverse sphericity S_{T} is computed using the 2×2 sphericity tensor $S_{ij} = \sum_k p_{ki} p^{kj}$ including all jets and isolated leptons. S_{T} is defined via the eigenvalues λ_1 and λ_2 of S_{ij}: $S_{\mathrm{T}} = \frac{2\lambda_2}{\lambda_1+\lambda_2}$.

6. $\geq$2 b-jets;
7. $\Delta\phi_{\min}(\text{jet}_{1..3}, E_{\text{T}}^{\text{miss}}) > 0.2$;
8. $M_{\text{eff}} > 800$ GeV.

Figure A.2 shows the M_{eff} distribution before applying the M_{eff} threshold for two signal points and for the background from SM processes. A good separation of SM background events and the signal events is visible for high M_{eff} values.

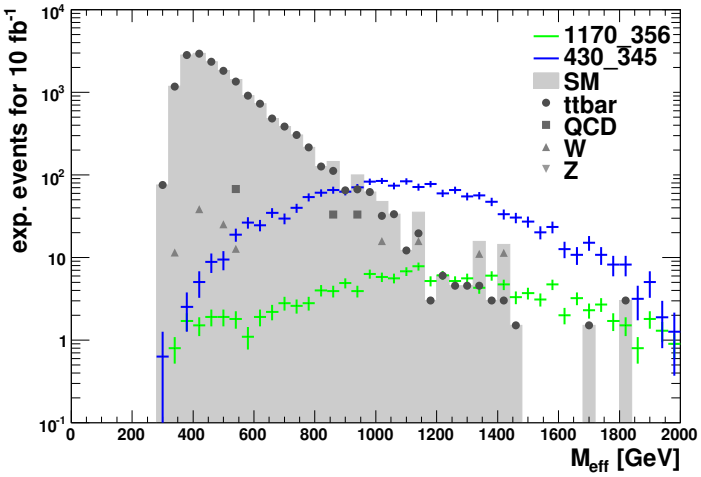

Figure A.2: Distribution of M_{eff} before applying the M_{eff} threshold for two signal points with $\tan\beta = 50$ and the SM background processes.

The numbers of expected events, corresponding to an integrated luminosity of 10 fb^{-1}, are shown in Table A.2 for all relevant background processes and in Table A.3 for two signal points (770_228 and 430_345 with $\tan\beta = 50$) together with the total SM background. The results are visualised in Fig. A.3. As can be seen, the requirement of two b-jets removes comparably large fractions of the W and Z backgrounds, while the $\Delta\phi_{\min}$ requirement is a powerful discriminator against the multi-jet QCD processes. The last selection on M_{eff} suppresses the $t\bar{t}$ contribution significantly. The main background after the event selection is $t\bar{t}$, which accounts for more than 80% of the total SM contribution.

cut	$t\bar{t}$	QCD	W+jets	Z+jets
1-3	$(1.719 \pm 0.006)\cdot10^5$	$(4.44 \pm 0.20)\cdot10^5$	$(1.05 \pm 0.01)\cdot10^5$	$(2.58 \pm 0.03)\cdot10^4$
4	$(1.156 \pm 0.005)\cdot10^5$	$(1.12 \pm 0.15)\cdot10^5$	$(6.52 \pm 0.09)\cdot10^4$	$(1.73 \pm 0.03)\cdot10^4$
5	$(7.29 \pm 0.04)\cdot10^4$	$(5.60 \pm 1.27)\cdot10^4$	$(3.54 \pm 0.07)\cdot10^4$	$(9.06 \pm 0.19)\cdot10^3$
6	$(1.79 \pm 0.02)\cdot10^4$	$(2.33 \pm 1.39)\cdot10^4$	167 ± 47	8 ± 6
7	$(1.61 \pm 0.02)\cdot10^4$	134 ± 67	142 ± 43	8 ± 6
8	564 ± 34	66 ± 47	54 ± 27	0 ± 0

Table A.2: Number of expected background events after the event selection, assuming an integrated luminosity of 10 fb^{-1} and a centre-of-mass energy of 10 TeV. The uncertainties represent the statistical uncertainties of the MC simulation.

Alternative Event Selections

The sensitivity of this analysis is also tested by adopting two alternative event selections.

cut	770_228	430_345	SM
1-3	$(2.62 \pm 0.02)\cdot10^4$	$(1.091 \pm 0.008)\cdot10^4$	$(7.47 \pm 0.20)\cdot10^5$
4	$(1.36 \pm 0.02)\cdot10^4$	$(7.77 \pm 0.07)\cdot10^4$	$(3.10 \pm 0.15)\cdot10^5$
5	$(1.08 \pm 0.01)\cdot10^4$	$(5.53 \pm 0.06)\cdot10^3$	$(1.73 \pm 0.13)\cdot10^5$
6	$(3.85 \pm 0.08)\cdot10^3$	$(1.68 \pm 0.03)\cdot10^3$	$(2.04 \pm 0.14)\cdot10^4$
7	$(3.49 \pm 0.08)\cdot10^3$	$(1.50 \pm 0.03)\cdot10^3$	$(1.64 \pm 0.19)\cdot10^4$
8	$(2.10 \pm 0.06)\cdot10^3$	$(1.25 \pm 0.03)\cdot10^3$	684 ± 64

Table A.3: Number of expected signal events for two selected points (770_228 and 430_345 with $\tan\beta = 50$) and the expected total number of background events from SM processes, assuming an integrated luminosity of 10 fb^{-1} and a centre-of-mass energy of 10 TeV. The uncertainties represent the statistical uncertainties of the MC simulation.

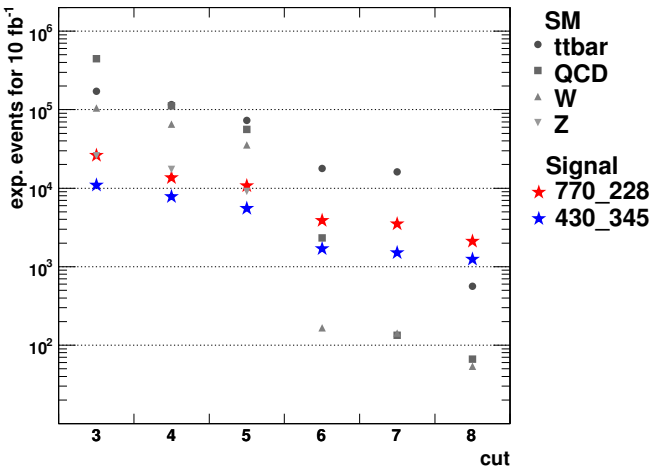

Figure A.3: Expected signal and background events at the different steps of the event selection, assuming an integrated luminosity of 10 fb^{-1} and a centre-of-mass energy of 10 TeV. For the two signal points a value of $\tan\beta = 50$ is assumed.

The CSC selection, based on an ATLAS study published in Ref. [109] and the TDR selection based on a study published by the the CMS collaboration [171][5]:

ATLAS CSC selection:

1. $\geq$4 jets;
2. $p_{\mathrm{T}}(\mathrm{jet}_1) > 100$ GeV;
3. $p_{\mathrm{T}}(\mathrm{jet}_2) > 100$ GeV;
4. $E_{\mathrm{T}}^{\mathrm{miss}} > 300$ GeV;
5. $\geq$2 b-jets with $p_{\mathrm{T}} > 50$ GeV;
6. No leptons (e or μ).

5 The hemisphere separation technique and the ΔR pairing of the b-jets are not applied here.

CMS TDR selection:

1. $\geq$4 jets with $p_{\mathrm{T}} > 30$ GeV;
2. $p_{\mathrm{T}}(\mathrm{jet}_1) > 200$ GeV;
3. $p_{\mathrm{T}}(\mathrm{jet}_2) > 150$ GeV;
4. $p_{\mathrm{T}}(\mathrm{jet}_3) > 50$ GeV;
5. $E_{\mathrm{T}}^{\mathrm{miss}} > 200$ GeV;
6. $\geq$2 b-jets.

A.3 Higgs Boson Signatures in SUSY Scenarios

The aim of this study is to evaluate how well possible Higgs boson decays into $b\bar{b}$ final states, appearing in SUSY decay cascades, can be identified. A study at parton level is presented in Section A.3.1 that adresses the Higgs content of the mSUGRA samples and other sources for b-quarks. The invariant mass of the reconstructed b-jets is used to access the Higgs boson resonance. The corresponding distributions are shown in Section A.3.2.

A.3.1 Parton Level Study

In mSUGRA, the lightest Higgs boson h may occur in $\chi_2^0 \to h\chi_1^0$ decays, if kinematically allowed by the SUSY mass spectrum. For the mSUGRA parameter configurations used in this analysis, the lightest Higgs boson produced in the cascades has a mass of $\sim$ 115 GeV. In Figure A.4, the percentage of events with two true b-jets[6] that contain at least one $h \to b\bar{b}$ decay is shown for both $\tan\beta$ scenarios. This fraction is found to be large for large $m_{1/2}$ and medium m_0 values.

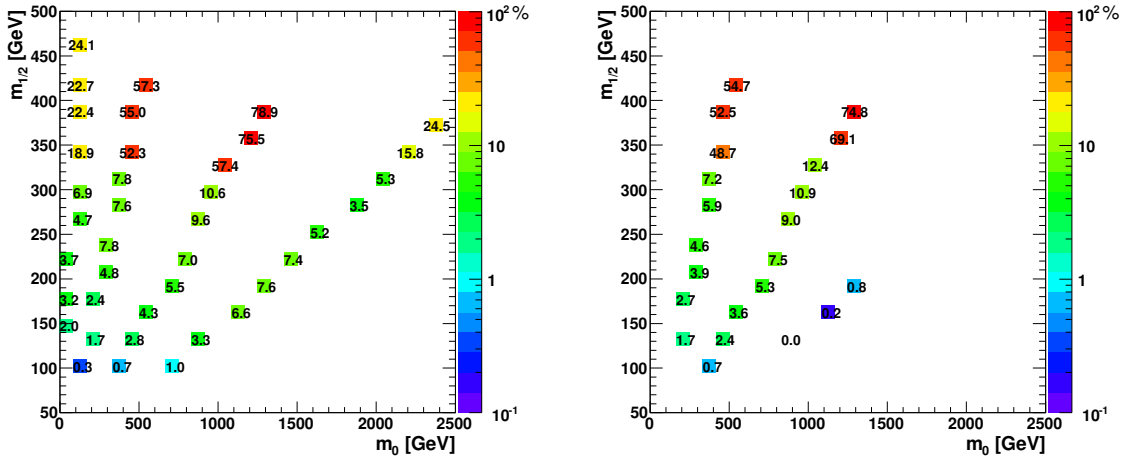

Figure A.4: Percentage of SUSY events with two true b-jets that have at least one $h \to b\bar{b}$ decay for $\tan\beta = 10$ (left) and $\tan\beta = 50$ (right) before the event selection.

Decays of particles involving b-quarks other than the Higgs boson are a source of background for the resonance search. Therefore, the different decays to b-quarks in SUSY cascades are investigated and considered as an additional background component. The percentage of

6 A true b-jet is defined by matching the b-jet to a b-quark at parton level.

decays into b-quarks is shown in Table A.4 for various sources of b-quarks for the reference signal points with $\tan\beta = 50$. It should be noted that the different decay processes can add up to more than 100% because more than one process may contribute in the SUSY decay chains of a single event. The numbers show that for all benchmark points gluino decays constitute the main source of background.

Point	$h \to b\bar{b}$	$Z \to b\bar{b}$	$\tilde{g} \to b\bar{b}\tilde{\chi}$	$\tilde{g} \to b\tilde{b}$	$\tilde{b}\tilde{b}$,$\tilde{b}\tilde{t}$,$\tilde{t}\tilde{t}$	$\tilde{\chi} \to b\bar{b}\tilde{\chi}$
230_170	2.6 %	0.88 %	0.045 %	90 %	6.6 %	7.9 %
770_228	7.5 %	3 %	86 %	0 %	1.9 %	20 %
1170_356	69 %	6.4 %	45 %	0 %	0.81 %	0 %
430_345	49 %	4.2 %	0.39 %	69 %	4.8 %	0.016 %

Table A.4: Percentage of the most dominant decays to b-quarks, normalised to the number of events with at least two b-quarks, for the reference signal points for $\tan\beta = 50$. A simplified notation is used: the three body decay $\tilde{g} \to b\bar{b}\tilde{\chi}$ includes $\tilde{g} \to b\bar{b}\tilde{\chi}^0$, $\tilde{g} \to t\bar{t}\tilde{\chi}^0$, $\tilde{g} \to b\bar{t}\tilde{\chi}^+$ and $\tilde{g} \to t\bar{b}\tilde{\chi}^-$. The column marked $\tilde{g} \to b\tilde{b}$ also includes $\tilde{g} \to t\tilde{t}$. Furthermore it should be noted that $\tilde{b}$, $\tilde{t}$ and t decay to $b + X$.

The Higgs boson resonance is expected to be visible in the distribution of the invariant mass of the b-jets, m_{bb}. In Figure A.5, the m_{bb} distribution at parton level is shown for the four reference signal points for $\tan\beta = 50$. For the points 1170_356 and 430_345, where a significant $h \to b\bar{b}$ contribution appears, a peak can be seen at the Higgs mass of 115 GeV. The bulk of the non-resonant distribution is due to b-quarks coming from gluino decays. This is illustrated in Figure A.6, where the m_{bb} distribution at parton level is shown separately for the different decays considered in Table A.4 for the two reference points with a large Higgs content.

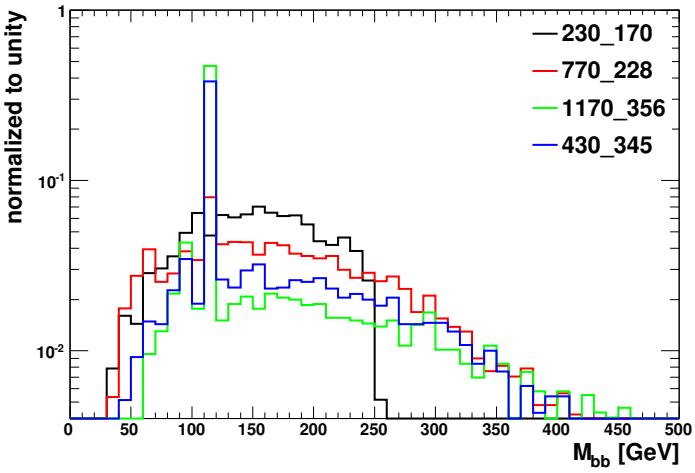

Figure A.5: Distribution of m_{bb} at parton level for the reference signal points for $\tan\beta = 50$, before the event selection.

Figure A.7 shows the p_{T} distribution of the b-quarks for the different decay modes. It can be seen that the b-quarks originating from Higgs decays tend to have lower p_{T} values than the ones from gluino decays, which reflects the different mass values of the decaying particles.

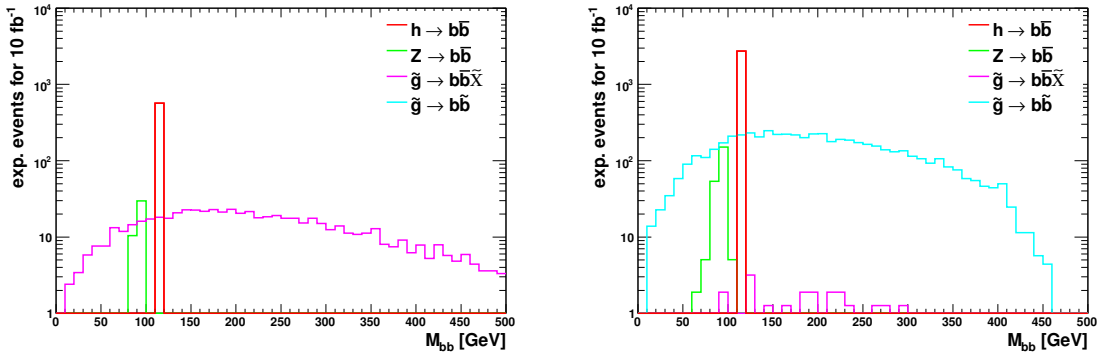

(a) 1170_356 **(b)** 430_345

Figure A.6: Distribution of m_{bb}, decomposed into the contributions from various $b\bar{b}$ decays, for the two reference points at $\tan\beta = 50$ with the highest Higgs content. The distributions are shown at parton level, before the event selection.

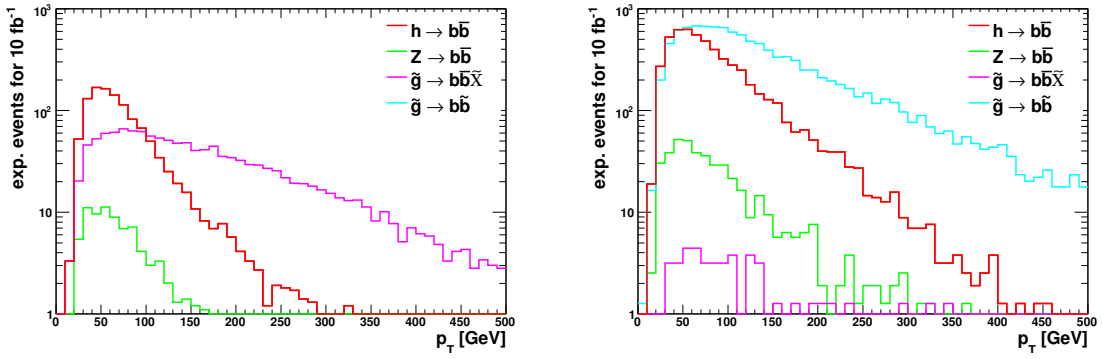

(a) 1170_356 **(b)** 430_345

Figure A.7: Distribution of p_T of the two b-quarks (two or more entries per event) at parton level separated for the origin of the b-jets for the reference points 1170_356 (a) and 430_345 (b) for $\tan\beta = 50$ before the event selection.

A.3.2 Reconstructed Mass Distributions

The m_{bb} distributions at reconstruction level are obtained by considering all possible combinations of all reconstructed b-jets, if more than two b-jets are identified in the final state. This leads to a significant increase of the combinatorial background. The distributions are shown in Fig. A.8 for the reference signal points for $\tan\beta = 50$, before and after the nominal event selection. As compared to Fig. A.5, the effects of the detector resolution and reconstruction lead to a significant degradation of the $b\bar{b}$ resonance.
In Figure A.9, the m_{bb} distributions are shown for the signal point 430_345 on top of the background from SM processes for the different event selections, as discussed in the previous section. The distributions suggest that the background from SUSY itself has a larger impact for the identification of the resonance than the SM background. Since Fig. A.7 suggests a difference in the p_T values of b-quarks from Higgs decays as compared to b-quarks from gluino decays, an additional upper p_T threshold on the b-jets of 150 GeV is applied for Fig. A.9b. Although there is still no convincing appearance of a Higgs resonance above the combinato-

rial background, the purity, defined as the fraction of events in the final sample containing a $h \to b\bar{b}$ decay, has slightly improved.
The comparison of the distributions for the different event selections shows that the signal-to-background conditions and in particular the shapes of the combinatorial background coming from SUSY itself depend on the selection. Therefore, accurate assumptions on the shapes are difficult to make.
For the simulated benchmark scenarios at $\sqrt{s} = 10$ TeV and $\mathcal{L} = 10$ fb^{-1} a possible discovery appears challenging. In order to quantify this statement and to extract a discovery significance, a dedicated study is presented in the following section.

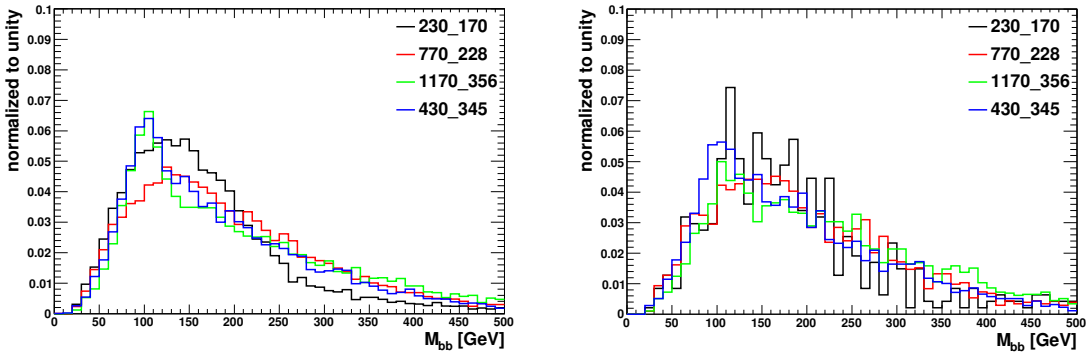

(a) before selection **(b)** after selection

Figure A.8: Distribution of m_{bb} for reconstructed b-jets for the reference SUSY points for $\tan\beta = 50$ (a) before and (b) after applying the event selection.

A.4 Discovery Potential for a $h \to b\bar{b}$ Resonance

A.4.1 Method

As an attempt to assess the potential for the discovery of a Higgs resonance on top of the SUSY combinatorial and Standard Model backgrounds, a fit of the m_{bb} distribution is performed assuming a Gaussian resonance on top of a smooth background. The width of the Gaussian has to be compatible with the expected detector resolution. The background distribution is parametrised using a simple polynomial function. It should be noted that in such a search the precise shape of the background is unknown. Even if the SM contribution can be constrained with some definite uncertainty, the SUSY background shape, which is unpredictable, is dominating. Hence, the only assumption in the procedure is that the overall background shape is smooth. In order to determine the significance for the discovery of a Higgs-like resonance when using collected data, the following procedure is established.

Fitting the m_{bb} distribution

In a first step the m_{bb} distribution is fitted with a third order polynomial plus a Gaussian:

$$p_0 + p_1 \cdot x + p_2 \cdot x^2 + p_3 \cdot x^3 + c \cdot \text{Gauss}\,(\mu,\sigma)\,, \tag{A.1}$$

where the Gaussian is assumed to describe the resonance peak while the combinatorial plus Standard Model background should be described by the polynomial. The Gaussian width is

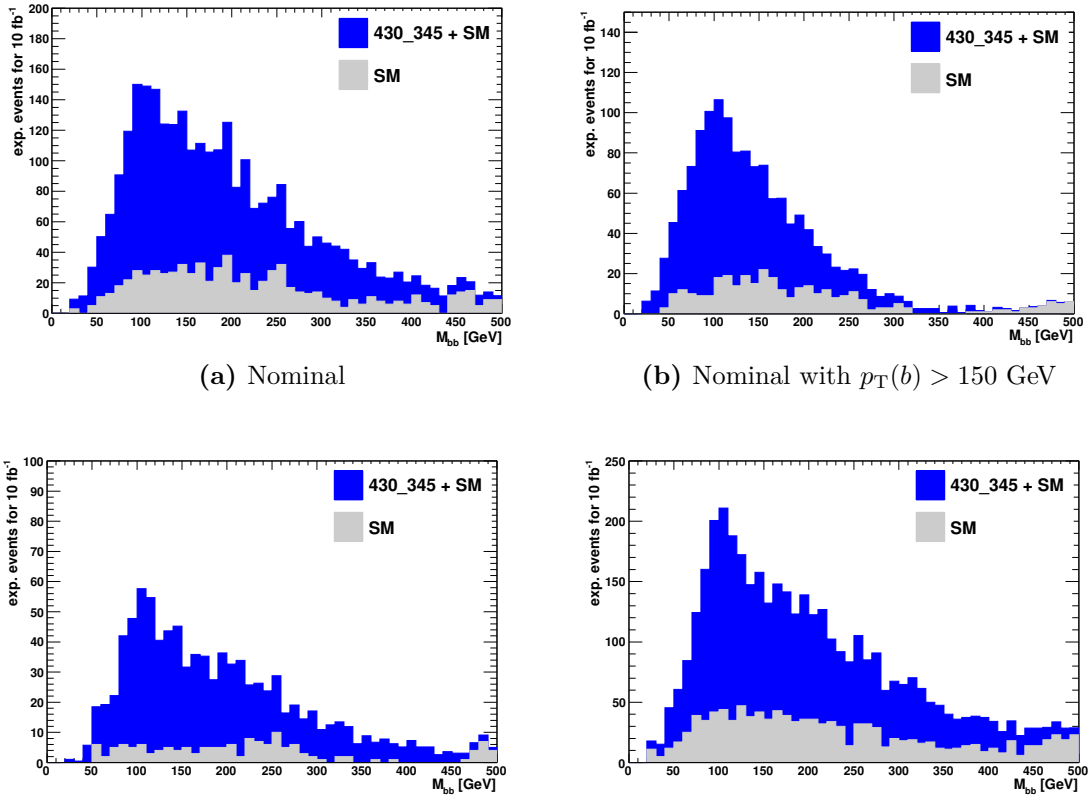

(a) Nominal

(b) Nominal with $p_{\mathrm{T}}(b) > 150$ GeV

(c) CSC

(d) TDR

Figure A.9: Distribution of m_{bb} for reconstructed b-jets for the different event selections (Nominal (a), Nominal plus an upper threshold of 150 GeV on the b-jet momenta (b), CSC (c), TDR (d)). The distributions for the signal point 430_345 are superimposed to the distributions of the SM background. An integrated luminosity of 10 fb^{-1} and a centre-of-mass energy of 10 TeV are assumed.

constrained to be within 5 and 30 GeV. This range has been chosen to be roughly consistent with a detector mass resolution of $\sim 10\%$ in the range of interest. These constraints have also been varied in order to study their impact on the fit (see below). The fit itself is performed over the mass range from 50 to 250 GeV.

Generation of a log-likelihood distribution for the background-only hypothesis

Using the resulting parameters of the polynomial (p_0,...,p_3), 10000 MC experiments are generated. The fit function is used to describe the true background shape and background events are generated according to this shape. Each histogram is filled with the corresponding number of events for a given luminosity and selection efficiency. The result of each MC experiment is fitted once with a polynomial and once with a polynomial plus Gaussian distribution. The fit is done using a binned likelihood. For each histogram, the log-likelihood ratio (LLR) is computed as the ratio of the likelihood values for the polynomial fit λ_{pol} and that for the polynomial plus Gaussian $\lambda_{pol+Gauss}$:

$$LLR = -2 \cdot \log\left(\frac{\lambda_{pol}}{\lambda_{pol+Gauss}}\right). \tag{A.2}$$

To determine the 5σ discovery limit, an exponential extrapolation of the LLR distribution is performed.

Generation of a log-likelihood distribution for the signal hypothesis
The same procedure as described above is applied, but this time the whole fitting function ($pol + Gauss$) is used for the generation of Monte Carlo experiments.

A.4.2 Results

The method described in the previous section is first applied using the nominal event selection. The fitted m_{bb} distributions and the corresponding distributions of LLR values are shown in Fig. A.10 for the signal points 430_345, both for $\tan\beta = 10$ and 50, and SU9. As anticipated from the m_{bb} distributions, where a small signal rate and a peak position close to the kinematic edge of the background distribution is observed, the Higgs boson cannot be discovered for the chosen signal points at 10 TeV with data corresponding to an integrated luminosity of 10 fb^{-1}. This is reflected in the large overlap of the LLR distributions for the signal and the signal+background hypotheses.
The results for the same signal points are also evaluated for the CMS TDR and the ATLAS CSC selections. The fitted m_{bb} distributions and the obtained distributions of LLR values are shown in Fig. A.11 and Fig. A.12 for the TDR and CSC selection, respectively.
Compared to the default selection, a better separation between the background and the signal+background hypotheses is visible for the TDR selection. The fraction of MC experiments for which the signal+background LLR takes values beyond the 5σ upper value of the background hypothesis is significantly increased. A discovery appears more difficult in the SU9 point. In this case also for the TDR selection, the fraction of events with LLR values for the (S+B) hypothesis exceeding the 5σ values of the background hypothesis is small, although again significantly larger than for the nominal selection discussed above. Also for the CSC selection a slight improvement of the LLR distribution compared to the standard selection is visible. However, it is not as large as the shift obtained using the TDR selection.
A more detailed comparison of the event selections is presented in Table A.5, where the fraction of MC experiments is shown for which the LLR value of the signal hypothesis exceeds the 5σ threshold of the background-only hypothesis for the three signal points (430_345 with $\tan\beta = 10$ and 50 and SU9). In addition to the nominal selection as defined in Section A.2, the same selection with an upper threshold on the p_{T} of the b-jets ($p_{\mathrm{T}}(b) < 150$ GeV) is also considered. It is found to provide a better performance for the 430_345 signal point than the nominal selection. For the signal point 430_345, the TDR selection leads to the highest fraction of successful MC experiments, while the CSC selection performs best for SU9.
Both the CMS TDR and the ATLAS CSC selections show a better performance than the nominal selection discussed in Section A.2, which was derived from the inclusive SUSY search with final states with b-jets. This illustrates that a careful optimisation of the event selection needs to be applied to optimise the performance for the resonance searches.

To estimate the behaviour for larger event yields, the procedure is tested for a centre-of-mass energy of 14 TeV and integrated luminosities of 10 and 30 fb^{-1}. When changing from $\sqrt{s} = 10$ TeV to $\sqrt{s} = 14$ TeV the signal cross-sections are increased by a larger factor than the cross-sections for SM background processes, leading to a better signal-to-background ratio. To estimate the discovery sensitivity for these scenarios, the expected numbers of events are scaled up according to the corresponding ratios for the relevant cross-sections. The results obtained for this estimation are shown in Fig. A.13 for the SU9 signal point. Using this

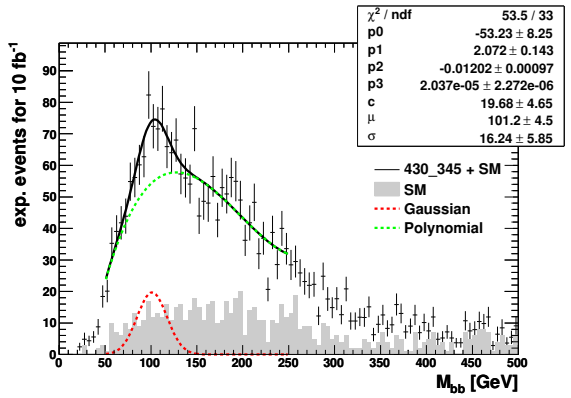

(a) 430_345 ($\tan\beta = 10$): m_{bb}

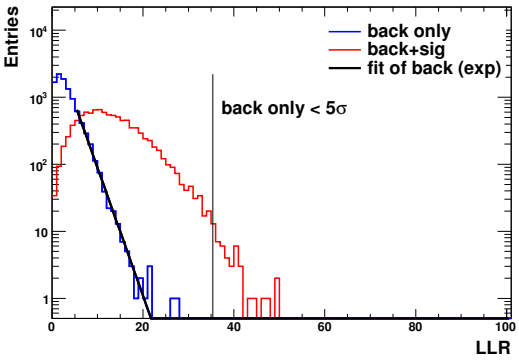

(b) 430_345 ($\tan\beta = 10$): LLR

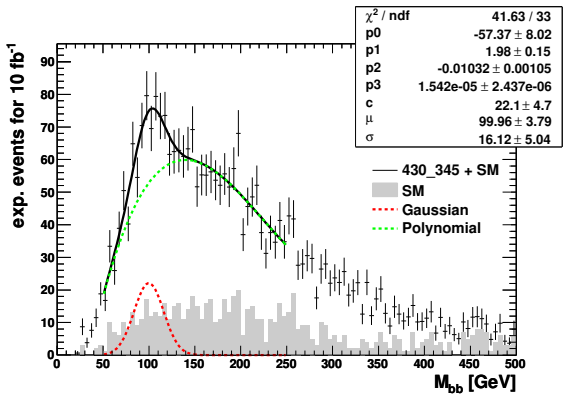

(c) 430_345 ($\tan\beta = 50$): m_{bb}

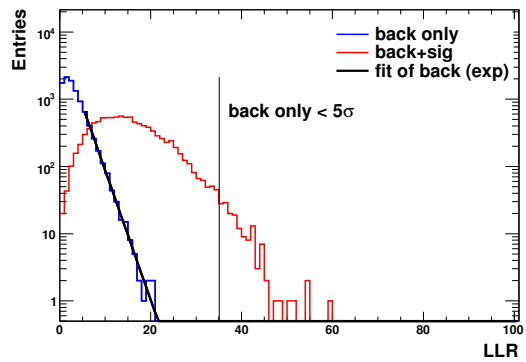

(d) 430_345 ($\tan\beta = 50$): LLR

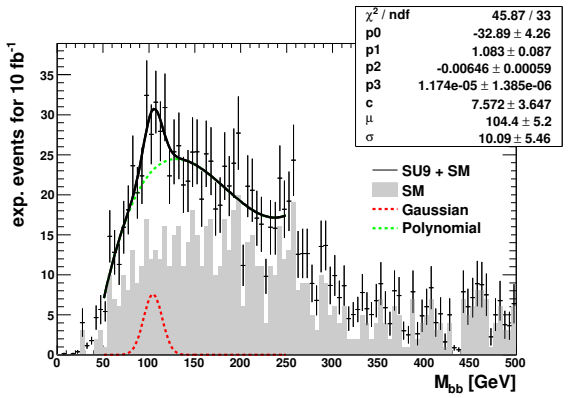

(e) SU9: m_{bb}

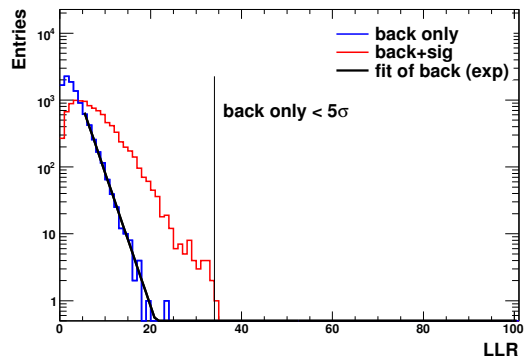

(f) SU9: LLR

Figure A.10: Fit of the m_{bb} distribution and distribution for the obtained LLR values for the nominal event selection for the signal points 430_345 for $\tan\beta = 10$ and $\tan\beta = 50$ and SU9 for $\sqrt{s} = 10$ TeV, assuming an integrated luminosity of 10 fb^{-1}. The LLR values are shown for the signal+background hypothesis (red) and for the background-only hypothesis (blue) (see Section A.4.1).

method, a Higgs boson discovery for the signal point SU9 seems to be possible with 30 fb^{-1} at $\sqrt{s} = 14$ TeV.

The discovery potential in the (m_0-$m_{1/2}$) plane for the two mSUGRA signal grids is also estimated assuming $\sqrt{s} = 14$ TeV and an integrated luminosity of 30 fb^{-1}. Since the number

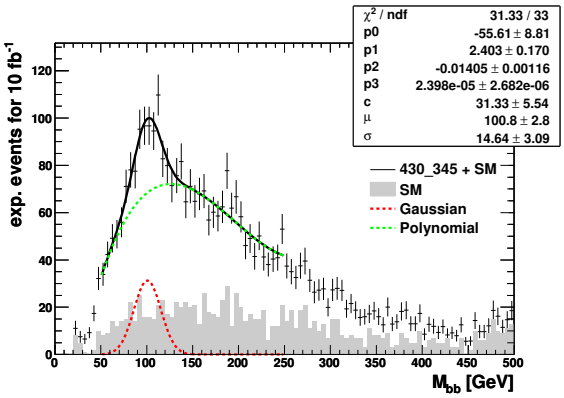

(a) 430_345 ($\tan\beta = 10$): m_{bb}

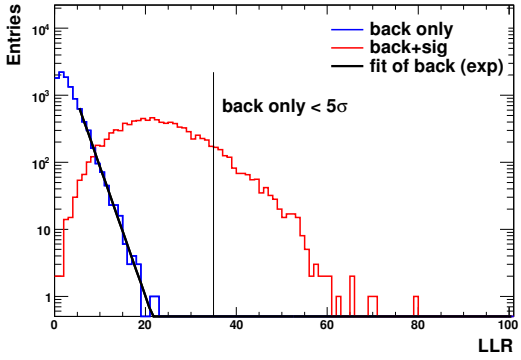

(b) 430_345 ($\tan\beta = 10$): LLR

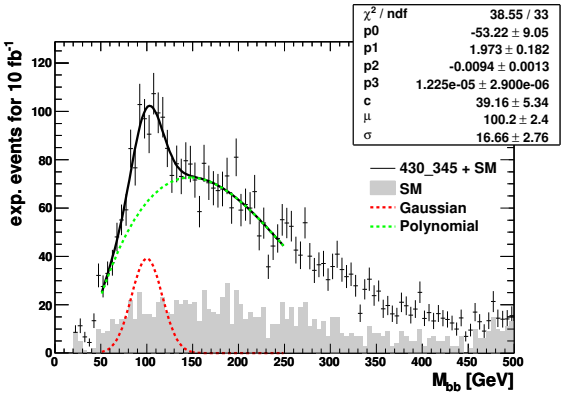

(c) 430_345 ($\tan\beta = 50$): m_{bb}

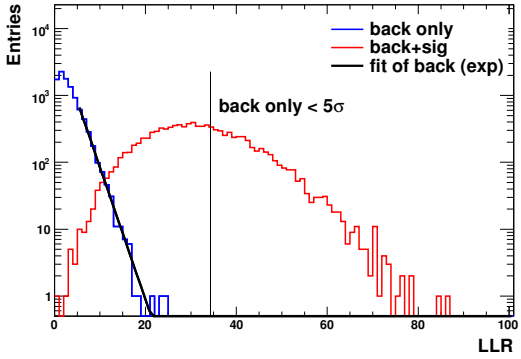

(d) 430_345 ($\tan\beta = 50$): LLR

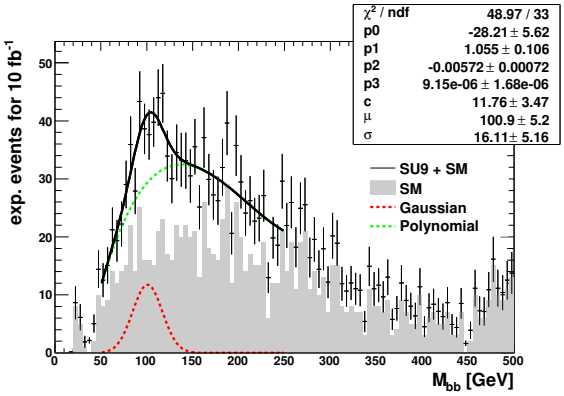

(e) SU9: m_{bb}

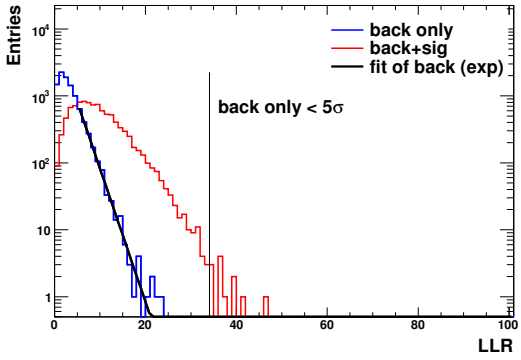

(f) SU9: LLR

Figure A.11: Distribution of m_{bb} (left) and the corresponding LLR values (right) for the CMS TDR selection for the signal point 430_345 for $\tan\beta = 10$ and $\tan\beta = 50$ and SU9 ($\sqrt{s} = 10$ TeV, $\mathcal{L} = 10$ fb^{-1}). The results of the fit are superimposed on the m_{bb} distributions.

of Monte Carlo events for each point is limited to 30000, the following procedure is applied in order to mimimise the effects of statistical fluctuations:

- Only points where at least 300 events pass the entire event selection are considered.

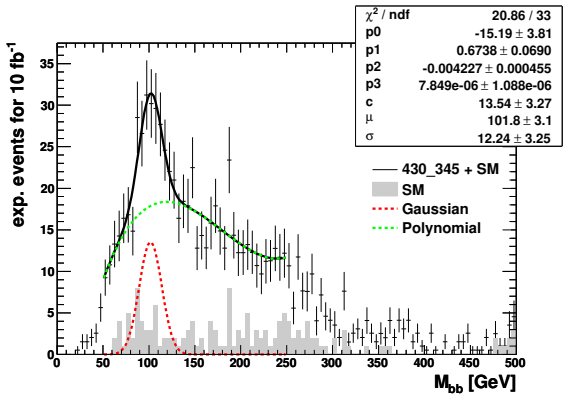

(a) 430_345 ($\tan\beta = 10$): m_{bb}

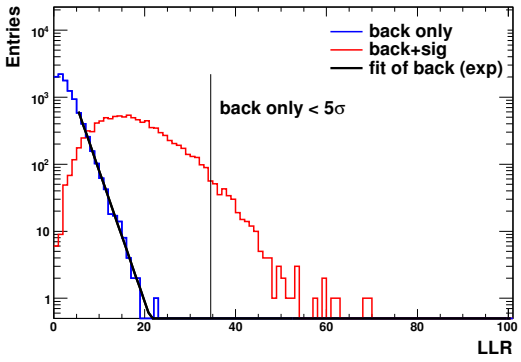

(b) 430_345 ($\tan\beta = 10$): LLR

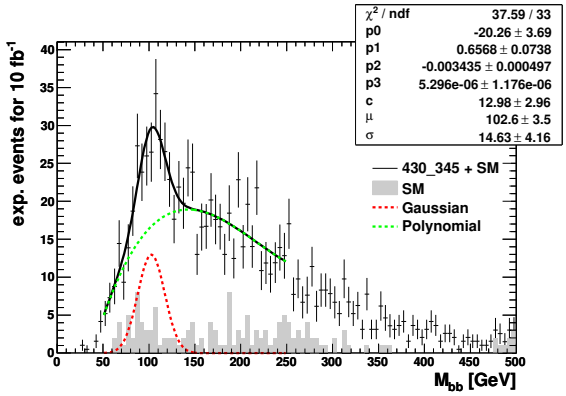

(c) 430_345 ($\tan\beta = 50$): m_{bb}

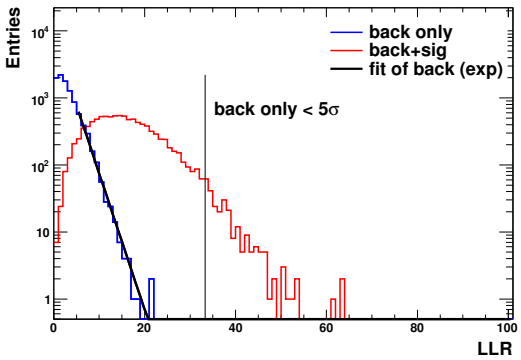

(d) 430_345 ($\tan\beta = 50$): LLR

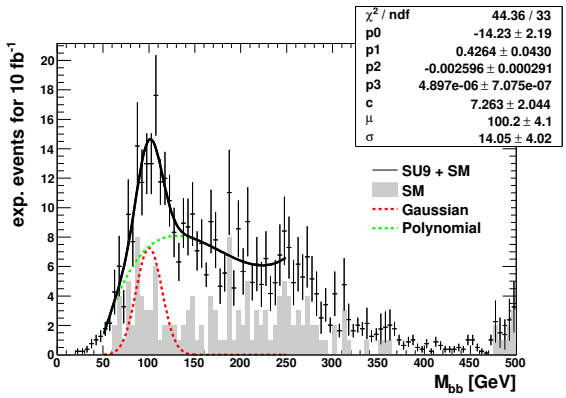

(e) SU9: m_{bb}

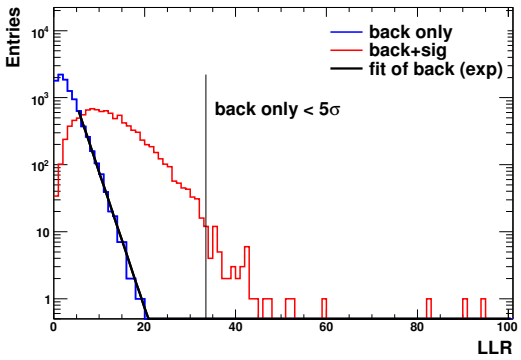

(f) SU9: LLR

Figure A.12: Distribution of m_{bb} (left) and the corresponding LLR values (right) for the ATLAS CSC selection for the signal point 430_345 for $\tan\beta = 10$ and $\tan\beta = 50$ and SU9 ($\sqrt{s} = 10$ TeV, $\mathcal{L} = 10$ fb^{-1}). The results of the fits are superimposed on the m_{bb} distributions.

- The m_{bb} distributions are smoothed separately for Higgs and non-Higgs events[7] and

7 The Higgs and non-Higgs events are separated by a matching procedure based the parton information stored in the MC samples. If less than 100 Higgs events are found, all Higgs and non-Higgs events are considered together.

Selection	430_345 ($\tan\beta = 10$)	430_345 ($\tan\beta = 50$)	SU9
Nominal	0.48 %	1.57 %	0.01 %
Nominal, $p_{\mathrm{T}}(b) < 150$ GeV	2.40 %	9.10 %	– %
CMS TDR	13.83 %	39.81 %	0.12 %
ATLAS CSC	3.5 %	2.66 %	0.62 %

Table A.5: Percentage of cases where the LLR value of the (S+B) hypothesis exceeds the 5σ LLR-threshold value of the background-only hypothesis ($\sqrt{s} = 10$ TeV, $\mathcal{L} = 10$ fb^{-1}). The results are shown for three different SUSY points and for different selections (see text).

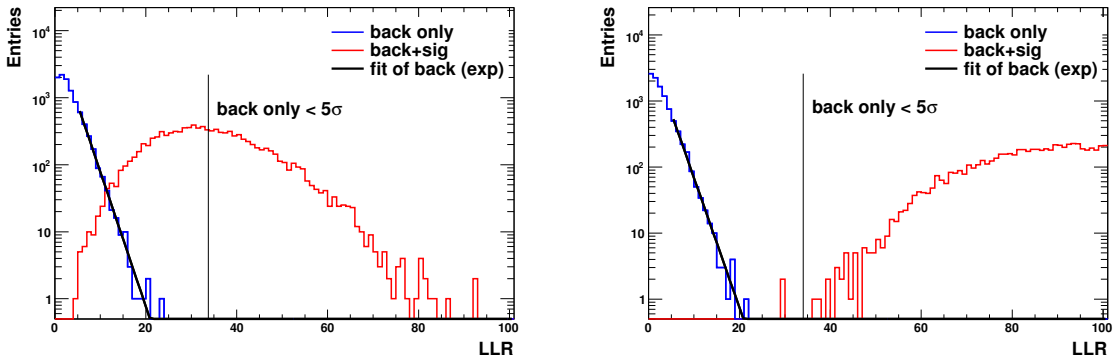

(a) $\mathcal{L} = 10$ fb^{-1} ($\sqrt{s} = 14$ TeV) **(b)** $\mathcal{L} = 30$ fb^{-1} ($\sqrt{s} = 14$ TeV)

Figure A.13: Distribution of the LLR values for the nominal selection for SU9, assuming $\sqrt{s} =$ 14 TeV and an integrated luminosity of 10 fb^{-1} (a) and 30 fb^{-1} (b). The LLR values are shown for the signal+background hypothesis (red) and for the background-only hypothesis (blue).

afterwards randomly filled with the number of events corresponding to $\sqrt{s} = 14$ TeV and 30 fb^{-1}.

The filling is performed 100 times providing 100 initial histograms on which to perform the LLR method as described before[8]. For each of those the percentage of cases where the signal LLR is above the 5σ threshold of the background-only LLR is computed. Finally, the mean values of the resulting percentages are calculated. For this part of the study the Gaussian resolution for the fits is restricted to be within 10 and 20 GeV. The results obtained are shown in Fig. A.14 for the three considered event selections. Making the conventional requirement that a point can be discovered, if the median of the MC experiments for the signal hypothesis is found beyond the 5σ LLR threshold for the background-only hypothesis, Higgs bosons decaying to $b\bar{b}$ can be discovered in the region at large $m_{1/2}$ values for m_0 values around 500 GeV. The performance of the CMS TDR selection is found to be superior and, compared to the other selections, the discovery region is larger. Since the CSC selection is based on harsher thresholds, the number of SUSY points for which the analysis is performed is smaller (due to the requirement on the expected event numbers).
An example of a signal point for which discovery could be claimed is shown in Fig. A.15. This figure should be compared to the corresponding figure at a lower centre-of-mass energy and a lower integrated luminosity (Fig. A.10).

8 The number of MC experiments is reduced to 1000 instead of 10000 to reduce the computing time.

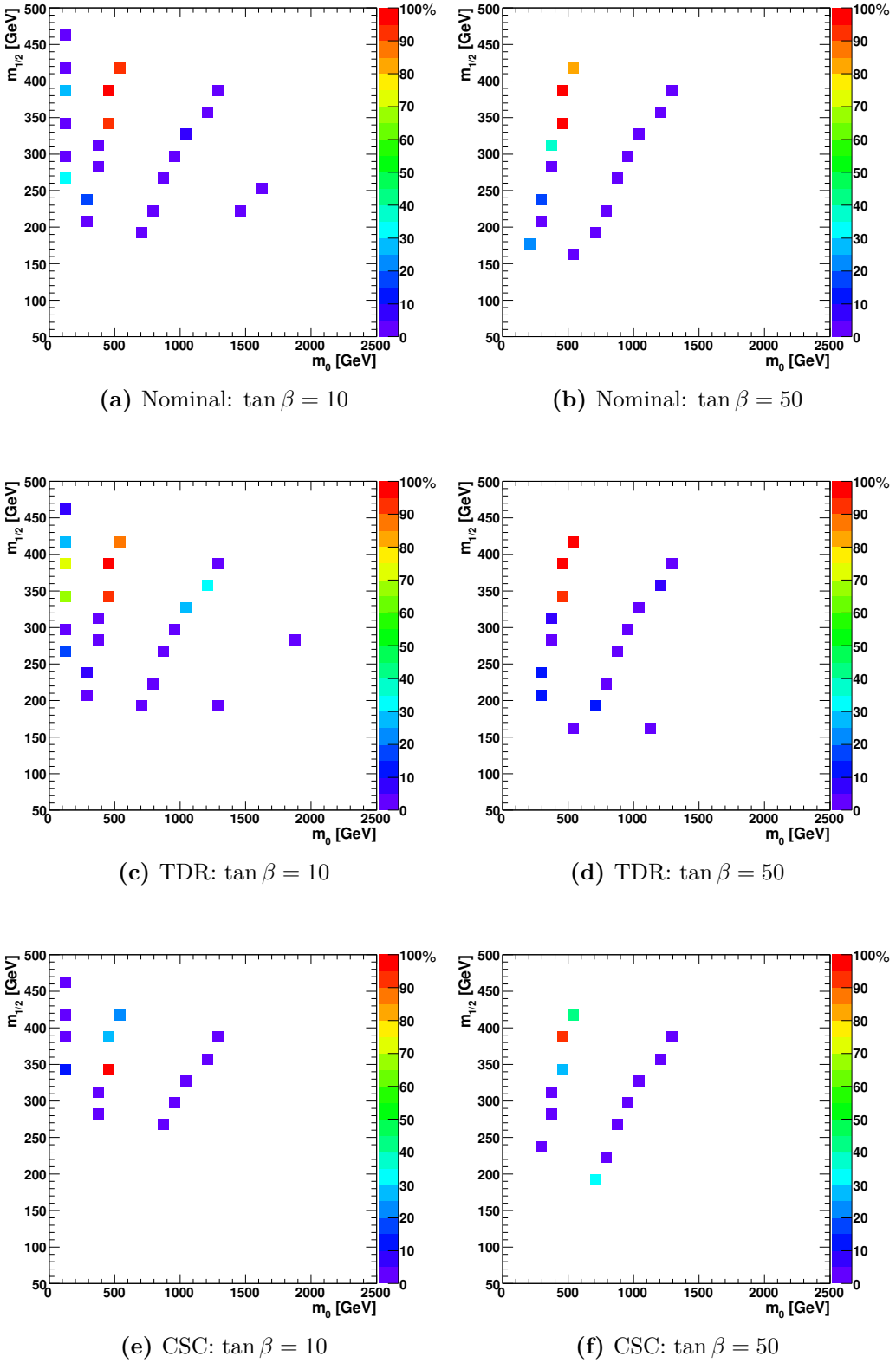

(a) Nominal: $\tan\beta = 10$ **(b)** Nominal: $\tan\beta = 50$

(c) TDR: $\tan\beta = 10$ **(d)** TDR: $\tan\beta = 50$

(e) CSC: $\tan\beta = 10$ **(f)** CSC: $\tan\beta = 50$

Figure A.14: The discovery potential for the nominal, the CMS TDR, and the ATLAS CSC event selections for $\tan\beta = 10$ (left) and $\tan\beta = 50$ (right), assuming $\sqrt{s} = 14$ TeV, and an integrated luminosity of 30 fb^{-1}. The fraction of Monte Carlo experiments is shown for which the LLR value for the signal hypothesis is above the 5σ threshold of the background-only hypothesis.

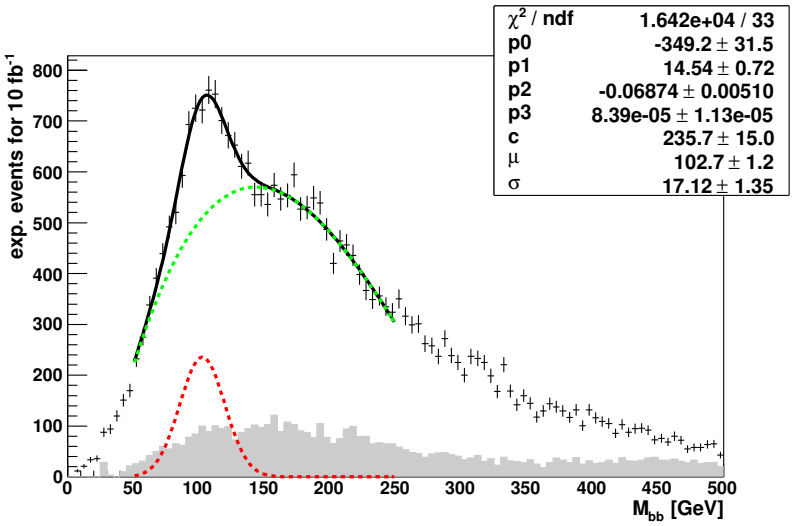

Figure A.15: Distribution of m_{bb} for the SUSY point 430_345 for $\tan\beta = 10$ after applying the whole event selection for $\sqrt{s} = 14$ TeV and assuming an integrated luminosity of 30 fb^{-1}. The result of the signal plus background fit is superimposed.

A.4.3 Effect of Systematic Uncertainties

The proposed procedure to extract the discovery significance has systematic uncertainties. The most important one is linked to the modelling of the background contribution. One important question is whether fake signals can be reconstructed if the polynomial parametrization is not adequate to describe the background shape. To answer this question, three different background shapes are assumed and used to generate the MC experiments. The background distributions are modeled according to the following functions:

- A Gamma distribution: GammaDist (5, 10, 30).
- A Gaussian distribution: Gauss (150, 75).
- A semi-circle distribution: $\sqrt{150^2 - (x - 150)^2}$.

In order to minimise the effect of statistical fluctuations and purely address the effect of the assumptions made on the shape, the distributions are randomly filled with 10000 events per MC experiment. The resulting background distributions are exemplarily shown in Fig. A.16. Following the procedure described in Section A.4.1, the distributions are fitted with a polynomial for the background-only hypothesis and a polynomial plus Gaussian distribution for the signal hypothesis to obtain the LLR values.
If the width of the Gaussian is left unconstrained, a non-physical width (too narrow) is fitted for most of the MC experiments. The fractions of experiments with reasonable results for the Gaussian width ($5 < \sigma < 30$ GeV or $10 < \sigma < 20$ GeV), i.e. compatible with the expected resolution of a Higgs resonance, are given in the second and third columns of Table A.6. They are found below 20% for Gaussian widths in the range of 10-20 GeV. Out of the MC experiments with a reasonable width, the fraction is calculated where the LLR value is above 20.[9] The resulting fractions are given in the third and fourth column of Table A.6. They are

9 The value of 20 is taken as a reference value. This is a conservative value concerning a 5σ discovery. As can be seen from the LLR distributions of the background-only fits presented in the previous sections, the 5σ thresholds are found for LLR values around 35.

found to be small, indicating that the probability to fake Higgs-resonance like signals due to the assumptions made on the background shape are small.
The corresponding LLR distributions for the MC experiments that have a Gaussian width compatible with the experimental resolution are shown in Fig. A.17 for the two regions of the Gaussian widths constraints. Although with the semi-circle shape model the largest fraction of fits with an acceptable Gaussian width is found, the fraction of experiments passing the $LLR > 20$ threshold is the smallest. From the background shapes considered, the Gamma distribution leads to the largest fraction of experiments in the tail.
The fraction of experiments in the tail, and therefore the systematic uncertainties due to the background model, can be largely reduced by tighter constraints on the LLR threshold and the accepted Gaussian width. For a search in data, the LLR threshold to claim a discovery should be raised to larger values in order to prevent a fake discovery. Thereby the discovery sensitivity would be slightly degraded. The size of the degradation also depends on the constraints that are put on the width of the signal shape.

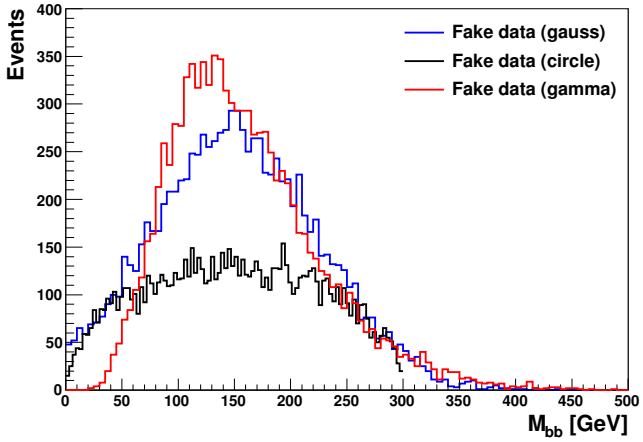

Figure A.16: Exemplary background distributions obtained for the three assumptions on the shape (Gaussian, semi-circular and Gamma distributed).

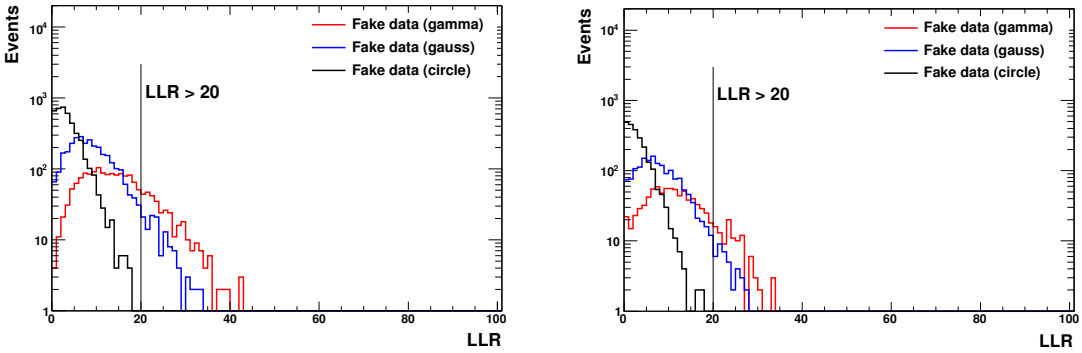

Figure A.17: Distributions of the LLR values for fits to the MC experiments based on the three background models discussed above. Only the LLR values of those experiments are considered, for which the fitted Gaussian width is found in the range of 5-30 GeV (left) and 10-20 GeV (right).

Background shape	σ in range		$LLR > 20$	
	5 – 30 GeV	10 – 20 GeV	5 – 30 GeV	10 – 20 GeV
Gamma distribution	16.7%	6.0%	0.57%	0.05%
Gauss distribution	31.3%	12.6%	0.39%	0.04%
Semi-circle distribution	42.1%	18.0%	–	–

Table A.6: Percentage of cases where the fitted Gaussian width of the MC experiments is found within 5 GeV $< \sigma <$ 30 GeV (second column) or within 10 GeV $< \sigma <$ 20 GeV (third column), and fraction of successful MC experiments with $LLR > 20$ for both cases where 5 GeV $< \sigma <$ 30 GeV (fourth column) or 10 GeV $< \sigma <$ 20 GeV (last column).

A.5 Summary

A strategy for the search of $b\bar{b}$ resonances in SUSY final states has been presented. Such resonances might appear via decays of Higgs bosons in cascade decays of SUSY particles. In order to identify a resonance in the presence of the Standard Model background and an unknown background from the production of SUSY particles, a model independent fit of the m_{bb} distribution is applied. No strong assumptions on the background are made, except that it has a smooth shape that can be parametrized by a polynomial. A Gaussian resonance on top of this background is assumed for the signal. A likelihood ratio approach was used to evaluate the ATLAS discovery potential. The probability to fake a signal due to an imperfect modelling of the background was studied and found to be small (below 0.1% for the assumed scenarios).

Applying the method to mSUGRA scenarios, the ATLAS discovery reach was studied for several benchmark points for $\tan\beta$ values of 10 and 50, $A_0 = 0$ and $\mu > 0$. A discovery seems possible for $400 < m_0 < 700$ GeV and $330 < m_{1/2} < 430$ GeV at $\sqrt{s} = 14$ TeV, for both $\tan\beta = 10$ and $\tan\beta = 50$ scenarios. It would, however, require integrated luminosities of 30 fb^{-1} or higher.

APPENDIX B

The DCS Data Viewer

In this appendix, the layout of the DCS Data Viewer (DDV) is presented. It is a web-based application that allows to access and visualise the historical data of the ATLAS DCS.
The DCS was shortly introduced in Section 3.2.5 and provides information for the monitoring of the infrastructure and the different subsystems of the ATLAS detector. All relevant data of the subsystems are written to an online database. The online database is replicated to an offline database which can be accessed via the DDV interface. In Figure B.1, the data access path is illustrated.

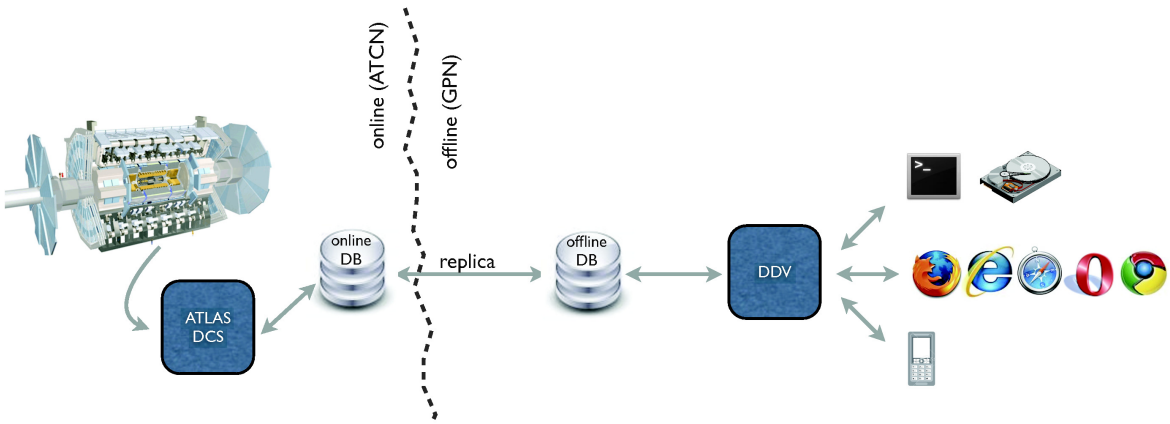

Figure B.1: Schematic illustration of the access to the DCS information via the DDV interface [172].

The DDV interface was developed considering the following specifications:

- platform and browser independence,
- reasonable startup (< 10 s) and response time ($\sim$ s),
- multiple data selection options,
- multiple output formats (chart, table, ASCII, ROOT),
- reproducible configuration of the output with the XML format,
- protection mechanism to avoid malicious use of the database.

The implementation is performed in a modular structure, based on a server-client model. The advantage of this approach is that the access to the data resources is centralised in

the server part, while the client part is flexible enough to integrate new output formats and plugins. Requests from the client to the server are made with the Hypertext Transfer Protocol (HTTP). A schematic view of the architecture is shown in Fig. B.2.
The main contributions within this thesis were made to the development on the client side. In particular a ROOT output format was implemented, multiple options were added to the default output plugin in form of a Java Applet chart and a user friendly menu to configure the options for the chart was implemented.
More information on the server and client setup are given in Sections B.1 and B.2, respectively.

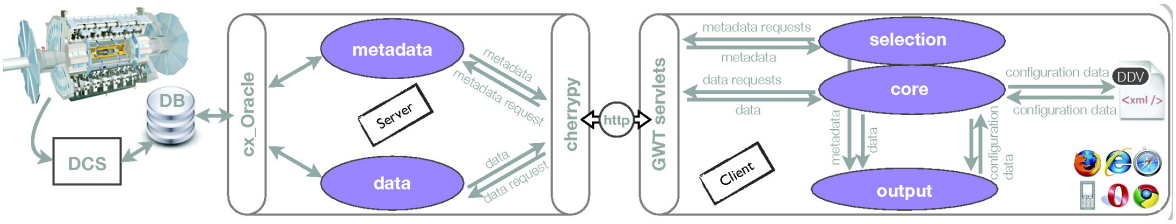

Figure B.2: Schematic illustration of the DDV architecture [172].

B.1 Server

The server is designed to handle the communication with the database. A copy of the metadata information (e.g. variable names of the archived data) is stored directly on the server to allow for a quick response time to metadata queries.[1] For the actual data this procedure is not possible because the number of stored items is too large ($\sim 10^8$). A request to the database contains the metadata information of the requested item (its variable name and the database schema the item belongs to) and the desired time range. The database response consists of the complete metadata information of the requested item and its recorded values and timestamps within the selected time range.

B.2 Client

The client part of DDV is developed in Java. It is compiled using the Google Web Toolkit (GWT) [173] to provide a browser independent AJAX-based (Asynchronous JavaScript and XML) [174] web application.
The selection and the configuration of the requests are managed with the GWT framework (via menu items, buttons, tables and other widgets). Variables can be selected by browsing the metadata information either through a column-based list or with the help of a search engine. The configuration primarily consists of the chosen options for the visualisation of the data (e.g. line colors and axis ranges). Is is possible to store the configuration in the XML format and reload it at a later time. The dataset information and configuration options are passed to the output plugins. The output can be either stored into files, e.g. in a ROOT or ASCII format, or directly visualised in the browser.

1 The metadata information is updated every 24 hours.

Java Applet Chart

The default output is a chart which is implemented in the form of a Java Applet and based on the JfreeChart libraries [175]. The data can be displayed as time series, and one- or two-dimensional histograms if applicable. In Fig. B.3, two examples for the configuration of the chart are shown. Some of the options to display the data can be changed interactively in the chart, others can only be accessed in the configuration panel.[2]

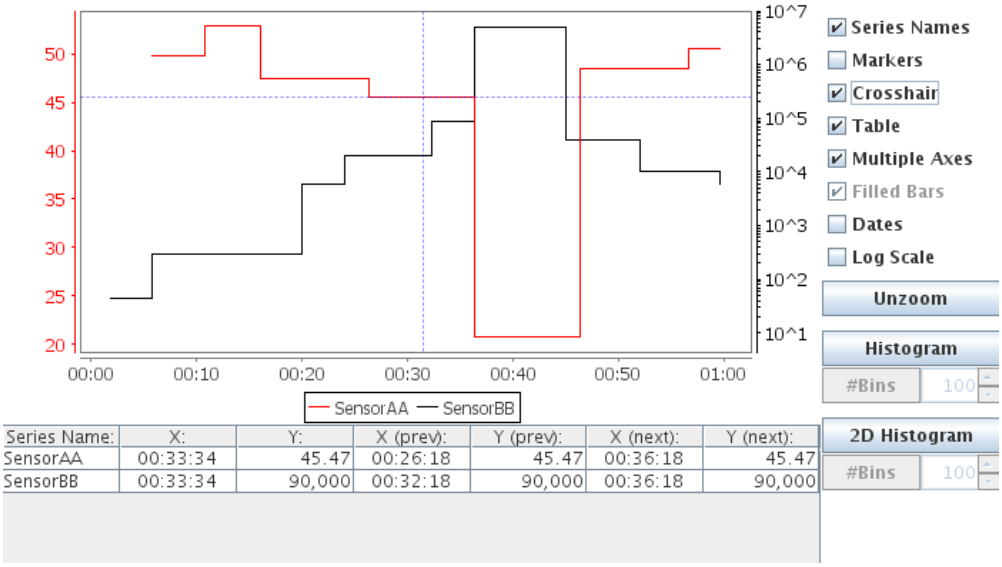

(a) option with multiple axis and crosshair information

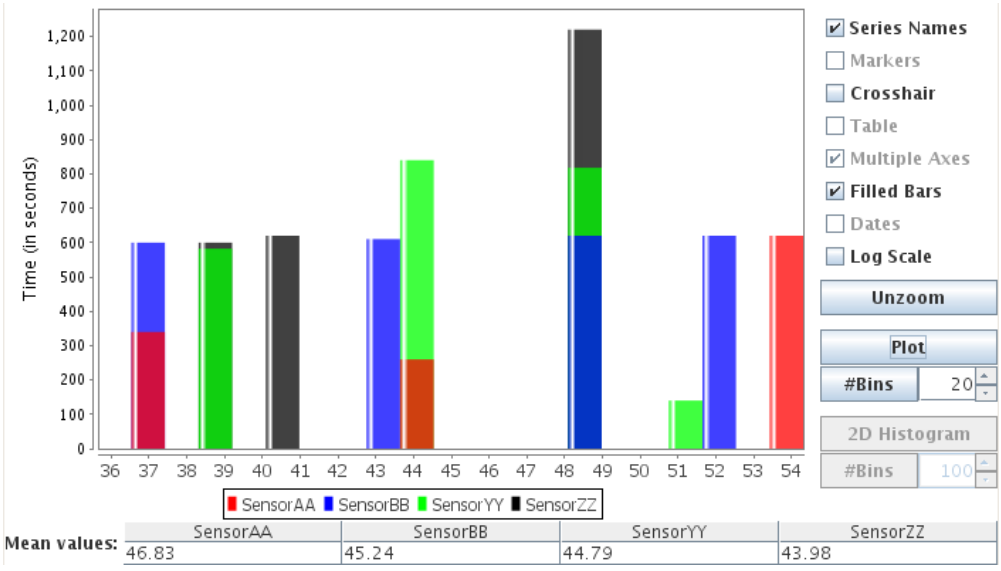

(b) histogram option

Figure B.3: Examples for the Java Applet chart output.

2 Also variables that are provided in a string format (e.g. *ON* and *OFF* for a power setting module) can be displayed. However, a reduced number of configuration options is available in this case.

APPENDIX C

Additional Information on Sbottom Validation Regions

Results for the validation regions, defined for the sbottom-pair production searches in Section 6.3.2, are presented here. The nominal no lepton validation regions are labeled as VR0L and the multi-jet enriched regions are labeled as VR0LQCD. The validation regions used to study the b-tagging stability are denoted by VR0L0B, VR1L1B and VR2L1B.
The results for the no lepton validation regions and the $e\mu$ selection, in case of SR2 and SR3, are shown in Table C.1 for SR1, C.2 for SR2 and C.3 for SR3. The b-tagging validation regions results are given in Table C.4 for SR1, C.5 for SR2 and C.6 for SR3.

channel	VR0L_SR1	VR0LQCD_SR1
Observed events	204	1113
Fitted bkg events	176.64 ± 28.12	518.31 ± 352.29
Fitted Top events	140.45 ± 32.22	55.81 ± 15.36
Fitted Z events	25.70 ± 5.35	15.68 ± 2.85
Fitted W events	7.77 ± 5.55	9.58 ± 6.19
Fitted QCD events	2.04 ± 2.03	435.74 ± 351.63
Fitted Others events	0.68 ± 0.53	1.51 ± 0.85
MC exp. SM events	190.40	533.76
MC exp. Top events	152.29	60.53
MC exp. Z events	24.69	15.06
MC exp. W events	10.71	13.20
MC exp. QCD events	2.04	443.46
MC exp. Others events	0.68	1.51

Table C.1: Results of the background-only fit and observed data events for the no lepton validation regions for SR1. Also the MC expectations before applying the fit are shown.

channel	VR0L_SR2	VR0LQCD_SR2	CR2LDF_SR2
Observed events	121	131	121
Fitted bkg events	110.51 ± 22.11	103.72 ± 57.49	96.21 ± 9.24
Fitted Top events	95.60 ± 22.90	15.50 ± 4.88	95.21 ± 9.35
Fitted Z events	9.28 ± 1.66	2.71 ± 0.60	—
Fitted W events	2.80 ± 1.09	4.33 ± 2.18	—
Fitted QCD events	2.20 ± 2.21	80.32 ± 56.85	—
Fitted Others events	0.63 ± 0.56	0.87 ± 0.55	1.00 ± 0.57
MC exp. SM events	117.27	81.36	103.59
MC exp. Top events	102.68	16.62	102.58
MC exp. Z events	8.95	2.62	—
MC exp. W events	2.80	4.34	—
MC exp. QCD events	2.20	81.36	—
MC exp. Others events	0.64	0.87	1.00

Table C.2: Results of the background-only fit and observed data events for no lepton validation regions for SR2. Also the MC expectations before applying the fit are shown.

channel	VR0L_SR3	VR0LQCD_SR3	CR2LDF_SR3
Observed events	2272	3762	54
Fitted bkg events	2259.01 ± 474.67	4307.92 ± 1717.73	51.39 ± 10.10
Fitted Top events	1810.47 ± 425.47	1153.83 ± 269.60	50.96 ± 10.10
Fitted Z events	128.39 ± 59.53	72.69 ± 29.13	—
Fitted W events	118.53 ± 46.04	78.09 ± 25.35	—
Fitted QCD events	169.21 ± 168.42	2973.57 ± 1653.12	—
Fitted Others events	32.42 ± 18.36	29.75 ± 17.51	0.44 ± 0.24
MC exp. SM events	2227.23	2954.96	51.11
MC exp. Top events	1803.54	1149.51	50.68
MC exp. Z events	103.52	58.61	—
MC exp. W events	118.47	78.06	—
MC exp. QCD events	169.21	2955.11	—
MC exp. Others events	32.38	29.72	0.44

Table C.3: Results of the background-only fit and observed data events for the no lepton validation regions for SR3. Also the MC expectations before applying the fit are shown.

channel	VR1L1B_SR1	VR2L1B_SR1	VR0L1B_SR1
Observed events	2244	1121	3241
Fitted bkg events	2231.80 ± 374.43	901.69 ± 147.92	2818.55 ± 491.36
Fitted Top events	1507.54 ± 316.56	71.23 ± 21.30	1124.88 ± 278.40
Fitted Z events	6.06 ± 1.41	784.51 ± 144.21	951.07 ± 189.77
Fitted W events	590.77 ± 449.66	—	660.20 ± 498.77
Fitted Others events	127.43 ± 63.66	45.95 ± 22.75	82.40 ± 40.94
MC exp. SM events	2580.16	876.58	3123.72
MC exp. Top events	1633.65	77.19	1219.26
MC exp. Z events	5.81	753.46	913.23
MC exp. W events	813.35	—	908.90
MC exp. Others events	127.34	45.92	82.34

Table C.4: Results of the background-only fit and observed data events for the one b-jet validation regions for SR1. Also the MC expectations before applying the fit are shown.

channel	VR1L1B_SR2	VR2L1B_SR2	VR0L1B_SR2
Observed events	4875	1121	1543
Fitted bkg events	5008.13 ± 501.14	899.52 ± 162.66	1361.02 ± 160.88
Fitted Top events	3413.93 ± 642.45	71.80 ± 21.82	284.87 ± 81.49
Fitted Z events	11.07 ± 2.86	782.03 ± 157.41	570.81 ± 117.64
Fitted W events	1412.34 ± 342.22	—	465.09 ± 100.07
Fitted Others events	170.78 ± 88.99	45.70 ± 23.60	40.27 ± 21.11
MC exp. SM events	5279.42	876.58	1362.50
MC exp. Top events	3680.12	77.19	305.85
MC exp. Z events	10.68	753.46	549.89
MC exp. W events	1417.08	—	466.18
MC exp. Others events	171.57	45.92	40.45

Table C.5: Results of the background-only fit and observed data events for the one b-jet validation regions for SR2. Also the MC expectations before applying the fit are shown.

channel	VR1L1B_SR3	VR2L1B_SR3	VR0L1B_SR3
Observed events	5886	1223	2667
Fitted bkg events	6455.88 ± 1017.20	1435.77 ± 339.94	2420.63 ± 357.02
Fitted Top events	5403.35 ± 1013.73	363.74 ± 101.77	994.42 ± 250.39
Fitted Z events	11.58 ± 5.11	1057.18 ± 354.83	647.61 ± 210.77
Fitted W events	1010.80 ± 246.37	0.56 ± 0.09	767.36 ± 180.88
Fitted Others events	30.15 ± 15.90	14.29 ± 7.39	11.25 ± 5.97
MC exp. SM events	6730.60	1041.30	2219.48
MC exp. Top events	5681.23	382.32	1045.38
MC exp. Z events	7.06	644.11	394.53
MC exp. W events	1012.13	0.56	768.30
MC exp. Others events	30.18	14.30	11.26

Table C.6: Results of the background-only fit and observed data events for the one b-jet validation regions for SR3. Also the MC expectations before applying the fit are shown.

Acknowledgments

In the first place, I want to thank Prof. Karl Jakobs for providing me the opportunity to work as a PhD student at the ATLAS experiment. It was a great pleasure to contribute to the interesting field of SUSY searches.
A very special thank goes to my supervisor Iacopo Vivarelli for his support and guidance. Thank you for your patience and focus to the relevant details in longer discussions. Also, I would like to thank my former supervisor Xavier Portell Bueso who introduced me to the field of SUSY searches with b-jets. Thanks for the fruitful collaboration in the SUSY with b-jets working group, in particular to Monica D'Onofrio, Davide Costanzo, Antoine Marzin, Alexandru Dafinca, Kerim Suruliz, Takashi Yamanaka, Bart Butler, Daniel Silverstein and Alan Tua. For their support in my service work I thank Charilaos Tsarouchas and Stefan Schlenker.
Thanks to the Freiburg ATLAS group and the Graduiertenkolleg for a pleasant work environment. A special thank goes to my office mates Stefan, Liv and Julian. I would also like to thank Felix and Julian for extensive computing support. Special thank goes to Christina Skorek for helping me with all administrative tasks. For their financial support, I thank the CNV foundation.
Finally, I thank all my family and friends accompanying me in the last years.
Daniel and Leonas, you are the central part of my life. Thank you, Daniel, for your patience and support. Thank you, Leonas, for the joy and cheerful distraction from work. Also, I would like to thank my parents Heike and Thomas for helping out in stressful situations.